Stability Analysis of CICCs by Measurement of Energy Deposition due to Pulsed Current Disturbances

by

MUSTAFA KAMAL AHMED
B.S. Electrical Engineering, MIT, 1992

Submitted to the Department of Nuclear Engineering
in partial fulfillment of the requirements for the degrees of

Nuclear Engineer

and

Master of Science

at the

MASSACHUSETTS INSTITUTE OF TECHNOLOGY

February 1996

Author.....
Department of Nuclear Engineering
February 12, 1996

Certified by.....
Joseph V. Minervini
Head of Fusion Technology and Engineering Division, PFC
Thesis Supervisor

Read by.....
Jeffrey Freidberg
Professor of Nuclear Engineering
Thesis Reader

Accepted by.....
Jeffrey Freidberg
Chairman, Departmental Committee on Graduate Students

Stability Analysis of CICCs by Measurement of Energy Deposition due to Pulsed Current Disturbances

by

Mustafa Kamal Ahmed

B.S. Electrical Engineering, MIT, 1992

Submitted to the Department of Nuclear Engineering
on February 13, 1996, in partial fulfillment of the
requirements for the degrees of
Nuclear Engineer
and
Master of Science

Abstract

The ability to accurately predict the stability margins for cable-in-conduit conductors is of fundamental importance to ensure the safe and reliable operation of large-scale superconducting magnets used in fusion applications, such as the toroidal field coils for ITER. These magnets are subject to absorption of energy due to electromagnetic and mechanical disturbances. For the conductors to be stable to these disturbances, their potential to handle such energy depositions needs to be ascertained. This requirement translates into the necessity to calculate the energy deposited in the conductor because of a disturbance efficiently and with a great deal of exactness. Traditional means of introducing disturbance energy into the CICC, namely inductive heating, involve the estimation of AC losses in the cable, a process which is not only quite complicated but also has doubtful dependability. There is a need to develop a methodology for inputting disturbance energy inside the cable which makes it computationally simple to estimate this energy, and therefore, promotes confidence in the prediction of stability margins for the cable. The pulsed current disturbances method of analyzing stability is investigated as a likely possibility.

An experiment was constructed which enabled the stability analysis of a CICC by using pulsed current disturbances. The experiment allows for the determination of the energy deposited in the CICC due to a pulsed current disturbance in a simple and reliable fashion. Based on the amount of energy needed to quench the conductor for varying operating conditions, the stability margin for the cable can be identified.

Two different sources of pulsed current were used in the experiments performed. The single pulser produced a single half sine-wave of current with a pulse width of 2 ms whereas the double pulser produced either one or two half sine-

waves of 10 ms duration. The time delay between the two pulses of the double pulser could be varied from zero to 100 ms. The pulse(s) generated by the pulser was superposed on the transport current through the sample CICC. The energy deposited by the pulse(s) in the conductor was calculated by integrating the product of sample voltage and current, measured independently, for the duration of the pulse. The integration gives an accurate measurement of resistive losses in the cable under the assumption of constant transport current and identical current distribution in the cable at the beginning and the end of the current pulse, since the reactive losses will integrate to zero. Three different CICCs were analyzed during the experiments: two CICCs were the US-DPC cable samples, one of them hybrid, and one was the TPX PF coil hybrid sample. As there was no variation in the background magnetic field, all the major components of AC losses except self-field losses were avoided. The self-field losses for the three cables were estimated and were found to be negligible compared to the resistive losses (usually in the 0.1-5% range) except for coupling losses of the filaments in each strand, which were found to be of the same order. Their calculation, however, made assumptions, which would overestimate them by at least an order of magnitude. These losses need to be investigated futher.

From the experimental results, the stability margins were deduced for the cables. Besides a few data points attributed to the training of the cables to the disturbances introduced, the results are in good agreement with theory. The stability margins in the well-cooled regime were as high as 600 mJ/cc. The hybrid cables have not been used in stability experiments using alternative methods, so no comparison of the results with results from other experiments was made.

Stability analysis of CICCs using pulsed current disturbances is deemed an attractive alternative to other methods including inductive heating due to the simplicity of its technique for calculating energy deposition and due to its avoidance of difficulties encountered in the measurement of AC losses. Although pulsed currents are not the probable disturbances during normal operation of ITER magnets, it is possible that the likely disturbances could be modeled as pulsed current disturbances in terms of energy deposition.

Thesis Supervisor: Joseph V. Minervini
Title: Head of Fusion Technology and Engineering Division, PFC

Acknowledgments

I would like to thank Joe for his dedicated support and extremely helpful guidance. He is, by far, the kewlest advisor around. My gratitude to Makoto and Sangkwon, from whom I have learnt a lot about what it means to be an experimentalist, especially being patient and thorough. Thanks also to Dan and Steve for helping with the experiments, but more importantly for having a sense of humor. I am grateful to Prof. Freidberg for being the reader.

Writing this thesis would not have been possible without having a friend like Bilal. I am completely indebted to him for always being there. Bilal, you are a wonderful friend. Thanks to Rhonda and Asif for helping out as well.

My dearest friends Wasiq and Sadia, thanks for keeping me sane. And thanks to Yasir and Sara for all the yummy biryanis and daals and making me feel cared for.

Finally, I would not have been where I am today if I did not have complete support of my family, especially Ammi. This thesis is dedicated to her.

To
Huzaifah

Contents

List of Figures

List of Tables

Chapter 1

Introduction

Cable-in-conduit conductors (CICC[1]) have become the leading choice of superconducting cables for use in large scale superconducting magnets, such as the ones which will be used in ITER[2]. Although CICCs have high-voltage integrity, have a robust structure, their helium inventory and AC losses are relatively low, and they can handle quench pressures safely, their stability is limited, and they are metastable. This is because the helium flowing in the conduit cannot be replaced quickly in the event of a quench, and a large perturbation will quench the superconductor. The stability of the CICC, as a consequence, is limited by the available helium enthalpy, but can be fairly high if the helium enthalpy is fully utilized. One of the main issues in stability experiments today is the estimation of the energy deposited inside the superconducting cable by a disturbance, electrical or mechanical, to aid in the determination of stability margins for the cable.

1.1 Background

In this section, the physical phenomenon of superconductivity is introduced and important physical aspects of superconductors are delineated, including a description of type-I and type-II superconductors. This is followed by a discussion of

[1]Also referred to as internally-cooled and cabled or force-cooled conductors
[2]International Thermonuclear Experimental Reactor

the advantages of CICCs, which have encouraged their use in fabrication of superconducting cables. These cables are employed in manufacturing large-scale high-current and high-field superconducting magnets for application in diverse areas such as magnetically-confined nuclear fusion [27, 48], particle acceleration [28] and magnetic levitation [37]. The various means of dissipation of energy in superconducting cables are briefly considered and the concept of stability in the context of superconducting cables is introduced.

1.1.1 Superconductivity

Superconductivity was discovered by Heike Kamerlingh Onnes [20] in 1911 in Leiden, the Netherlands. In an experiment that he performed with his colleagues, Onnes observed that as the temperature of an extremely pure mercury thread was reduced to 4.2 K, its electrical resistance dropped by a factor of about 10000 within a temperature change of 0.02 K (See Fig. 1-1 on page 19). Onnes claimed that mercury passed into a new state called the superconducting state because of its electrical properties. Since then, not only a large number of metallic elements have been found to be superconductors, but also quite a few alloys and metallic compounds, and more recently, certain ceramic compounds as well.

Superconductors are characterized by three threshold variables, namely critical temperature (T_c), critical current density (J_c) and critical magnetic field (B_c), which determine the region in the BJT plane (see Fig. 1-2 on page 20) where the superconducting properties of the material are preserved. Superconductors, in general, tend to be very bad conductors outside this regime. If any of the three threshold values is exceeded during operation, the superconductor loses its superconducting behavior and starts operating in the so-called normal regime, that is, it exhibits a finite, relatively high value of electrical resistance.

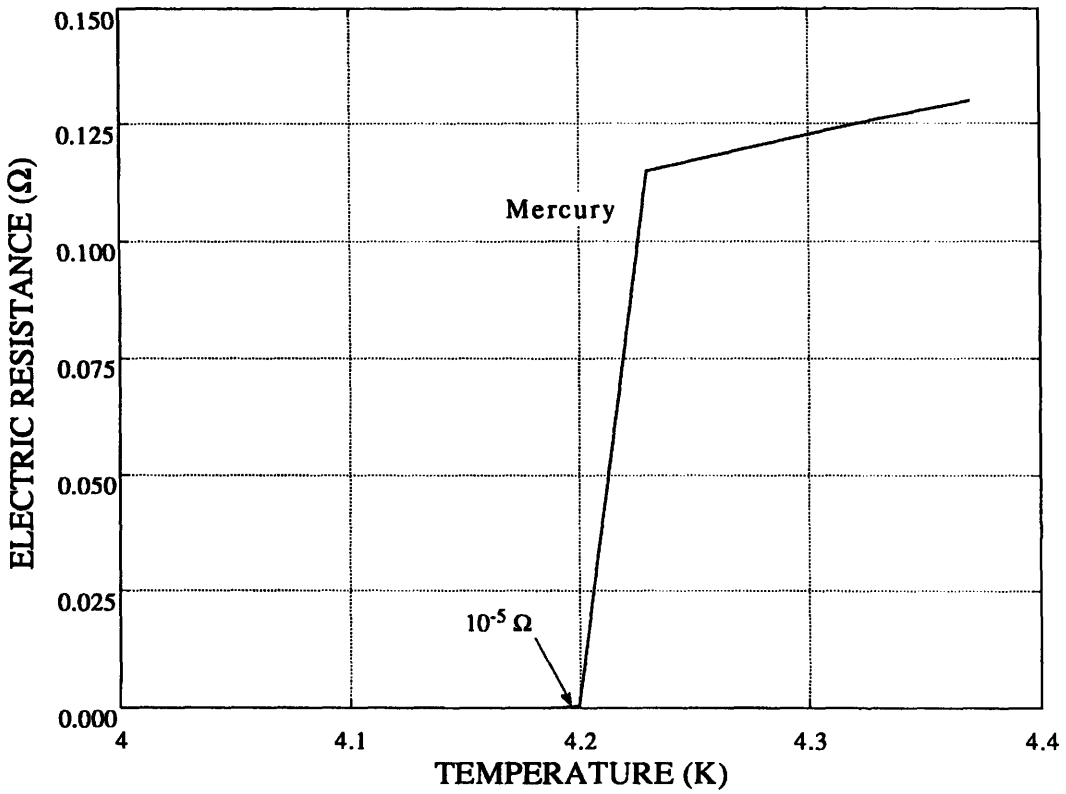

Figure 1-1: Electrical resistance of mercury near 4.2 K, as observed by Onnes in 1911. (From Gung, 93.)

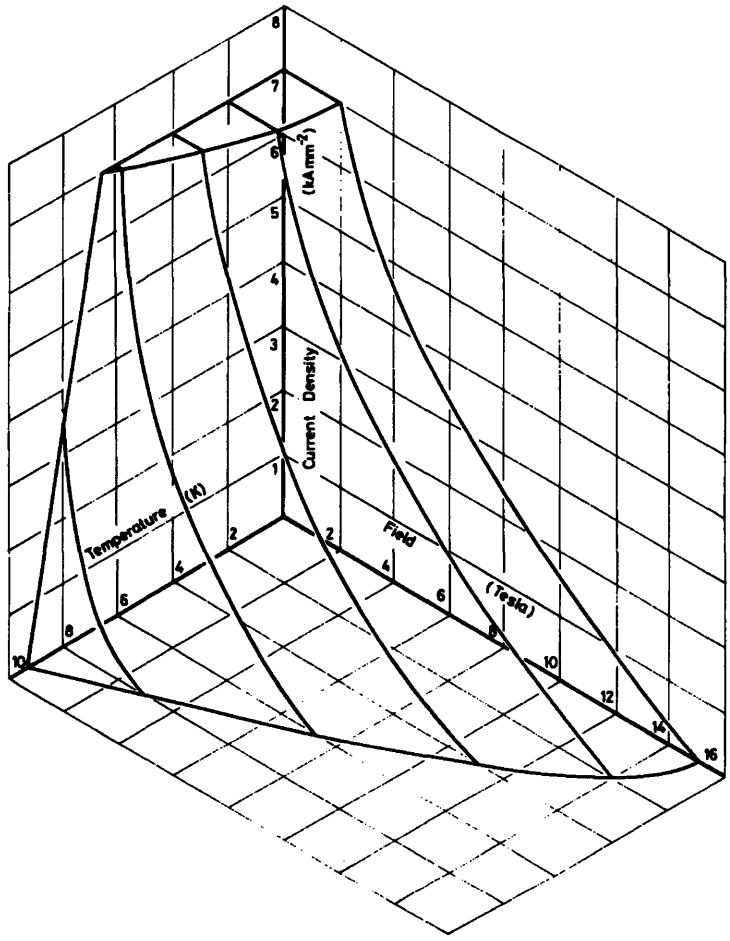

Figure 1-2: Critical-current surface for a commercial superconducting alloy of NbTi. (From Wilson, 83.)

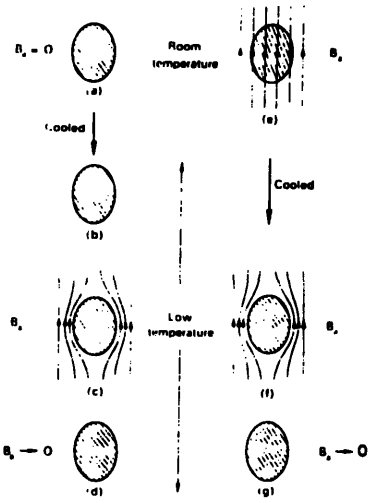

Magnetic behaviour of a superconductor. (a)–(b) Specimen becomes resistanceless in absence of magnetic field. (c) Magnetic field applied to superconducting specimen. (d) Magnetic field removed.

(e)–(f) Specimen becomes superconducting in applied magnetic field. (g) Applied magnetic field removed.

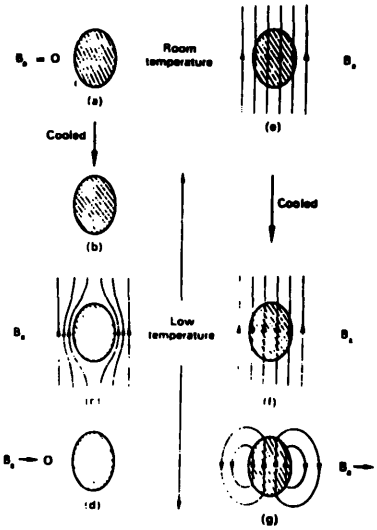

Magnetic behaviour of a "perfect" conductor. (a)–(b) Specimen becomes resistanceless in absence of field. (c) Magnetic field applied to resistanceless specimen. (d) Magnetic field removed.

(e)–(f) Specimen becomes resistanceless in applied magnetic field. (g) Applied magnetic field removed.

Figure 1-3: Comparison of magnetic behavior of a superconductor and a perfect conductor. (From Rose-Innes and Rhoderick, 78.)

Meissner Effect

In 1933, Meissner and Ochsenfeld discovered that below the critical magnetic field, the magnetic flux density inside a single tin crystal was zero [20]. This discovery led to the generalization that superconductors are perfectly diamagnetic (type-II superconductors are not perfectly diamagnetic above the first critical field, as elucidated later in this section). This property differentiates superconductors from perfect conductors, since the latter conserve the magnetic flux inside them as opposed to expelling it completely as superconductors. The difference in behavioral response to applied fields between metallic superconductors and perfect conductors is shown in Fig. 1-3 on page 21. The figure demonstrates that for a perfect conductor the magnetization would depend on the history of conditions of temperature and application of magnetic field, whereas for a superconductor only the existing values of temperature and applied magnetic field B_a determine the magnetization.

Type-I and Type-II Superconductors

Superconductors are classified into type-I and type-II superconductors, based on their magnetic properties. The essential difference between the two types is that type-I superconductors have only a single critical magnetic field H_c, below which they are superconducting and perfectly diamagnetic, whereas, type-II superconductors have two critical magnetic fields, and their magnetic behavior is identical to type-I superconductors only below the lower critical magnetic field, H_{c1}. Type-II superconductors are not perfectly diamagnetic for external field values between the lower critical magnetic field intensity H_{c1} and the higher critical magnetic field intensity H_{c2}, although they continue to have zero DC resistance. Therefore, type-I superconductors exhibit a single magnetic state in the superconducting regime, the Meissner state of perfect diamagnetism, for applied field intensities less than H_c, at temperatures below T_c. Type-II superconductors, on the other hand, have two distinct magnetic states. For applied field intensities below H_{c1}, they display a Meissner state similar to type-I superconductors, but for field intensities between H_{c1} and H_{c2} they are in a mixed state, wherein the magnetic flux inside the superconductor is not zero but it stays superconducting.

A complete physical description of the mixed state can be found in [61] but a brief explanation is as follows. For applied field intensities $H_a \leq H_{c1}$, the surface current produces a field opposing the applied field and the whole superconductor stays diamagnetic, similar to Meissner's effect in type-I superconductors. When the applied field intensity becomes greater than H_{c1}, the diamagnetic surface current remains circulating, but the superconductor is threaded by cylindrical regions of normal material called *normal cores*, parallel to the applied field. The bulk of the material is still diamagnetic due to the diamagnetic current circulating on the surface of the bulk material, but within each core there is a single quantum of magnetic flux [3] in the same direction as that of the applied field. This flux within each normal core is generated by a current vortex enclosing it in a direction opposite

[3] also called a fluxoid given by $\Phi_0 = h/2e = 2.07 \times 10^{-15}$ webers.

to the direction of rotation of the diamagnetic surface current. The vortex current for each core interacts with the field generated by the vortex current of every other core, and since there is mutual repulsion between any two cores (fields produced by individual current vortices are in the same direction), the final arrangement is a periodic hexagonal array of normal cores within the bulk of the superconductor (See Fig. 1-4 on page 24). The underlying physics involves minimizing the free energy of the mixed state by maximizing the surface area to volume ratio of normal cores, and therefore, these cores have very small radii. As a consequence, the superconductor seems to be embedded with an array of filaments which are normal. If an external current is introduced in the superconductor such that the current density $J \leq J_c$, it flows without resistance in the superconducting part of the bulk material, and thereby, type-II superconductors maintain their zero DC electrical resistivity. As the external field is increased, the density of normal cores increases, and finally, when the applied field becomes H_{c2}, the normal cores start to overlap, and no superconducting path for the current is available. Thus, at the upper critical field the whole superconductor becomes normal.

The superconducting and normal states of a type-I superconductor are defined thermodynamically in terms of the free energies of the two states, namely the normal resistive state and the superconducting state. Basically, if the energy density of a magnetic field with the critical field intensity H_c is added to the superconducting state, a transition to the normal state is achieved. Thus, the critical field is given by [61]

$$H_c = [\frac{2}{\mu_0}(g_n - g_s)]^{\frac{1}{2}} \tag{1.1}$$

where g_n and g_s are the free energy densities in the normal and superconducting regimes respectively in the absence of an applied magnetic field and μ_0 is the permeability of free space. Eq. 1.1 is used to define a *thermodynamic critical field* H_c for type II superconductors as well, since they too have a characteristic free energy difference $(g_n - g_s)$ between the completely superconducting and completely normal states in the absence of an applied field, for performance comparison with type -I

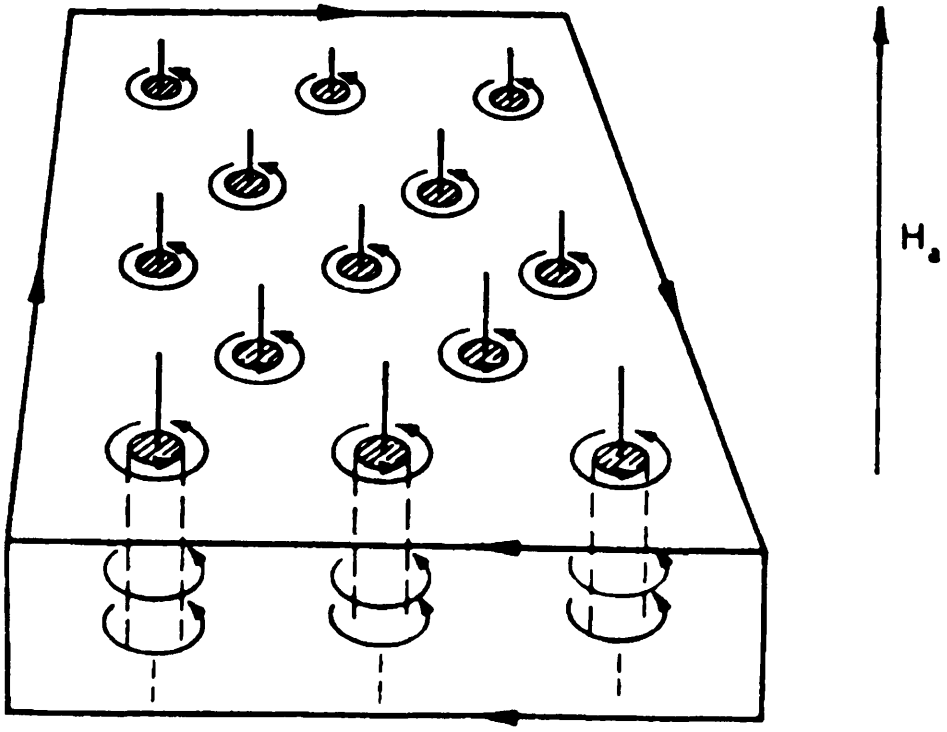

Figure 1-4: The mixed state, showing normal cores and encircling supercurrent vortices. (From Rose-Innes and Rhoderick, 78.)

superconductors. For type-II superconductors, H_c is the field value which makes the area under the actual magnetization curve from zero to H_{c2} equal to the area under a curve constructed by extending the actual magnetization curve below H_{c1} to H_c.

Imperfect Type-II Superconductors

The critical field for most type-I superconductors is less than a few hundred gauss [56]. The lower critical field of most type II superconductors is of the same order but the upper critical field can be on the order of tens of teslas which presents a much larger range of superconducting operation. However, the flow of electric current through type-II superconductors, operating in the mixed state, creates a problem: the movement of the current vortices due to the resulting Lorentz force causes an electrical resistance called *flux flow resistance*, which is proportional to the normal resistance of the superconductor [62] but still less than it. The current dissipates energy due to flux flow resistivity and as a result, the critical current for perfect type-II superconductors is quite small. Fortunately, it was discovered [61, 62] that in the mixed state, if the type-II superconductor has impurities or structural imperfections and dislocations, the movement of the vortices is halted due to their getting pinned into these imperfections (also referred to as pinning centers). As a consequence, the critical currents of imperfect type-II superconductors are much higher, given by the current which creates a strong enough Lorentz force to unpin the vortices from the pinning centers [62].

Another important property which differentiates perfect and imperfect type-II superconductors is the reversibility of magnetization. Perfect type-II superconductors have reversible magnetization while imperfect ones show some irreversibility because of the pinning of the vortices [61]. As the external field is increased beyond H_{c1}, the normal cores formed at the surface might get pinned and would not be able to move into the inner region of the superconductor. Similarly, when the external field is decreasing and goes below H_{c1}, some pinned vortices might not be expelled and their enclosed flux will be trapped. Fig. 1-5 on page 26 shows the resulting

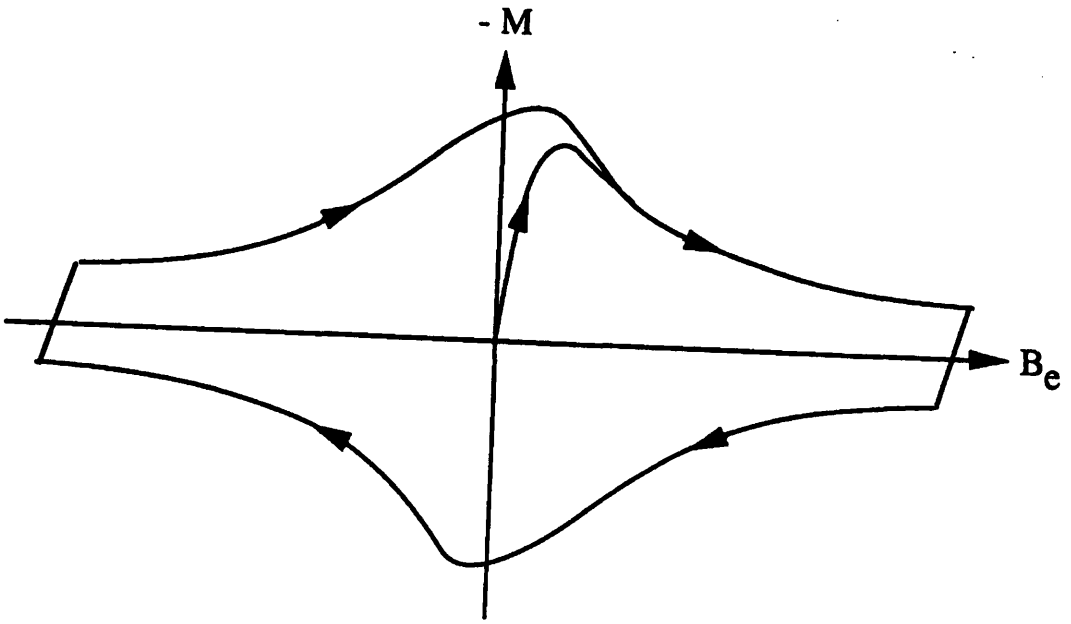

Figure 1-5: Magnetization Loops for an Imperfect Type-II Superconductor. (From Gung, 93.)

hysteresis loop when the magnetization of an imperfect superconductor is plotted against the external field. The area inside the hysteresis loop represents the energy lost during each field cycle.

Usually, type-II superconductors are imperfect because even with careful fabrication procedures, some imperfections persist. These imperfect superconductors, also called *hard superconductors*, are of importance in the construction of high-field high-current superconductors [62] because of their high upper critical field and high critical current values. In general, hard superconductors exist in the form of an alloy or a compound, and the most prominently in use in the industry are NbTi and Nb_3Sn [79].

1.1.2 Superconducting Cables

As mentioned earlier, superconducting cables are in wide use in high-current and high-field magnet applications, which requires superconducting cables to be able to carry a high current without resistance in high magnetic fields. Presently, low T_C type-II superconductors are in primary use in the manufacturing of wires for such

cables. The fabrication of these cables is done with extreme care because a lot of degradation in performance is attributed to defective manufacturing process. The cables need to be stable to anticipated external disturbances during their operation also, to meet standardized robustness criteria.

External disturbances deposit energy within the volume of the superconductor in the form of heat, and if the resulting heating of the superconductor is greater than its ability to remove heat deposition locally then the temperature of the superconductor will increase. This increase in temperature will cause the critical field and critical current density values to deteriorate and can eventually quench [4] the cable [79]. Quenching of a superconducting magnet is a very undesirable process, as it results in releasing all the energy stored in its magnetic field into the superconducting cable in the form of heat, which can structurally damage the magnet and its surroundings. For the operation of superconducting magnets to be safe, it is imperative that they should be stable against physical disturbances and perform under quench-free conditions.

Quenching can be prevented by improving the heat removal efficiency (or ameliorating the cooling conditions) or by reducing the possibility of sudden energy inputs into the superconducting cable volume. One of the main sources of production of heat in the superconducting cable is the internal and external Lorentz force on it. External Lorentz forces move the wires and wire motion generates heat due to friction, while internal Lorentz forces disengage fluxoids from the pinning centers and the resulting flux motion dissipates heat. Initially a small heat pulse due to some disturbance is deposited in the cable, which raises the temperature of the cable if the heat is not promptly removed by the available cooling conditions. Due to the increase in temperature, the critical current density of the cable decreases, and the decreased current density cannot totally shield the cable from the externally applied field. The unshielded field moves into the conductor and this flux motion

[4]Quenching is a term used to describe the transition of a part of a superconductor from the superconducting state to the normal resistive state without recovering back to the superconducting state

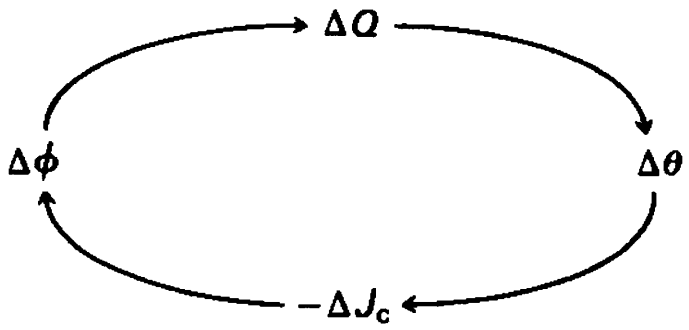

Figure 1-6: Positive feedback loop for a flux jump. (From Wilson, 83.)

generates more heat, which will raise the temperature even more. This positive feedback (shown in Fig. 1-6 on page 28) will cause an avalanche of heat generation and flux motion, called a flux jump, which will quench the superconductor. Flux jumps can be avoided by reducing the available physical region for flux motion, and also by conducting away the heat generated quickly before it can participate in the positive feedback. Both these methods for obviating flux jumps require a fine subdivision of the superconductor [79].

Filamentary Composites

For NbTi at 4.2 K and 6 T [5], flux jumps occur if the radius of the wire is greater than 115 μm [79]. Since making superconducting wires with such a small diameter is not an easy task, and winding magnets with it would be even harder because of insulation problems and the number of turns needed to be wound, commercial superconductors are manufactured in the form of filamentary composites as shown in Fig. 1-7 on page 29. Fine filaments of superconducting material are embedded in a normal metal matrix called *stabilizer*, usually of copper. Such a composite structure of many filaments in a matrix is termed *multifilamentary zone*. As mentioned before, superconductors in general, and hard superconductors in particular, have a much higher electrical resistivity when operating in the normal regime than conventional conductors such as copper or aluminum. Annealed electrical copper at 4.2 K

[5]Tesla, the SI unit of magnetic field. 1 T = 10^4 gauss.

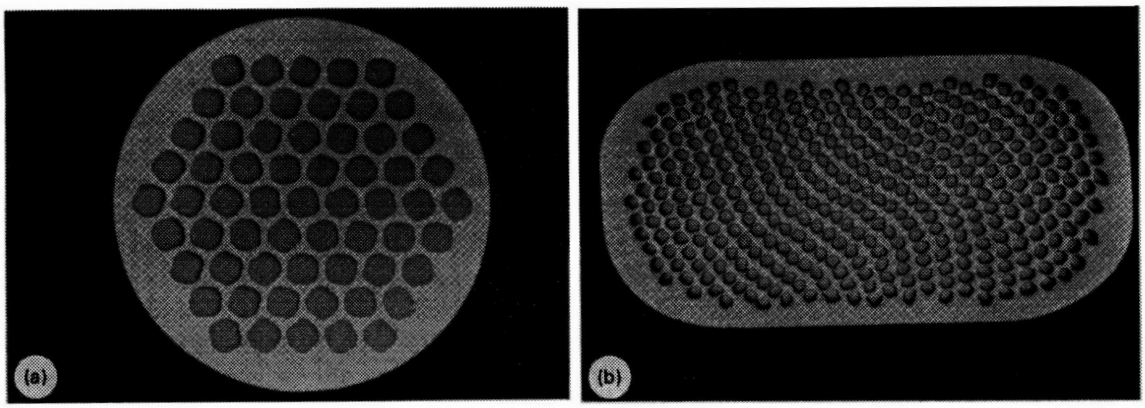

Figure 1-7: Cross-sections of two typical superconducting composites of NbTi in a copper matrix comprising (a) 61 filaments in a 0.5 mm diameter wire and (b) 361 filaments in a 1.0 mm x 2.0 mm rectangular strip (courtesy of IMI Titanium Ltd). (From Wilson, 83.)

and 6 T has electrical resistivity $\rho \simeq 3 \times 10^{-10}\,\Omega$ m and thermal conductivity $k \sim 350\,\mathrm{W\,m^{-1}\,K^{-1}}$ and therefore the factor k/ρ for copper is 7.5×10^6 higher than for NbTi [79]. Copper is very ductile also, which helps in the fabrication process of the composite. The good electrical conductivity of the stabilizer provides an alternative low-resistance path to the current, in case of part of the superconductor becoming normal due to a disturbance, and thus promotes the dynamic stability of the superconducting wire against flux jumping and protects the superconductor in the event of a quench. The high thermal conductivity of the stabilizer enhances heat removal and improves stability. Therefore, the stabilizer not only prevents a quench from occurring but protects the superconductor during a quench. Usually, the multifilamentary zone is enclosed in a cladding of normal material, which augments the functionality of the stabilizer [79].

However, the stabilizer in the multifilamentary composite has a serious disadvantage: its low-resistivity allows the filaments to be coupled together in changing magnetic fields. Coupling between the filaments is undesirable because it causes flux jumping. Instead of the filament size being the characteristic flux jump size, the composite radius becomes the size of the flux jump, which is usually much larger than allowable under stability concerns. Fortunately, coupling can be reduced by twisting the composite with a short enough twist pitch which ensures

that the distance between reversals is insufficient for transverse currents to build up, and the filaments stay decoupled. Such a multifilamentary composite wire, twisted in the final stages of drawing the wire with the appropriate twist pitch, is called a *superconducting strand.*

Two kinds of conductors utilizing multifilamentary composites have been developed for fusion applications: pool-boiling cooled conductors and cable-in-conduit conductors.

Pool-boiling Conductors

Pool-boiling conductors are simply superconducting strands placed in a liquid helium bath, and were used to construct the first truly stable magnets by Stekly [35, 68] and Laverick [38]. These magnets would recover their superconducting state irrespective of the size of the thermal perturbation they were exposed to. This stable behavior was achieved by immersing the magnet cables in pools of liquid helium and reducing the current density by adding stabilizer to the conductor until the Joule power generation on the conductor surface in the normal state was less than the minimum film boiling heat flux. This form of stability enforced by overwhelming Joule heating by cooling is called *cryostability.* Although cryostability is tempting because it relieves the magnet designer from worrying about the nature and exact extent of expected perturbations, it strictly stifles the limiting current density which gets translated into bulkier magnets for the same operating parameters ($\leq$ 3 kA cm^{-2} at 8 T for NbTi magnets) [24] and thus, higher costs. Stekly's cryostabilizing condition is overly conservative, and Maddock, James, and Norris [47] demonstrated that cryostability can be preserved at higher current densities than allowed by Stekly's criterion. Maddock introduced the concept of *cold-end recovery* in which recovery starts at the ends of the normal zone and proceeds inward, the center of the disturbance being the last point to recover. In contrast, according to Stekly's criterion the whole normal zone recovers instantaneously, and all parts of the normal zone disappear simultaneously. Cryostability, even with Maddock's criterion, limits the current density to unacceptably low values. After much efforts

to increase the current density of pool-boiling magnets, by trying to improve heat transfer between helium and conductor or using superfluid helium [6] for example, they have been renunciated in favor of internally-cooled conductors.

Cable-in-Conduit Conductors

Cable-in-conduit conductors have become the primary choice of superconducting cables for use in large-scale high-field superconducting magnet applications such as magnetically levitated high-speed trains (MAGLEV), superconducting magnetic energy storage (SMES), high energy particle physics detectors, magneto-hydrodynamic (MHD) propulsion, and most notably, in magnetically-confined fusion power generation. Presently, he most important project being pursued by the fusion community is the International Thermonuclear Experimental Reactor (ITER), and all of the principal magnet systems of this tokamak namely the toroidal field (TF) coils, the poloidal field (PF) coils and the central solenoid (CS) will incorporate cable-in-conduit conductors. The reason is that the superconducting magnets constructed by using CICCs are characterized by structural robustness, relatively low AC losses, low inventory of helium coolant, and high voltage integrity, which enables them to support high electrical currents with minimal energy losses and produce high magnetic fields. The magnets used in ITER will generate fields as high as 13 T. As the magnets will have to endure intense structural, thermal and electromagnetic loads during operation, it is of utmost importance that their stability to the severe operating conditions is predetermined.

A typical CICC is shown in Fig. 1-8 on page 32. It consists of a twisted, multi-strand cable wound in many stages and enclosed in a structural alloy conduit. The strands, as described earlier, are multifilamentary composites with many superconducting filaments embedded in a normal metal stabilizer matrix, usually copper. The stabilizer makes about 60% of the strand volume. The superconducting filaments are normally made of either NbTi or Nb_3Sn. The strands may

[6] liquid helium under low pressure at low temperatures changes its phase to He-II, a liquid phase with unusual properties when used as a coolant.

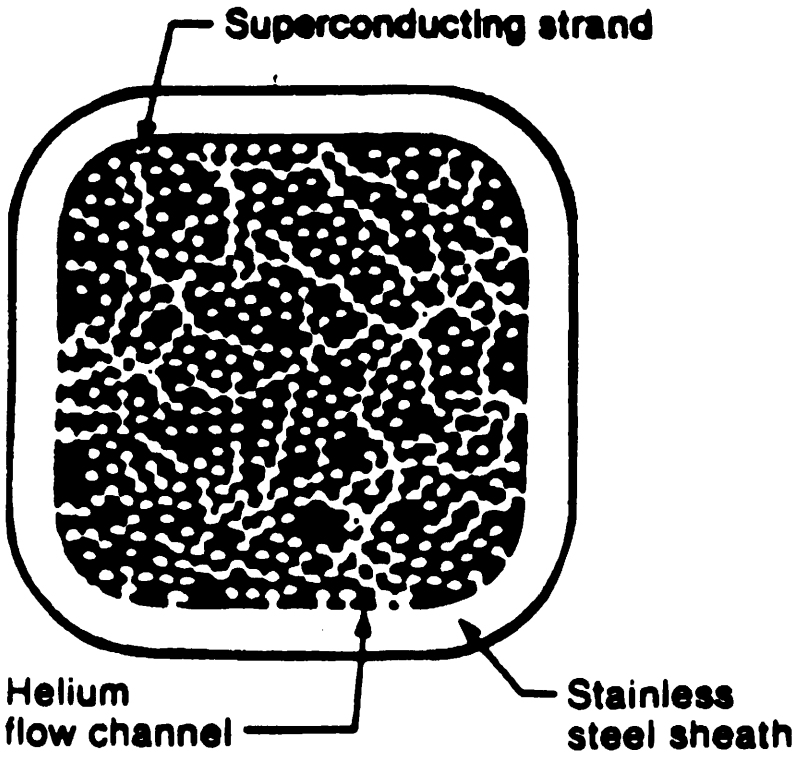

Figure 1-8: A typical cable-in-conduit conductor. (From Dresner, 83.)

be chrome-plated to reduce transverse eddy-current losses in the cable when it is exposed to magnetic field or current transients, such as ramping field. Good heat removal is facilitated by pressurized supercritical liquid helium flow through the conduit. The helium flow area is about 40% of the total cable space cross-sectional area, also called void fraction. The conduit serves both as the structural support and as the channel for the liquid helium coolant. Wrapping the conduit with insulation gives it electrical integrity. Unlike pool-cooled conductors, the helium flow path inside a CICC can be quite long (upto a kilometer for ITER magnets), and the frictional forces can be substantial due to forced-flow of helium through the constricted space available in the conduit. As a result, CICCs have a high inlet pressure to overcome the frictional drag. Due to the strength of the conduit material, CICCs can handle high quench pressures easily.

In the CICC, each strand is in direct contact with the coolant, resulting in very efficient heat transfer. In contrast, monolithic conductors, which use epoxy (or

something similar) to hold the superconducting strands together, have a much lower heat transfer capability because of the low thermal conductivity of epoxy [65]. The idea of subdividing the superconductor into thin strands dates back to Chester [17], who remarked,

> another important parameter in the stability condition is the thermal capacity of the superconductor . . . the superconductor may be combined with another material of high thermal capacity . . . the most effective material would clearly be liquid helium or high-pressure helium if this could be retained in close thermal contact with the superconductor, perhaps by using a hollow tubular conductor with the helium trapped inside. Clearly, excellent thermal contact is desirable between the superconductor and the thermal ballast . . . this is achieved by subdivision of the superconductor to present greater interfacial area.

CICCs were introduced to their present day popularity by Heonig, Iwasa and Montgomery [30] who demonstrated the advantages of subdividing back in 1975.

As far as stability is concerned, CICCs are not cryostable but metastable due to the nature of helium residence in them. Recovery from a thermal disturbance takes on the order of tens of milliseconds but the residence time of helium in a coil can be a few minutes even at high flow rates [22], which limits the inventory of helium available for recovering from the disturbance. Depending on the magnitude of the disturbance, enough heat might be deposited into the surrounding helium at a fast-enough rate to raise its temperature above the current-sharing threshold. In this situation, the helium will not be able to take away any more heat and the cable temperature will increase until the cable finally quenches. The stability of CICCs is discussed in more detail in Chapter 3.

1.1.3 Loss Mechanisms in Superconducting Cables

It is fundamental to the understanding of superconducting cable stability to comprehend the different loss mechanisms which behave as antecedents for the pro-

cesses of heat generation and quenching in these cables. For stability analysis of a certain cable, the amount of heat generated per unit time and the locality within the cable of its generation are the parameters which are important, and not the means by which this heat is produced. The specific method which is utilized in heat generation emphasizes itself in terms of these parameters. It is this independence of stability calculations from the specific loss mechanism, causing energy deposition within the cable volume, that suggests using a technique of initiating thermal perturbations in the cable which is well-understood, computationally simple, and experimentally feasible, for studying the stability requirements of superconducting cables.

When a cable is in the superconducting steady state, there is no heat deposition in the cable volume, as all the current is in the superconducting filaments in the strands. Since the only DC heat generation mechanism in composite superconductors is *joule heating* in the event that some of the DC current paths are through the low-resistivity stabilizer, in the superconducting steady state, there will be no DC losses. The perturbations expected in real-life experimental situations are transient anyway, and are not supposed to be part of the steady state status.

The major AC loss mechanisms[7], which can occur in superconducting cables operating under normal conditions are [26]:

1. Hysteresis losses.
2. Coupling current losses.
3. Penetration losses.
4. Transport-current losses.
5. Self-field losses.

[7]These losses are covered in more detail, with an explanation of the underlying physics, in Chapter 2

Hysteresis Loss

All hard superconductors experience hysteresis losses when present in a time-varying magnetic field [56, 57, 79]. Hysteresis loss is the result of the irreversibility of magnetic flux motion in the imperfect type-II superconductor induced by an external magnetic field varying with time at a certain frequency. The flux moves into the superconductor with an increase in external magnetic field beyond the lower critical field H_{c1}, and gets pinned at the pinning centers, but does not move out when the external field is reduced below H_{c1}. Due to the dependence of hysteresis on flux motion and flux pinning, hysteresis loss becomes a function of the size and the critical current density of the superconductor.

Coupling Loss

Coupling losses are a consequence of the resistive matrix stabilizer in the composite superconductors. The superconducting filaments are electrically connected by the resistive matrix material and current loops can be formed between filaments if an electric potential drop exists between them, across the resistive matrix material. Thus, in time-varying fields, the induced electric potential drives currents across the resistive matrix and links the shielding currents flowing in the superconducting filaments, forming closed current loops transverse to the applied field [13, 57, 79]. This eddy current flowing through these closed current loops is termed *coupling current*. Due to Faraday's law, the induced electric potential is proportional to the area enclosed by these current loops, which is proportional to the rate of change of applied magnetic field, therefore, if the external field changes at a high enough frequency, all the filaments in the composite cable will be linked. In this situation, the whole multifilamentary zone acts like a bulk conductor, which increases the region of flux motion from a single filament radius to the size of the strand. As a result, a flux jump in a single filament causes a flux jump in all filaments, and heat generation due to flux jumping becomes manifold.

The problem is resolved for external time-varying fields by twisting the multi-

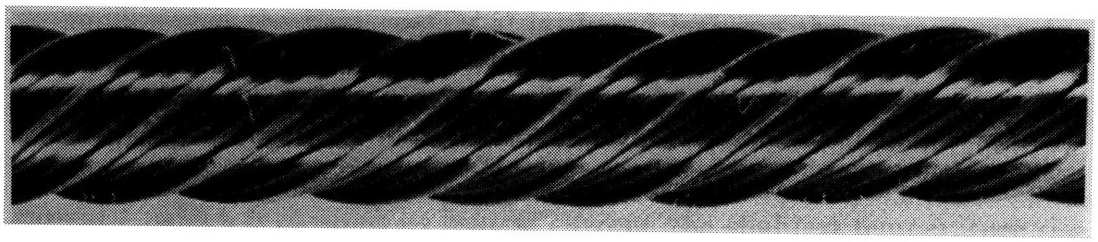

Figure 1-9: A twisted multifilamentary composite wire. (From Wilson, 83.)

filamentary wire as shown in Fig. 1-9 on page 36. Due to twisting, the area available for inducing electric potential is greatly reduced, as the electric field caused by the changing field reverses every half twist pitch. The twist pitch can be made short enough, so that the electric field and the resulting coupling currents are so low that the filaments are essentially decoupled. As the coupling current flows through the resistive matrix, it produces joule heating, and the dissipated energy is termed coupling loss.

Penetration Loss

The screening currents produced to shield the composite wire from the variation in the external field are assumed to be flowing in a thin current sheet at the boundary of the multifilamentary zone. In reality, they flow in a sheet of finite width depending on the value of current density, the larger the current density required for shielding the larger the width. The part of the composite wire which supports these coupling currents at the critical current density is considered to be saturated. At a certain high frequency, the whole composite wire may be saturated and act like a bulk superconductor penetrated by external field, since the coupling currents produce a secondary magnetic field to screen the whole composite wire from variations in the external field [51, 53, 60, 82]. Penetration loss is the loss associated with the penetration of flux through the saturated zone to the inner boundary due to the magnetization caused by the coupling currents flowing in the superconducting filaments in the saturated region [60].

Transport Current Loss

Transport current is the DC current flowing in the superconducting cable, driven by an external power supply. As opposed to the shielding current which flows at the outer edge of the filaments, transport current flows in their inner region because of flux pinning, and changes the spatial distribution of the shielding current as a result [53, 79]. With an increase in external field, the filament area occupied by shielding currents increases, and the transport current is limited to a smaller area. If the transport current becomes larger than what can be taken by the inner region available for it, it starts to fill in the outer region where the shielding current is flowing. According to Wilson [79, p. 172], the presence of a transport current produces additional hysteresis losses. These additional losses are small for field variations below the value corresponding to full penetration of the superconducting filaments, but can become quite appreciable for higher field oscillations.

Self-field Loss

The losses caused by the interaction of transport current and the transverse field produced by it are called self-field losses. The magnetic field due to the transport current is in the form of concentric circles around the wire, and as the current is reduced or increased, these circular field lines representing the flux move into or out of the wire, dissipating energy as they move. Usually, the self-field of a single strand is much smaller than the applied field, and therefore, the self-field loss of a single strand is negligible when compared with other types of losses. But in the case when there is no variation in the applied field and only the transport current is time-varying, the only non-negligible AC loss mechanism is self-field loss, and needs to be taken into account.

The energy these loss mechanisms deposit inside the superconductor is impossible to be distributed into its individual sources, specially when losses of more than one kind are present, which is normally the case. As will be elucidated in Chapter 2, the calculation of AC losses accurately, even for very simple cable geometries,

can be painstakingly difficult. Stability considerations call for a methodology of calculating energy deposited inside a cable by a disturbance exactly and reliably. AC losses depend not only on the applied field and transport current but also on properties of the wire, which are affected by its design and manufacturing [53, 75, 79]. This means that AC loss calculations depend on the superconducting cable parameters and cannot be computed analytically with a great deal of accuracy. Any computational method designed for measuring energy deposition in the cable based on predicting AC losses needs to solve the arduous problem of calibrating these losses in terms of known and calculable experimental parameters, for each and every superconducting cable designed and constructed. On the other hand, if a systematic way of doing the same calculation could be found which bypassed AC loss measurements, at least to a large extent, it would greatly simplify the ambitious task of measuring the amount of energy deposited within a superconducting cable by an artificially prepared perturbation introduced into it. This thesis investigates one such possibility.

1.2 Problem Statement

1.2.1 Introduction

Many researchers have performed stability experiments on CICCs, and reviews have been done by Lue [41] and by Dresner [25]. Among the most important results of these experiments are the discovery and understanding of the multiple or multivalued stability of CICCs [10, 46], the independence of cable recovery from helium flow velocity [32], that is, the realization that induced helium velocity due to early conductive heating of the helium is the most important factor in recovery, and the determination of a limiting current (I_{lim}) in the conductor [23], which demarcates the boundary between high and low stability margins. The high stability regime is also the well-cooled regime and the stability margin is limited by helium enthalpy between the helium operating temperature (T_{op}) and

the current-sharing temperature T_{cs}[8]. In the low stability regime or the ill-cooled regime, the stability margin is limited by only the cable enthalpy from T_{op} to T_{cs}, which could be up to two orders of magnitude less than the well-cooled stability limit. But, in these experiments, the energy that dissipates inside the conductor due to the perturbation is not measured exactly, but only estimated by indirect methods. Another important consideration is the uncertainty in the amount of heat that actually is deposited inside the cable part of the CICC and gets translated into a temperature rise of the cable, as opposed to the amount which directly boils off helium without effecting the temperature of the cable. Therefore, there is a need for developing a method to measure this input energy directly, with a good deal of accuracy.

1.2.2 What are Stability Margins?

The stability of a superconducting cable is experimentally determined by establishing stability margins for it. Stability margins can be simply visualized as curves in two-dimensional space, which result when two variables which determine the cable's stability are plotted against one another (see Fig. 1-10 on page 40). The curve separates the locus of points identifying stable perturbations from the ones which are unstable. Usually, one of the variables is the energy deposited in the cable and the other one is one of the principal operating variables such as transport current or magnetic field at the conductor (only one variable is varied at a time). From this plot, the highest amount of energy which a disturbance can deposit inside the superconductor and not quench it can be readily estimated, for a range of operating parameters.

[8]Current-sharing temperature is the temperature at which the extra current, which cannot flow in the superconducting filaments as they already have the critical current density, starts flowing in the resistive matrix of the composite wire.

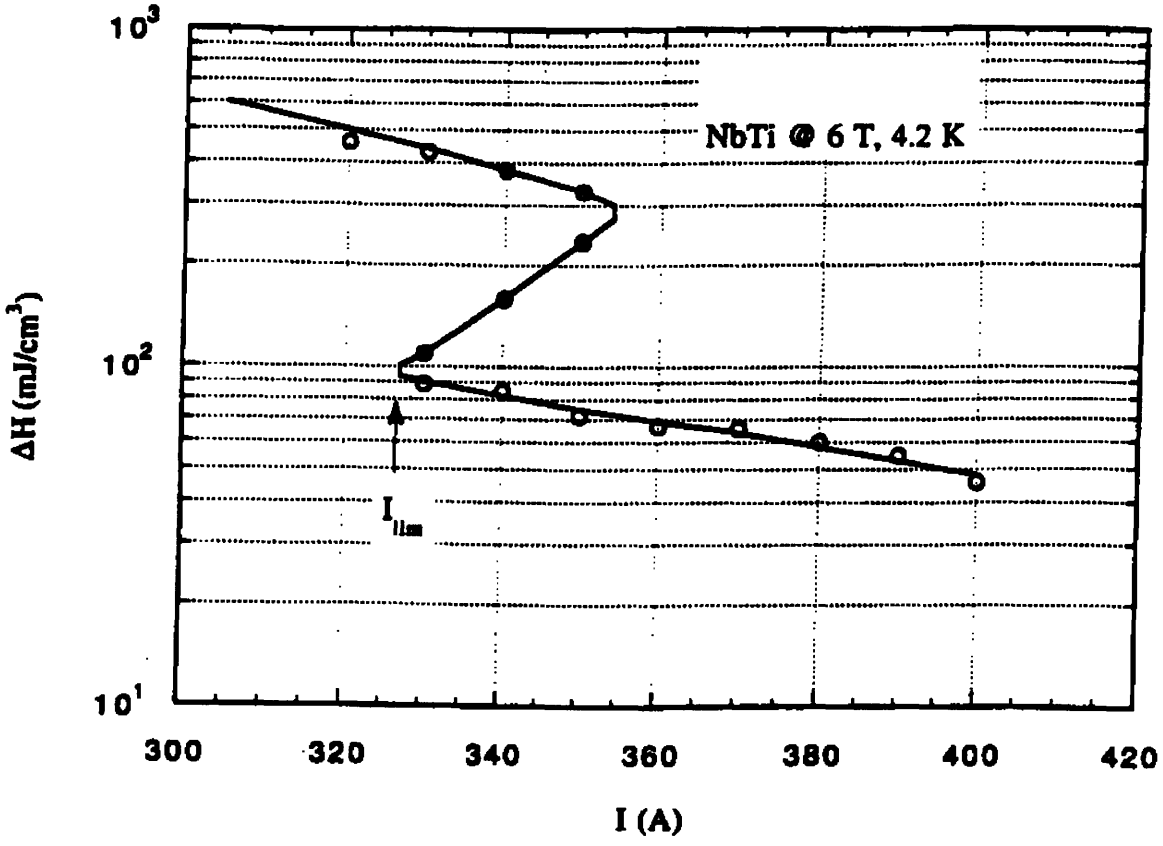

Figure 1-10: Stability margin for a CICC. (From Lue, 94.)

1.2.3 Perturbation Techniques

There are mainly three ways to introduce a disturbance, that is to deposit energy in the conductor, which have been successfully used in stability experiments. Firstly, energy can be released into the conductor directly, in the form of heat, by a point or line heating source embedded in the cable [42, 43, 46, 77], with external means of controlling the amount of heat released, for example, in terms of the time the heater is turned on at constant power output . Secondly, the sample can be heated indirectly by inductive heating [2, 44, 50, 59, 64]. In this method, energy in the cable is deposited due to AC losses when there is a changing current in a coil coupled inductively to the sample cable. Lastly, energy can be put in the cable by direct joule heating. This can be achieved by superposing a current pulse on the transport current through the cable [40]. The idea is that the pulsed current is high enough to have the total current, which is the sum of the transport current and the pulsed current, to exceed the critical current (I_c) for part of the duration of the pulse. During this time, joule heating will be produced as current transfers to the copper stabilizer. Since the transport current is DC, it will quench the cable if current does not transfer back to the superconductor after the pulse, as it will act as a continuous heat source, limited only by the power supply outputting the transport current.

The disadvantage of the first method is that the heating is very localized, or may go directly to helium, which is not a very good representation of the actual anticipated disturbances for large scale magnets, such as AC losses encountered in toroidal field magnets during a plasma disruption in a tokamak. The inductive heating method is a much better representation of such disturbances, but it is extremely difficult to calibrate the energy actually deposited in the cable due to known current change in the primary coil, as it depends on the determination of AC losses in the cable, either by measurement or calculation, which may not be accurate to more than 20-30 percent [49]. The third method has the advantage, like the first method, of having the source and the sample magnetically decoupled. The

losses due to joule heating for the part of the sample above T_{cs} can be calculated exactly if the resistive voltage across the sample and the current flowing through it are known by measurement and is given by

$$E = \int VIdt \tag{1.2}$$

The AC losses caused by the changing self-field of the superconducting cable sample, due to the time-varying pulsed current, have to be estimated to evaluate whether they are negligible compared to the resistive losses. Since there is no change in transverse field, other forms of AC losses must be much less in this case than in the case of inductive heating.

The pulsed current method, due to its bypassing of the difficulty involved in estimation of AC losses, is considered as an alternative for providing a disturbance to the superconducting cable for analyzing its stability.

1.2.4 Thesis Objectives

The primary goal of this thesis is to investigate the pulsed current method as a reliable way of inputting disturbance energy into a superconducting cable, and to incorporate it into an experimental methodology of performing stability analysis on such cables which is dependable and accurate. More specifically, it needs to be determined whether the energy deposition in the CICC due to a pulsed current disturbance can be easily calculated or not in a way which is, more or less, independent of cable parameters. If the energy deposited inside the CICC, or more appropriately the power dissipated inside the CICC, due to a current pulse, which forces joule heating in the CICC for a limited time, can be calculated exactly, then the response of a certain cable to this pulse should be the same as if the disturbance was initiated in some other fashion but dissipated the same power. The ability to predict the stable or unstable behavior of a certain CICC in this manner, to a known energy input inside the conductor due to a perturbation, will greatly enhance stability analysis of CICCs. In order to achieve the objective of this thesis,

the following tasks need to be performed:

1. design and construction of a stability experiment using apparatus which outputs pulsed current.

2. development of a method to calculate the energy deposited in the CICC by a current pulse.

3. calculation of energy dissipation in a given CICC due to pulsed current disturbances using the above method and relating the results to relevant experimental parameters.

4. establishment of stability margins for the CICC used in experiments based on these calculations.

The topic of stability of CICCs is explained in Chapter 3 along with a detailed look at AC losses in multifilamentary composites and their stability in Chapter 2 as a building block for analyzing stability of CICCs. In Chapter 2, first a review of AC losses including hysteresis loss, coupling current loss, penetration loss, transport current loss and self-field loss is made, explaining the difficulties involved in their calculation.

Chapter 3 introduces the concepts for extending the topic of stability to CICCs and examines the stability of CICCs in detail, including a review of stability experiments done in the past, and a discussion of their results. Finally, the merits of performing stability experiments using pulsed current disturbances as opposed to other alternatives are discussed and the need for the development of such experiments is emphasized.

The core of the contribution of this thesis work is the development of a stability experiment which uses the pulsed current method for introducing perturbation energy into a CICC, and provides means of estimating the energy dissipated in the CICC as a result of the disturbance introduced. Chapter 4 describes the complete details of this experiment including the experimental setup, the apparatus, and the

procedures. Data acquisition techniques of the experiment are covered as well in the same chapter.

A thorough analysis of the data generated in the experiments performed is presented in Chapter 5. The results are presented and analyzed to ascertain the credibility of the methodology of the suggested experiment. The success of the experiment is assessed based on the results of the analysis.

The issue of self-field losses is resolved in Chapter 6. The chapter includes a derivation of self-field losses for multifilamentary composite superconductors and extends this model for application to CICCs. Based on this extension, the self-field losses in the CICCs used in the experiments performed are estimated and compared with resistive losses to verify their negligibility.

Conclusions and recommendations for future work are given in Chapter 7.

Chapter 2

Multifilamentary Composites: Stability and AC Losses

In section 1.1.3, a brief introduction to the mechanisms of AC losses in multifilamentary composites was presented. These losses are covered in much more detail in this chapter, and are followed by a presentation of stability criteria for composite superconductors.

2.1 AC Losses in Composite Superconductors

The analysis of AC losses in composite superconductors made here is meant to be neither comprehensive nor mathematically thorough, but only complementary to the thesis material. A complete analysis of AC losses in multifilamentary composite superconductors has been done by Gung [26], and detailed studies of the material can be found in texts by Carr [13], Wilson [79], and Ogasawara [57]. The reason why these losses are termed AC losses is because they are a consequence of the presence of time-varying fields in and around the superconducting composite.

In the discussion of imperfect type-II superconductors in section 1.1.1, the electrical resistance due to the viscous movement of quantized magnetic flux lines or fluxoids called flux flow resistance was introduced. It is this resistance which causes AC losses, and therefore, AC losses are resistive in nature. The electric field

E generated in the superconductor associated with the electromotive force (EMF) created by the changing magnetic field drives the current inside the superconductor to its critical value J_c whence the superconductor enters the flux flow region. Due to the highly steep nature of the flux flow resistance line, the current in the superconductor remains at its critical value, resulting in the power generation per unit volume of $E.J_c$. Since the flux flow resistance is highly non-linear, these losses are independent of field change cycle time and are also called *hysteresis losses*.

If the sample geometry is complicated or in cases where the induced J_c changes the B inside, and therefore E, it is more convenient to calculate loss in terms of the magnetization M, which is the total magnetic moment per unit volume of the superconducting sample. For applied H which is spatially uniform over the sample, the total loss per cycle per unit volume is

$$Q_h = \int H\, dM = \int M\, dH \tag{2.1}$$

In a multifilamentary composite, the filaments are coupled electromagnetically by time-varying fields, which greatly enhances AC losses. Since, the coupling currents resulting from this electromagnetic coupling are eddy-current type, the loss per cycle becomes a function of the cycle time.

2.1.1 Hysteresis Losses

The hysteresis loss in a type-II superconductor was successfully analyzed only after the introduction of a model in 1960 by C.P. Bean [4, 5, 6], which describes the magnetization of a type II superconductor using its spatially averaged electromagnetic properties. It is assumed in the model that the current in the superconductor distributes itself spatially such that the current density in an arbitrary region is either the critical current density J_c or zero. This is why this model is also called the critical state model [56].

The Bean Critical State Model

The Bean model, although highly simplifies the microscopic nature of the underlying physics of superconductivity, has been quite successful in predicting experimental results. The main assumptions of the model are:

- The superconductor is characterized by a bulk J_c, in the region of field penetration, which is a material property.
- There is no flux jumping during the period of applied field variation.
- J_c is not a function of the applied field.

The model is shown at work in Fig. 2-1. When a magnetic field B_y is applied parallel to the broad face of the superconducting slab shown, currents are induced on the surface which try to shield the inside of the slab from the applied field. The figure shows the penetrated field profile of B_y for various values of the external field B_{ext}. Initially this induced current density is very high, therefore it decays resistively to J_c, and then stays constant. As a result, the field penetrates a little bit. For an initial increase in field of ΔB, the penetration depth p can be calculated by using Ampere's law

$$\frac{\partial B_y}{\partial x} = \mu_0 J_c = \frac{\Delta B}{p} \tag{2.2}$$

Once the increases in field penetrate the whole slab, any further increase does not change the pattern of the screening currents. In this model, J_c is set by the applied field in the beginning and any changes in it due to a temperature increase will not be recorded, hence the model is good if the temperature stays constant. Flux jumps generate heat and raise the temperature and must be avoided. The theory of adiabatic and dynamic stability to flux jumping is introduced in Sections 2.2.1 and 2.2.2. Both theories suggest a fine subdivision of the superconductor.

The loss produced by a given field change also depends on sample history, but for cyclic field changes the loss is different only for the virgin state as initially there are no screening currents. For the second and subsequent cycles, the loss

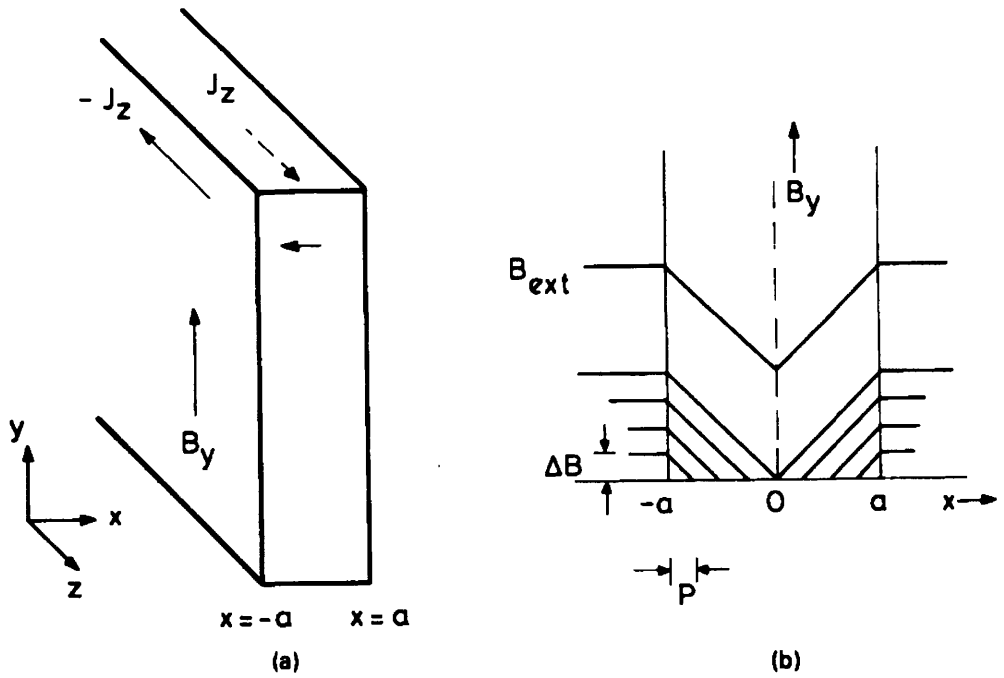

Figure 2-1: (a) Screening currents induced to flow in a slab by a magnetic field parallel to the slab surface; (b) Magnetic field pattern across the slab showing the reduction of internal field by screening currents. (From Wilson, 83.)

is the same for each cycle. In the following cases, the loss considered is for this pre-conditioned state, after at least one cycle.

Slab Parallel to the Field

Using the critical state model the field patterns are given in Fig. 2-2. The loss over a small slab width dx for every half cycle is $J_c\phi(x)dx$ where $\phi(x)$ is the magnetic flux linked across this width. The loss averaged over the sample is

$$q_h = \frac{1}{a}\int_0^p J_c\phi(x)dx = \frac{1}{a}\int_0^p J_c\mu_0 J_c x^2 dx = \frac{1}{3}\mu_0 {J_c}^2\frac{p^3}{a} \tag{2.3}$$

where p = $B_m/2\mu_0 J_c$. If B_p is the field amplitude which penetrates to the center ($p = a$), then

$$B_p = 2\mu_0 J_c a \tag{2.4}$$

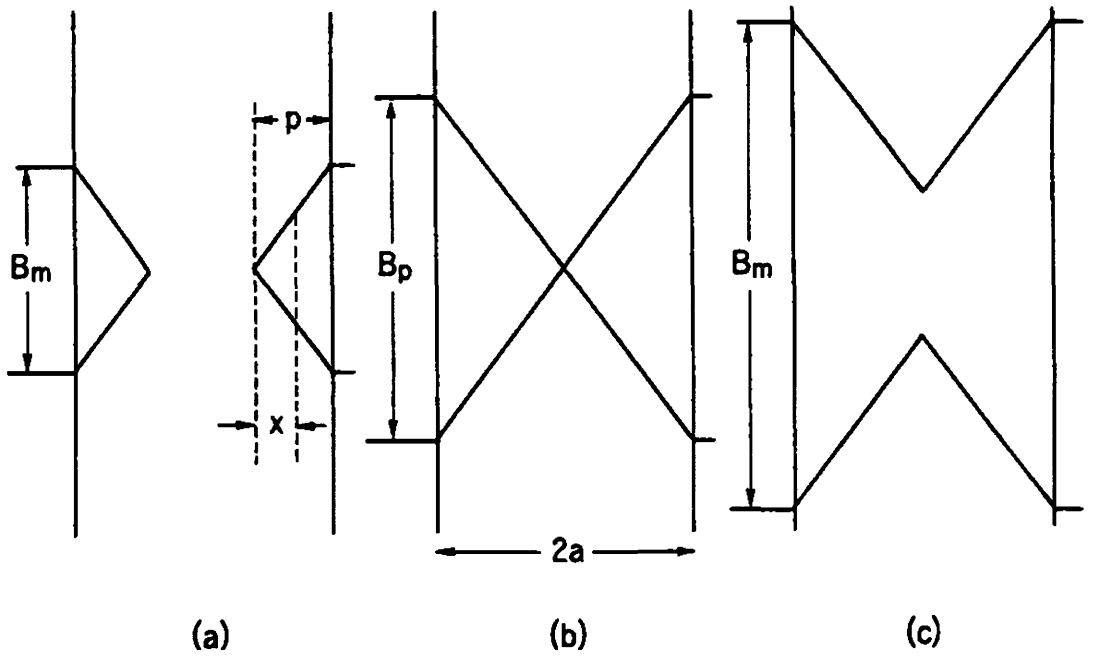

Figure 2-2: Field profiles within a superconducting slab subjected to field changes; (a) small peak-to-peak amplitude B_m; (b) B_m equal to the penetration field B_p; (c) large amplitude B_m. (From Osamura, 94.)

and a dimensionless field β can be defined as

$$\beta = \frac{B_m}{B_p} = \frac{B_m}{2\mu_0 J_c a} \tag{2.5}$$

which gives the average loss per cycle per unit volume to be

$$Q_h = \frac{{B_m}^2}{2\mu_0}\frac{\beta}{3} = \frac{{B_m}^2}{2\mu_0}\Gamma(\beta) \quad for\ \beta < 1 \tag{2.6}$$

and for $B_m > B_p$

$$Q_h = \frac{{B_m}^2}{2\mu_0}\left(\frac{1}{\beta} - \frac{2}{3\beta^2}\right) = \frac{{B_m}^2}{2\mu_0}\Gamma(\beta) \quad for\ \beta \geq 1 \tag{2.7}$$

$\Gamma(\beta)$ is called the loss factor because it represents the fraction of available magnetic energy ${B_m}^2/2\mu_0$ dissipated, and is plotted in Fig. 2-3.

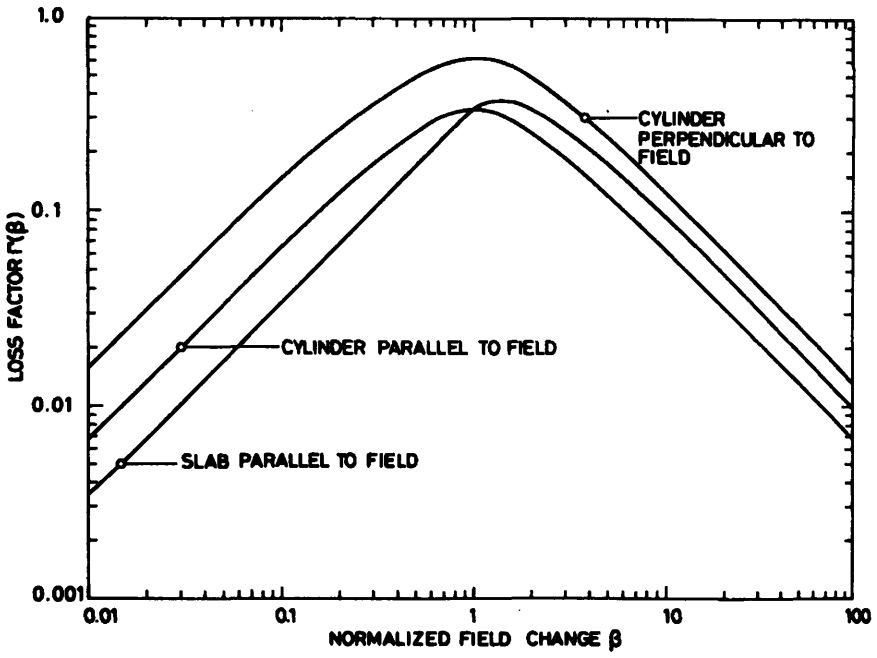

Figure 2-3: Loss factor for hysteresis loss per cycle in different shapes of superconductor (From Wilson, 83.)

Cylinder Parallel to the Field

In the case of the oscillating field parallel to the axis of a long cylinder, the field and current patterns are as shown in Fig. 2-4 and the loss expressions are [79, p. 164]

$$Q_h = \frac{{B_m}^2}{2\mu_0}\left(\frac{2\beta}{3} - \frac{\beta^2}{3}\right) = \frac{{B_m}^2}{2\mu_0}\Gamma(\beta) \quad for\ \beta < 1; \tag{2.8}$$

$$Q_h = \frac{{B_m}^2}{2\mu_0}\left(\frac{2}{3\beta} - \frac{1}{3\beta^2}\right) = \frac{{B_m}^2}{2\mu_0}\Gamma(\beta) \quad for\ \beta \geq 1 \tag{2.9}$$

The loss factor is plotted in Fig. 2-3. Due to the symmetry of the geometry β includes only the part of J_c which flows in the azimuthal direction, $J_c = J_{c\phi}$.

Cylinder Perpendicular to the Field

This case is similar to actual magnet windings, where both DC and pulsed fields are transverse to the cylindrical conductor. Due to the orientation of the field, the screening currents and penetrated field patterns are two-dimensional and much

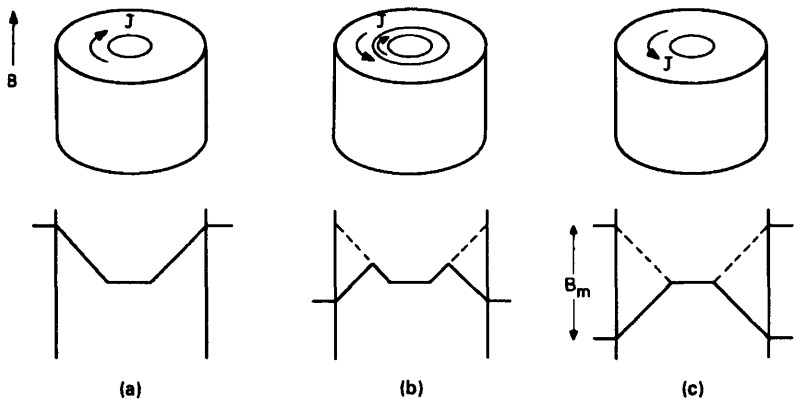

Figure 2-4: (a) Pattern of screening current in cylinder of superconductor subjected to a small longitudinal field change; (b) as the field is reduced; (c) when the field reaches the minimum value before rising again. (From Wilson, 83.)

harder to calculate. No analytical solutions exist and approximate solutions are based on using the magnetization and Eq. 2.1. The screening currents must produce a uniform field inside the superconductor which is equal and opposite to the applied field change. The field required can be produced with a cosine or overlapping ellipse distribution but the boundary is cylindrical, hence only an approximate model is possible, in which the shielding currents assume an elliptical inner boundary, whose ellipticity changes to keep up with the varying field as shown in Fig. 2-5. The fully penetrating field B_p is given by

$$B_p = \frac{4}{\pi}\mu_0 J_c a \tag{2.10}$$

where a is now the radius of the cylinder. The normalized field now becomes

$$\beta = \frac{B_m}{B_p} = \frac{\pi B_m}{4\mu_0 J_c a}. \tag{2.11}$$

The hysteresis losses calculated by Carr [13, p. 63] and Wilson [79, p. 169] are

$$Q_h = \frac{{B_m}^2}{2\mu_0}(1.44\beta) = \frac{{B_m}^2}{2\mu_0}\Gamma(\beta) \quad for\ \beta \ll 1; \tag{2.12}$$

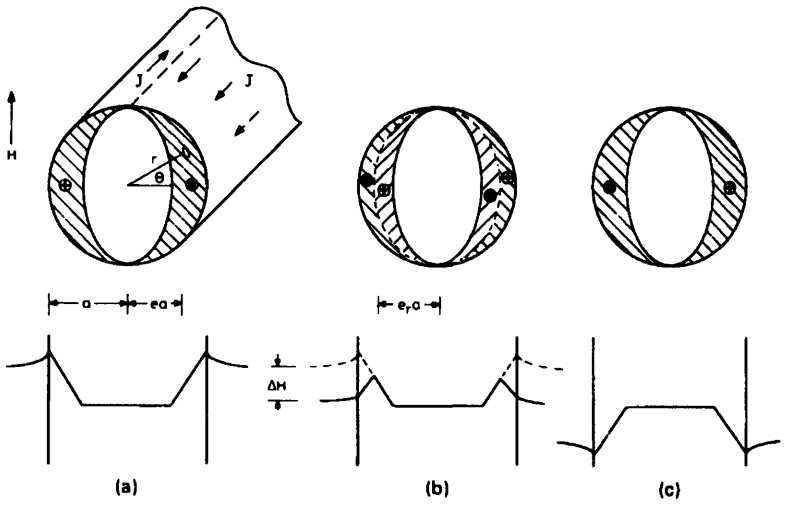

Figure 2-5: (a) Pattern of screening current in cylinder of superconductor subjected to a small transverse field change; (b) as the field is reduced; (c) when the field reaches the minimum value before rising again. (From Wilson, 83.)

$$Q_h = \frac{{B_m}^2}{2\mu_0}\left(\frac{4}{3\beta} - \frac{0.710}{\beta^2}\right) = \frac{{B_m}^2}{2\mu_0}\Gamma(\beta) \quad for\ \beta > 1 \tag{2.13}$$

The loss factor $\Gamma(\beta)$ is plotted in Fig. 2-3. The losses are larger than the case of a cylinder in parallel field because the screening field has a component outside the conductor which adds to the external field, and the sample feels a much stronger field than is applied. Using the field dependent J_c based on the model by Kim, et al. [36], with J_{c_0} and B_0 as constants,

$$J_c(B) = \frac{J_{c0}B_0}{B + B_0} \tag{2.14}$$

and the high β approximation of Eq. 2.13, Ogasawara [57, p. 216] calculated the hysteresis losses for NbTi alloy at B_m = 5 T to be Q_h = 11 mJ/cc.

Zenkevitch [82] and Ashkin [3] used complex polygonal functions with undetermined coefficients, instead of the simple ellipse used by Wilson, to model the boundary of the screening critical currents in the cylinder, but discovered that the hysteresis loss is not very sensitive to the choice of the contour representations of the flux penetration boundaries. Zenkevitch et al. [82] formulated simple expressions

for magnetization for cylinders in transverse field from their numerical analysis which they verified by experimental measurements [83]. These expressions are

$$Q_h = \frac{{B_m}^2}{2\mu_0}(\frac{4\beta}{3} - \frac{2\beta}{3}) = \frac{{B_m}^2}{2\mu_0}\Gamma(\beta) \quad for\ \beta < 1; \tag{2.15}$$

$$Q_h = \frac{{B_m}^2}{2\mu_0}(\frac{4}{3\beta} - \frac{2}{3\beta^2}) = \frac{{B_m}^2}{2\mu_0}\Gamma(\beta) \quad for\ \beta > 1 \tag{2.16}$$

In multifilamentary composites, there is an array of more or less equally-spaced cylindrical filaments, and the interaction of these filaments with one another has to be taken into account. Zenkevitch et al. [84] investigated this issue and found that field perturbations from neighboring filaments roughly canceled each other and the resulting loss was almost equal to the case of the cylinder being isolated.

2.1.2 Coupling Current Losses

As mentioned before, the filaments in a multifilamentary composite superconductor are coupled together due to time-varying magnetic fields, because of the low-resistance matrix metal present between them. Due to the induced potential by changing fields, screening currents can flow across the resistive matrix and dissipate heat. This coupling increases the effective flux jump distance from the radius of the filament to the strand radius as well, which is highly undesirable. Twisting the composite solves the flux jumping problem for uniform fields. The current which flows across the resistive matrix is called coupling current. Coupling current losses are of an eddy-current type so they depend on the cycle time of field change, unlike hysteresis losses.

Coupling and Eddy Current Loss in Twisted Multifilamentary Composites

There have been two types of theories developed for analysis of coupling and eddy current losses in twisted composites. One approach is the circuit model, by Ries [60] for example. The other one assumes that the filament structure is sufficiently fine for the composite to be treated as an anisotropic and homogeneous material

suggested by Morgan [51] and extensively worked on by Carr [14, 15, 16]. The two approaches give the same results which are presented here on the basis of the second approach.

A twisted filamentary composite placed in a uniform external field B_e with rate of change $\dot{B}_e$ is shown in Fig. 2-6. The field inside the composite B can be shown to be uniform. It can be shown [79, p. 177] that as a result of the external field change a uniform vertical current density $J_y = \dot{B}L/2\pi\rho_t$ will flow throughout the interior of the composite, where L is the twist pitch and ρ_t is the transverse resistivity. Carr [15] calculated the transverse resistivity and found it to lie between two limiting extremes. For no contact resistance between the filaments and the matrix, the superconductor shorts some of the matrix and the resistivity is reduced to

$$\rho_t = \rho_m \frac{1-\lambda}{1+\lambda} \tag{2.17}$$

where ρ_m is the matrix resistivity and λ is the filling factor of superconductor in the composite strand. For high contact resistance the effective resistivity becomes

$$\rho_t = \rho_m \frac{1+\lambda}{1-\lambda} \tag{2.18}$$

but it has been shown experimentally that it can be much higher than this.

Most multifilamentary zones are surrounded by a thin layer of copper, and the effective transverse resistivity after taking into account the resistivity of this outer layer is given by

$$\frac{1}{\rho_{et}} = \frac{1}{\rho_t} + \frac{w}{R_f \rho_m} + \frac{R_f w}{\rho_m}\left(\frac{2\pi}{L}\right)^2 \tag{2.19}$$

where R_f is the radius of the multifilamentary zone and w is the width of the outer layer and the power loss can be calculated to be [79, p. 180]

$$P = \frac{\dot{B}^2}{\rho_{et}}\left(\frac{L}{2\pi}\right)^2 = \frac{2\dot{B}^2}{\mu_0}\tau \tag{2.20}$$

where the loss time constant is given by

$$\tau = \frac{\mu_0}{2\rho_{et}}\left(\frac{L}{2\pi}\right)^2 \tag{2.21}$$

The effective transverse resistivity is dependent on the cross sectional structure of the wire and therefore on wire fabrication, and its calculation is made difficult due to the uncertainty in the spatial distribution of ρ_m in the multifilamentary zone which is never homogeneous, specially for composite Nb_3Sn wires made by a tin diffusion process.

The effective transverse resistivity is also effected by the purity of the material, the temperature (due to RRR [1] which is another material property), and the magnetic field (due to magnetoresistivity $\rho(B)$ [2]), and usually cannot be computed analytically.

The coupling loss calculations for different types of field changes, constant, exponential, and sinusoidal field changes for example, have been reviewed by Hlásnik [29].

2.1.3 Penetration Losses

Screening currents in the composite superconductor are assumed to be flowing in a thin current sheet at the outer surface, shielding the whole conductor against changes in applied field. In reality, these currents occupy a finite width of the multifilamentary zone, occupying the necessary cross-sectional area on the outside boundary, with superconducting filaments carrying the critical current density. This region is considered *saturated*. The current density required for shielding increases with increases in $\dot{B}$ and L and decreases in ρ, and so does the region of saturation. As the region of saturation expands, with more superconducting filaments carrying the critical current density, there is loss associated with penetra-

[1] RRR = residual resistivity ratio = $\frac{Resistance\ at\ 300\ K}{Resistance\ at\ 4.2\ K}$

[2] Magnenoresistivity of copper wire at 4.2 K has been determined experimentally to be $\rho(B) = \frac{\rho(B=0,\ T=300\ K)}{RRR} + \beta_M B(\Omega m)$ with $\beta_M = 4.8 \times 10^{-11}$ (Ω m).

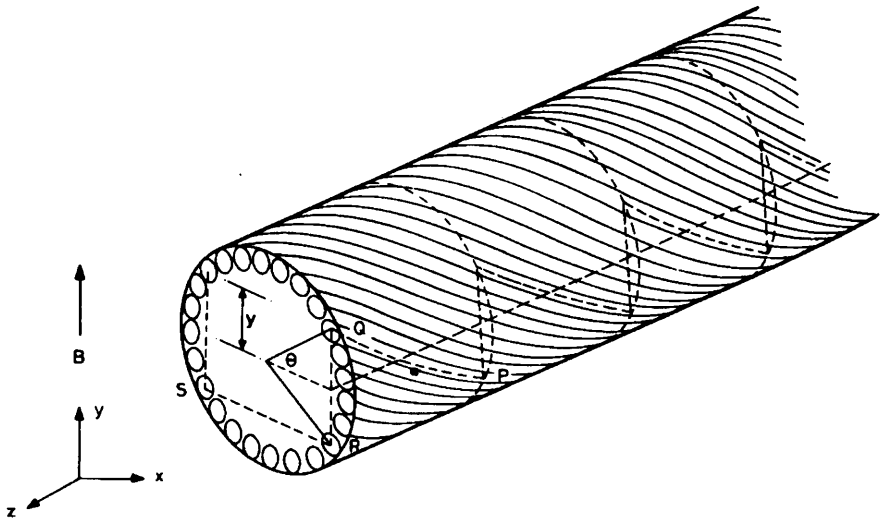

Figure 2-6: Twisted filamentary composite in changing transverse field. (From Wilson, 83.)

tion of flux through the saturated zone to its inner boundary. This loss has been analyzed by Ries [60] and by Ogasawara et al. [53, 54]. The analysis by Ries is considered here.

Ries was successful in drawing an analogy between penetration loss in a multifilamentary composite and hysteresis loss in a single filament (at low β). Both situations have an outer layer in which the spatial distribution of critical current density is roughly of cosine or elliptical form, and the boundary condition on the inner boundary layer is $E = 0$. This similarity implies that penetration loss in a multifilamentary composite can be approximated by hysteresis loss in a single wire of the same radius, with a current density λJ_c and with the same field difference $(B_e - B)$ between external and internal fields.

As an example, consider a twisted composite immersed in a ramped magnetic field with $\dot{B}_e = B_m / T_m$, which creates a difference $(B_e - B) = B_m \tau / T_m$. The analogous single filament has to be subjected to a field change of amplitude $B'_m = 2B_m \tau / T_m$ which gives the equivalent expression for dimensionless field (using eq 2.11)

$$\beta' = \frac{\pi B_m \tau}{2\mu_0 \lambda J_c a T_m} \tag{2.22}$$

The loss factor $\Gamma(\beta')$ can be calculated numerically. The expression for penetration loss becomes

$$Q_p = \frac{{B'_m}^2}{2\mu_0}\Gamma(\beta') = \frac{{B_m}^2}{2\mu_0}\frac{4\tau^2}{{T_m}^2}\Gamma(\beta') \tag{2.23}$$

Again, calculation of penetration losses is very approximate and completely dependent on wire parameters.

2.1.4 Transport Current Losses

In the models considered so far, it has been assumed that the only currents flowing in the superconducting filaments or the stabilizing matrix part of the multifilamentary composite are the screening currents induced by external magnetic field change or coupling currents. In reality, superconducting cables carry a transport current, AC or DC, which is provided by an external current source, for example, a power supply. This current is responsible not only for self-field losses, considered in detail in Chapter 6, but also changes hysteresis and coupling losses considerably. The effect of transport current on hysteresis and coupling losses is discussed below.

Effect of Transport Current on Hysteresis Losses

Consider the case of the slab in Section 2.1.1. Fig. 2-7 shows the field patterns for a slab with transport current I_t subjected to field changes of magnitude B_m. Fig. 2-7 (c) shows that the penetration field is given by $B_p(i) = 2\mu_0 J_c a(1-i)$ where $i = I_t/I_c$. When $B_m < B_p(i)$, the field patterns are the same as Fig. 2-2 and so the loss is given by

$$Q_h = \frac{{B_m}^2}{2\mu_0}\frac{\beta}{3} = \frac{{B_m}^2}{2\mu_0}\Gamma(\beta) \quad for\ \beta < (1-i) \tag{2.24}$$

For $B_m > B_p(i)$, that is above penetration, the field pattern is shown in Fig. 2-7 (d), and the loss becomes [57, p. 218]

$$Q_h = \frac{{B_m}^2}{2\mu_0}\left[\frac{1+i^2}{\beta} - \frac{2(1-i^3)}{3\beta^2}\right] = \frac{{B_m}^2}{2\mu_0}\Gamma(\beta) \quad for\ \beta \geq (1-i) \tag{2.25}$$

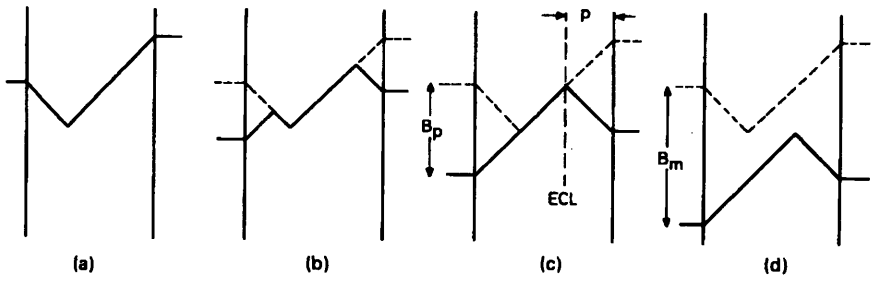

Figure 2-7: (a) Slab carrying fixed transport current in external field; (b) as the field is reduced; (c) when the field change penetrates the entire slab; (d) when the field reaches minimum value before rising again. (From Wilson, 83.)

The loss factor $\Gamma(\beta)$ is plotted in Fig. 2-8. Just above penetration a massive increase in hysteresis loss can be seen, and it is recommended to have $\beta \gg 1$ to avoid this region, which is achieved if there is fine subdivision of the superconductor. The loss in this case becomes

$$Q_h = \frac{{B_m}^2}{2\mu_0}\frac{1+i^2}{\beta} \quad for\ \beta \gg 1 \tag{2.26}$$

Hence, the presence of transport current increases the hysteresis loss, which has two sources in this situation. The external magnetic field source shows up as magnetization losses while the transport current source shows up as dynamic resistance losses. In practical experimental conditions the transport current increases the hysteresis losses by a factor of $(1 + i^2)$ [57].

Effect of Transport Current on Coupling Losses

Transverse field losses in multifilamentary composites carrying transport currents have been investigated by Ogasawara et al. [53, 54]. They have shown experimentally that the transport current is uniformly distributed over the cross-section of the composite after a few field cycles and the loss becomes the sum of hysteresis losses in the superconducting filaments and eddy current losses. When the field rate of change is high, the filaments are coupled so that the composite behaves as

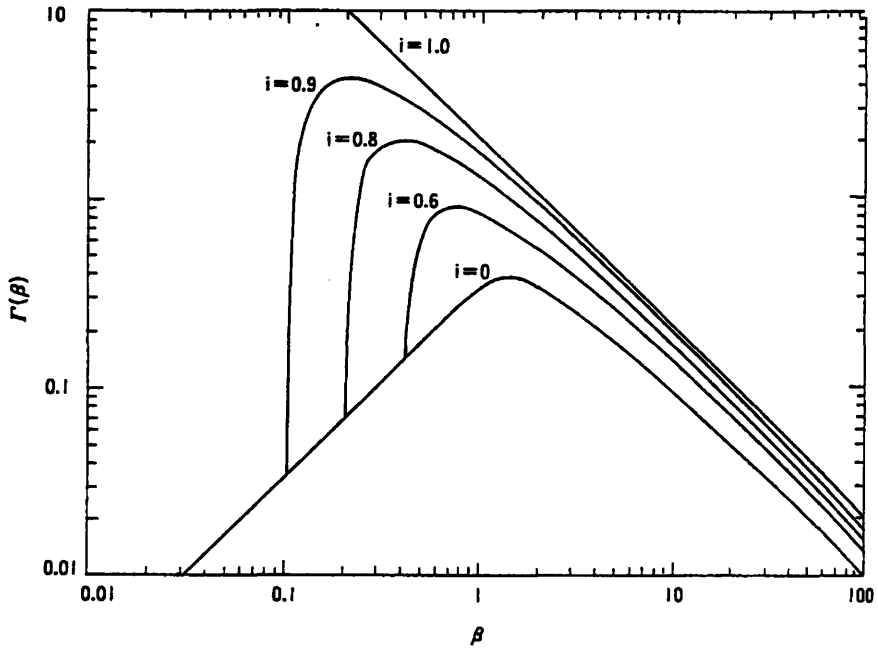

Figure 2-8: Hysteresis loss in a slab carrying DC transport current $I_t = iI_c$ and subjected to AC field. (From Osamura, 94.)

one thick conductor with current density λJ_c. By Eq. 2.26, the total loss increases by a factor of $(1 + i^2)$. At low rates of field change, on the other hand, the situation is not that simple: the loss stays almost constant till a characteristic value of $i = i_0$, and then increases sharply. This value i_0 is given by

$$i_0 = 1 - \frac{dB_e/dt}{B_{ps}/\tau} \tag{2.27}$$

where $B_{ps} = \mu_0 \lambda J_c R_f$ is the penetration field of a solid conductor equivalent to the composite. Clearly, if $dB_e/dt \ll B_{ps}/\tau$ then i_0 becomes close to 1 and the loss is nearly independent of transport current for $0 \leq i < 1$, which is the case when the sweep rate of B_e is low.

2.1.5 Concluding Remarks

As has been shown in this section, calculation of AC losses can be difficult and very approximate. In experiments which calculate these losses by indirect methods like calorimetric methods, it is not possible to evaluate each loss separately, unless some analytical expression is possible. For calorimetric methods of AC loss measurements, the results are extremely sensitive to the exact nature of data acquisition and interpretation. As a result, calorimetric measurements have questionable repeatability and are inconsistent when cross-examined with data gathered by other experimentalists in a similar fashion. In general, evaluation of AC losses can be very heuristic.

Self-field losses are covered in detail in Chapter 6 so they will not be addressed here. Their introduction presented in Section 1.1.3 should be sufficient for now. It should be remembered that self-field losses are usually negligible.

2.2 Stability Criteria for Multifilamentary Composites

All CICCs have cables containing many strands which are multifilamentary composites, originally proposed by Wilson et al. [80]. Therefore, before delving into a

discussion of stability of CICCs in Chapter 3, the stability criteria established for their basic component, the multifilamentary composites, are examined.

2.2.1 Adiabatic Theory of Flux Jumping

The positive feedback shown in Fig. 1-6 is the basic cause of flux jumps in the superconducting filaments. Consider the slab introduced in Fig. 2-1 when the critical state model was discussed. Assume this slab is thermally isolated and a quantity of heat ΔQ_s is supplied to it, which raises the temperature of the slab by ΔT. Due to the rise in the temperature the critical current density J_c will be reduced. The screening currents, at the former current density, will now be flowing in the flux flow regime and will dissipate heat due to flux flow resistivity. Once the resistive component of the screening current has decayed, the field profile will be as depicted in Fig. 2-9 with the dotted lines. The resistive voltage is driven by the change in flux due to field penetration resulting from the reduction of screening currents. In Fig. 2-9, the strip of width δx encloses a flux change $\delta\phi(x)$, and for small ΔJ_c, the current in the strip can be assumed to be constant, given by $J_c\delta x$. The heat generated in the slice, $\delta q(x)$ is the integration of resistive power generated over the time of decay of the resistive component of the screening currents

$$\delta q(x) = \int I(x)E(x)dt = J_c\,\delta x\,\delta\phi(x). \tag{2.28}$$

The flux change at x is calculated by integrating the field change from the slab mid-plane to x

$$\delta\phi(x) = \int_0^x \Delta B(x)dx = \int_0^x \mu_0\Delta J_c(a-x)\,dx = \mu_0\Delta J_c(ax-\frac{x^2}{2}). \tag{2.29}$$

The average heat generated per unit volume is

$$\Delta Q = \frac{1}{a}\int_0^a \delta q(x)\,dx = \frac{1}{a}\int_0^a \mu_0 J_c\Delta J_c(ax-\frac{x^2}{2})dx = \mu_0 J_c\Delta J_c\frac{a^2}{3}. \tag{2.30}$$

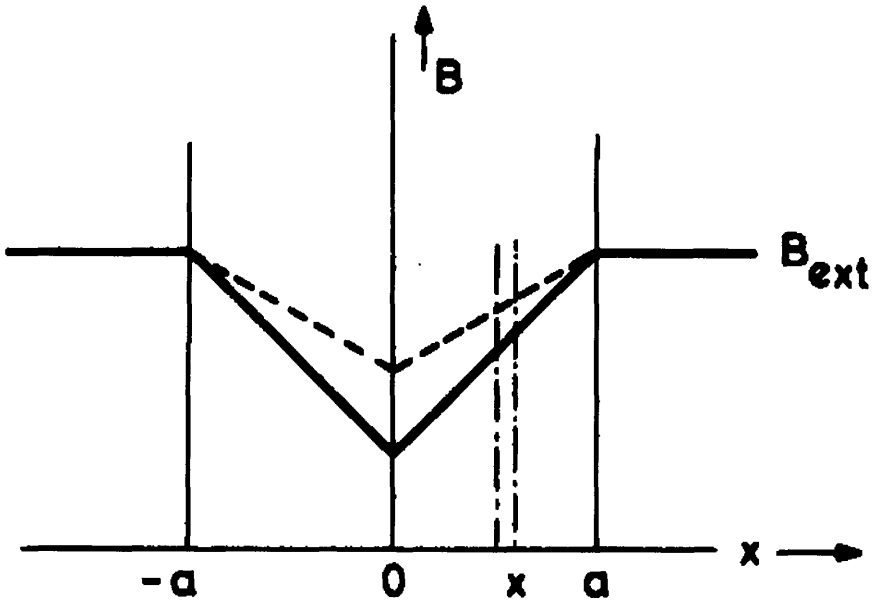

Figure 2-9: Change in screening current and internal field pattern due to heat input ΔQ_s. (From Wilson, 83.)

Using a linear relationship between temperature and critical current density (see Eq. 2.34), the heat balance condition for the slab becomes

$$\Delta Q_s + \frac{\mu_0 {J_c}^2 a^2}{3(T_c - T_{op})}\Delta T = \gamma C \Delta T \tag{2.31}$$

where C is the specific heat and γ is the density of the slab. The effective specific heat per unit volume, that is the amount of heat needed for a unity increase in temperature, given by $\Delta Q_s / \Delta T$, is clearly reduced. The condition which makes this effective specific heat zero, and allows for the smallest heat input to raise the temperature without any limitation namely cause a flux jump is [79, p. 134]

$$\frac{\mu_0 {J_c}^2 a^2}{\gamma C(T_c - T_{op})} = \beta < 3. \tag{2.32}$$

β is called the stability parameter, and the above condition is the condition for adiabatic stability to flux jumping. It is this condition which requires superconducting filaments to be no more than a few hundred μm. Since C increases rapidly with temperature, this stability criterion improves, and some flux jumps may die out before the critical temperature is reached. These flux jumps are called partial flux jumps.

2.2.2 Dynamic Stabilization

In Section 2.2.1 the stability condition for adiabatic stability against flux jumps was derived, which necessitates the superconducting filament diameter to be less than a few hundred μm, depending upon the material of the superconductor and the operating field and transport current values. The adiabatic theory of flux jumping does not take into account the movement of heat generated by flux motion. It is a good approximation for most practical superconductors, since their magnetic diffusivity D_m is much higher than their thermal diffusivity D_T, but is untrue for multifilamentary composites due to the presence of the stabilizer. The stability criteria derived without neglecting the diffusion effects of heat, magnetic flux and

Table 2.1: Thermal and Magnetic Diffusivities (4.2 K)

	Thermal conductivity k(W.m^{-1}.K^{-1})	Specific heat γC(J.m^{-3}.K^{-1})	Thermal diffusivity D_T(m^2.s^{-1})	Resistivity $\rho(\Omega.m)$	Magnetic diffusivity D_m(m^2.s^{-1})
NbTi	1.1×10^{-1}	5.4×10^{3}	2.0×10^{-5}	6×10^{-7}	4.8×10^{-1}
Nb_3Sn	4.0×10^{-2}	1.2×10^{3}	3.3×10^{-5}	7×10^{-7}	5.6×10^{-1}
Copper					
$B = 6$ T	1.0×10^{3}	8.9×10^{2}	1.1	2.0×10^{-10}	1.6×10^{-4}
$B = 6$ T	2.6×10^{2}	8.9×10^{2}	3.0×10^{-1}	4.2×10^{-10}	3.3×10^{-4}

current in the copper stabilizer are for *dynamic stability*. The diffusion equations for heat, current and magnetic flux are given by

$$\begin{aligned} D_T \nabla^2 T &= \frac{\partial T}{\partial t} \\ D_m \nabla^2 T &= \frac{\partial B}{\partial t} \\ D_m \nabla^2 T &= \frac{\partial J}{\partial t} \end{aligned} \tag{2.33}$$

where the thermal diffusivity $D_T = k/\gamma C$ and the magnetic diffusivity $D_m = \rho/\mu_0$, k being the thermal conductivity, γC the volumetric specific heat, and ρ the resistivity in normal state. In the simplified model of a slab with half-width a, solving Eq. 2.33 gives the characteristic diffusion time $\tau = 4a^2/\pi^2 D$. After consulting Table 2.1, which lists values of D_m and D_T for NbTi, Nb_3Sn and copper, it becomes clear that for NbTi and Nb_3Sn the characteristic time for magnetic diffusion τ_m is much less than for thermal diffusion τ_T, but the situation reverses for copper. As a consequence, in pure superconductors, field penetrates before any heat can diffuse out and the condition of adiabaticity is satisfied. However, in composite superconductors, the presence of copper in the matrix slows down flux movement significantly, thus reducing power dissipation due to flux motion and involving the coolant in the heat balance due to the fast diffusion of thermal energy generated to the strand surface.

Consider a strand with the superconducting filaments carrying current density J. To calculate the dynamic stabilization criterion, a heat pulse is supplied to the

strand which uniformly raises the temperature by ΔT. Due to the increase in temperature J_c reduces. If the heat pulse is large enough J_c will reduce to an extent that $J > J_c$ and the superconducting filaments can not carry the operating current any longer. Just enough current transfers into the copper matrix as is needed to lower the current density in the superconducting filaments to the reduced value of J_c. The current which transfers to the copper matrix produces joule heating due to the finite resistivity of copper. If this heat generation is less than the cooling capacity of the helium in intimate contact with the strand surface, the strand recovers and ΔT reduces to zero. The recovery happens in two stages:

1. Copper is cooled by liquid helium.

2. Superconductor is cooled by thermal conduction.

The competition between heat generation in the copper matrix and cooling by liquid helium is what determines the *Stekly criterion* of *cryogenic stabilization* discussed in Section 2.2.3. Now, consider the superconductor being cooled by thermal conduction, in the simplified slab model for ease of calculation. At constant B, J_c varies linearly with temperature as shown in Fig. 2-10 on page 66, which implies

$$J_c(T) = J_c(T_{op})\frac{T_c - T}{T_c - T_{op}} \tag{2.34}$$

where T_c is the critical temperature and the operating temperature $T_{op} = T_{He}$, the liquid helium coolant temperature (bath temperature). The temperature at which current transfer starts from the superconducting filaments to the copper matrix, the current-sharing temperature T_{cs}, can be ascertained from Eq. 2.34. It is the temperature at which the critical current density $J_c(T)$ becomes equal to the operating current density J_{op}. At the current-sharing temperature, any further reduction in critical current density due to a temperature increase forces the resulting change in critical current to transfer to copper and dissipate joule heat. Using Eq. 2.34, the

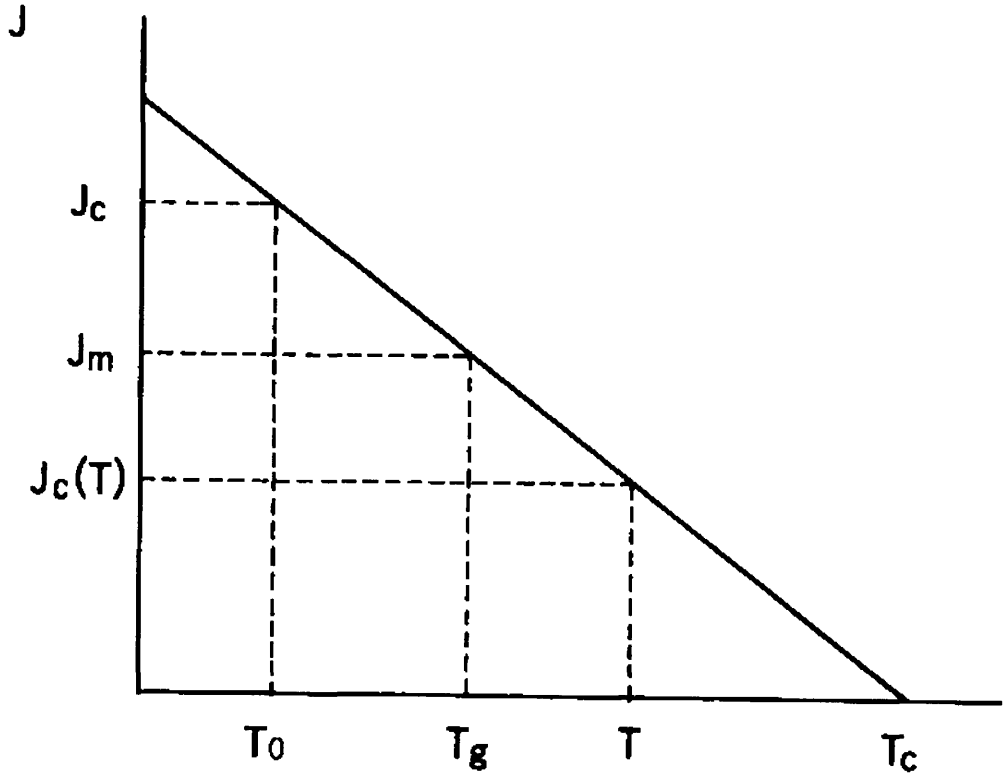

Figure 2-10: Critical current density as a function of temperature (T_g is the current sharing temperature T_{cs}). (From Osamura, 94.)

change in critical current density ΔJ_c for an increase in temperature ΔT is

$$\Delta J_c = J_c \frac{\Delta T}{T_c - T_{op}} \tag{2.35}$$

With λ as the ratio of superconductor in the strand (also called filling factor), the electric field set in the stabilizer due to this overflowing current through it is

$$E = \frac{\lambda}{1-\lambda} \rho \Delta J_c \tag{2.36}$$

The heat generation rate g_{sc}, defined per unit volume of the superconductor, that is, $g_{sc} = J_c E$. Combining Eqs. 2.35 and 2.36 gives an expression for the generation rate

$$g_{sc} = \frac{\lambda}{1-\lambda} \rho {J_c}^2 \frac{\Delta T}{T_c - T_{op}} \tag{2.37}$$

and the heat balance equation for the superconductor becomes

$$\gamma C_{sc} \frac{\partial}{\partial t} \Delta T = k_{sc} \nabla^2 (\Delta T) + \frac{\lambda}{1-\lambda} \rho {J_c}^2 \frac{\Delta T}{T_c - T_{op}} \tag{2.38}$$

where the subscript sc refers to the appropriate parameters of the superconductor. The solution of this partial differential equation, with the boundary condition that at the surface of the superconductor $\Delta T = 0$, is given by Ogasawara [57, p. 190] for a slab geometry, and the resulting condition for dynamic stability is

$$d^2 < \pi^2 \frac{k_{sc}(T_c - T_{op})}{\rho {J_c}^2} \frac{1-\lambda}{\lambda} \tag{2.39}$$

which gives characteristic distance of the superconductor $d < 59 \mu$m for typical values of k, T_c, ρ etc. The above treatment of dynamic stability considers the conductor to be a homogeneous mix of superconductor and copper (a superconducting slab sandwiched between two copper slabs) but real composites have inhomogeneous filamentary structure. According to Wilson [79, p. 156], finite filament size reduces the effective critical temperature rise by a factor of (1 - $a^2/8d^2$), where d is the characteristic distance defined by Eq. 2.39 and a is the filament radius. The

homogeneous theory can be safely applied to the heterogeneous composite if the correct reduction factor is applied to the temperature change ($T_c - T_{op}$). Stability needs the effective critical temperature rise to be non-zero or $a < 2\sqrt{2}d$. Thus, the dynamic stability criteria for filament size is very similar to the adiabatic stability against flux jumping, even though flux jumping depends on the specific heat of the superconductor, whereas the dynamic stability is a function of the thermal conductivity of the superconductor and the resistivity of the normal matrix material. Wilson considers this to be purely coincidental.

2.2.3 Cryogenic Stabilization

A multifilamentary composite designed on the basis of the criteria defined by adiabatic and dynamic stability is stable against flux jumping, but practical magnets need to be made stable against a variety of disturbances besides flux jumping, like energy dissipation due to wire motion in response to Lorentz forces and due to wire friction. The dissipated energy has to be removed quickly so that the normal zone which develops because of it does not propagate and quench the magnet. Cryogenic stabilization describes the conditions to be met in order to achieve this requirement.

Most conductors are cooled by boiling helium at an ambient temperature of 4.2 K in intimate contact with the strand surface area. The cooling condition which determines the amount of heat which can be efficiently removed is determined in terms of the heat transfer condition applicable and the way it unfolds in time. Fig. 2-11 shows the heat transfer curve for a strand with a copper surface in liquid helium boiling at 4.2 K. Starting from the left hand side, the first leg represents the nucleate boiling region, where the liquid is in good contact with the surface, and therefore, the heat transfer is good. As the liquid evaporates, a vapor film is deposited on the surface of the conductor which inhibits heat transfer, shown as the third leg, which represents film boiling and less efficient heat transfer. The transition region represented by the second leg, with a negative slope, is unstable

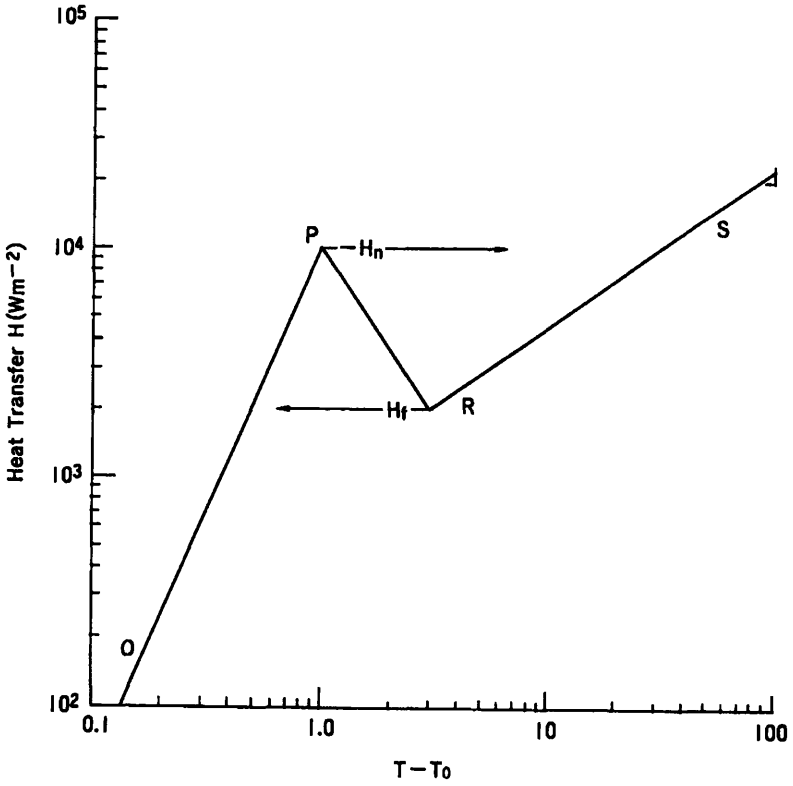

Figure 2-11: Heat transfer from a metal surface to liquid helium boiling at 4.2 K. (From Osamura, 94.)

and is hardly observed in practical situations. From Fig. 2-11, it is evident that for small disturbances which do not involve temperature changes of more than 1 K, the high heat transfer region of nucleate boiling can be utilized.

As mentioned earlier, at constant background magnetic field, the critical current density is a linear function of temperature given by Eq. 2.34 and shown in Fig. 2-10. For the operating current density $J_{op} < J_c$, Eq. 2.36 becomes

$$E = \frac{\lambda}{1-\lambda}\rho[J_{op} - J_c(T)] \tag{2.40}$$

and the heat generation per unit volume of the composite becomes

$$g = \lambda J_{op} E = \frac{\lambda^2}{1-\lambda}\rho J_{op}[J_{op} - J_c(T)] \tag{2.41}$$

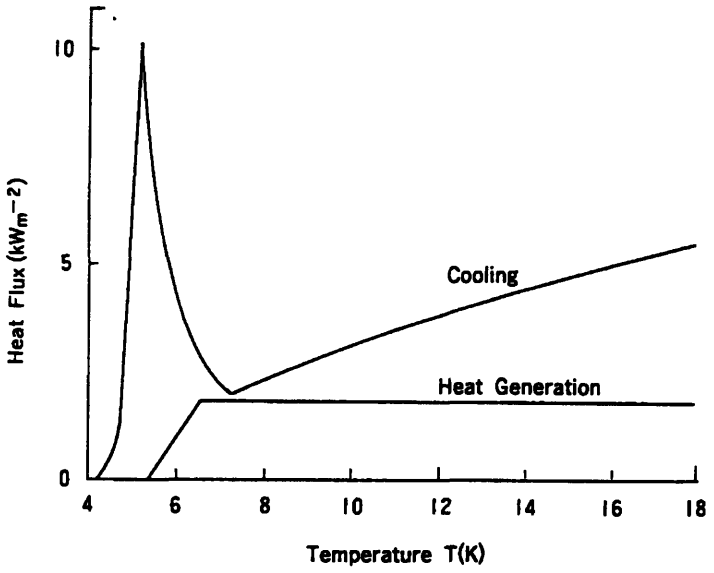

Figure 2-12: Heat generation and cooling of NbTi 6-T conductor operated at full stabilization (From Osamura, 94.)

From Eq. 2.34 and Eq. 2.41, it can be easily extrapolated that g is zero for $T < T_{cs}$, increases linearly for $T_{cs} < T < T_c$, and becomes constant for $T > T_c$ given by the value

$$g_{op} = \frac{\lambda^2 \rho {J_{op}}^2}{1-\lambda} \tag{2.42}$$

When the conductor is heated to the critical temperature T_c, the superconducting filaments cannot support any current and all of the current transfers to copper, which is why the generation is constant above the critical temperature. The resulting heat generation curve is shown in Fig. 2-12. The cooling per unit volume of the strand is given by

$$q = \frac{P}{A} h(T - T_{op}) \tag{2.43}$$

where P and A are the wetted perimeter and the cross-sectional area of the conductor, and h is the heat transfer coefficient between the conductor and the coolant. If $T_{op} = T_{cs}$ then $J_{op} = J_c(T_{op}) = J_o$ (say), and for this case if the perturbation is strong enough that the temperature raises to T_c, the ratio of g and q becomes the

Stekly parameter α

$$\alpha = \frac{\rho\lambda^2 J_o{}^2 A}{(1-\lambda)Ph(T_c - T_{op})} \tag{2.44}$$

Since for complete cryogenic stabilization, it is considered enough that generation be always less than cooling capacity, the simplest criterion for cryogenic stability is

$$\alpha < 1 \tag{2.45}$$

which was postulated by Stekly and Zar (1965) [68] and Stekly, Thome and Strauss (1969) [67]. For normalized heat generation and cooling and the heat transfer coefficient independent of temperature, the heat generation and cooling curves are plotted as functions of normalized temperature in Fig. 2-13 on page 72 for various values of α. The points where the heat generation equals cooling are points of equilibrium and the stability or instability of the equilibrium is determined by comparing the slope of the two curves. For stability, the increase in generation due to an increase in temperature has to be less than the accompanied increase in cooling. As Fig. 2-13 shows, with g and q as normalized heat generation and cooling, $t = (T\text{-}T_{op}) / (T_c\text{-}T_{op})$, and $i = I_{op}/ I_c$, that for $\alpha < 1$, since $g < q$, the sample is fully or perfectly stable. For $\alpha = 1$, $g = q$ for all $0 \leq t \leq 1$. The sample can take any value of t at equilibrium and since the slopes are equal the superconductor will not recover the superconducting state. Stekly and Zar [68] and Stekly et al. [67] also showed that for $\alpha > 1$, the sample is partially stabilized and is fully stable if $i < \alpha^{-0.5}$. This model does not take into account the heat conduction along the wire, and therefore, is quite conservative.

Equal-Area Criterion

The cryogenic stability criterion derived earlier neglects the possibility of conduction of heat axially along the conductor length. This treatment assumes that the normal zone is very large in length and at uniform temperature. However, in reality, the normal zone is finite in extent and is enclosed by a cold superconducting region at the ends. Due to the temperature gradient at the hot and cold regions,

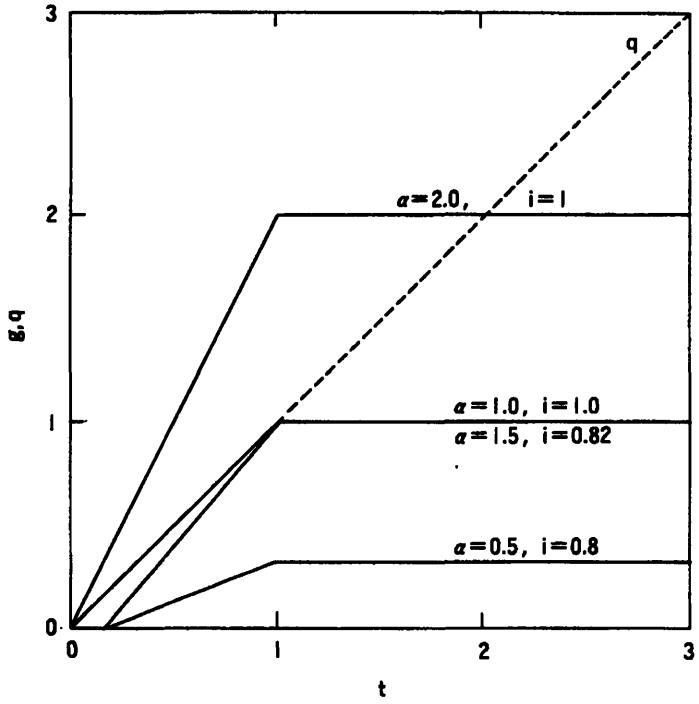

Figure 2-13: Normalized heat generation and cooling plotted as functions of normalized temperature. (From Osamura, 94.)

there will be heat conduction which will assist in cooling the conductor. If enough heat is removed by conduction, the normal zone will shrink and disappear, even though the simple cryogenic criterion is not satisfied.

The effect of end heat conduction was incorporated into the condition for cryogenic stability by Maddock, James, and Norris [47]. They introduced an elegant theorem which describes the equilibrium of an interface between hot and cold zones on a long heat-generating bar immersed in a coolant. As a result, they came up with what is called the *equal area criterion*, whose mathematical derivation can be found elsewhere [79, p. 94], but a simple geometrical interpretation follows. The equal-area criterion requires that no net area is enclosed between the heat generation and cooling curves as shown in Fig.2-14. The surplus heating represented by the area of the polygon on the right should be equal to the surplus cooling represented by the area of the polygon on the left. If the cooling is more, the normal zone will shrink and disappear. If the heating is more, the normal zone will grow in time and quench the conductor. The equal-area criterion when applied to the cryostability problem is also termed as the *cold end recovery* condition.

Transient Stability

In the treatment so far, the coolant is assumed to have the capability of absorbing a infinitely large amount of energy, that is the stability is steady-state. The disturbances that actually occur in operating magnets decay in short periods of time, and the amount of energy to be dealt with by the coolant is finite. The maximum allowable energy determines the limit of transient stability. The disturbances seen in practice are categorized as either distributed or localized.

For distributed disturbances, if the disturbances are weak so that the temperature excursion is less than 1 K then the cooling stays in the nucleate boiling region, and stability is given by the condition $\alpha < 1$ where α is the Stekly parameter given in Eq. 2.44. Tsukamoto and Kobayashi [74] and Steward [69] observed that the pulsive heat increases significantly as the pulse width decreases for forcing a transition from nucleate to film boiling. Iwasa [31] proposed the *critical current margin*

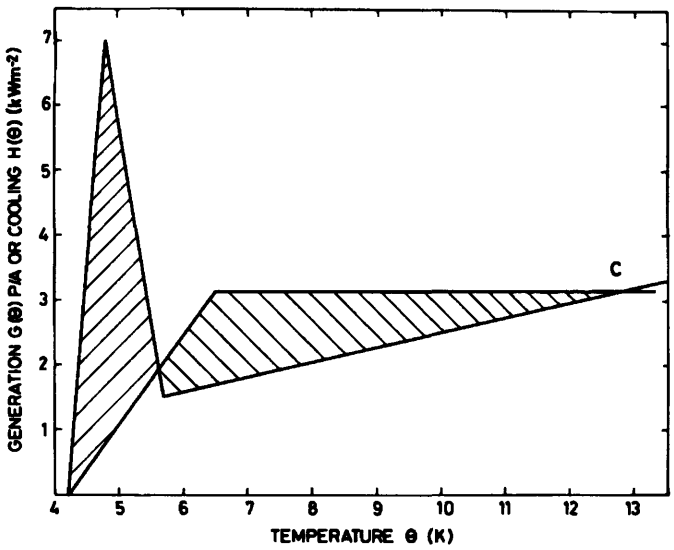

Figure 2-14: Equal-area condition for cryogenic stability of a normal zone with cold superconducting regions at either end (for NbTi at 6 T with $T_c = \Theta_c = 6.5$ K). (From Wilson, 83.)

theory which claims that transient stability requires the temperature change due to the disturbance to be less than the range allowed before the current transition temperature is reached

$$\Delta T < (T_{cs} - T_{op}) \tag{2.46}$$

so that there is no joule heating. Wilson [78] suggests adiabatic stability by using the latent heat of helium available effectively.

For localized, point disturbances, stability is established in terms of minimum propagating zone (MPZ) . For stability, the disturbance energy has to be less than the formation energy of the MPZ after the disturbance is over. The evaluation of this formation energy is a non-trivial task because it requires the solution to the heat balance equation

$$\gamma C \frac{dT}{dt} = \frac{d}{dz}(k_z \frac{dT}{dz}) + G + G_d(z,t) - Q \tag{2.47}$$

where $G_d(z,t)$ is the disturbance. This issue has been addressed by Nishi et al. [52].

Now, that an understanding of stability of composite superconductors has been accomplished, the stability of CICCs can be addressed.

Chapter 3

Stability of CICCs: Past and Present

3.1 Introduction

CICCs have become the leading choice of superconducting cables for building large-scale superconducting magnets for fusion research. The typical CICC, to be used in ITER TF and PF coils for example, is a multiple-strand multi-stage cable with multifilamentary strands in a copper stabilizer matrix encased in a structural alloy conduit. The typical CICC for ITER with a central cooling channel is shown in Fig. 3.1. The stability margin in cables for large-scale magnets for fusion applications has been studied analytically [8, 11, 18, 23] and experimentally [1, 2, 30, 46, 50] by quite a few researchers in the fusion community. The reason for this importance given to stability is because it is one of the determining factors in the design of cable-in-conduit conductors, such that they are optimized for applications in fusion devices. Stable operation of these CICCs is vital to the success of the magnetic fusion program, because the magnets used in tokamaks store huge amounts of magnetic energy (about 10 GJ for prospective ITER TF coils), which is released suddenly if the magnet quenches and is a very undesirable event. Tokamak magnets are subject to magnetic field variations of a large magnitude, especially when a plasma disruption occurs or when the plasma current is generated by swinging the ohmic solenoid field, and therefore, are always subjected to fairly large disturbances even during normal operation. As a consequence, the approach

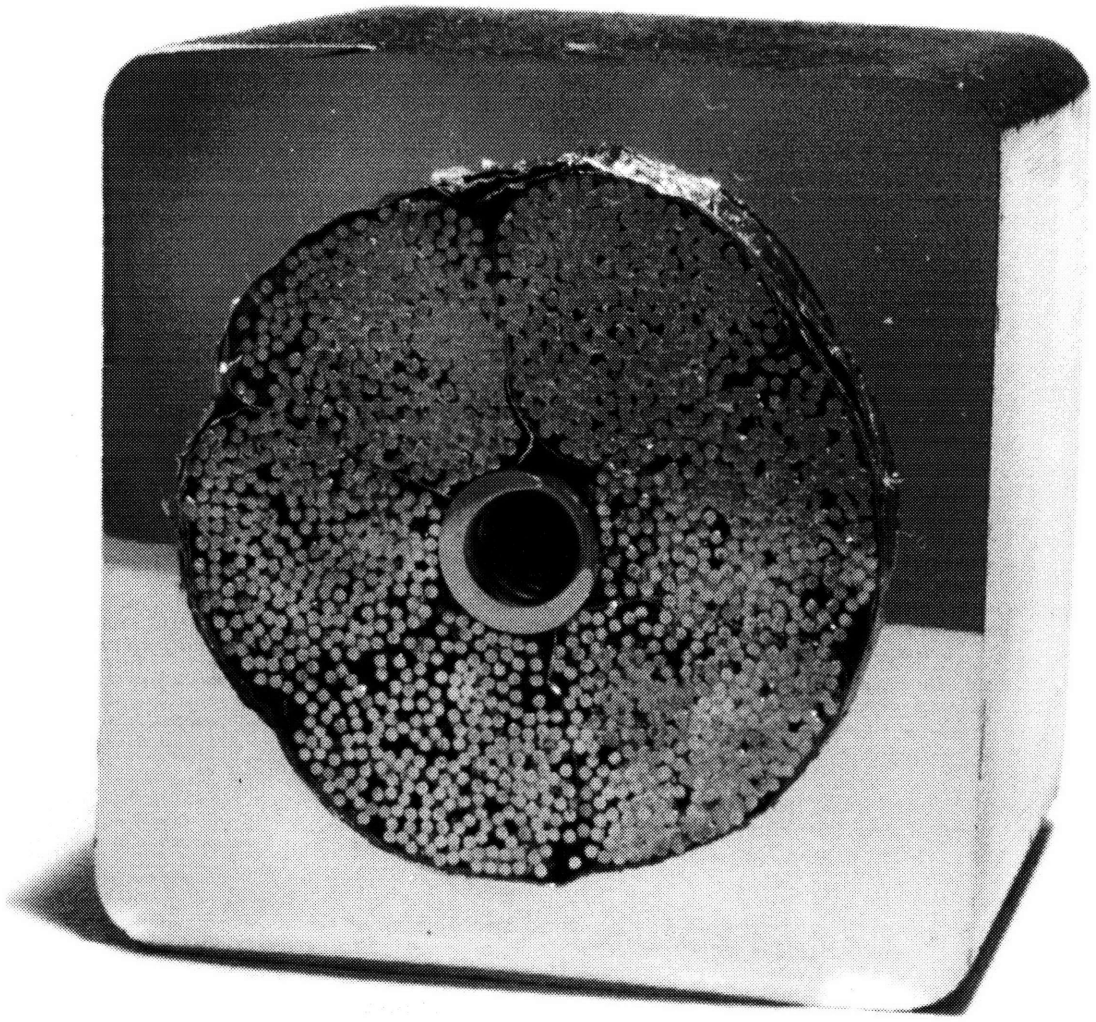

Figure 3-1: CICC with central cooling channel under development for ITER.

of stabilizing the magnet by reducing or perhaps eliminating the possibility of perturbations is not viable at all.

Since the most probable source of disturbance energy during the regular functionality of these large-scale magnets is field variation, it is fundamental to understand the reasons and physical manifestation of AC losses. Therefore, AC losses were discussed in some detail in chapter 2. A much more detailed analysis of AC losses has been done by Gung [26].

3.2 Background

Before attempting to analyze, in detail, the concept of stability of CICCs, it is a prerequisite to become familiar with its theoretical and experimental basis. The relevant definitions and ideas which are key to comprehending these foundations are presented in this section.

3.2.1 Definition of Stability

In general terms, stability is understood in reference to a state of equilibrium of a system. Any system for which a state of equilibrium, dynamic or static, can be defined, is considered stable or unstable to well-defined perturbations on the following basis: when the system's state of equilibrium is perturbed, if it reclaims its state of equilibrium after the perturbation is over it is considered stable against this specific perturbation, if not, it is unstable.

Stability of superconducting cables is defined by Iwasa, Hoenig and Montgomery [32] in terms of the energy deposited in the cable as the maximum, sudden, and uniform energy deposition, due to some disturbance, from which recovery to superconducting state is still possible, assuming this disturbance drives part or whole of the superconducting cable normal. Usually, it is assumed that a long enough length of the conductor goes normal so that axial conduction along the cable, also referred to as *end conduction*, is negligible compared to heat transfer to the helium, and is ignored. The energy absorbed by the cable and helium increases their temperature, and for stability both the cable and helium temperatures have to drop below the current-sharing temperature (T_{cs}) after the disturbance is over. Energy depositions typical of stable perturbations in CICCs are in the range of 50-200 mJ/cc [1] of cable volume [25] for NbTi conductors and up to a few thousand mJ/cc for Nb_3Sn conductors for low transport currents, typically less than 20% of the critical current value [2, 49].

[1] cc = cm^3 = cubic centimeter

3.2.2 Stability Margin of a CICC

The stability margin of a CICC is defined as the maximum sudden energy input into the conductor that it can absorb and still recover its superconducting state. It is measured in units of mJ/cc. Thus, the stability margin is visualized in terms of transient stability of the conductor.

With an empirical heat transfer coefficient h, imposed by the conditions of the experiment (by the nature of coolant flow-rate, pressure requirements, and phase of the coolant for example), the stability margin curve as a function of the applicable heat-transfer coefficient h looks like curve A in Fig. 3-2. The stability margin (ΔH or ΔE) is low for low values of h until h reaches a certain limit. Above this limit ΔH increase rapidly and reaches a plateau value. Further increase in h does not increase the stability margin noticeably. This plateau value is limited by the available helium enthalpy between the current sharing temperature T_{cs} and the ambient helium bath temperature T_b. It defines the amount of energy that can suddenly be absorbed by the helium without the cable's transition into the current-sharing region of joule heating. Hence, if the heat transfer coefficient is high enough to be above this threshold value, the stability margin of the CICC expressed in mJ/cc of cable volume is approximated by

$$\Delta H = \frac{A_{He}}{A_{cable}} \int_{T_b}^{T_{cs}} c_p dT \tag{3.1}$$

where A_{He} is the cross-sectional area of helium, A_{cable} is the total cross-section of the cable, and c_p is the specific heat of helium.

Due to the involvement of the ratio of cross-sectional areas, the stability margin as given by Eq. 3.1 becomes a function of the void space f_v (fraction of conduit inner space not occupied by the cable) and the ratio of copper to superconductor f_{Cu} in the cable strands. It has been shown [8, 21] that this dependence can be exploited and CICCs can be optimized in terms of having the largest stability margin for a unique pair of values for f_v and f_{Cu}.

Using experimental data, stability margins are usually plotted against one of

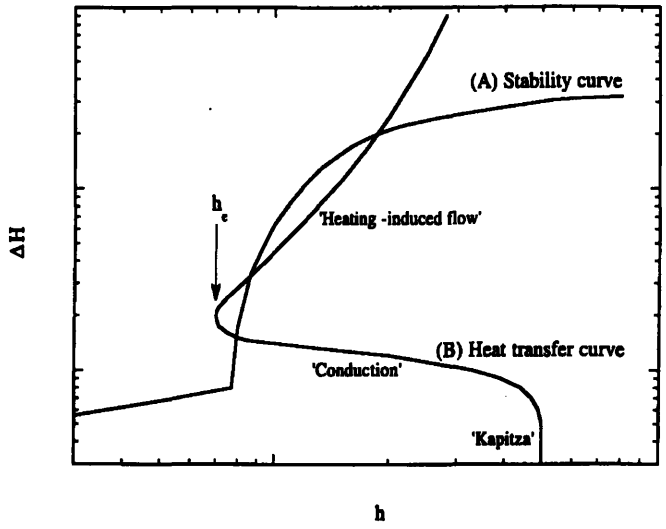

Figure 3-2: Combined plots of stability curve and heat transfer curve of a CICC. The labels on the heat transfer curve denote the dominant mode of heat transfer from metal to helium for the relevant region of the curve. (From Lue, 94.)

the principal operating parameters such as transport current. The stability margins for the experiments carried out by Lue et al. [46] and Ando et al. [2] are examples as shown in Fig. 3-3. The values of ΔH on the curves defines the largest amount of energy that can be absorbed in the cable at the associated transport current and not quench eventually. Fig. 3-3 (a) also implies that stability margins can be multiple-valued.

3.2.3 Cooling Regimes and Limiting Current

As seen in Fig. 3-3, the stability margin shows a sharp transition at a specific current value called limiting current I_{lim}. This transition was observed in the results of many stability experiments and numerical studies on CICCs. This transition has been explained in terms of the cooling capacity available for heat removal. Fig. 3-4 helps explain the situation. The so-called *well-cooled regime,* characterized by the high stability margin, is on the left hand side and is limited by the wire

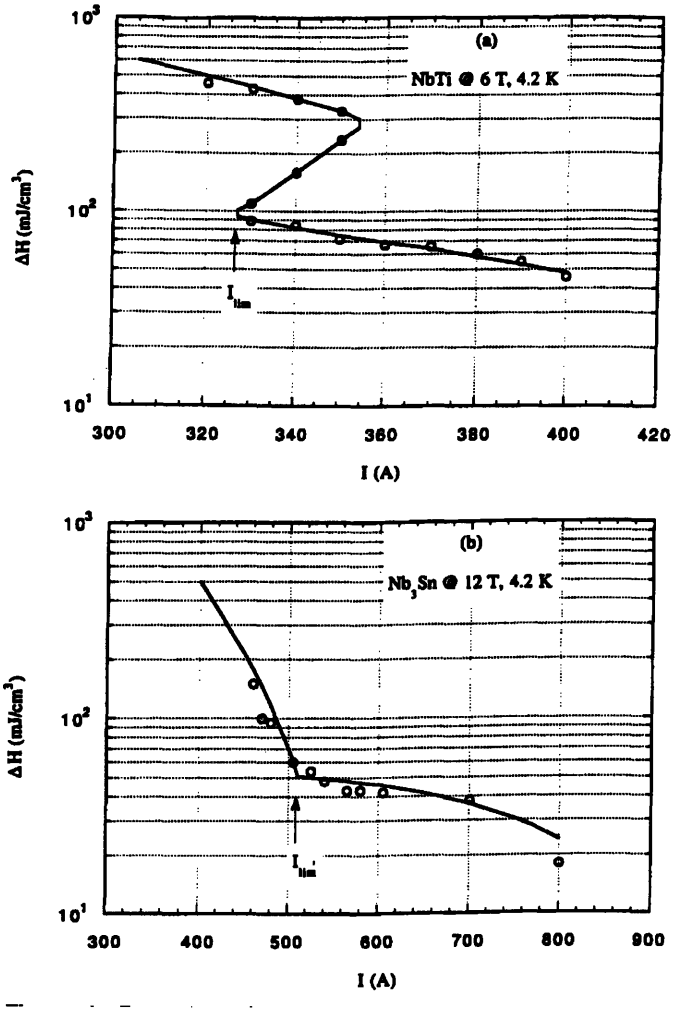

Figure 3-3: Examples of stability margins as functions of transport currents in a CICC based on (a) NbTi data taken from the experiment by Lue et al. and (b) Nb_3Sn data taken from the experiment by Ando et al. (From Lue, 94.)

plus helium enthalpy. The *ill-cooled regime* on the right hand side is limited by only the wire enthalpy and shows a much lower stability margin. The initial model given by Bottura [8] (originally by Minervini and Shultz) was based on a sharp boundary between the ill-cooled and well-cooled regimes, occurring at the limiting current I_{lim}. The model assumes that below I_{lim} the energy margin is equal to the overall helium heat capacity between the operating temperature T_{op} and the current-sharing temperature T_{cs}, and above I_{lim} the margin is equal to the cable enthalpy available between these temperatures, which is very small and is neglected. The fact that the volumetric heat capacity of helium is much larger than typical strand materials translates into the energy margin in the well-cooled regime being about 2-3 orders of magnitude higher than in the ill-cooled regime. A zero-dimensional power balance at the strand surface between heating and cooling gives the value of limiting current to be

$$I_{lim} = \sqrt{\frac{ph_e A_{Cu}(T_c - T_{op})}{\rho}} \tag{3.2}$$

which looks similar to the Stekly criterion with $\alpha = 1$ which is the stability limit for pool-cooled magnets. Since we have forced-flow cooled cables, the helium available for stabilization is limited, as opposed to the infinite amount available in pool-cooling. This limitation on the available heat capacity of helium changes the behavior of the stability margin as a function of I_{op} [18]. As a result, Eq. 3.2 does not correspond to the real situation in CICCs.

Bottura [9] developed a model which is a more realistic representation of CICCs, which was based on earlier models [8, 11] and followed the direction suggested by Ciazynski and Turck [18]. He defined a maximum recovery temperature T_{rec} as the common temperature of helium and strands at the end of recovery from an energy input equal to the stability margin at that operating point. Based on this model, $T_{rec} = T_{cs}$ below I_{lim}^{low} and $T_{rec} = T_{op}$ above I_{lim}^{upp}. This defines three regions based on this temperature, distinguished by the limiting current values of the lower limiting

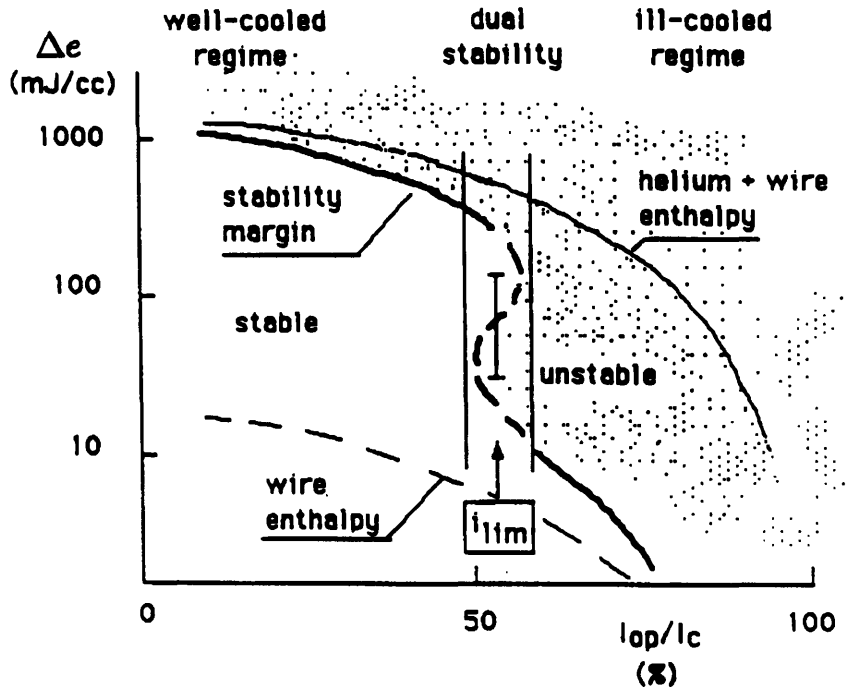

Figure 3-4: Ill-cooled and well-cooled regimes for a CICC. (From Bottura, Mitchell, and Minervini, 91.)

current I_{lim}^{low} and the upper limiting current I_{lim}^{upp} given by

$$I_{lim}^{low} = \frac{ph_e A_{Cu}(T_c - T_{op})}{\rho I_c} \tag{3.3}$$

and

$$I_{lim}^{upp} = \sqrt{\frac{ph_e A_{Cu}(T_c - T_{op})}{\rho}} \tag{3.4}$$

where $I_{lim}^{upp} = I_{lim}$. The main results of the model are:

1. The well-cooled regime is defined as the region where $I_{op} < I_{lim}^{low}$, where the helium temperature is allowed to go all the way to T_{cs} while maintaining a power balance which is favorable for recovery.

2. Above I_{lim}^{upp} the power balance is unfavorable for recovery, and so defines the ill-cooled regime.

3. For $I_{lim}^{low} < I_{op} < I_{lim}^{upp}$, there exists a transient regime, where T_{rec} decreases from T_{cs} to T_{op}. If the energy input is such that helium temperature does not rise to more than T_{rec} then power balance will be favorable for recovery, otherwise not. As T_{rec} decreases from T_{cs} to T_{op} in the transition region, the energy margin drops from its value in the well-cooled regime to its value in the ill-cooled regime. Fig. 3-5 shows this behavior.

The energy margin in the ill-cooled regime is zero, while in the well-cooled regime it is given by [9]

$$\Delta E = \frac{1 - f_{Cu} - f_{nc}}{f_{Cu} + f_{nc}} \rho C_p (1 - i)(T_c - T_{op}) \tag{3.5}$$

where i = I_{op}/ I_c, ρ and C_p are the helium density and specific heat, and f_{Cu} and f_{nc} are the fractions of copper and non-copper in the cable space. Bottura also gives the energy margin in the transition regime as

$$\Delta E = \frac{1 - f_{Cu} - f_{nc}}{f_{Cu} + f_{nc}} \rho C_p (1 - \alpha)(T_c - T_{op}) \tag{3.6}$$

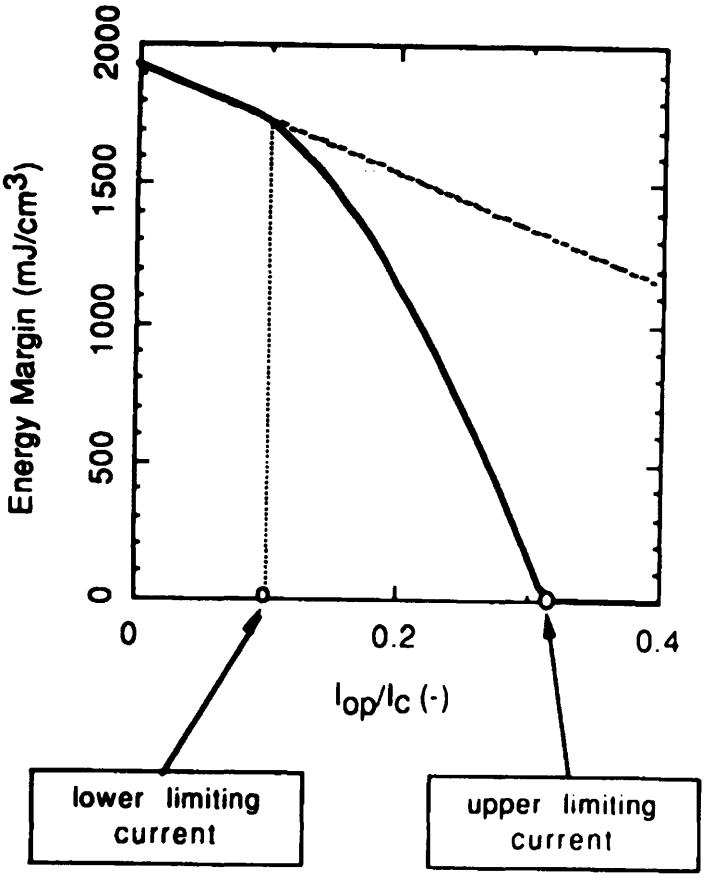

Figure 3-5: Behavior of energy margin ΔE as a function of operating current I_{op}. Lower and upper limiting currents are indicated and mark the points at which the energy margin curve shape changes. The dashed line shows the total heat capacity available in the helium till T_{cs}. (From Bottura, 94.)

This model does make the assumptions of instantaneous heating and negligible metal heat capacity.

3.2.4 Multiple Stability of a CICC

As shown in Figs. 3-3 (a) and 3-4, the stability margin of a CICC can be multivalued as the operating current is varied. For a certain range of operating currents around I_{lim}, the cable was sometimes stable to small energy inputs, unstable to large ones, stable again for still larger ones, and unstable for the largest ones. This multivalued nature of stability curve is related to the discovery by Shanfield [66] (later used by Iwasa et al. [32]) that recoveries of a CICC were quite independent of the helium flow and were possible even at zero flow. Based on their experiments, Lue et al. [45, 46] concluded that induced flow produced by conductive heating of the helium, early in the recovery process, is extremely important for determining the stability of a CICC, especially for CICCs cooled by supercritical helium. Fig. 3-2 shows the different stages of heat transfer, for a conductor cooled by supercritical helium. In the first stage, the heat transfer is dominated by the high value of Kapitza conductance, which is followed by heat diffusion in the helium boundary layer, and finally there is a convective steady state heat transfer phase when the a low-density boundary layer is fully developed [41].

The multivalued stability was successfully explained by Dresner [22] by combining the two curves in Fig. 3-2. Basically, the conductor is stable to a heat input ΔH if the heat transfer curve lies to the right of the stability curve and unstable if its vice versa. In the event that the two curves cross each other more than twice, multiple stability will be observed.

3.2.5 Stability Criterion for CICCs

For fusion magnets, reliability requires that they be operated in the well-cooled high stability region at operating currents less than $I_{lim} = I_{lim}^{low}$ as given by Eq. 3.3. This ensures the availability of helium enthalpy all the way upto T_{cs}, and gives

stability margins of up to a few J/cc for Nb_3Sn conductors.

The effective heat transfer coefficient h_e is required for estimating and comparing the virtues of different cooling conditions. It can be calculated from Eq. 3.3 as well if I_{lim} can be experimentally determined. The I_{lim} calculations require knowledge of the heat or energy input into the conductor from a known perturbation and the ability to obtain this knowledge is integral to the success of a stability experiment.

3.3 Stability Experiments

As mentioned in section 1.2.1, many experiments have been done with the motivation to determine the stability margin in large cables for the construction of large-scale magnets used in a variety of applications. For fusion magnets, for example the ones used to generate the toroidal field in a tokamak, particular attention has been given to analyzing the stability margin of cable-in-conduit conductors, which are the main choice of cables for ITER magnets. More recently, CICCs with a central coolant channel have become popular, the central hole providing a low impedance hydraulic path for quick transport of warm helium, which would take much longer in the compact void space in traditional CICCs [39]. For any new cable design, it is important to determine its viability in terms of stability to external and internal disturbances as part of the design process. Important concepts relevant for understanding stability of CICCs have been covered in the previous section. In this section, a review of the stability experiments performed thus far is presented. The perturbation techniques employed to simulate the disturbances faced during normal operation of large-scale magnets, especially fusion magnets, are discussed. Finally, the heart of this thesis, the pulsed current stability experiment is introduced.

3.3.1 Perturbation Methods used in Experiments

The basic mechanism of performing a stability experiment is fairly simple and routine. The sample CICC is provided with normal operating conditions, that is the field, current density, and temperature are below critical values. Then some disturbance is initiated which deposits some energy in the cable, thus forcing it to depart from its equilibrium position. The disturbance energy may be able to force the cable to a permanent departure from the superconducting state, in which case the cable is unstable to the disturbance, otherwise it is stable. A series of disturbances can be analyzed and in this manner, and a stability margin predicted for the sample cable. For this stability information to be useful, the disturbances have to be somehow calibrated in terms of the actual energy they end up depositing inside the cable, because the physical phenomenon important for stability analysis is the amount, rate, and spatial distribution of the energy inputted, and not its source.

As previously examined, there are three major techniques used to input this disturbance energy inside the superconductor which have been used by researchers involved in stability experiments. Firstly, a line or point heating source is embedded inside the cable during cable fabrication [42, 43, 46, 77]. The amount of heat and the rate at which it is deposited inside the cable is controlled by means of controlling the heater pulse duration, shape, and amplitude externally. There are a few major disadvantages of this method. The heater acts as a local heat source and cannot be used to simulate disturbances which provide a uniform source of heating very well. Also, the heat generated by the heater might directly go to the helium and result in an inflated reading for the energy deposited inside the cable. The source is decoupled from the sink though, as changes in the conductor will not effect the heater in any way.

The second method, which is widely popular because of the similarity of the way it deposits energy inside the cable to anticipated disturbances in a tokamak [2, 44, 50, 59, 64], is the method of inductive heating. Simply stated, an external

coil produces a varying magnetic field linked with the sample cable and generates AC losses in the cable. The calibration of AC losses is a non-trivial process. Heat generation is fairly uniform though.

In the third method, a current pulse of known pulse width, amplitude, and shape is superposed on the transport current [40]. The idea is to produce joule heating in the sample by forcing more than the critical current through the sample for part of the duration of the pulse. The heat generation is again expected to be uniform depending on the uniformity of the resistive stabilizer. The source is decoupled from the sample as in the first method. The only real disadvantage is that pulsed current disturbances are hardly the kind of disturbances one would expect during normal tokamak operation.

Another deciding factor for the choice of method for introducing perturbations into the conductor is the amount of energy needed to be deposited inside the conductor. During normal operation, wire motions in a bundled conductor can cause a thermal disturbance for a duration of 1 to 10 ms, generating a heat input of a few hundred mJ/cc in the metal volume of the strands for Nb_3Sn conductors. Therefore, the source has to deliver about 2 - 3 J/cc to determine the stability margin. The inductive heating method is best suited for inputting such energies in general, but with high voltage current pulsers it is possible to employ the third method.

3.3.2 Stability Experiments in the Past: A Review

Some details of the important stability experiments done in the past on CICCs are given in Table 3.1 [41], which emphasizes a comparison of limiting currents. As is evident from the table, all of these experiments were done on NbTi conductors, except for the last three which used Nb_3Sn conductors.

For operating currents above the limiting current I_{lim} the stability margins observed were 100 mJ/cc or less irrespective of which conductor was used. This implies that wire enthalpies were more or less the same across the board. For

operating currents below I_{lim}, the stability margins were a few hundred mJ/cc for NbTi conductors and a few thousand mJ/cc for Nb_3Sn conductors. Thus, Nb_3Sn conductors are attractive because of their high stability.

I_{lim} calculation was not difficult for the conductors which had a high high stability margin in the well-cooled regime because the transition to ill-cooled region was very sharp clearly identifying I_{lim}. For low upper stability margins, the transition was more broad and I_{lim} was hard to pinpoint. For some experiments [50], no I_{lim} was observed since presumably $I_{lim} > I_c$. It was found that J_{lim} ranged from 5 to 8 kA / cm^2 for NbTi conductors and 9 to 15 kA /cm^2 for Nb_3Sn conductors.

In their experiment on the DPC-EX coil, Yoshida et al. [81] found that the measured stability margin was in good agreement with heat capacity of helium in the range of 4-6 K but the agreement was unacceptable for higher temperatures specially in the 8-9 K range. They used the inductive heating technique. Another inductive heating experiment on the DPC-TJ coil by Sasaki et al. [63] had even larger deviations between experimental results and the ones expected based on a reduced model experiment although

> "The stability margins of the DCT-TJ coil and 1/18 reduced scale show the same tendency with regard to operating current."

In general, stability experiments based on inductive heating show an uncertainty of about 20-30 %.

3.3.3 The Pulsed Current Stability Experiment

The pulsed current stability experiment, whose investigation as a reliable experiment to perform stability experiments on CICCs is the main purpose of this thesis, is very similar to the experiment performed by Lottin and Miller [40]. The experiment uses pulsed current superposed on transport current to initiate disturbance energy into the cable. As the current density increases inside the conductor, the current sharing temperature decreases as shown in Fig. 2-10 on page 66. If the pulse has high enough amplitude, T_{cs} will decrease to T_{op} and current sharing will

Authors	Conductor	L_s (m)	d_w (mm)	f_v (%)	B (T)	T_b (K)	I_{lim} (kA)	J_{lim} (kA cm^{-2})
Hoenig and Montgomery	57 strand NbTi	3.0	1.05	43.0	8	4.3	5.0	6.1
Lue *et al.*	3 strand NbTi	3.3	1.00	44.0	6–7	4.2	0.325	7.1
Lue and Miller	3 strand NbTi	4.8	1.00	44.0	2–7	4.2	0.340	7.5
Lue and Miller	3 strand NbTi	5.2	1.00	44.0	7	4.2	0.208	4.6
Lottin and Miller	2 strand NbTi +2 strand Cu	2.0	0.75	45.0	6–8	1.8–4.2	0.194	6.2
Lue and Miller	36 strand NbTi +21 strand Cu	340	0.72	43.0	5–7	3.3–4.2	3.64	8.6
Ando *et al.*	3 strand NbTi	?	1.32	49.0	7–9	4.2	0.410	5.1
Phelan *et al.*	12 strand NbTi, insulated	6.4	2.03	46.0	7	4.2	1.92	2.7
Schmidt [a]	1 strand NbTi	1.1	1.25	77.0	0	4.2	0.250	4.7
Wachi *et al.*	54 strand NbTi, insulated	34.3	0.65	36.6	6.6	4.1–5.0	2.10	7.4
Takahata *et al.*	486 strand NbTi, insulated	45	0.67	40.0	1.5–3	4.5	15.0	5.2
Takahata *et al.*	486 strand NbTi	34.5	0.71	34.5	2–3.2	4.5–7.5	21.0[c]	7.2
Miller *et al.*	162 strand Nb_3Sn +27 strand Cu	4.0	0.69	35.0	8	4.2	>17.0[b]	14.5
Minervini *et al.*	27 strand Nb_3Sn	3.8	0.70	32.0	10	4.2	>1.35[b]	8.8
Ando *et al.*	4 strand Nb_3Sn	1.0	1.04	34.5	11–13	4.2	0.600	11.6

[a] Experiment performed in a closed volume of helium rather than a cable-in-conduit form
[b] No limiting currents were observed in these tests. The highest test currents were taken as I_{lim}
[c] It was not clear if there was a limiting current in this test. The critical current was taken as I_{lim}

Table 3.1: Stability Experiments on CICCs (Part I).

Authors	ℓ (m)	τ (ms)	v_{He} ($m\,s^{-1}$)	p (atm)	B (T)	T_b (K)	I_{lim} (kA)	h_e ($W\,m^{-2}\,K^{-1}$)	k
Hoenig and Montgomery	3.00	9.0	0.31	3.0	8.0	4.3	5.0	1260	0.30
Lue *et al.*	3.25	16.7	0	5.0	6.0	4.2	0.325	1200	0.26
Lue and Miller	4.80	5.0	0	5.0	6.0	4.2	0.340	1310	0.22
	4.80	50.0	0	5.0	6.0	4.2	0.232	610	0.14
Lue and Miller	0.99	10.0	0	5.0	7.0	4.2	0.208	680	0.19
	2.04	10.0	0	5.0	7.0	4.2	0.225	800	0.19
	3.62	10.0	0	5.0	7.0	4.2	0.244	940	0.19
Lottin and	2.00	1.0	0	2–3	6.0	4.2	0.194	1250	0.17
Miller [a]	2.00	1.0	0	2–3	6.0	3.6	0.210	1160	0.16
	2.00	1.0	0	2–3	6.0	1.8	0.315	1600	0.22
Lue and	1.10	3.5	0.60	1.1	5.8	4.2	3.64	1770	0.39
Miller [a]	1.10	3.5	0	0.5–1	7.0	3.7	4.40	3080	0.68
Ando *et al.*	0.04	0.1	0	6.5	7.0	4.2	0.530	1760	0.85
	0.04	0.1	0	6.5	8.0	4.2	0.410	1540	0.75
Phelan *et al.*	0.06	0.4	0	5.6	7.0	4.2	1.92	480	0.44
Schmidt	1.10	10.0	0	4.0	0	4.2	0.250	430	—
Wachi *et al.*	0.10	5.0	0.63	10.0	6.6	4.1	2.10	760	0.22
	0.10	5.0	0.67	10.0	6.6	5.0	1.20	440	0.13
Takahata *et al.*	0.10	5.0	0.24	9.8	1.6	4.5	15.0	160	0.06
Takahata *et al.*	0.10	5.0	0.47	10.0	2.8	7.5	21.0	1900	0.61
Miller *et al.* [a]	3.40	10.0	0	5.0	8.0	4.2	>17.0	>1380	0.22
Minervini *et al.*	3.76	20.0	0	2.5	10.0	4.2	>1.35	>670	0.07
Ando *et al.*	0.04	0.1	0	10.0	11.0	4.2	0.600	1050	0.25
	0.04	0.1	0	10.0	12.0	4.2	0.515	940	0.22
	0.04	0.1	0	10.0	13.0	4.2	0.480	1000	0.23

[a] Extra copper strands were not included in the calculation of A_{Cu} but were included in P

Table 3.2: Stability Experiments on CICCs (Part II).

proceed with joule heating resulting from it. The heating may increase the temperature which will further deteriorate the current sharing situation. After the pulse is over, if some of the transport current is still in the current sharing stage, it will be a DC heating source and the conductor will quench.

The energy lost in joule heating can easily be calculated by integrating the product of current through the sample and the voltage across it. If the self-field losses in the cable due to the pulsed current can be proved to be negligible, the integration result would give a fairly accurate measurement of the energy actually dissipated inside the conductor. No complicated calibration is required in this case. However, if that is not the case, then the energy dissipated will represent only part of the energy margin, and some calibration will be needed.

The experiment is introduced in complete detail in Chapter 4.

Chapter 4

A Pulsed Current Stability Experiment

To fulfill the main objective of this thesis, a stability experiment was devised which enabled the stability analysis of a sample CICC to pulsed current disturbances. Two different experimental apparatus setups were used in the stability experiments performed. They were exactly the same conceptually but had minor distinguishing parts in the source used for pulsed current and in the data acquisition system. This chapter discusses the ideology of the experiment, the apparatus which was needed for it, and the procedures involved in performing the experiment and securing the resulting experimental data.

4.1 Theoretical basis

Stability experiments using pulsed current disturbances have been done by Lottin and Miller [40] back in 1982 and the basis of this stability experiment is similar to theirs. The CICC is operated within its region of superconductivity, that is with external field $B_e < B_c$, transport current $I_t < I_c$ and ambient temperature $T < T_{cs}$. An external source provides pulsed current, which is superposed on the transport current, and depending on the amplitude of the current pulse, the total current through the sample cable may exceed the critical current I_c for part of the duration

of the pulse. This will trigger current transfer of the exceeding current to the copper matrix, which will dissipate joule heat in the matrix. The heat generated is removed by the helium surrounding the individual strands in the CICC. Assuming the cooling conditions stay more or less constant, the heat generated by the pulsed current overflowing into the copper matrix may be efficiently removed and the CICC will recover the superconducting state after the pulse is over. The CICC is stable to such pulses. Otherwise, the superconducting state will not be recovered in the duration of the pulse, and the presence of transport current in the CICC, with the conductor at a temperature $T > T_{cs}$, will quench the conductor. These pulses will demarcate the locus of perturbations to which the particular CICC is unstable.

4.1.1 Prediction of Stability Margin

If the pulse width is constant, and the operating variables namely the transport current I_t, the background external magnetic field B_e and the ambient bath temperature of the cable T_b are held constant as well, then the amplitude of the current pulse can be used as a parameter to predict the demarcating boundary between stable and unstable perturbations. It is important to take into account the factor of training to the perturbations which the conductor will go through inevitably. Basically, by undergoing training the conductor will quench at higher pulse amplitudes for the same set of operating parameters as time progresses. The process of training is limited, of course, and the conductor will finally establish a fair deal of repeatability of results for identical experimental conditions. Thus, these current pulses can be used to predict the boundary which distinguishes stable perturbations from unstable ones. This boundary is referred to as the *stability margin*.

4.1.2 Calculation of Energy Deposition

The calculation of energy deposited in the conductor as a result of the pulsed disturbance is particularly simple, at least in theory, and is one of the major attractions of this experimental method to perform stability analysis. Since their is no change

in B_e, their are no hysteresis losses, coupling losses, or penetration losses as advocated by $B_m = 0$ in Eqs. 2.12 and 2.23 and $\dot{B} = 0$ in Eq. 2.20 as $\dot{B}_e = 0$. The losses due to rate of change of transport current or self-field losses are analyzed in Chapter 6. In the event that these self-field losses due to the rate of change of total current during the pulse duration are negligible as compared to the resistive losses in the CICC as a consequence of current sharing, the power in the conductor for the duration of the pulse is

$$P_{tot}(t) = V_{sam}(t) I_{tot}(t) \tag{4.1}$$

where V_{sample} is the voltage measured across the relevant length of the CICC and I_{tot} is the current through the CICC, which is the sum of the pulsed current I_p and the transport current I_t. Integrating Eq. 4.1 for the time period of the pulse t_p gives the energy deposited in the conductor during the pulse E_d

$$E_d = \int_0^{t_p} P_{tot} dt \tag{4.2}$$

Technically speaking, the integration should give pure resistive power which is the required observation, since due to the identical nature of initial and final states of stored energy in the conductor, the reactive power should integrate to zero. This fact is extremely important because it makes the required calculation even simpler, and will be elaborated here further.

In circuit jargon, the sample can be represented by a resistor R_{sam} and an inductance L_{sam} in series. The actual voltage which will show up on the voltage tap will consist of a resistive component V_R and an inductive component V_L. The inductance is just a measure of flux per unit current, $L = \phi / I$, and according to Faraday's law, $V_L = d\phi/dt = d(LI)/dt$, so that Eq. 4.2 becomes

$$E_d = \int_0^{t_p} (V_R + V_L) I dt = \int_0^{t_p} V_R I dt + \underbrace{\int_0^{t_p} I \frac{d}{dt}(LI) dt}_{inductive\ term} \tag{4.3}$$

The inductive term, after integration by parts, gives

$$\int_0^{t_p} I\frac{d}{dt}(LI)dt = \underbrace{LI^2|_0^{t_p}}_{term\,1} - \underbrace{\int_0^{t_p} LIdI}_{term\,2} \tag{4.4}$$

L is usually an intrinsic property of the geometry of the cable and is not a function of the current through it, that is, it is constant. But assuming that the geometry is effected by current distribution during the pulse, for example if the current flows through different strands in different magnitudes, L can become an instantaneous function of current. Although, in this case, it can be further assumed that $L = L(I)$, that is L is a function of I only. Whether L is constant or a function of I, as long as its value at $t = 0$ and $t = t_p$ is the same, since transport current stays constant, term 1 and term 2 will evaluate to zero. Therefore,

$$E_d = \int_0^{t_p} V_{sam} I_{tot} dt = \int_0^{t_p} V_R I_{tot} dt \tag{4.5}$$

4.1.3 Consistency of Operating Conditions

For this experiment to be reliable, it is very important that the operating parameters which are considered constant in the calculations in fact stay constant. This condition requires that the transport current I_t and the external magnetic field B_e stay constant while the pulse current is flowing through the CICC. The background magnetic field B_e usually qualifies easily, since it is not actively coupled with the sample and the energy dissipation does not affect its source. The transport current I_t, in contrast, can become a problem if its source has power output limitations which are too low to keep the current constant while the sample load dissipates energy. If this is the case, then the assumption of constant transport current during the pulse can no longer be satisfied. The constancy of background magnetic field B_e and the transport current I_t is heavily dependent on the available source equipment and their controllability.

Another important requirement for the validity of the experiment is that the

cooling conditions are fairly identical for all pulses, independent of what they are: pool boiling in He-I or forced-flow with a certain fixed velocity of He-II (superfluid helium). In the event of a quench, the sample has to be cooled down to the helium bath temperature, before it can be tested again, otherwise, the stability margin will be reduced because of the existing conductor temperature being closer to the current sharing temperature, and the deduced stability margin will be less than it actually is.

The consistency of cable parameters is necessary as well, including the superconducting sample, its connecting leads, and all other wires used in the experimental arrangement of the necessary apparatus. The reason is that if characteristics like contact resistance, total resistance, insulation integrity, inductance etc. changes over time, it will adjust the amplitude and pulse width of the pulsed current even when all operating parameters are identical. Fortunately, it is not very difficult to meet this requirement usually, unless part of the CICC is damaged due to an extended quench.

4.1.4 Graphical Representation of Stability Margins

As mentioned earlier in Section 3.2.2, stability margins are visualized graphically as 2-D graphs in which one of the variables is the energy deposited in the conductor per unit volume in mJ/cc and the other one is one of the operating variables. The graph demarcates the region which forms the locus of points representing perturbations to which the cable is stable from the region which consists of a representation of unstable perturbations. Only the operating variable used in the graph is varied. The reason for this is that depositing identical amount of energy in the conductor for different operating conditions is bound to output different responses, in general, although some particular combinations of these parameters might have the same results.

The typical stability margin, as calculated by Lottin and Miller [40] in their experiment using a 5-strand NbTi cable (2 superconducting strands in Cu matrix

and 3 pure Cu strands) in a stainless steel conduit is shown in Fig. 4-1 (b). Their cable's cross-section is shown in Fig. 4-1 (a). Their experiment was performed in superfluid He-II at 1.8 K.

The stability margin clearly shows the limiting current discussed in Section 3.2.3 specially for the curve for B_e = 8 T. Since stability margins are normally smooth functions of operating parameters, a few data points are enough to precisely distinguish stable regions from unstable ones.

4.1.5 Advantages and Disadvantages

From the review of the pulsed current stability experiment so far, it becomes clear that the forte of this experiment is its methodology of energy deposition into the cable which greatly simplifies the calculation of this energy, primarily by avoiding the need to calculate AC losses. The source of pulsed current is decoupled from the sample due to its large input resistance as seen from the side of the sample, during the time of pulse activation. It is practically disconnected at all other times. Unlike for perturbation initiation by embedded heaters in the conductor, the energy deposition is quite uniform, and unlike inductive heating induced energy dissipation, the calculation of AC losses is circumvented. The cable parameters do not enter energy calculations except for the calculation of conductor volume, which is needed for computing energy dissipation per unit volume. The independence of calculations from details of the cable geometry at the filament level such as twist pitch, orientation of pulsed field with respect to the conductor and the extent of their spatial uniformity within the composite is definitely an attractive feature of this method. Also the difficulty of calibrating the AC loss in each cable sample for each experiment conducted against particular field variations is avoided. These calibrations can be sensitive to the vertical and horizontal orientations of the sample to the pulsed field.

There is an important distinction between the energy calculated in stability experiments employing disturbances initiated by inductive heating and the ones

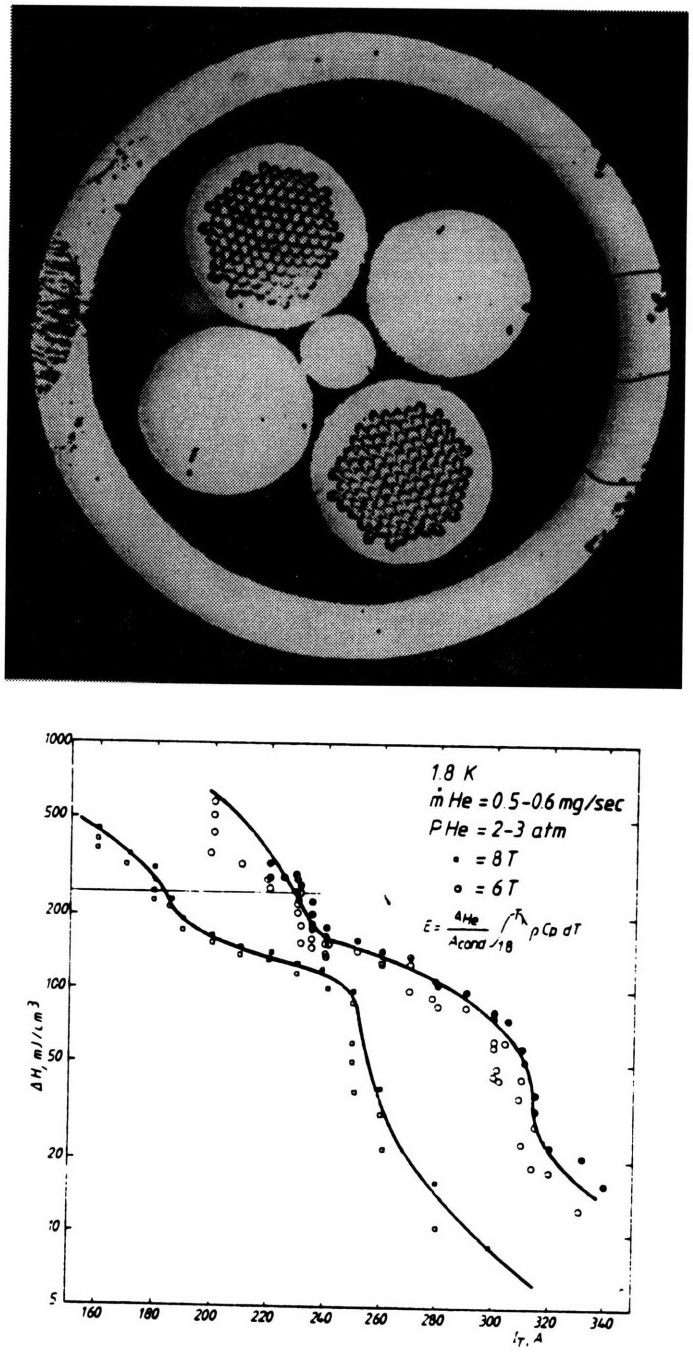

Figure 4-1: For the stability experiment by Lottin and Miller, shown here is (a) the test conductor; (b) the stability margin of the test conductor as a function of transport current at 1.8 K and 6 T, 8 T background field and a current pulse of 1 ms duration: open symbols = recovery, closed symbols = quench. (From Lottin and Miller, 83.)

using pulsed current disturbances. The inductive heating experiments use calorimetric methods and estimate the energy deposited in the cable through the temperature rise of the coolant. This calculation is an indirect way of calculating the energy actually dissipated inside the cable. The pulsed current stability experiments use the technique of power integration which gives a direct measurement of the energy dissipated in the cable, before it can boil off any helium. This distinction in energy calculation makes it easy to identify the specific part of the conductor where the energy is dissipated by having a large number of voltage taps in the pulsed current stability experiment, which is much more accurate than such a distinction made by using temperature sensors or pressure transducers incorporated in calorimetric methods. This identification process can be particularly helpful in studying normal zone propagation.

On the other hand, pulsed current disturbances are not the kind of perturbations expected during normal operation of large-scale magnets for fusion research. The perturbations which are expected are due to pulsed and transient fields in addition to mechanical disturbances. The remedy for this concern is that because pulsed current disturbances are a source of uniform energy deposition in the cable, the perturbations expected during normal operation of such magnets can be carefully modeled in terms of pulsed current disturbances. Any such modeling has not been done to date and is beyond the scope of this thesis.

Another disadvantage of this method may be the non-uniform current distribution of the pulsed current in the strands of the CICC, which affects the veracity of the depiction of the observations made. Large non-uniformity in current distribution can translate into completely incorrect prediction of the stability margin for the cable. The issue of current distribution has been addressed by Vysotsky [76], and he plans to study current distribution in multiple-strand cables using segmented rogowski coils. These experiments are planned in the future. The presence of helium between strands inhibits current transfer between them, so non-uniform current distribution probably happens at the point where the conduit jacket is brazed onto the connecting current lead usually in the form of a bus bar, perhaps

due to imperfect connections. At the present time, however, enough information is not available about the topic and it will not be further investigated.

4.2 Experiment: Setup and Procedures

All the experiments were performed in the high magnetic field facilities of the Francis Bitter National Magnet Laboratory (FBNML) at MIT. The 6B magnet located in cell 13 was used to produce the background DC magnetic field in the experiments. The 6B magnet is a water-cooled solenoid which produces DC field with negligible variation. The setup of the experimental apparatus used for performing the suggested stability experiments using pulsed current disturbances is delineated below. Two different preparations of the experiment were utilized, which will be termed *stability experiment A* and *stability experiment B* in the future. Both experiments were exactly the same theoretically, with some important discriminating particulars in the functionality of the equipment used which will be identified soon. The block diagram of the circuit arrangement for the two experiments is shown in Fig. 4-2. The circuit block diagram shows the arrangement of the circuit connections between the CICC sample, the transport current power supply and the pulsed current power supply and includes any measurement devices that may be part of the circuit, for each experiment. A picture of the probe and dewar sitting in the magnet during one of the experiments is shown in Fig. 4-3. The actual experimental setup (for stability experiment A) showing the locations of the various equipment is depicted in Fig. 4-4.

Fig. 4-2 shows that, in both experiments, the power supplies furnishing the transport current and the pulsed current are connected to the sample load in parallel, thus enabling the superposition of the two currents.

Experimental runs 1-8 were of type A and stability experiments number 9 and 10 were of type B.

The main components of the experiment setup were the following:

- the dewar and probe with the test sample mounted on it.

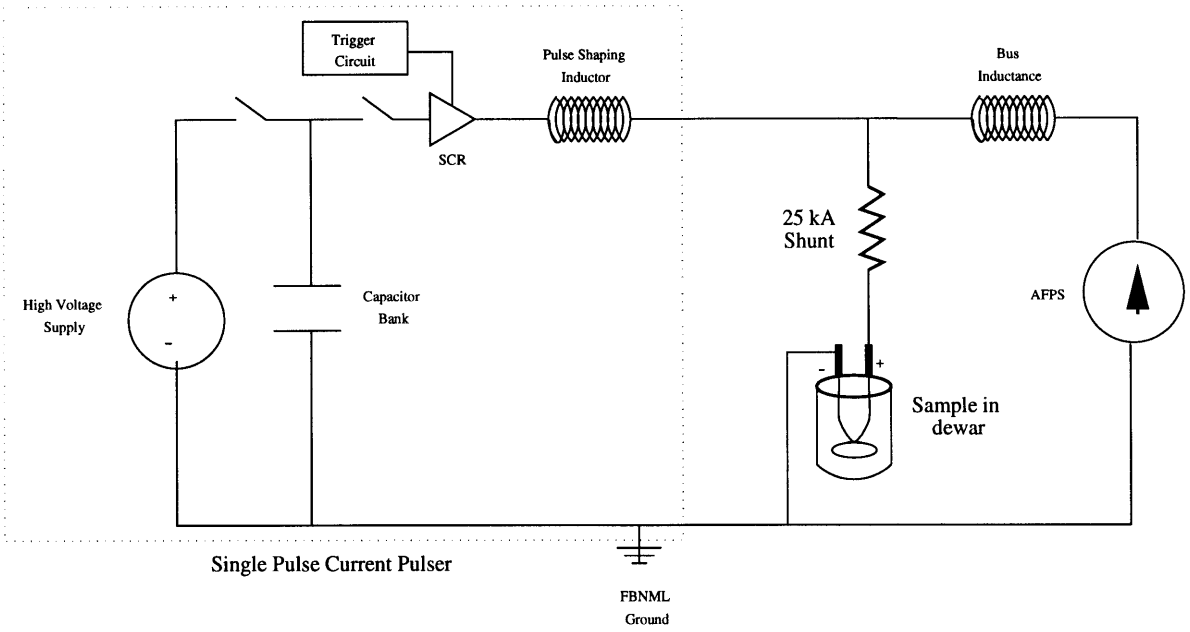

(a) Block diagram for Stability Experiment A

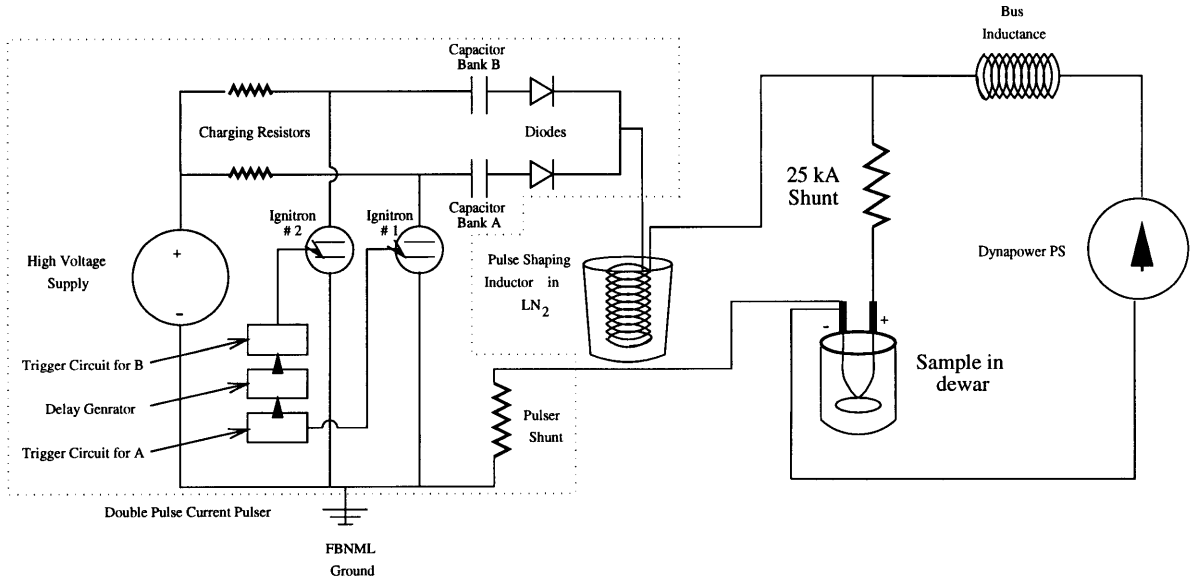

(b) Block diagram for Stability Experiment B

Figure 4-2: Block diagram showing the connections of the power supplies to the sample for the circuit of (a) stability experiment A; (b) stability experiment B.

Figure 4-3: A picture of the probe and dewar in the 6B magnet in cell 13 at FBNML.

- the cryogenic system.
- the sample CICC.
- the transport current power supply.
- the pulsed current power supply.
- the current measurement system.
- the voltage measurement system.
- the data acquisition system.

4.2.1 The Dewar and Probe

To utilize the 6B magnet, the 6" dewar was used, which is a an 89" long cryostat with a 6" inner diameter on its lower end or the tail which fits into the inside of the 6B magnet (see Fig. 4-5). The sample, which is mounted on a probe which sits inside the dewar, ends up being inside the central cavity of the solenoid and sees a constant vertical bitter field. The probes used for stability experiment A

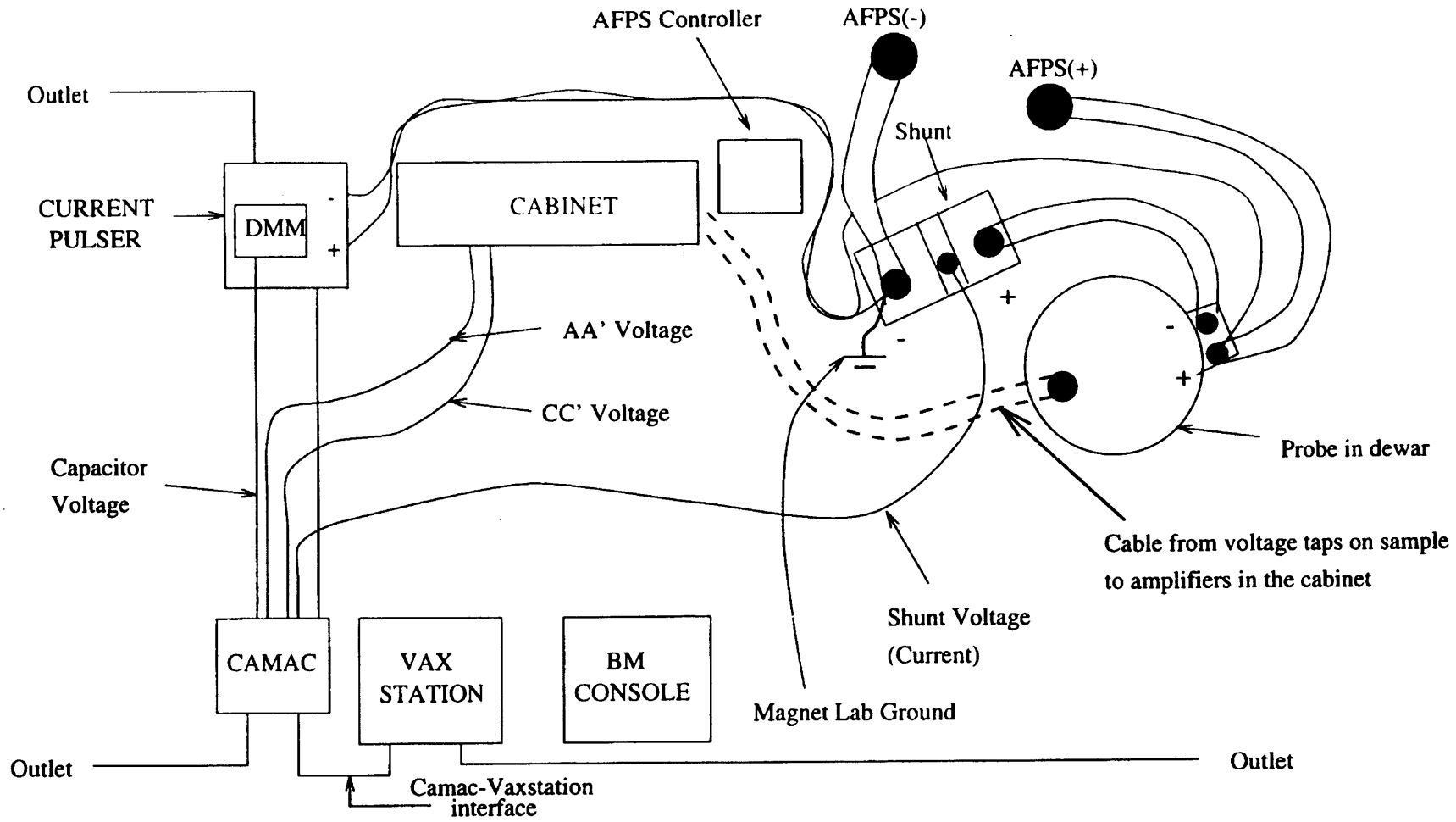

Figure 4-4: A depiction of the experimental apparatus arrangement for stability experiment A (run # 5) in cell 13 of FBNML.

and B were different. The purpose of the probe is to provide a robust structure for mounting the test sample cable so that it can be safely inserted into the dewar for operation in cryogenic conditions. The sample conduit is brazed onto long high-conductivity bus bars to minimize contact resistance and the bus bars are connected to high-amperage current leads which allow for inputting high-amplitude currents. The probe also provides for reliable electrical connections between the sample and the top of the probe for signals from any measurement equipment that might be installed on the sample or elsewhere on the probe. These signals can be directed to the appropriate data acquisition system or other display devices from 32-pin connectors on top of the probe. The pin connections and resistances are recorded for reference to assure continuity of measurement circuits and to aid in identification of any damaged wires without dislodging the probe. Checking these connections is one of the preliminary checkups which is necessitated before the start of an experimental run.

The probe used in stability experiment A is shown in Fig. 4-6. It is called the J_c 10 K probe because it was primarily used for critical current density measurement experiments and was rated at a transport current of 10 kA. The figure also shows the connections for the two liquid helium sensors which are connected to a 32-pin connector and are used to have information about the cooling situation inside the vessel during the experiment. Experiment B used the TPX probe, which is a bulkier probe with some extra features not used in the stability experiment, including the pulsed field coils and the supercritical helium system. The current rating of the TPX probe was 7 kA. To ensure that the sample was infact in the right location for exposure to DC bitter field when the probe was put in, the height of the dewar was adjusted such that the height from the dewar flange to the magnet mid-plane was 75.1" for the J_c probe and 76.75" for the TPX probe. The task of setting the dewar and probe correctly is non-trivial and extremely important to ensure the necessary cryogenic conditions during the experiment and due care should be given to its carrying out. Two cranes and some extra manpower are used for this purpose.

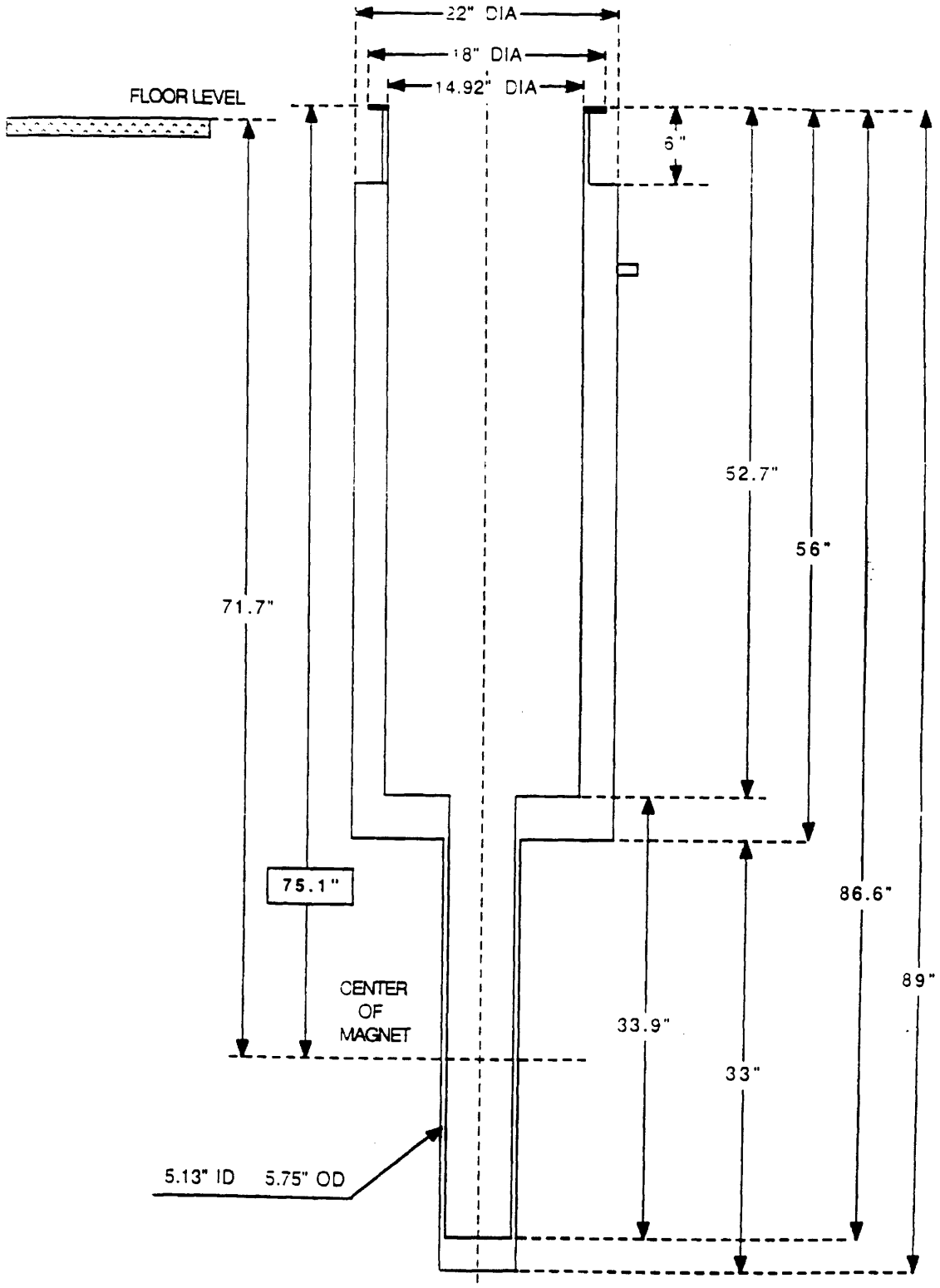

Figure 4-5: The 6" dewar used in the stability experiments.

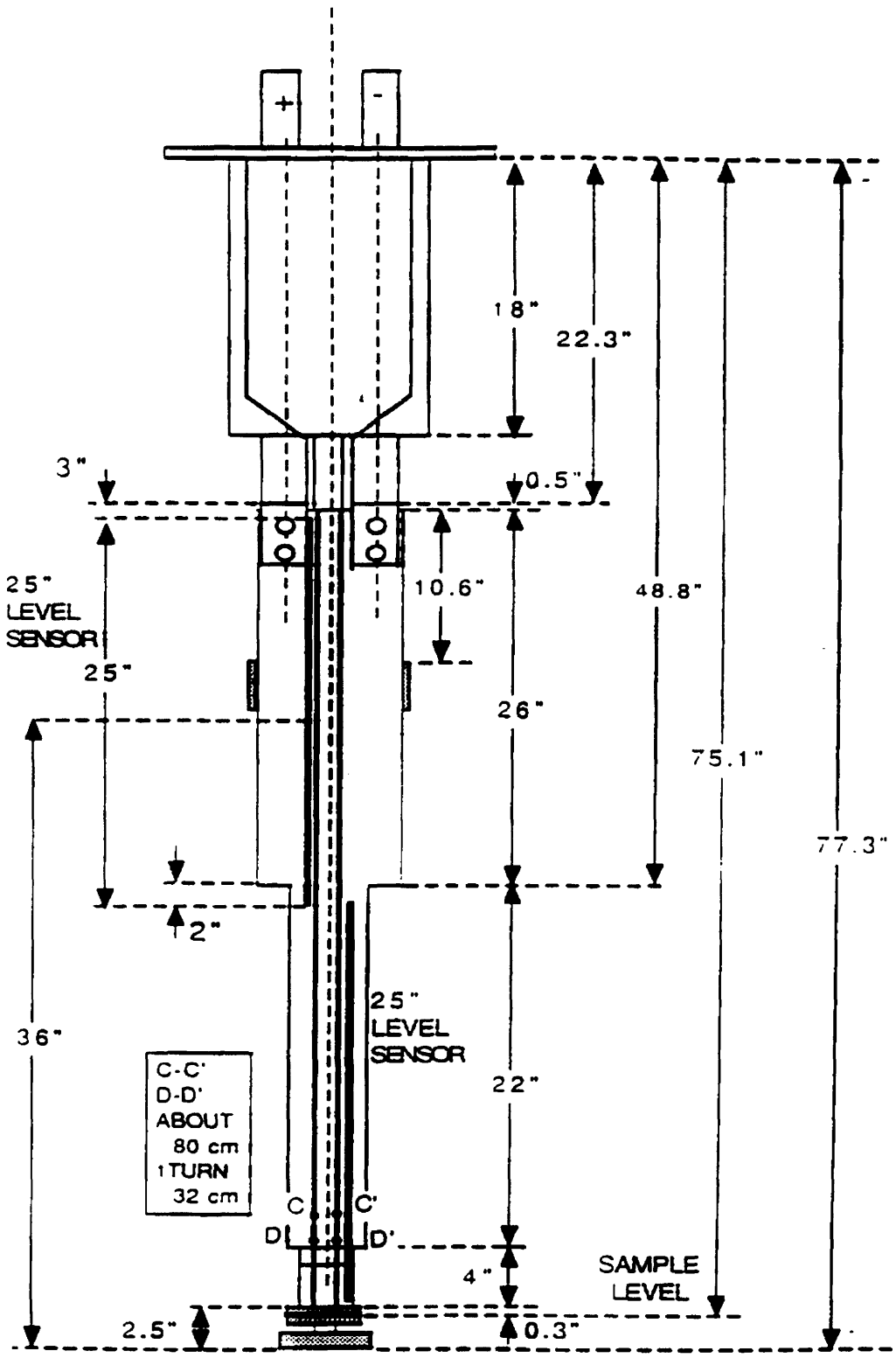

Figure 4-6: The J_c 10 K probe used in stability experiments of type A.

4.2.2 The Cryogenic System

It was very important for the success of the experiment that the cryogenic conditions be maintained in order to ensure the appropriate cooling conditions for the sample. The experiment was conducted with simulated liquid helium forced-flow conditions at 4.2 K with zero velocity, that is the sample was bath-cooled. As suggested in Chapter 3, the CICC recoveries are somewhat independent of the helium flow velocity.

There was a pre-cooling stage for the experiment which started about three days before an experimental run. In this stage, the space between the inner and outer jackets of the dewar was filled with liquid nitrogen (LN_2) and its level maintained. This essentially pre-cooled the dewar and probe to about 77 K. As seen in Fig. 4-5, when the probe is put in the dewar, it seals the top opening of the dewar, thus creating an isolated compartment inside referred to as *helium space*. The sealing of the helium space in the dewar was checked. A good vacuum is created in this space by consecutive pumping down with a roughing pump and filling up with helium gas at 3 psig [1] a few times. This gets rid of any moisture present which would otherwise freeze at cryogenic temperatures and cause flow problems. Similar purging of the supercritical helium line with He gas was performed with a line pressure of 20-40 psig for the TPX probe, although supercritical helium was not used. The flexible helium transfer line and tee transfer line were checked for leaks and pumped down as well. Liquid helium transfer was performed a few hours before the start of the experimental run. Liquid helium (LHe) was provided by the MIT Cryogenic Engineering Laboratory. On average, about 300 liters of LHe were used in an experimental run.

There were two helium level sensors on each probe accessible through the 32-pin connectors on top of the probes. They were referred to as the 12" and the 24" level sensors. The level sensors were used to make sure that there was enough liquid helium inside for the sample to be safe. To prevent buildup of high pressures

[1] pounds per square inch gauge pressure

inside the dewar in the event of a quench a relief valve was installed with a cracking pressure of around 80 psig.

4.2.3 The Sample CICC

Three different sample CICCs were used in the experiments. Stability experiments of type A were performed on one hybrid cable called *hybrid # 1* and one regular 27-strand multi-stage cable called *US-DPC sample*, whereas experiments of type B used the *TPX sample*. The TPX sample was a hybrid cable as well. The parameters of the three CICCs are given in table 4.1. The samples were fabricated in the laboratories of the Superconducting Magnet Development Group at the Plasma Fusion Center. Both of the samples used in experiment A consisted of a single-turn inductively wound CICC while the TPX sample was a two-turn non-inductively wound CICC.

The hybrid cable #1 consisted of 27 strands, with 18 superconducting strands of Nb_3Sn US-DPC [2] wire [58]. The other 9 strands were made of stainless steel. The stainless steel strands were used to investigate the effect of having low-resistance non-superconducting strands in the conduit for current sharing during current transfer, in addition to the copper matrix in the superconducting filaments, on the stability of the CICC. Stainless steel has an RRR value of 1.6 as compared to the Cu usually used, which has an RRR value in the 150-400 range. This made it possible to establish if these strands were involved in recovering from disturbances or not. The TPX cable [34] is also 27 strands with 18 superconducting strands of TPX PF coil wire and 9 Cu strands making up the hybrid part. The US-DPC sample's 27 strands were all superconducting in a so-called 26+1 configuration. One of the strands was separated from the rest to aid in studying transverse conductance of the strands and their contact resistance.

[2] United States Demonstration Poloidal Coil

Table 4.1: Sample cable parameters of the 27 strand hybrid CICCs.

	Hybrid Cable # 1	US-DPC Test Cable	TPX Hybrid Cable
Superconducting strands			
Type	US-DPC	US-DPC	IGC-TPX
Number	18	27	18
Cu/non-Cu ratio	1.174:1	1.174:1	3.1:1
Filling factor (λ)	0.46	0.46	0.244
Diameter (mm)	0.78	0.78	0.79
Hybrid strands			
Type	Stainless steel	NA	Copper
Number	9	0	9
Diameter (mm)	0.787	-	0.78
RRR	1.6	-	180
CICC			
Cooling	Bath-cooled	Bath-cooled	Bath-cooled
Conduit Material	Incoloy 905	Incoloy 905	Incoloy 903
Conduit Inner Diameter (mm)	5.05	6.1	0.51
Conduit Outer Diameter (mm)	6.35	6.7	6.35
Void Fraction	0.352	0.38	0.35
Sample length (m)	0.88	0.8	1.8

4.2.4 The Transport Current Power Supply

The block diagram in Fig. 4-2 on page 103 shows the placement of the transport current power supply in the experimental apparatus. The I_t PS was one of the differences between stability experiment A and stability experiment B.

Stability experiment A used the old Air Force power supply (AFPS) which had a peak DC current output of 20 kA and a peak DC voltage of 5 V. The AFPS exhibited some problems in keeping the current constant in the event of a quench due to the increased load. It was operated by its own remote control panel at the site of the experiment. The power supply itself sits in the basement of FBNML. When the pulsed power supply was connected in parallel to the AFPS, the Reese cables and bus bars from the dewar to the basement ensured a large enough input impedance to the current pulse, so that the safe operation of the power supply required no additional precautions.

Stability experiment B employed the new Dynapower 10 kA power supply with a 20 V peak DC voltage. The new power supply is very powerful and robust and has the capability to output ramped transport current, etc. It was used in the stability experiment to provide DC current only. The issue of safely connecting

the pulsed power supply was resolved with the help of a Dynapower employee [7]. A simulation program was run with the loading configuration of experiment B and it was guaranteed that the voltage across the power supply would stay within prescribed limits. The Dynapower PS showed power output limitations during quenches as well.

4.2.5 The Pulsed Current Power Supply

The pulsed current is provided by a capacitor bank which discharges when triggered through a trigger circuit, whose control circuitry assures the output of a one-half sine wave of current, termed the *current pulse*. The pulse width is a function of the capacitance of the capacitor bank and the inductance across it, while the amplitude is regulated by the charge voltage of the capacitor bank. The machine consisting of the capacitor bank and its charging voltage supply, the pulse shaping coil providing the inductance, and the trigger and control circuitry is called *current pulser*. The functionality of the current pulsers used in the experiments is displayed as part of the block diagrams shown in Fig. 4-2.

Single Pulse Current Pulser

Stability experiment A used the single pulse current pulser (SPCP). It consisted of a capacitor bank with a capacitance of 3060 μF, which could be charged upto 2 kV by a high-voltage power supply. The capacitor could be discharged by triggering a silicon diode rectifier (SCR) into a load through a thick 100 μH coil. The SCR was triggered by a pulse generated by the trigger circuit when it was manually triggered. The result was a half sine-wave current pulse of width t_p = 2 ms and a peak value as high as 8 kA. As the capacitor bank discharge voltage reverses, the SCR turns off, and no current can flow in the opposite direction. The capacitor bank is then discharged through a bleed resistor before it can be charged again for more output. A network of interlocks and magnetic relays ensures that the trigger circuit cannot be armed until the voltage source is disconnected from the capacitor

bank. Also, the capacitor bank cannot be charged unless it is disconnected from the load. When the bleed resistor is engaged, the capacitor bank is exclusively connected to it. These prohibitions ensure the safe and reliable operation of the current pulser. The voltage on the capacitor bank was read by a digital multimeter across a 1:1000 voltage divider for reference while charging the capacitor bank.

The SPCP could not be operated at voltages higher than about 1.6 kV because of sparking problems. It seems that the voltage was high enough to spark through the bottom base of the pulser cabinet to the FBNML electrical ground. Fortunately, the need to go to these high voltages was minimal.

Double Pulse Current Pulser

The double pulse current pulser (DPC) was utilized in stability experiment B. It consisted of two capacitor banks, *capacitor bank A* and *capacitor bank B*, which could be discharged at the same time or with bank B discharging from zero to 100 ms after when bank A's discharge was complete. The output of each bank was a current pulse with a pulse width of 10 ms, and current amplitude proportional to the charge voltage on the banks. Both banks were charged by a single high-voltage power supply, so that both banks were charged to the same setting voltage. The voltage on the banks was displayed on a digital multimeter across a 1:1000 voltage divider installed inside the pulser cabinet, and was used for reference when charging the banks. The maximum setting voltage of the charging voltage power supply was 2 kV. As seen in the Fig. 4-2 (b) the power supply charges the two banks through charge resistors. When an external trigger is initiated, it fires the ignitron controlling capacitor bank A right away while the ignitron controlling capacitor bank B is fired after the delay time generated by the delay circuitry. The low inductance shunt with a calibration of 300 A/ 50 mV measures the pulsed current through the load, which happens to be the sample mounted on the TPX probe.

The pulse shaping inductor is external to the pulser cabinet for this pulser which allows for adjustment of the pulse width. The double coil solenoid shown in Fig. 4-7 was used as the pulse shaping inductor and had a measured inductance of 2.47 mH.

It had two solenoidal coils, wound on concentric cylinders. The inner coil had an average diameter of 0.0735" and the length of copper wire wound on it was 220 feet, whereas the outer coil's average diameter was 0.0898" and the length of the wire wound was 121 feet. It was calculated that the coil would generate too much heat if used at room temperature due to joule heating by the pulsed current, which would have challenged the integrity of the coil in addition to a noticeable decrease in the energy available to be deposited in the superconductor. The temperature increase was reduced to less than 4 K when the coils were assumed to be at the boiling point of nitrogen (77 K) due to the highly reduced resistivity of Cu, even with the assumption of adiabatic heating, and therefore, the double coil was immersed in LN_2 for the duration of the experimental runs.

The double pulser allowed for the use of just one pulse at a time by disengaging the ignitron of capacitor bank B. When two pulses were used, the delay time of the second pulse became an important parameter in establishing the nature of the disturbance introduced by the two pulses, and called for a brief analysis of the dependence of the results on the delay time setting.

4.2.6 The Current Measurement System

The two most important physical quantities which required accurate measurement for the success of the experiment were sample voltage and sample current, as advocated by Eq. 4.1. Because of its importance, due time was given to developing a technique appropriate for measuring current under the circumstances. The total current consisted of DC transport current and pulsed AC current. The two currents could be measured as a single value of total current or separately and then added to get the total current.

The sample current measurement system evolved quite a bit before it was finalized for experiment A. The AFPS did not have an accurate enough methodology of communicating the DC current output. It had a digital display and an associated voltage reading but they were inaccurate because of an unknown bias voltage and

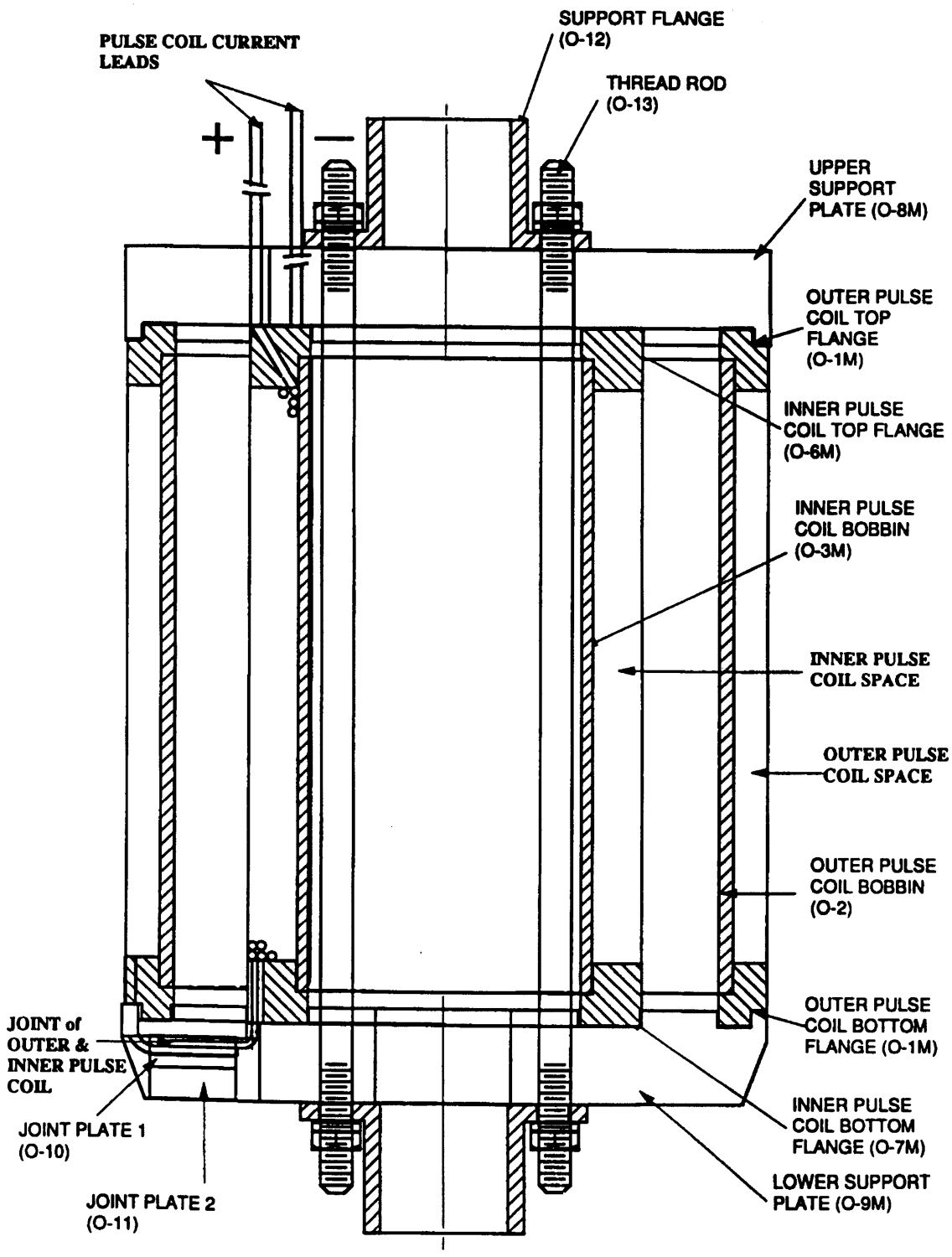

Figure 4-7: The two-solenoid coil used as the pulse-shaping coil for the double pulse current pulser.

a fairly large swing voltage. These readings could only be used to give an approximate idea of DC current. It was decided to use a low-resistivity high-accuracy linear output shunt for the measurement of DC current. The measurement of pulsed current was a bit more tricky. Initially, the FBNML current monitor was used, which was like a pickup coil, and based its reading on integrating flux changes through it. The current monitor had a calibration of 5 mv/A. Unfortunately, it was found to be sensitive to the spatial placement of the cable carrying the pulsed current through it. This problem had not been resolved when the current monitor, for some unknown reason, stopped working, and the idea of using it for pulsed current measurement was discarded. In the meantime, some test pickup coils were built. Each coil consisted of a phenolic base of 2" × 1" × 0.75" on which 150 turns of gauge 36 Cu wire (d = 0.127 mm) were wound in two layers in a fine groove of approximately 0.254 mm made on the side with a width of 0.75". The signal picked up by the coil was fed into a low-pass RC filter. The coils were mounted on the cables from the pulser cabinet to the current leads on the probe. The coils showed unexpected non-linearity in their calibration against the FBNML current monitor. The coils were also sensitive to the distribution of current in the cable, since they based their results on average changes in magnetic flux through their enclosed area. The non-linearity in the coils and the uncertainty in their measurement based on minute physical changes in their physical orientation with respect to the cable deemed them inappropriate for use in the experiment.

Finally, a very low-inductance shunt was used for getting the pulsed current measurement. The shunt called the *25 kA shunt* when calibrated against a dependable 5 kA DC shunt (10mV/5kA) showed extremely good linearity till 5 kA. Since, transport currents higher than 4 kA were not expected, the calibration was considered sufficient. The shunt had an added advantage of measuring the pulsed current and transport current as one signal. It was observed that the shunts inductive voltage reading was negligible, unless it became too hot due to continuous operation with transport currents of about 5 kA or higher. The shunt performed decently with fan cooling at room temperature, and was used in the experimental

runs of stability experiment A.

The shunt was used in experiment B as well but only as an alternative total current measurement for comparison. The pulsed current was read from the pulser shunt mentioned earlier. Due to the use of the new Dynapower supplies, the transport current was read directly from the output on its control panel. The use of rogowski coils was intended as an alternative pulsed current measurement, but due to the difficulty involved in installing a full-circle, non-segmented rogowski coil on the TPX probe, lack of time, and the dependability of the shunt, no such coil was made.

4.2.7 The Voltage Measurement System

The voltage measurement system was less evolutionary compared to the current measurement system. It consisted of voltage taps on the sample cable, which were placed on the conduit after the sample had been mounted on the probe. The only difference for the probes in terms of the voltage measurement system was the number of voltage taps and their locations on the conduit which dictated the length of the part of the sample whose voltage was recorded.

The voltage taps were connected to the 32-pin connector, from where the signal could be guided to the data acquisition system for display and storage. The wires connecting the voltage tap connections on the conduit to the 32-pin connector were made as non-inductive as possible by twisting. The voltage taps placement for the samples used in experiment A is depicted in Fig. 4-8. Only the voltage taps AA' and CC' were used in the experiments. For the TPX sample the voltage taps used were $\pm$V4 (pair A-B), +V5/+V6 (pair C-D), +V6/+V7 (pair E-F), $\pm$V7 (pair G-H), and -V6/-V7 (pair J-K) (See Fig. 4-9). One of the important parts of preliminary check before the start of an experimental run was to make sure the voltage taps being used were in working condition. This was easily achieved by noting the resistance across the voltage taps in LHe conditions and comparing them with pre-recorded values.

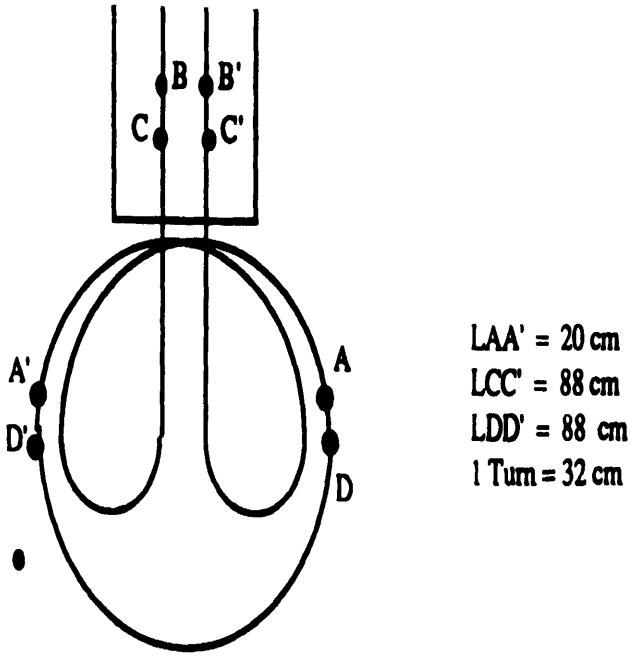

Figure 4-8: Voltage taps on CICCs used in Experiment A.

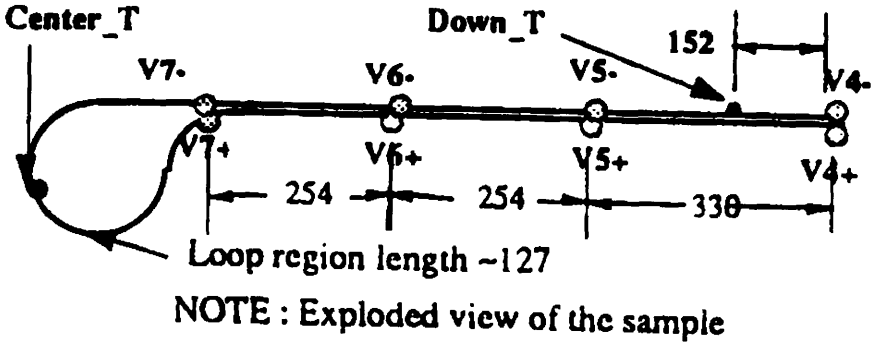

Figure 4-9: Voltage taps on the TPX hybrid cable used in experiment B (all lengths in mms).

4.2.8 The Data Acquisition System

Last but not least, the signals of interest in the experiments were amplified if necessary, recorded and stored, with real-time display for immediate feedback, by the data acquisition system. This system consisted of the amplifiers, the data acquisition modules and the computer with the data acquisition program controls and disc storage for recording acquired data for future reference and analysis.

For experiment A, the signals of interest were the voltage signals from the voltage taps AA' and CC', the total current converted to voltage signal from the 25 kA shunt, and the capacitor bank voltage on the SPCP. These signals were fed through Preston amplifiers with reasonable gain and no filtering to a LeCroy CAMAC Model 8212 high-accuracy simultaneous-sampling data logger. With four inputs, the sampling rate was 40 kHz (25 μs/ data point) and the saturation voltage was $\pm$ 5V. It recorded a total of 32678 point per channel when triggered by an external source, which happened to be the trigger to the current pulser. This recorded data in a time window of 0.8192 seconds centered around the 2 ms current pulse. The CAMAC was controlled by an IDL/MDS program on a VaxStation II called Merlin, and the data was stored on it as well, which displayed selected data from the recently processed shot on Merlin's terminal, so that the parameters for the next shot could be determined. The sample voltage AA' was also read by a chart recorder, so that as soon as a quench was observed the transport current could be turned off.

In experiment B, due to the unavailability of Merlin, the DAQ-950 Macintosh was used for data acquisition. The signals of interest were the five voltage taps mentioned in Section 4.2.7, the pulsed current reading from the shunt in the DPCP, the total current reading from the 25 kA shunt, and the DC transport current reading from the Dynapower control panel. These went through amplifiers to the Labview data board device # 1 in 8-channel single-ended mode of operation. A printout of the Labview data acquisition program's visual is shown in Fig. 4-10. As can be seen in the figure, the number of data points and the number of channels can be

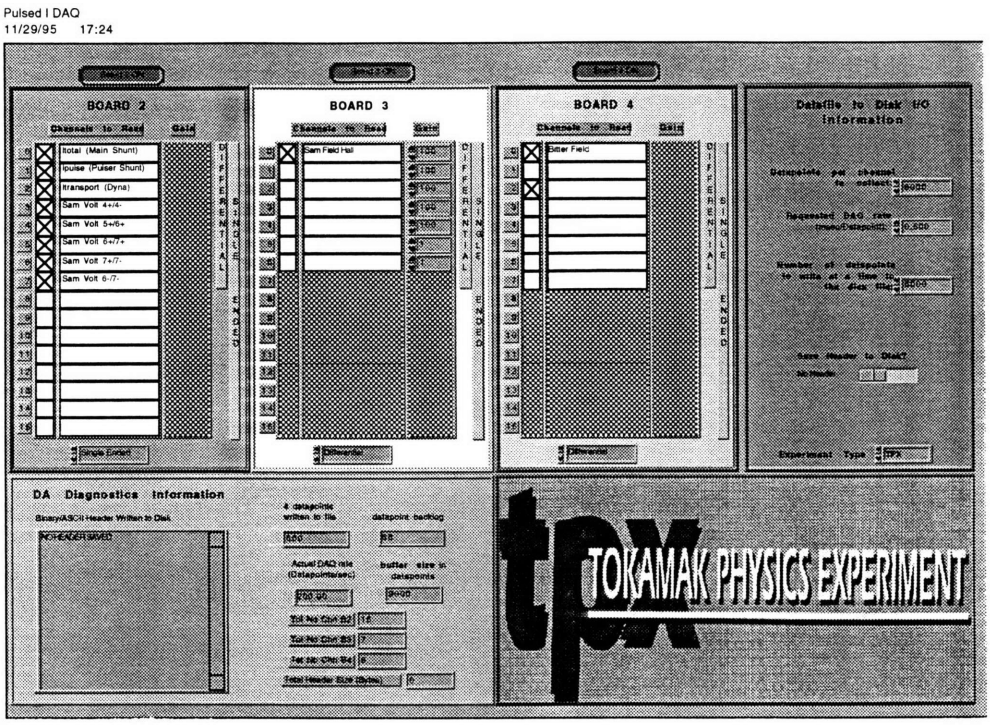

Figure 4-10: The Labview program schematic which was used for data acquisition in stability experiment B.

chosen on an adhoc basis as well as choosing which channels to record. The data was stored as binary files on the computer and could be later analyzed. A similar approach as in experiment A was used for quench detection using the Yokogawa chart recorder.

This concludes the description of the experiments.

Chapter 5

Data Analysis and Results

The details of the ideology, experimental setup and procedural implementation of the stability experiments were introduced in chapter 4. The analysis of the data acquired in these experiments is presented here along with the results and a bench mark comparison of the resulting stability margins with an analytical model developed for this specific experimental situation.

5.1 Introduction

As mentioned earlier, the data acquired in experiment A was stored on a Vax Station II in the form of binary files. Each file stored the four signals received by the CAMAC crate, namely the capacitor bank voltage, the total current through the sample, and the voltage signals on voltage taps AA' and CC'. Each signal was stored for a duration of 0.41 seconds before and after the time at which the pulsed current was initiated by triggering the SCR in the single pulse current pulser (see fig. 4-2. The stored data was retrievable using the MDS facility available on the Vax VMS mainframe node "MERLOT" at the Plasma Fusion Center at MIT. The data analysis was carried out using code generated in IDL [1] because of its compatibility with the MDS facility. The IDL code used for the analysis is included in Appendix C.

[1]Interactive data language: A research analysis oriented computer language which exploits the the good virtues of both FORTRAN and C.

The data acquired in experiment B was stored on the DAQ-950 Macintosh computer using a binary format. It was retrieved using the general binary loader facility (GBLoader) in IgorPro and analyzed using the established data manipulation algorithms in IgorPro.

About 130 shots of useful data were produced in the experimental runs of experiment A and less than 20 runs were acquired for experiment B. More experimental runs of experiment B could not be run because of lack of time availability and limitation of resources.

Because of the amount of data available for experiment B, the analysis will concentrate on analyzing the results of experiment A. Nonetheless, the promise held by experiment B will be explicated and some results will be presented. Data was acquired in experimental runs 4-8 and in run number 10. Data in shots 839-855, 1527-1543, 1700-1719 and 2615-2656 corresponds to hybrid sample # 1. Data is shots 2764-2795 is for the US-DPC test sample. Data in run number 10 (shots 6-21) was not enough to identify the stability margin for the TPX hybrid cable but will be included for completeness and some results will be discussed.

5.2 Preliminary Calculations for Experiment A

The preliminary calculations for experiment A were done by a straightforward implementation of Eq. 4.5 reproduced below

$$E_d = \int_0^{t_p} V_{sam} I_{tot} dt = \int_0^{t_p} V_R I_{tot} dt \tag{5.1}$$

5.2.1 Numerical integration

The product of sample voltage and total current signals was integrated numerically for the duration of the pulse $t_p = 2ms$ using a Simpson integration routine. The rectangular and trapezoidal integration routines were also tried for comparison but due to the parabolic shape of the current pulse, the Simpson routine seemed to give

the least error. The error was conceived as the result of the suggested integration when it was assured that the sample never entered the current-sharing stage so that the power implied by the current-voltage product was purely reactive. Since, in this case, the reactive power should integrate to zero, the Simpson's routine was chosen as it gave results whose absolute value was closest to zero, although the results of the trapezoidal routine were very close to zero as well. This comparison was made for shots processed at zero background magnetic field, ensuring that the sample did not traverse into the current-sharing region for the operating conditions present.

5.2.2 Inductance of the Sample

Initially, it was considered possible to infer the inductance for the sample from the voltage and current traces of the sample. The idea was to assume that the sample did not hit the current-sharing temperature threshold for a brief period at the beginning of the current pulse, which was reasonable since the sample was not operating at critical current. The actual time of this period was dependent on how far the operating conditions were from this threshold and on how quickly current increased, that is on the peak amplitude of the current pulse. The time period of purely inductive voltage at the beginning of the current pulse decreased as the peak amplitude of the pulse increased, as this meant that the time it took the sample to reach critical current, if at all, was reduced.

Based on this assumption, the initial period of the first derivative of the current pulse was compared with the voltage signal to determine the proportionality constant. This proportionality constant was the lumped inductance of the sample L_{sam}. Although, the geometry of the cable is not supposed to vary from shot to shot and therefore there is no reason for the inductance to change but the reason becomes evident when current distribution is taken into consideration. The L_{sam} is a direct translation of current distribution effects. If the distribution stays the same, the L_{sam} value should not change either. This assumes that the only voltage

induced on the voltage tap is due to the time-varying pulsed current.

The voltage-current integration was done only for the period of the current pulse because external energy was introduced primarily only during this period. The dissipation due to transport current after the pulse was a secondary effect and did not represent perturbation energy. The idea was that if the same external energy as calculated for the duration of the pulse was input at the same rate by some other method, the secondary effects would be similar.

5.2.3 Results and Problems in Data Interpretation

Fig. 5-1 shows the traces for total current and the voltage on sample voltage tap AA' for shot # 1542 for hybrid sample # 1. The sample voltage shows a small offset value which was compensated for during integration. The current reading from the shunt verifies its low inductance. There were quite a few problems encountered in the experiment which became obvious during data analysis.

Spikes in Data

One of the first problems encountered in the interpretation of data is clarified by looking at the traces in Fig. 5-1. There are big spikes at the beginning and end of the pulsed current in the two traces. The spikes were observed in all traces at the same location. In some data there was more than one spike, one after the other, at the same locations on the time frame of reference. The source of the spikes was identified as the turning on and off of the SCR, and its interaction somehow with the CAMAC crate. Since the CAMAC was triggered by the same trigger which triggered the SCR to avoid timing problems, there was no simple way to get rid of this interaction. It was decided, therefore, to remove these spikes numerically, which was possible as seen in Section 5.3.

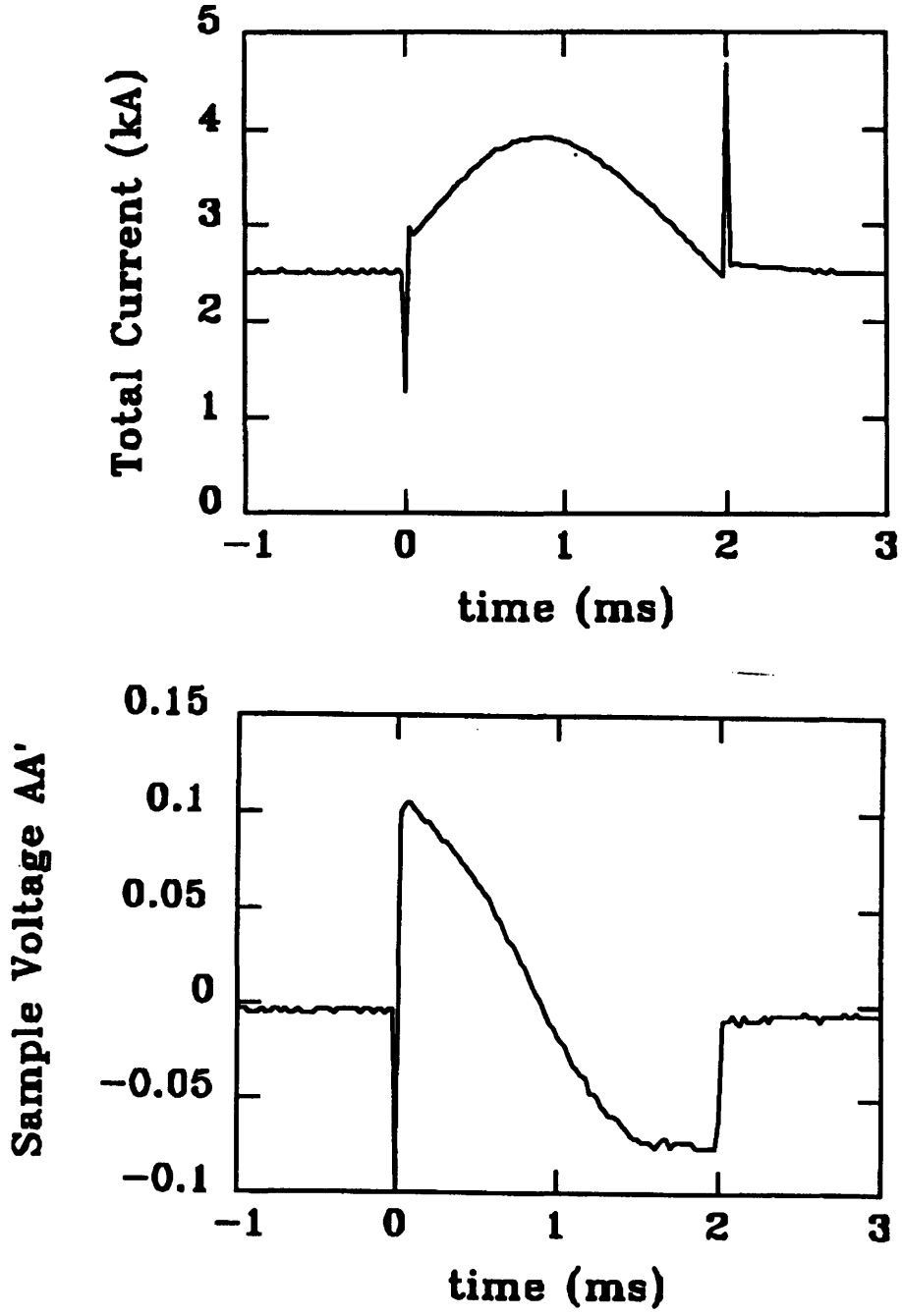

Figure 5-1: Experiment A (Shot # 1542): Traces for the total current through the sample and voltage on sample voltage tap AA'.

Superposed Oscillations

The second major problem in analyzing data was not encountered until the first experimental run with background magnetic field was performed.

It can be seen in Figs. 5-2 and 5-3, which represents the raw data for shot # 849. As can be seen from the traces of sample voltage taps AA' and CC' in Fig. 5-2, the traces have more than just the inductive voltage seen in Fig. 5-1. There is an oscillatory voltage superposed on the signal and its oscillatory nature becomes more evident when seen in the extended version of the same traces in Fig. 5-3. The oscillations continue even after the pulse has terminated, and show a damping behavior. The source of the oscillations could not be convincingly identified. They could be a result of oscillatory looping currents in the loops formed by any two strands at the bus bar termination, assuming comparatively high inter-strand contact resistance inside the conduit. They could also be related to oscillatory strand motion in the void space inside the conduit, as indicated by the calculation below.

Oscillations: A result of strand motion?

Consider the case of shot # 849, in which the sample did not quench, the transport current was zero and the background field was 9 T. The pulsed current due to a capacitor bank voltage of 530.1 volts had a peak value of 2.3 kA. The oscillations show a base frequency with an approximate time period of 0.5 ms, and higher harmonics. The oscillations show a maximum voltage with an absolute value of 0.1 volts. According to Faraday's law, the loop voltage is just the flux change through the loop

$$V_{loop} = -\frac{d\Phi}{dt} = -\frac{d}{dt}\oint B.dA \tag{5.2}$$

Considering just a single strand with the length of the circular part of the single-turn CICC with a circumference of about 0.3 m, the effective radius of the loop becomes 4.77 cm. Since the field is DC, the cross-sectional area of the loop has to increase or decrease in time to induce voltage. As an order of magnitude comparison is intended, only the value for peak induced voltage can be calculated.

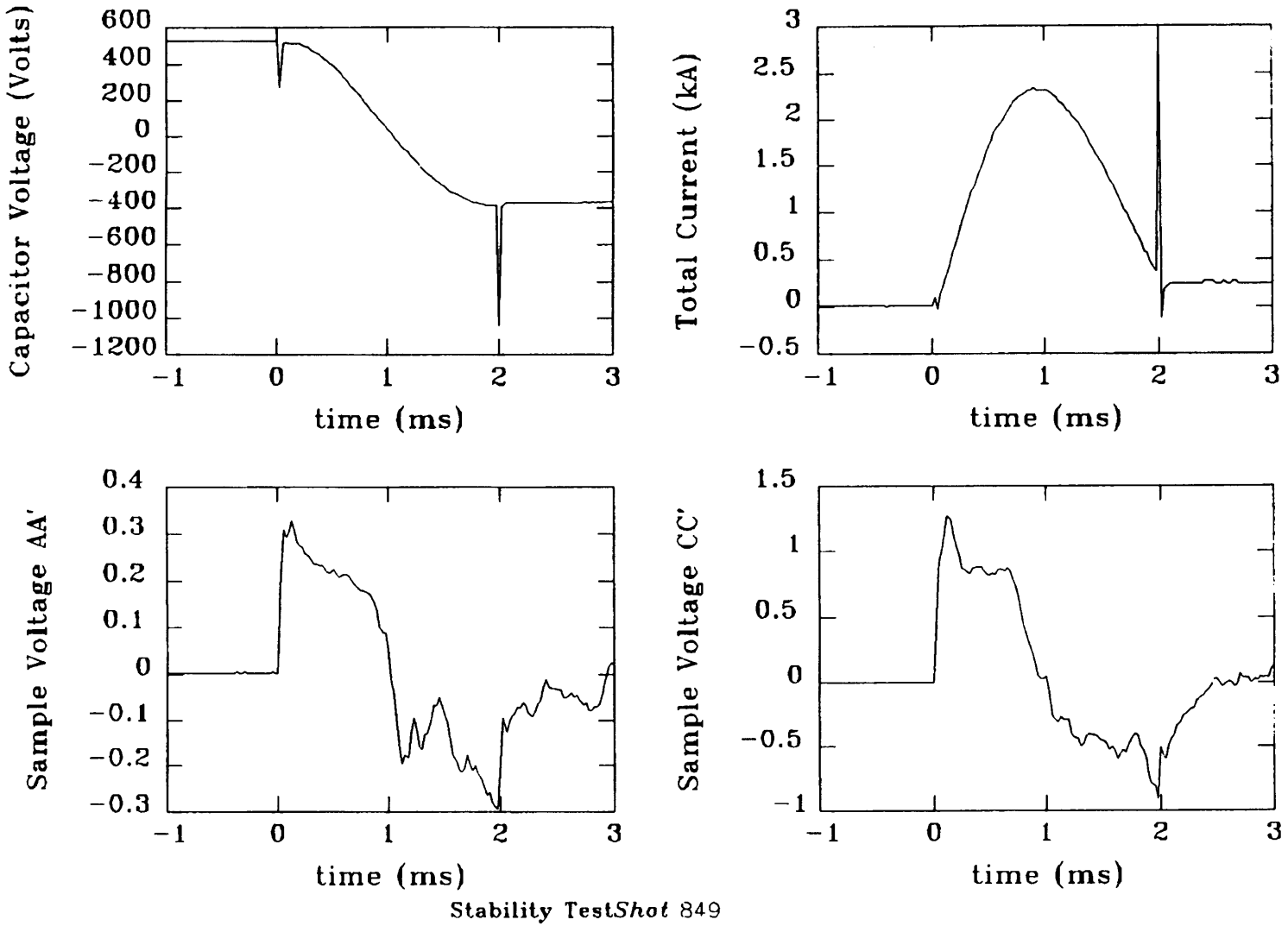

Figure 5-2: Experiment A (Shot # 849): Traces for the total current through the sample, the capacitor bank voltage and the voltages on sample voltage taps AA′ and CC′ for pulse duration.

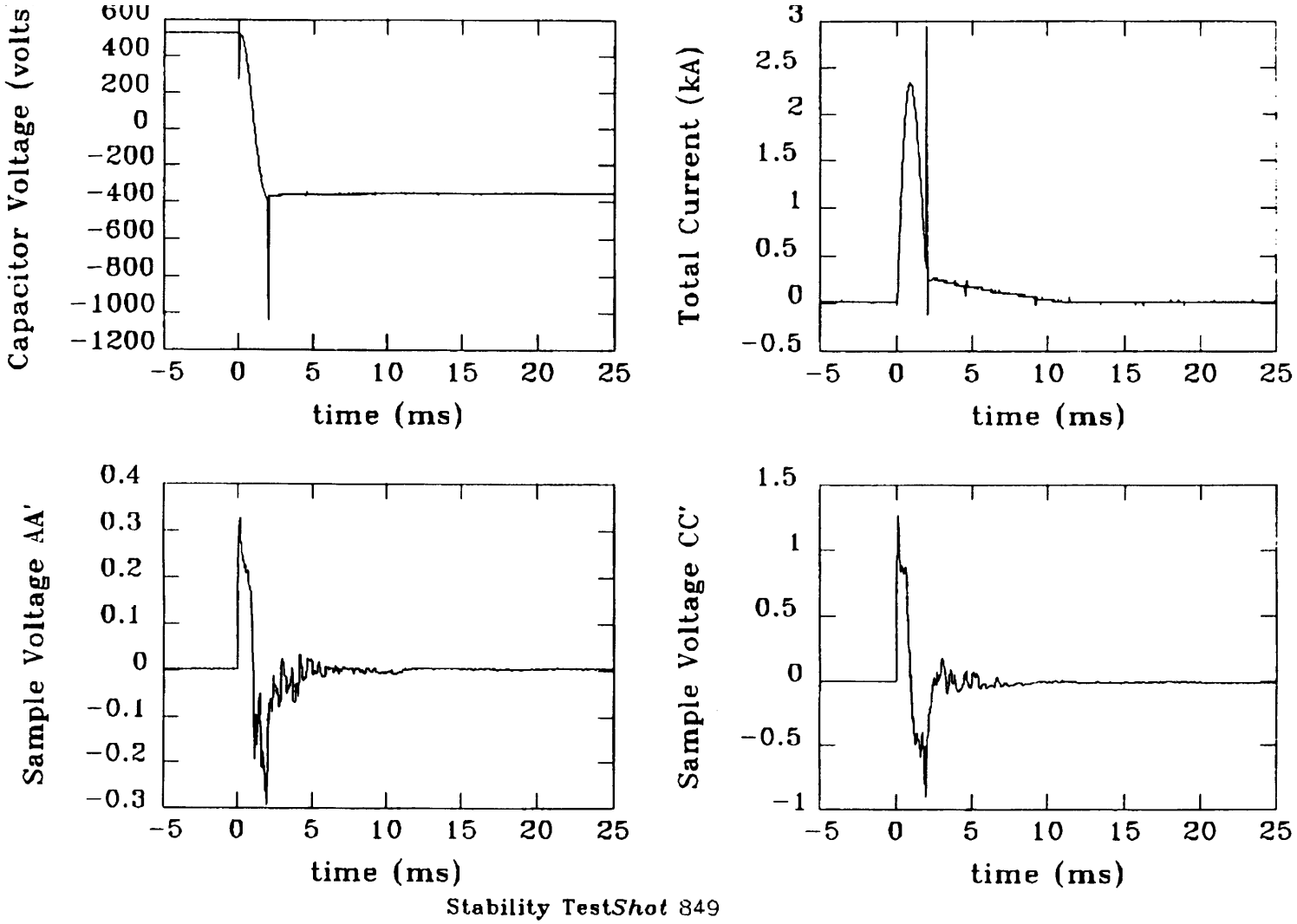

Figure 5-3: Experiment A (Shot # 849): Extended traces for the total current through the sample, the capacitor bank voltage and the voltages on sample voltage taps AA′ and CC′.

Working in SI units, the change in area required in a small time Δt is

$$\frac{\Delta A}{\Delta t} = -\frac{V_{loop}}{B} = \frac{0.1V}{9T} = 0.011m^2/s \tag{5.3}$$

Assuming this change in area occurs over the time period of the oscillation, the change in area becomes

$$\Delta A = 0.11m^2/s \times 0.5 \times 10^{-3}s = 5.55 \times 10^{-6}m^2. \tag{5.4}$$

The change in radius $\Delta r = r_2 - r_1$ can be found by noticing

$$\Delta A = \pi[r_1^2 - r_2^2] \tag{5.5}$$

which for $r_1 = 4.77$ cm (the loop part was 0.3 m long) gives

$$\Delta r = 58.08\mu m \tag{5.6}$$

which is very possible value for transverse strand motion being about 7.5 % of the strand diameter. Although, a similar situation will arise due to the pendulum motion of the probe inside the dewar, but since there was no change in the oscillatory behavior seen after impeding such motion by putting G-10 spacers on the probe, to fit inside the tail of the dewar, this possibility was ruled out.

Inductance of low-inductance shunt

The low inductance shunt did a good job of total current reading for the most part. However, in experiment # 8, it showed a large inductive component, which effected the energy calculations in a direct manner. To show that this was a time dependent phenomenon, Fig. 5-4 compares the current pulse reading for comparable current pulses for shot numbers 2766 and 2794 which were from the same experimental run i.e. run # 8. Shot # 2766 was in the beginning of the experiment while shot # 2794 was towards the end. The comparison makes it clear that the shunt is

performing reasonably fine in the first shot while it has a large inductive component, proportional to the first derivative of current, in the other one.

Additional Problems

The other problems encountered during data analysis were not critical but will be mentioned nonetheless. Some of the shots had the traces surpassing the saturation limits of the CAMAC and were not included in the analysis. Some shots showed a lot of 60 hz noise.

The data was read at the rate of 25 μs / datapoint which gave 80 data points in the 2 ms window. Due to the oscillating behavior of the pulses, this number was considered insufficient to give good integration results.

5.3 Solutions for Problems in Experiment A

Most of the problematic issues which were discovered in Section 5.2.3 were resolved with some success. The techniques employed to achieve this task are considered below.

5.3.1 Numerical Manipulation

The issue of spikes could not be corrected at its source because it was not possible to unlink the CAMAC system from the current pulser completely and still harmonize the triggering process. Coming up with a complicated triggering mechanism was not advisable because it did not assure a solution to the problem. Fortunately, the spikes were concentrated in a small part of the actual data, and therefore, removing them numerically without affecting the real data appreciably was considered a viable option. The code in IDL written for numerically removing the results is given in Appendix C. To get an idea of how successful this method was, consider the situation in Fig. 5-5. As the figure suggests, the program removes spikes quite successfully. The code uses predefined ranges of data, around the beginning and

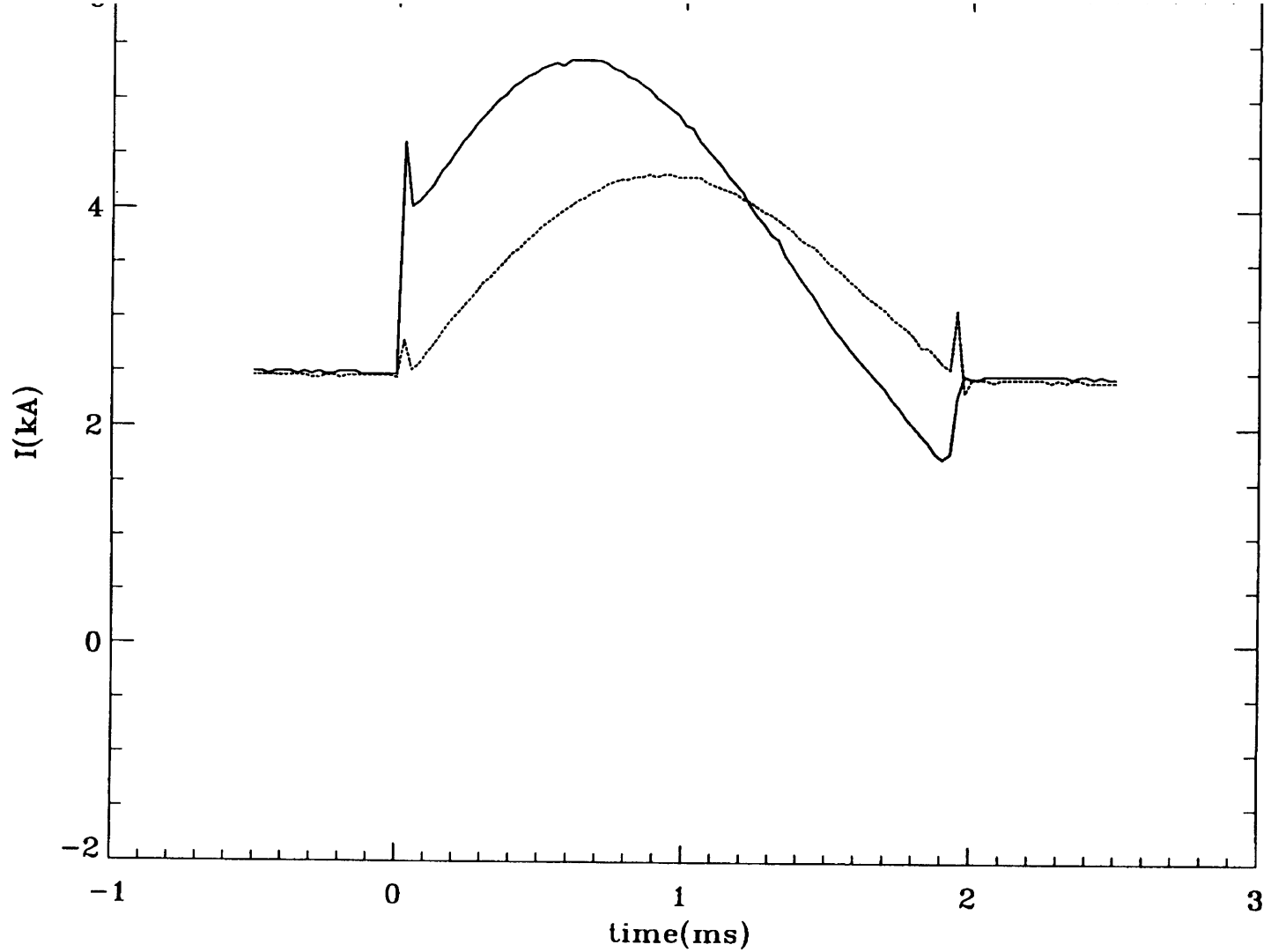

Figure 5-4: Shunt performance: comparison of total current traces for shot number 2766 and 2794. The transport current of shot # 2794 has been compensated to aid in the visual comparison. (Shot 2766: dashed, Shot 2794: solid)

end of the current pulse, and removes consecutive points with oppositely signed slopes. Once all such points are removed the gaps are recovered with approximated data points by using cubic or spline interpolation.

The calculation of dissipated energy by integration of the signal which was a result of multiplying the voltage signal and the current signal after spike removal is referred to as the *direct method.*

5.3.2 Spectral Analysis

After quite a bit of brainstorming it was decided to treat the oscillation problem with spectral analysis. It was assumed that since the only disturbance introduced is a 2 ms current pulse with a time period of 4 ms, the only important frequency is 250 hz. With this perspective, the frequency spectrum of the acquired data on the voltage taps was determined. Fig. 5-6 shows the spectrum plotted for the two voltage taps AA' and CC' between zero frequency (DC) and the nyquist frequency (20 khz for data sampled at 40 khz) for shot # 2618. The plots are normalized to the amplitude of the maximum component in the spectrum which is at zero frequency. The peaks at 250 hz can be clearly seen, and so can be all the extraneous frequencies.

After experimenting a bit with digital filtering routines including notch filters, a low-pass non-recursive digital filtering routine was implemented. To determine the best choice of the frequency cutoff of the low-pass filter, a test voltage waveform was constructed from a 250 hz continuous sinewave. Only one half wavelength of the signal was used. The leftover points in a 0.8192 second wave were set to zero to resemble the actual current pulse. A scaled version of this voltage signal was considered the current signal and these two signals were multiplied to construct the power signal. For comparison, the voltage signal was filtered with low-pass filters with varying frequency cutoffs before multiplication with the current signal. A frequency cutoff of about 1.5 khz passed about 99.9 % of the energy represented by the resulting power signal and was used as the cutoff frequency of the filter used for spectral analysis. The energy calculations based

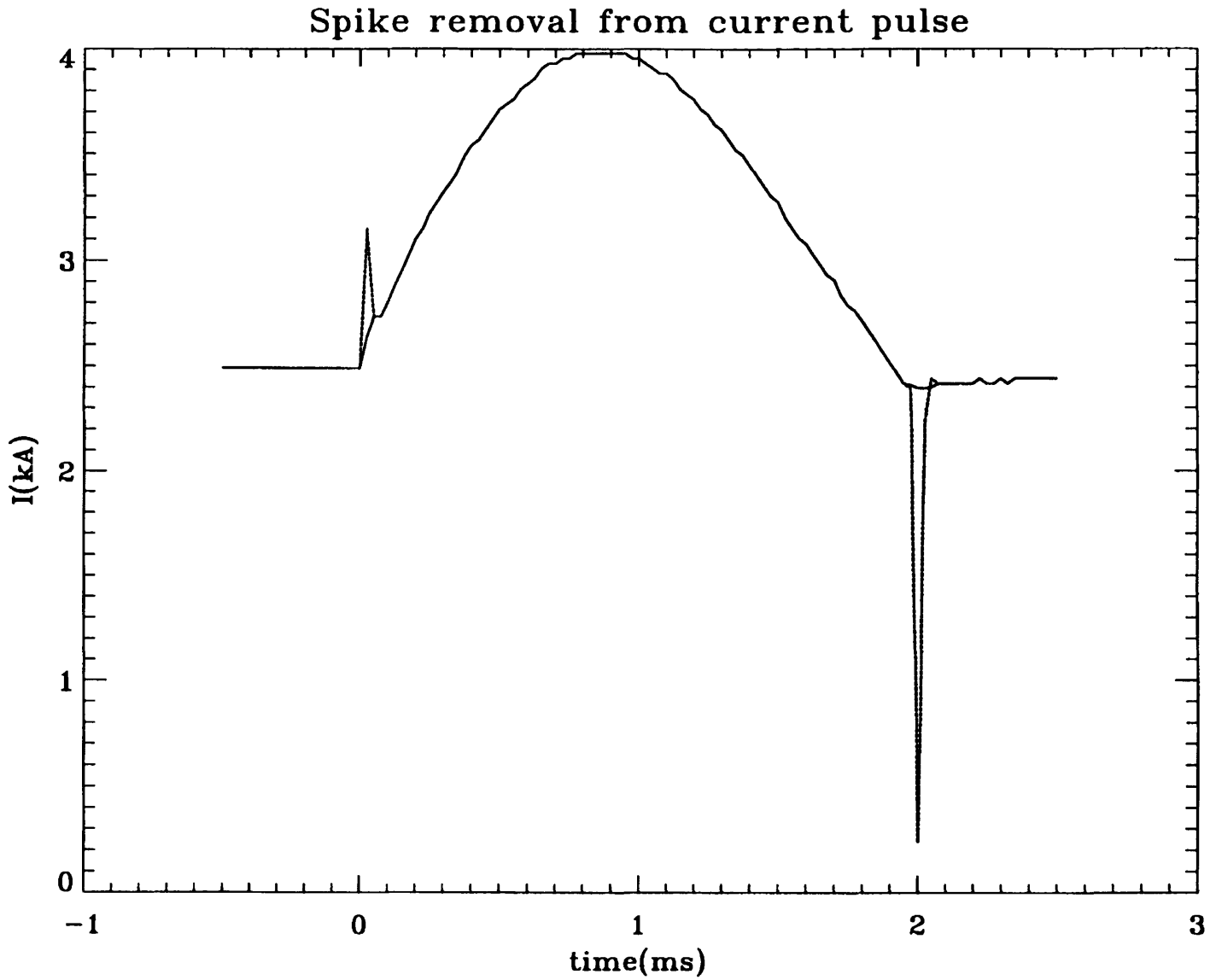

Figure 5-5: Spike removal from current pulse trace for shot # 2770. (Before: dashed, After: solid)

on the integration of the product of the current signal after spike removal and the voltage signal after filtering is called the *spectral method*. The "before and after" traces of the sample voltages representing the data are shown in Fig. 5-7 for shot # 2618. The traces are much clearer now and show the underlying voltage curve with more precision. The pulse does expand a little bit to compensate for the missing high frequencies that get slaughtered along with the undesirable frequencies, which are needed to produce the slope changes required at the ends of the current pulse. This produces slight inaccuracy in the voltage-current integration results. Nevertheless, the advantage of smoothing out the irregular behavior of the spikes and the oscillations is compromised with the following concern: resistive voltage is directly proportional to the total current if the resistance of the sample cable was constant, but that is not the case in this situation. The resistance builds up at a rate which is the function of the length and propagation of the normal zone resulting from the current sharing that the current pulse may induce. Hence, the resistive voltage signal may consist of frequencies which get chopped off in the filtering process and an energy deposition measurement in this situation will be incorrect. However, as the results in Table 5.1 indicate, the spectral and direct integration methods produce values which are within 5 % of each other in most cases. Even in extreme cases like shot # 2618, the energy value calculated by spectral method was 91.2 % of the one calculated by the direct method for voltage tap AA'. For voltage tap CC', the ratio was 95.4 %. This means that the even with the large-amplitude oscillations in the real data, the high frequency components are reactive and do not contribute to energy dissipation. Therefore, the direct method gives a pretty accurate value of the resistive energy dissipated during the pulse duration inside the sample cable. The results of the direct method were used to extract information about the stability margins for each individual CICC.

Cooling of the Shunt

It was realized that the shunt displayed the inductive component only when it was heated to a temperature considerably higher than room temperature. This was

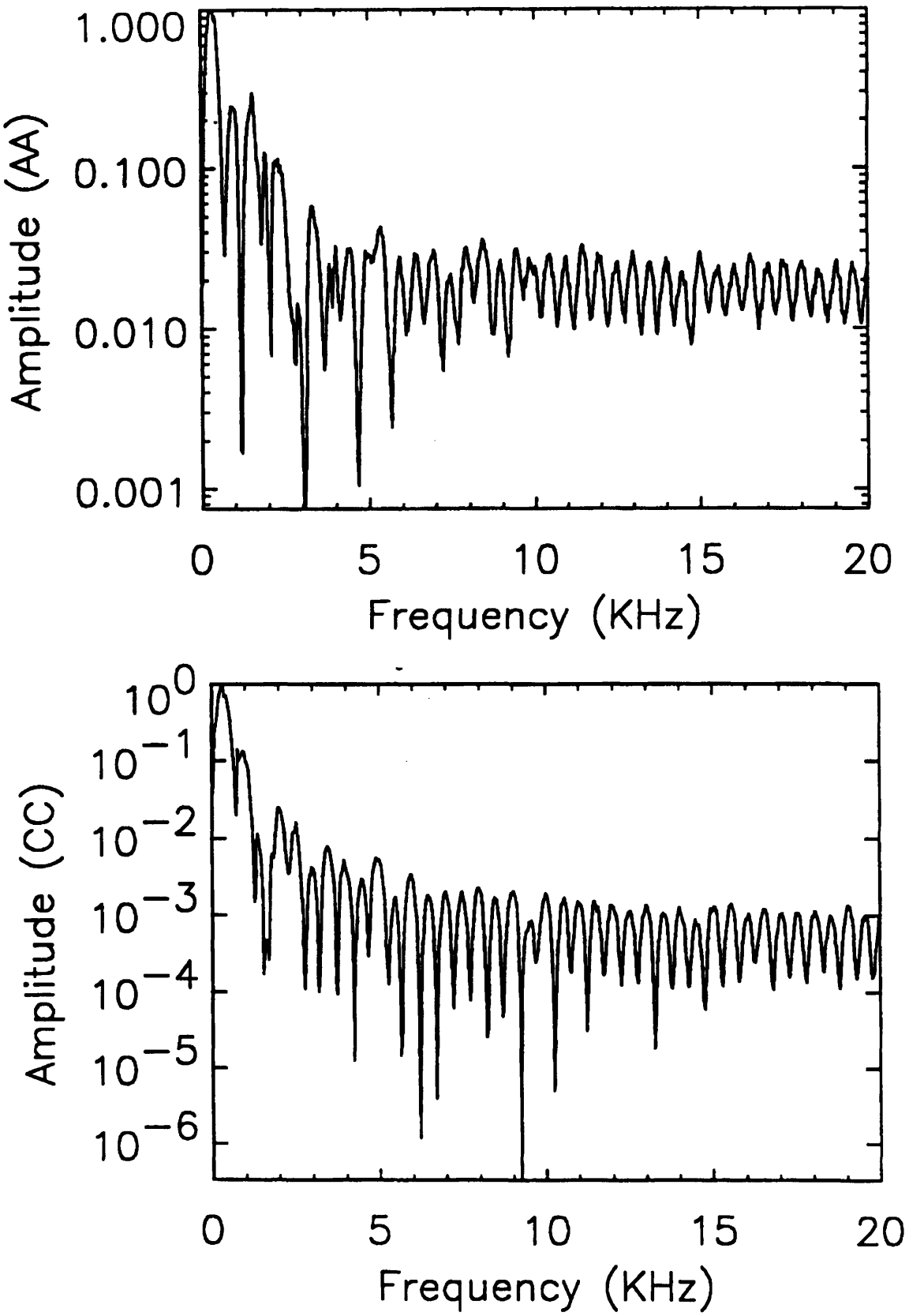

Figure 5-6: Spectral power density of the data for sample voltage taps AA′ and CC′. (Shot # 2618)

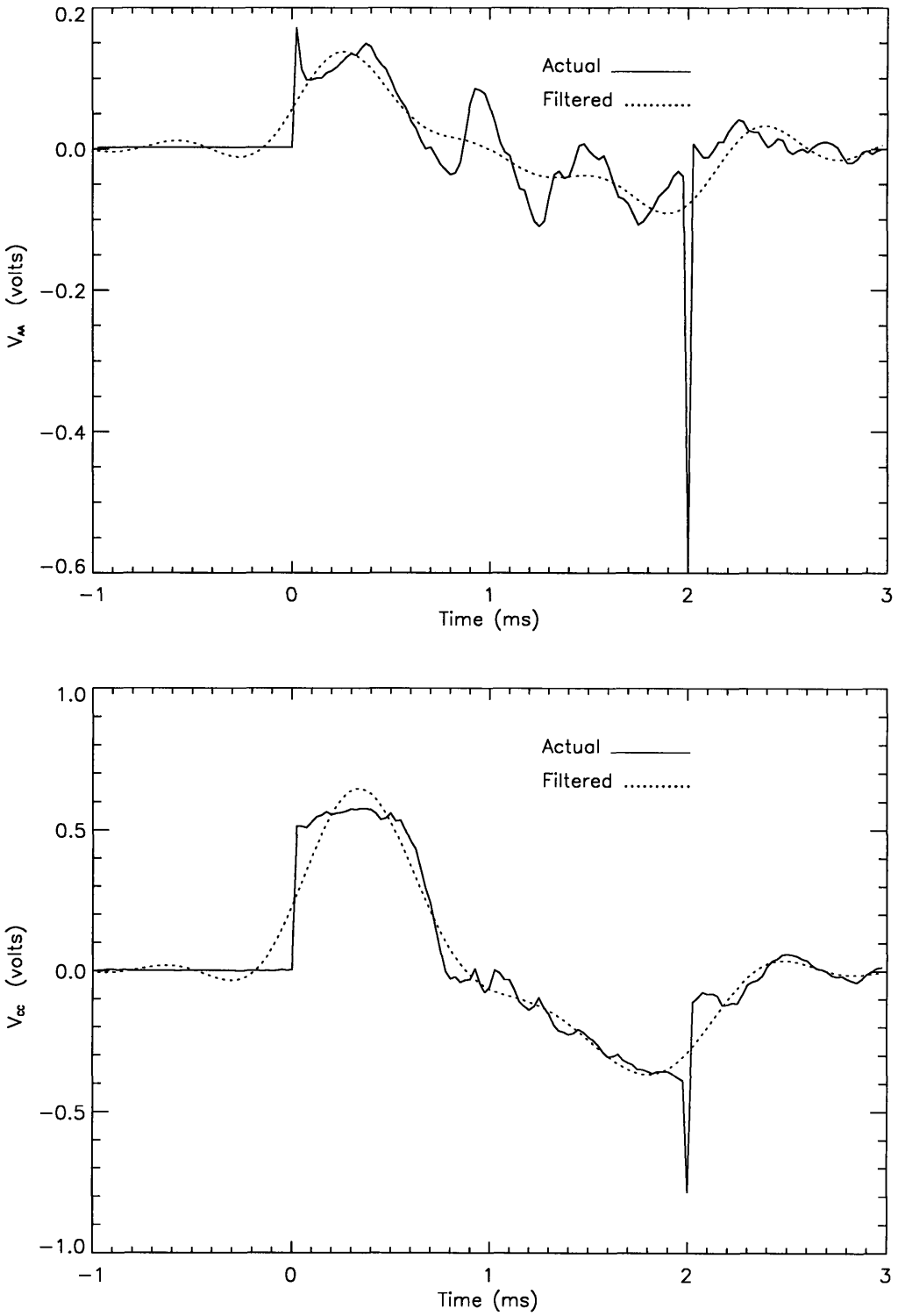

Figure 5-7: The results of spectral analysis: the traces before and after filtering with a 200-point low-pass filter with $f_c = 1.5$ khz of the voltage on (top) voltage tap AA′ (bottom) voltage tap CC′. (Shot # 2618)

the case in experimental run # 8, because for part of the experimental time which was allocated for ramp-rate limitation tests on the sample cable, the shunt was subjected to a continuous transport current of 5 kA or more. In a later test, it was determined that the shunt's performance was satisfactory with air cooling with a fan as long as it was not exposed to high transport currents ($I_t > 5kA$) for more than ten minutes. This requirement was religiously fulfilled in later experiments.

5.3.3 Results

The final results were based on the direct method of dissipated energy calculations which estimated the energy deposition made by the pulse into the cable during the current pulse duration. The spectral method was used on sample voltages AA' and CC' for comparison with the direct method so that the integrity of the direct method could be established. The current pulse after spike removal looked satisfactory. In the spectral method, the power spectrum of the two voltages was plotted first to identify its frequency content. They were then passed through a non-recursive low-pass digital filter with a cutoff frequency of 1.5 khz. The resulting curves were free of oscillations and spikes but were scaled slightly along the time axis as a result of the filtering. These filtered curves were multiplied by the total current trace which was made spike-free and then the product was integrated for the duration of the pulse using Simpson's method. In the direct method, the integration was performed on the original voltage curves after multiplying with the spikes-adjusted current curve. Cubic spline extrapolation was performed on the voltage curves to aid in the integration process. This essentially reduced the value of the interval or step-size of integration which improved the error in integration. The useful data from all experiments is listed in Table. 5.1. The calculated energy is listed as having been calculated by either "spectral method" or by "direct method." It is important to note that the voltage tap AA' was not consistently used because it had functionality problems during the experimental runs. Hence, whenever the signal on AA' was considered ridiculous, the energy deposition was not calculated. Also,

shots 2618-2656 used the tap DD' instead while shots 2786-2795 used the voltage tap BC. t_{delay} represents the time it took after the end of the current pulse to the onset of monotonically increasing resistive voltage in the event of a quench. The conclusionary stability margins and comparisons with the analytical model will therefore be based on the data acquired from voltage tap CC' and the results based on the direct method.

The voltage tap CC', as shown in Fig. 4-8, had a length of 88 cms, while AA' was 20 cms long. The resulting cable volumes based on Table 4.1 for use in the energy calculations per unit volume of the cable are given in Table. 5.2. The cable volume is taken as the product of the cross-sectional area of all strands, whether superconducting or not, with the length of the voltage tap across which the voltage of the sample was measured and is given by

$$V_{cable} = \pi[\frac{d_{sc}^2}{4}N_{sc} + \frac{d_{hybrid}^2}{4}N_{hybrid}]l_{V_{tap}} \tag{5.7}$$

where d_{sc} and d_{hybrid} are the diameters of the superconducting and hybrid strands and N_{sc} and N_{hybrid} are the respective number of such strands in the cable. $l_{V_{tap}}$ is the length of the cable across which the total voltage, resistive plus inductive, is measured.

The direct method for calculation of the energy deposited inside the cable integrates the product of the current signal, after the removal of spikes from it, with the voltage tap signal involved for the duration of the pulse. The following integration rule, also called Simpson's three-point formula, was used for numerical integration

$$\int_{x_0}^{x_1} f(x)\,dx = h[\frac{1}{3}f(x_0) + \frac{4}{3}f(x') + \frac{1}{3}f(x_1)] + O(h^5 f^{(4)}) \tag{5.8}$$

where $h = 25\mu s$ was the sampling time, x' was calculated by a cubic spline algorithm, and $f^{(4)}$ is the fourth derivative of the function f evaluated at an unknown place in the interval, and represented the error term in the integration.

Shot‡ #	Quench?	B (T)	I_t (kA)	V_{cap} (V)	Peak I_p (kA)	t_{delay} (ms)	$E_{CC'}$ (J) Spectral Method	$E_{CC'}$ (J) Direct Method	$E_{AA'}$ (J)† Spectral Method	$E_{AA'}$ (J)† Direct Method
839	Yes	9	2.457	108.0	0.326	39.0	9.579×10^{-02}	1.043×10^{-01}	1.714×10^{-01}	1.870×10^{-01}
840	No	9	2.460	83.9	0.177	-	6.104×10^{-02}	6.375×10^{-02}	5.844×10^{-02}	5.732×10^{-02}
842	No	7	2.484	108.9	0.372	-	3.373×10^{-02}	4.281×10^{-02}	6.405×10^{-03}	8.943×10^{-03}
843	No	9	2.515	217.8	0.780	-	1.946×10^{-01}	2.107×10^{-01}	2.538×10^{-01}	2.677×10^{-01}
845	Yes	9	2.488	317.9	1.125	2.0	3.603×10^{-01}	3.724×10^{-01}	3.055×10^{-01}	3.060×10^{-01}
846	Yes	9	2.466	423.0	1.562	2.0	1.115	1.118	5.846×10^{-01}	5.827×10^{-01}
847	Yes	9	2.452	317.9	1.162	6.0	3.381×10^{-01}	3.478×10^{-01}	2.569×10^{-01}	2.564×10^{-01}
849	No	9	0.024	530.1	2.295	-	3.451×10^{-01}	3.405×10^{-01}	8.757×10^{-02}	8.528×10^{-02}
850	No	9	0.024	738.3	3.174	-	7.400×10^{-01}	7.221×10^{-01}	3.417×10^{-01}	3.381×10^{-01}
851	No	9	0.024	738.3	3.149	-	7.683×10^{-01}	7.579×10^{-01}	3.401×10^{-01}	3.358×10^{-01}
853	Yes	9	2.439	738.3	2.688	2.0	4.301	4.263	1.729	1.722
855	Yes	9	2.505	737.8	2.671	2.0	4.566	4.561	1.878	1.885
1704	No	7	0.025	215.3	0.903	-	3.860×10^{-02}	3.932×10^{-02}	1.792×10^{-03}	1.959×10^{-03}
1706	No	7	0.025	850.8	3.588	-	1.168	1.164	-	-
1707	No	7	0.025	841.9	3.539	-	1.045	1.042	6.837×10^{-01}	6.833×10^{-01}
1708	No	7	0.025	840.9	3.515	-	1.077	1.071	-	-
1709	No	7	0.026	843.4	3.514	-	9.957×10^{-01}	9.923×10^{-01}	-	-
1710	No	7	0.025	845.4	3.539	-	9.953×10^{-01}	9.931×10^{-01}	1.021	1.021
1711	No	7	0.025	843.6	3.539	-	8.808×10^{-01}	8.745×10^{-01}	1.352	1.352
1715	Yes	7	2.501	843.7	3.016	2.0	4.577	4.635	2.524	2.543
1716	No	7	2.477	425.6	1.527	-	5.174×10^{-01}	5.336×10^{-01}	2.739×10^{-01}	2.790×10^{-01}
1717	Yes	7	2.541	636.0	2.317	2.0	8.116×10^{-01}	8.326×10^{-01}	2.721×10^{-01}	2.765×10^{-01}
1718	Yes	7	2.542	529.6	1.926	3.0	7.934×10^{-01}	8.046×10^{-01}	3.747×10^{-01}	3.776×10^{-01}
1719	Yes	7	2.538	476.9	1.734	400.0	5.404×10^{-01}	5.550×10^{-01}	2.589×10^{-01}	2.647×10^{-01}
2616	No	7	2.468	423.3	1.512	-	6.539×10^{-01}	6.684×10^{-01}	5.656×10^{-01}	5.565×10^{-01}
2617	Yes	7	2.517	476.8	1.731	2.0	7.736×10^{-01}	7.774×10^{-01}	6.433×10^{-01}	6.398×10^{-01}
2618	No	7	2.488	403.3	1.467	-	4.856×10^{-01}	5.088×10^{-01}	8.265×10^{-02}	9.062×10^{-02}

† DD′ (Shots 2618-2656), BC (Shots 2786-2795)

‡ Hybrid Cable # 1: Shots 839-2656 ; US-DPC Test Sample: Shots 2764-2795

Continued on next page ⟹

Table 5.1: Experimental Results for Stability Experiment A. (page 1 of 4)

Shot‡ #	Quench?	B (T)	I_t (kA)	V_{cap} (V)	Peak I_p (kA)	t_{delay} (ms)	$E_{CC'}$ (J) Spectral Method	$E_{CC'}$ (J) Direct Method	$E_{AA'}$ (J)† Spectral Method	$E_{AA'}$ (J)† Direct Method
2619	Yes	7	2.539	445.2	1.612	32.0	5.356×10^{-01}	5.521×10^{-01}	1.148×10^{-01}	1.190×10^{-01}
2621	No	7	2.488	413.2	1.492	-	4.681×10^{-01}	4.828×10^{-01}	1.043×10^{-01}	1.081×10^{-01}
2622	No	7	2.517	435.3	1.584	-	4.654×10^{-01}	4.631×10^{-01}	7.345×10^{-02}	7.282×10^{-02}
2623	No	7	2.489	439.4	1.588	-	5.534×10^{-01}	5.525×10^{-01}	1.499×10^{-01}	1.451×10^{-01}
2624	No	7	2.514	445.4	1.612	-	5.045×10^{-01}	5.183×10^{-01}	9.920×10^{-02}	1.057×10^{-01}
2625	No	7	2.488	450.5	1.614	-	4.818×10^{-01}	4.929×10^{-01}	9.614×10^{-02}	1.036×10^{-01}
2626	No	7	2.467	454.2	1.658	-	4.513×10^{-01}	4.598×10^{-01}	8.006×10^{-02}	7.422×10^{-02}
2627	Yes	7	2.463	459.7	1.688	400.0	5.372×10^{-01}	5.184×10^{-01}	1.477×10^{-01}	1.325×10^{-01}
2628	Yes	7	2.468	466.2	1.707	38.0	5.201×10^{-01}	5.376×10^{-01}	1.532×10^{-01}	1.600×10^{-01}
2629	Yes	7	2.469	462.4	1.681	22.0	5.605×10^{-01}	5.770×10^{-01}	1.766×10^{-01}	1.807×10^{-01}
2630	Yes	7	2.982	374.3	1.364	12.0	4.285×10^{-01}	4.373×10^{-01}	1.303×10^{-01}	1.359×10^{-01}
2631	Yes	7	2.932	343.6	1.268	37.0	3.625×10^{-01}	3.786×10^{-01}	1.269×10^{-01}	1.308×10^{-01}
2633	No	7	2.963	266.8	0.968	-	2.420×10^{-01}	2.619×10^{-01}	8.600×10^{-02}	9.055×10^{-02}
2634	No	7	2.949	318.0	1.153	-	3.440×10^{-01}	3.288×10^{-01}	1.362×10^{-01}	1.167×10^{-01}
2635	No	7	2.946	340.1	1.253	-	3.166×10^{-01}	3.262×10^{-01}	1.002×10^{-01}	1.038×10^{-01}
2636	No	7	2.950	346.1	1.249	-	3.413×10^{-01}	3.475×10^{-01}	9.097×10^{-02}	9.783×10^{-02}
2637	No	7	2.948	350.3	1.276	-	3.945×10^{-01}	3.992×10^{-01}	9.342×10^{-02}	9.701×10^{-02}
2638	No	7	2.952	356.0	1.296	-	3.856×10^{-01}	3.975×10^{-01}	7.390×10^{-02}	7.984×10^{-02}
2639	No	7	2.942	361.0	1.306	-	4.062×10^{-01}	4.064×10^{-01}	9.845×10^{-02}	1.014×10^{-01}
2640	No	7	2.947	366.2	1.350	-	4.234×10^{-01}	4.221×10^{-01}	1.012×10^{-01}	9.932×10^{-02}
2641	No	7	2.955	371.3	1.366	-	3.968×10^{-01}	4.067×10^{-01}	8.257×10^{-02}	9.128×10^{-02}
2642	No	7	2.934	376.8	1.387	-	3.927×10^{-01}	3.623×10^{-01}	6.680×10^{-02}	4.640×10^{-02}
2643	No	7	2.949	381.9	1.397	-	4.084×10^{-01}	3.957×10^{-01}	7.238×10^{-02}	6.659×10^{-02}
2644	Yes	7	2.940	387.9	1.406	42.0	4.298×10^{-01}	4.397×10^{-01}	8.671×10^{-02}	9.596×10^{-02}
2645	No	7	1.980	476.0	1.731	-	5.744×10^{-01}	5.604×10^{-01}	1.270×10^{-01}	1.168×10^{-01}
2646	No	7	1.978	502.4	1.831	-	5.513×10^{-01}	5.926×10^{-01}	9.338×10^{-02}	1.103×10^{-01}
2647	No	7	1.992	528.7	1.938	-	6.097×10^{-01}	6.039×10^{-01}	9.294×10^{-02}	8.118×10^{-02}

† DD' (Shots 2618-2656), BC (Shots 2786-2795)

‡ Hybrid Cable # 1: Shots 839-2656 ; US-DPC Test Sample: Shots 2764-2795

Continued on next page ⟹

Table 5.1: Experimental Results for Stability Experiment A. (page 2 of 4)

Shot‡ #	Quench?	B (T)	I_t (kA)	V_{cap} (V)	Peak I_p (kA)	t_{delay} (ms)	$E_{CC'}$ (J) Spectral Method	$E_{CC'}$ (J) Direct Method	$E_{AA'}$ (J)† Spectral Method	$E_{AA'}$ (J)† Direct Method
2648	No	7	1.982	553.7	2.047	-	6.380×10^{-01}	6.368×10^{-01}	7.348×10^{-02}	5.284×10^{-02}
2649	No	7	1.991	571.0	2.087	-	6.904×10^{-01}	7.186×10^{-01}	9.476×10^{-02}	9.977×10^{-02}
2650	No	7	1.983	575.1	2.094	-	7.175×10^{-01}	7.497×10^{-01}	8.510×10^{-02}	9.338×10^{-02}
2651	No	7	1.972	581.5	2.130	-	6.867×10^{-01}	7.181×10^{-01}	8.006×10^{-02}	9.118×10^{-02}
2652	No	7	1.986	592.2	2.091	-	7.037×10^{-01}	7.302×10^{-01}	7.304×10^{-02}	7.713×10^{-02}
2653	No	7	1.978	597.0	2.197	-	7.151×10^{-01}	7.460×10^{-01}	7.730×10^{-02}	8.513×10^{-02}
2654	No	7	1.977	602.4	2.197	-	7.277×10^{-01}	7.583×10^{-01}	8.184×10^{-02}	8.751×10^{-02}
2655	No	7	1.977	607.5	2.222	-	7.334×10^{-01}	7.667×10^{-01}	7.851×10^{-02}	8.560×10^{-02}
2656	No	7	1.982	617.4	2.291	-	8.124×10^{-01}	8.516×10^{-01}	1.025×10^{-01}	1.176×10^{-01}
2764	No	9	2.460	424.5	1.495	-	5.930×10^{-01}	6.154×10^{-01}	-	-
2765	Yes	9	2.461	625.4	2.202	2.0	1.262	1.316	-	-
2766	Yes	9	2.450	528.0	1.847	40.0	7.938×10^{-01}	8.216×10^{-01}	-	-
2767	Yes	9	2.441	501.1	1.734	45.0	7.837×10^{-01}	8.264×10^{-01}	-	-
2768	Yes	9	2.515	474.9	1.635	45.0	6.983×10^{-01}	7.164×10^{-01}	-	-
2769	Yes	9	2.465	449.0	1.563	50.0	5.851×10^{-01}	6.201×10^{-01}	-	-
2770	Yes	9	2.487	422.8	1.468	50.0	6.272×10^{-01}	6.358×10^{-01}	-	-
2771	Yes	9	2.514	370.7	1.295	50.0	5.722×10^{-01}	5.923×10^{-01}	-	-
2772	No	9	2.488	317.8	1.101	-	5.323×10^{-01}	5.250×10^{-01}	-	-
2773	No	9	2.513	215.2	0.710	-	2.862×10^{-01}	3.059×10^{-01}	-	-
2778	No	9	2.431	239.7	0.742	-	5.701×10^{-01}	5.896×10^{-01}	-	-
2779	No	9	3.810	132.7	0.414	-	4.296×10^{-01}	4.457×10^{-01}	-	-
2780	Yes	9	3.765	187.0	0.580	27.0	6.916×10^{-01}	7.264×10^{-01}	-	-
2781	Yes	9	4.695	107.3	0.334	18.0	4.561×10^{-01}	4.857×10^{-01}	-	-
2782	Yes	9	4.767	81.7	0.213	21.0	5.606×10^{-01}	5.816×10^{-01}	-	-
2783	No	9	4.784	31.2	0.074	-	2.665×10^{-01}	2.733×10^{-01}	-	-
2784	No	9	3.230	212.7	0.676	-	5.322×10^{-01}	5.431×10^{-01}	-	-
2785	No	9	3.246	240.1	0.758	-	6.089×10^{-01}	6.445×10^{-01}	-	-
2786	Yes	9	3.224	266.5	0.853	58.0	7.397×10^{-01}	7.598×10^{-01}	8.947×10^{-02}	1.024×10^{-01}

† DD′ (Shots 2618-2656), BC (Shots 2786-2795)

‡ Hybrid Cable # 1: Shots 839-2656 ; US-DPC Test Sample: Shots 2764-2795

Continued on next page ⟹

Table 5.1: Experimental Results for Stability Experiment A. (page 3 of 4)

Shot‡ #	Quench?	B (T)	I_t (kA)	V_{cap} (V)	Peak I_p (kA)	t_{delay} (ms)	$E_{CC'}$ (J) Spectral Method	$E_{CC'}$ (J) Direct Method	$E_{AA'}$ (J)† Spectral Method	$E_{AA'}$ (J)† Direct Method
2787	No	9	1.955	318.0	1.023	-	8.306×10^{-01}	8.529×10^{-01}	2.932×10^{-01}	3.065×10^{-01}
2788	No	9	1.970	426.1	1.351	-	1.406	1.464	4.581×10^{-01}	4.873×10^{-01}
2789	No	9	1.953	473.8	1.465	-	1.554	1.623	5.113×10^{-01}	5.428×10^{-01}
2790	No	9	1.956	579.6	1.829	-	2.152	2.243	7.046×10^{-01}	7.480×10^{-01}
2791	Yes	9	1.982	735.7	2.290	77.0	2.657	2.712	9.339×10^{-01}	9.661×10^{-01}
2792	Yes	9	1.981	684.3	2.121	98.0	2.794	2.875	9.661×10^{-01}	1.020
2793	No	9	1.973	606.2	1.884	-	2.128	2.220	7.921×10^{-01}	8.336×10^{-01}
2794	No	9	1.470	843.4	2.608	-	4.196	4.271	1.232	1.277
2795	Yes	9	1.473	1038.0	3.142	110.0	5.816	6.010	1.704	1.783

† DD' (Shots 2618-2656), BC (Shots 2786-2795)

‡ Hybrid Cable # 1: Shots 839-2656 ; US-DPC Test Sample: Shots 2764-2795

Table 5.1: Experimental Results for Stability Experiment A. (page 4 of 4)

	Hybrid Sample # 1		US-DPC Test Sample	
	AA′	CC′	AA′	CC′
Length (cm)	20	88	20	80
Volume (cc)				
Total	2.5958	11.4216	2.5803	10.3213
Superconducting strands only	1.7202	7.5689	2.5803	10.3213

Table 5.2: Volumes of the cable used in energy calculations for Experiment A.

The resulting stability margins are plotted in Figs. 5-8 and 5-10. Fig. 5-8 plots the results showing the energy deposited in hybrid cable # 1 over the length of voltage tap CC′ at 7 T for different operating transport currents for the direct method. Fig. 5-10 plots the results for the US-DPC test sample for the voltage tap CC′ at a background field of 9 T.

The results for hybrid cable # 1 show that we are operating above the limiting current as we show stability margins of 100 mJ/cc or less. The shots at the transport current value of 2 kA, 2.5 kA, and 3.0 kA, all show a significant amount of training, as the cable is capable of staying stable after energy depositions which previously quenched it. Unfortunately, the data does not cover the transition region and the only prediction possible is that the upper limiting current is less than 2.0 kA. Clearly, more experiments need to be done to obtain the data for the high energy margin area.

The results for the US-DPC test sample are more promising. A large portion of the stability margin is traced and an upper limiting current I_{lim}^{upp} of approximately 2.5 kA is identified. With the direct method, the cable shows a stability margin of over 600 mJ/cc. The low stability margin above the upper limiting current is clearly established at about 50 mJ/cc.

The two cables seem to have a similar energy margin in the ill-cooled region, but the copper hybrid CICC definitely has a higher limiting current. The results will be compared with a theoretical approach in Section 5.5.

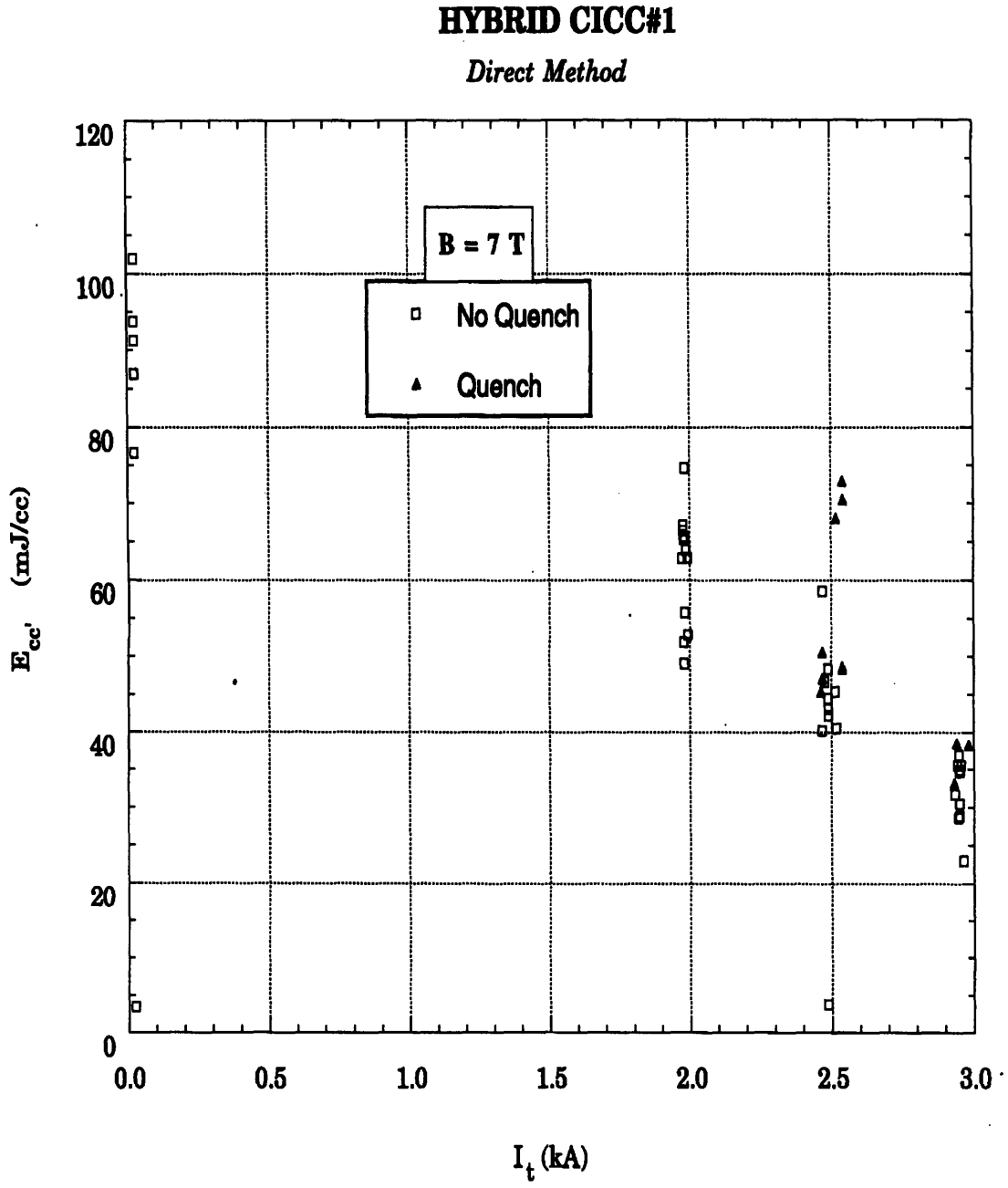

Figure 5-8: Stability margin of hybrid CICC # 1 (direct method).

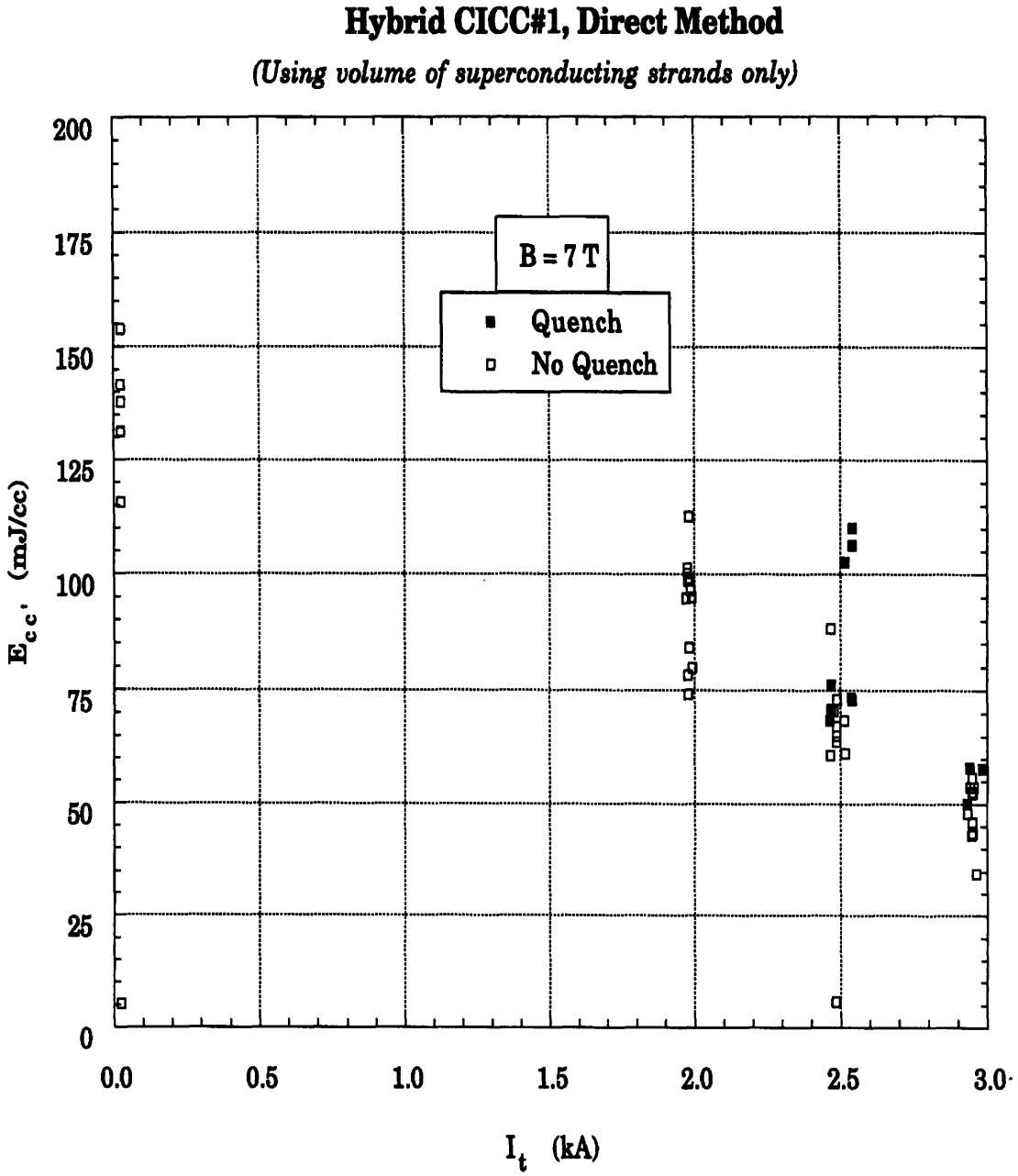

Figure 5-9: Comparison of the stability margin of hybrid CICC # 1 (direct method using volume of only superconducting strands).

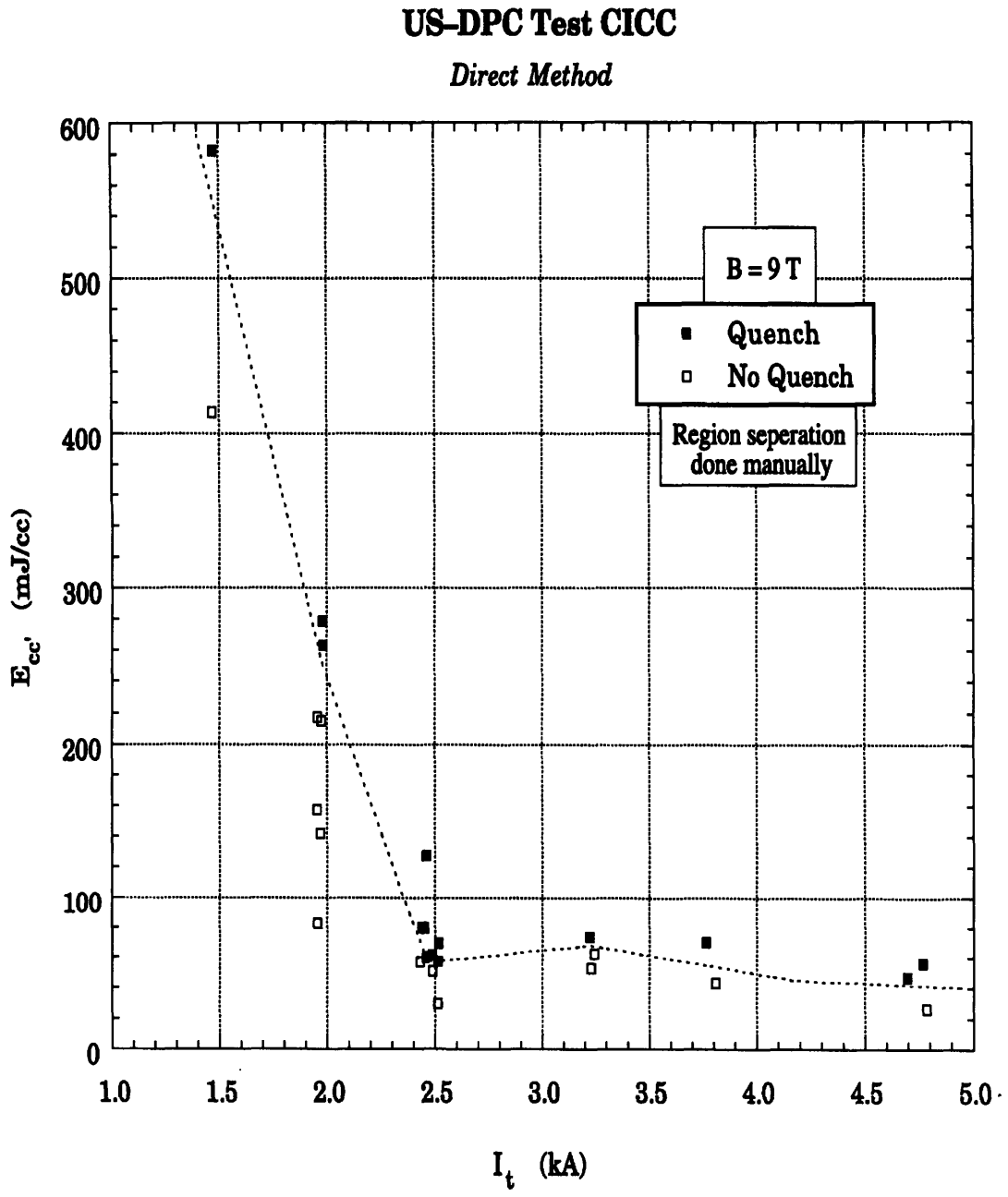

Figure 5-10: Stability margin of US-DPC sample CICC (direct method).

Care Required in Application of the Spectral Method

The spectral energy of a signal is given by Parseval's theorem

$$\sum_{k=0}^{N-1} |h_k|^2 = \frac{1}{N} \sum_{n=0}^{N-1} |H_n|^2 \tag{5.9}$$

where h_k is the magnitude of the kth frequency and H_n is the magnitude of the nth data point. By low pass filtering, the high frequency content is thrown away thus reducing the left-hand side of Eq. 5.9. This results in the reduction of the H_n values. However, if the high frequencies have negligible energy content then the results should not change after low-pass filtering. The resistive signal is in phase with the current signal, and therefore, should not have any energy content in the stop-band of the filter. But since there are only 80 data points in the pulse and the rest of the signal is DC, a digital filter cutoff frequency has to be carefully chosen so that the spectral energy peak at 250 hz is not chopped off. The filter which was implemented uses the Kaiser window. The way the filter works is that first the coefficients for use in the filtering based on the Kaiser window are evaluated. For more details about the coefficients of Kaiser window, which use the zeroth-order modified Bessel function of the first kind, see Oppenheim and Shafer (1989) [55, p. 452]. The IDL code is given in Appendix C. The window shape is determined by the specified pass-band frequencies and the value of Gibb's phenomenon. The window points are multiplied by the required sinc function to generate the filter coefficients. The filter coefficients are such that they have a Fourier transform which is the frequency response of the filter. It has an amplitude of unity in the pass band and zero in the stop band with a transition range and stop-band ripple which depends on the number of filtering coefficients, which is also the order of the filter. Since low-pass filtering is equivalent to multiplying the two frequency responses, the window coefficients are convolved with the time signal to give the filtered data.

The frequency response of the filter improves as the order of the filter is increased. Depending on the choice of the cutoff frequency, the filter may not have

an acceptable frequency response with a low number of coefficients. The comparison of the frequency amplitude responses of two filters with the same cutoff frequency, but an order of magnitude difference in the number of filter coefficients, is shown in Appendix B. It shows that the 20-point filter will scale down the amplitude of passing frequencies by a factor of three or four on average while the 200-point filter does not scale the amplitude. Therefore, in this case, the results based on the 20-point filter would be completely wrong.

In the spectral analysis performed, a 200-point low-pass filter with a cutoff frequency of 1.5 khz was employed. Its frequency response is plotted in Fig. B-3 in Appendix B.

Quench Delay

An interesting observation was made for the experimental shots which quenched as a result of the pulsed current disturbance. For the cases in which a rising resistive voltage was observed within the 0.41 second data window available after the completion of the current pulse, the delay time t_{delay} was recorded. t_{delay} was defined as the time it took from the completion of the current pulse to the onset of monotonically increasing resistive voltage on the voltage tap indicating a quench (See Fig. A-4 in Appendix A). Fig. 5-11 displays an inverse correlation between t_{delay} and the energy deposited inside the conductor for the same values of background field and transport current. There were not enough data points to corroborate this correlation exactly but an exponential curvefit is shown which gives

$$E_{CC'}(mJ/cc) = 135.62e^{-0.015087t_{delay}} \quad (Residual = 0.96761) \qquad (5.10)$$

with t_{delay} in ms. If a distinctive correlation could be found, it would be an interesting way to estimate the energy deposited inside the cable in the event of a quench.

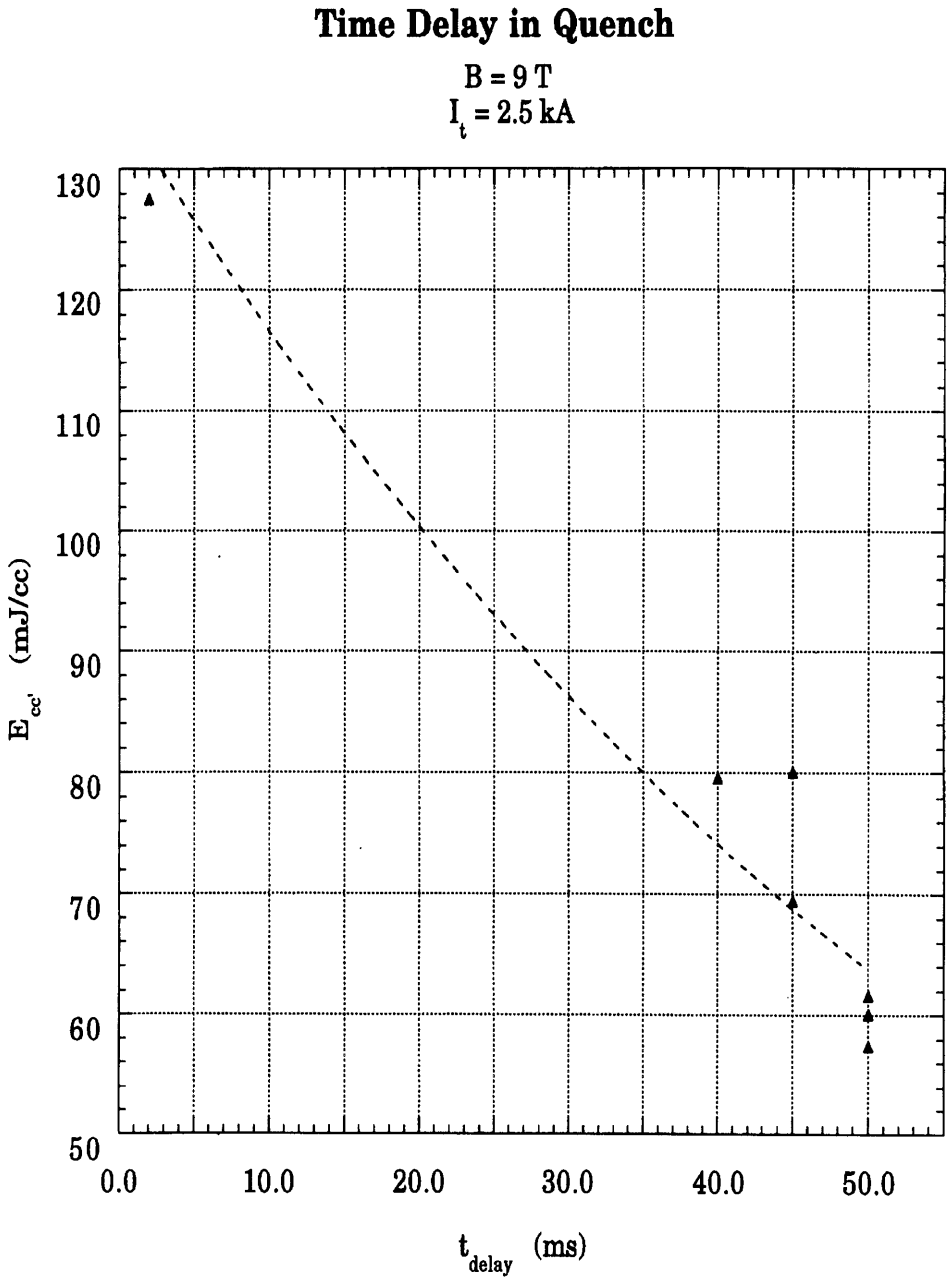

Figure 5-11: Time delay in quench for US-DPC test sample: B = 9 T, I_t = 2.5 kA.

5.4 Analysis of Data from Experiment B

The data in experiment B consisted of 8 data variables stored at a digitizing frequency of 4.5 khz (0.22 ms/ data point) for a total of 1.33 seconds. The data acquisition was triggered manually by pressing the appropriate button on the data acquisition program in Labview developed for such experiments. This needed excellent communication between the operators of the DPCP, the Dynapower supply control panel, and the DAQ-950 Macintosh computer. The time length of the data window was enough to ensure acceptable triggering control. As mentioned earlier, these 8 variables were:

1. the pulser current signal from the pulser shunt.
2. the total current signal from the main shunt.
3. the transport current signal from the Dynapower supply control panel.
4. the voltage signal from voltage tap $\pm V_4$ (pair A-B).
5. the voltage signal from voltage tap $+V_5/+V_6$ (pair C-D).
6. the voltage signal from voltage tap $+V_6/+V_7$ (pair E-F).
7. the voltage signal from voltage tap $\pm V_7$ (pair G-H).
8. the voltage signal from voltage tap $-V_6/-V_7$ (pair J-K).

The data was stored as binary files on the Macintosh and later recovered by using the general binary loader facility (GBLoader) in IgorPro. There are three data boards connected to the Macintosh, and all of them have to be kept on during data acquisition. As a result, the binary files have 54,000 points (9 channels $\times$ 6000 points per channel). The points are interleaved in the storage format applied.

There were a few important differences noticeable, even in the limited data available for experiment B. There were no spikes of the sort encountered in experiment A, neither were there superposed frequencies. There was however an unacceptable signal to noise ratio. The results will be presented only for the voltage

Shot #	B (T)	I_t (kA)	Quench?	I_p Peak		E_{AB} (J)†	
				Pulse 1	Pulse 2	Pulse 1	Pulse 2
6	5	1.97	No	0.415	0.426	0.5082	0.2302
7	5	2.93	No	0.600	0.603	0.4474	0.1101
8	7	3.01	Yes	0.502	0.472	4.6390	9.5917
9	7	2.96	No	0.320	0.340	0.4405	0.3266
10	7	2.97	Yes	0.418	0.432	3.5309	9.9474
11	7	2.97	Yes	0.371	0.370	3.4083	11.6080
12	7	2.80	No	0.500	0.000	0.5104	0.0000
13	7	2.80	No	0.595	0.000	0.9593	0.0000
14	7	2.80	No	0.865	0.000	0.6651	0.0000
15	7	2.83	No	0.710	0.000	0.9795	0.0000
16	7	2.80	Yes	1.327	0.000	9.8094	0.0000
17	7	2.79	No	0.467	0.466	-0.0916	0.6610
18	7	2.80	No	0.516	0.484	0.6250	0.1677
19	7	2.78	No	0.643	0.622	0.7712	0.2850
20	7	2.80	No	0.733	0.703	0.8936	0.3707
21	7	2.80	Yes	0.900	0.890	2.7102	3.6207

† Also referred to as the voltage tap $\pm V_4$.

Table 5.3: Results of Experiment B.

tap pair AB ($\pm V_4$) because of its highest signal to noise ratio, about an order of magnitude higher than the most voltage tap signals. Fig. 5-12 shows the comparison. Although V_{jk} has a good signal to noise ratio as well but it was over a much shorter length of the sample (127 mm compared to 965 mm as shown in Fig. 4-8).

The pulser shunt signal was in complete agreement with the main shunt signal and therefore the main shunt signal was employed during integration. Using Eq. 4.5, the energy deposited during each pulse was calculated using an in-built trapezoidal integration routine in IgorPro. The results are presented in Table 5.4. Some of the shots used only a single capacitor bank. The observations made below are fairly sketchy because of the limited amount of data gathered in the experiment, but are interesting nonetheless.

In all quenching events, it looks like the quench initiated in the early part of the first pulse, such that the second pulse deposited a lot of energy due to the presence of the transport current in an already quenched cable. In stable events, the energy

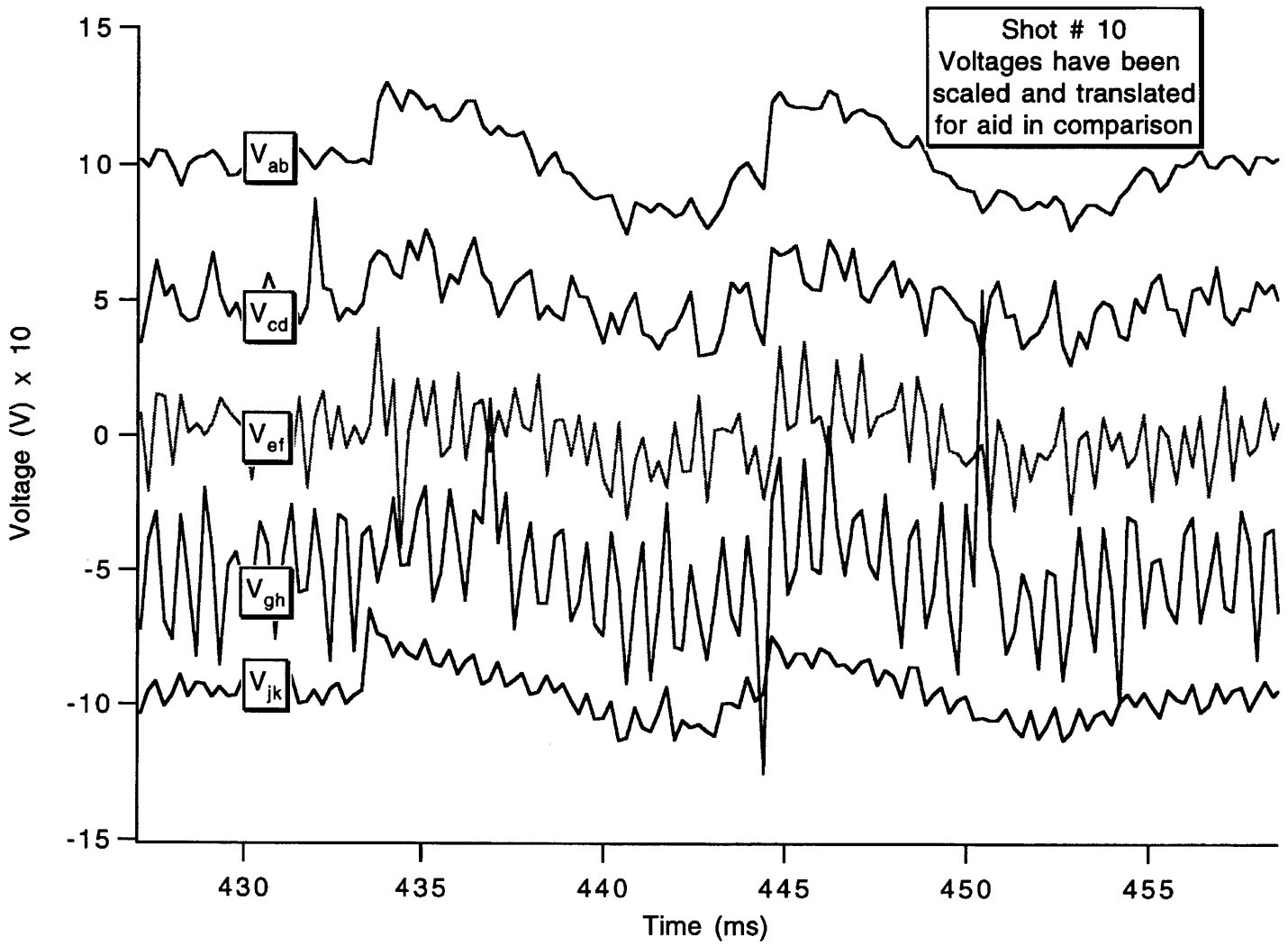

Figure 5-12: Comparison of voltage signals on the different voltage taps on the sample.

deposited during the first pulse was always greater than the second pulse, as long as the current sharing started early in the first pulse. The only exception was shot # 17 in which no energy was deposited in the first pulse which implies that the current sharing temperature was never reached during the first pulse. This observation could not be explained. A test shot towards the end of the experiment, which was not recorded, showed that increasing the delay time of the second pulse could make the conductor stable to the same level of pulsed current, at the same field and transport current, which quenched it initially.

The energy deposited by the first pulse is plotted in Fig. 5-15 versus the transport current.

Fig. 5-15 shows the results graphically. Only the energy deposited during the first pulse is plotted. The plot shows that we are operating in the ill-cooled region with energy margin values of about 100 mJ/cc which are similar to those found in experiment A. The transition region cannot be identified and therefore no comparison could be made with the hybrid cable used in experiment A.

Experiment B holds a lot of potential for doing interesting measurements. The possibility of modeling more complicated energy deposition processes is evident just by the limited amount of data available. At the moment only the delay time between the two pulses of fixed pulse width is the variable of interest, but it is possible to configure the capacitor banks in such a way that different discrete pulse widths will be available in addition to the variable delay between the two pulses. This gives much more control over the rate and duration at which energy is deposited inside the cable, which is the important parameter to consider for stability, rather than the source of this energy.

5.5 Analytical Model for Bench Mark Comparison

An analytical model was developed based on the existing experimental conditions, with the theoretical stability margin calculated in a manner similar to Eq. 3.1

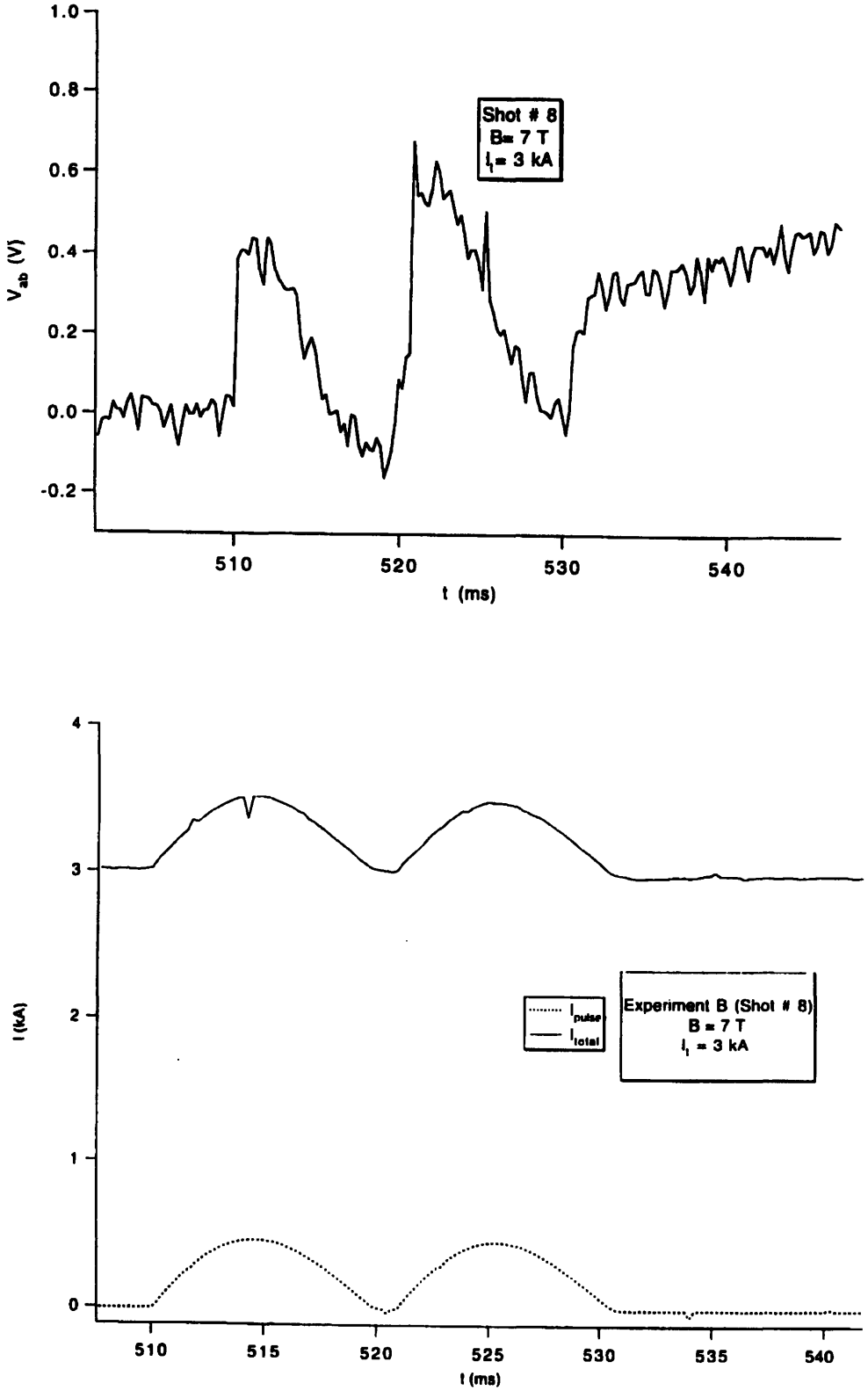

Figure 5-13: I_{pulse}, I_{total} and V_{AB} for shot # 8 showing the characteristic signal shapes around the pulses.

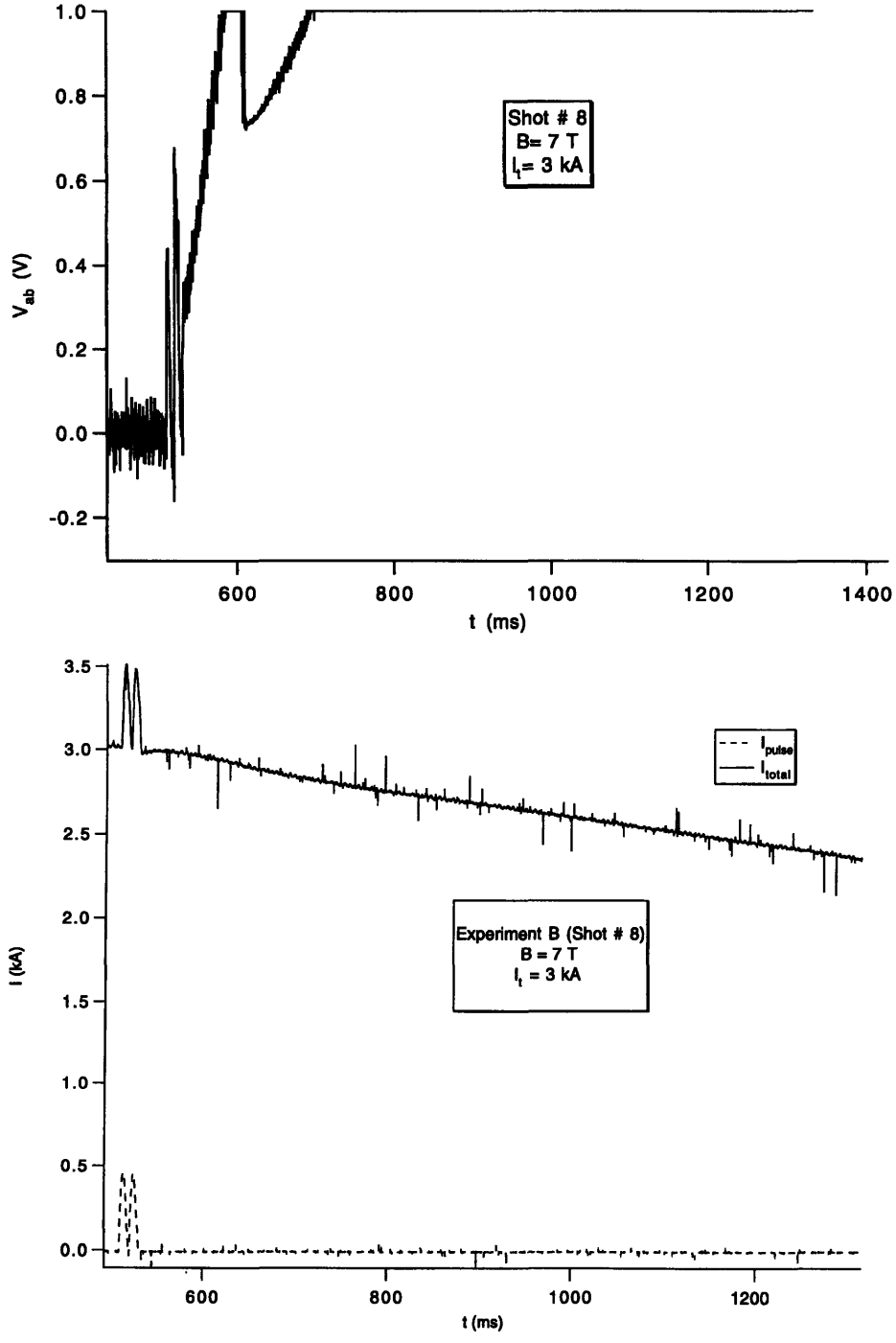

Figure 5-14: I_{pulse}, I_{total} and V_{AB} for shot # 8 showing quench development.

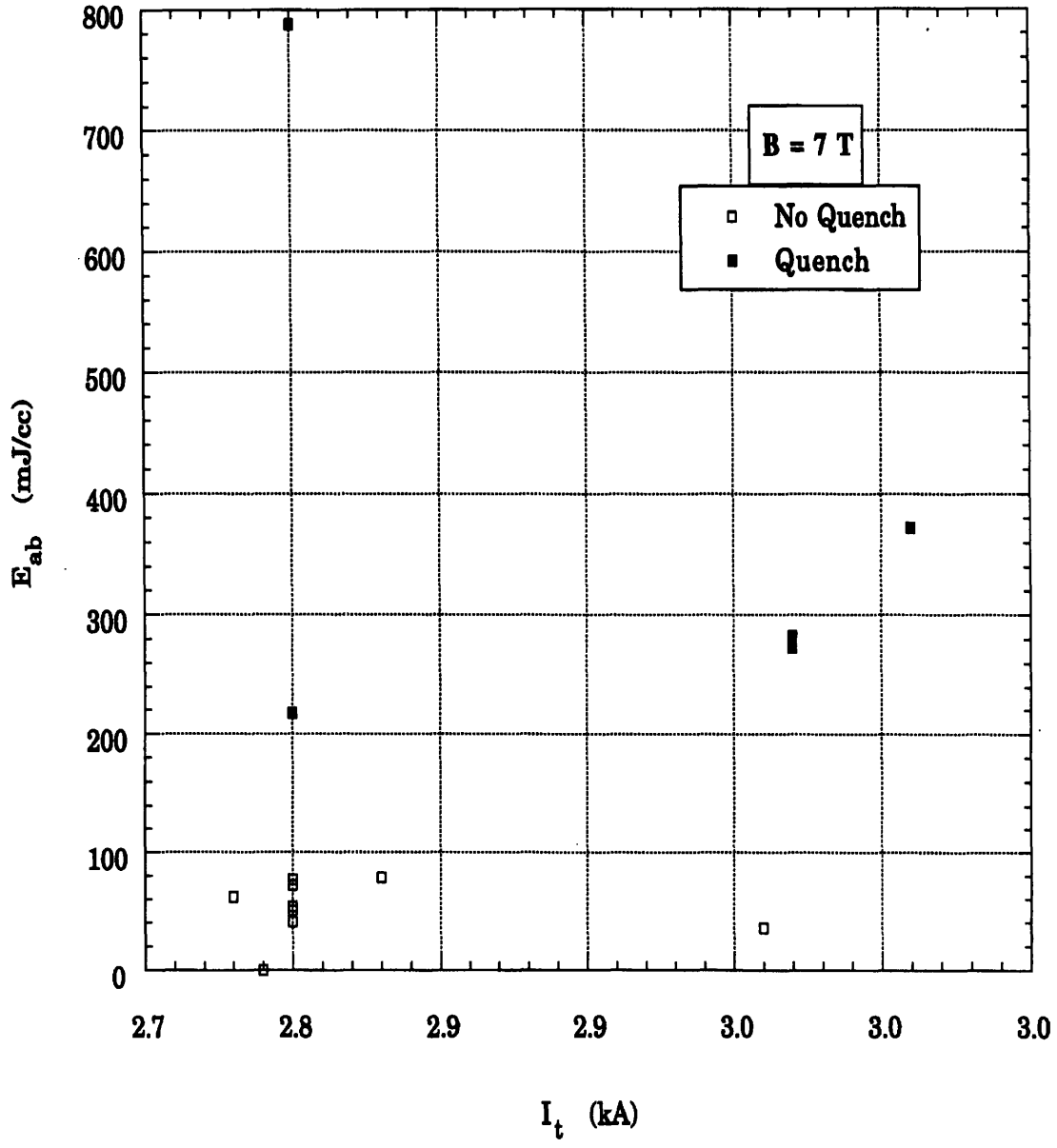

Figure 5-15: Stability margin of TPX sample.

reproduced below

$$\Delta H = \frac{A_{He}}{A_{cable}} \int_{T_b}^{T_{cs}} c_p dT. \tag{5.11}$$

As elucidated in Chapter 3, the stability margin is bounded by the available helium enthalpy in the well-cooled region and by the cable enthalpy in the ill-cooled region. Strictly speaking, these are the upper and lower bounds of the margin, since a disturbance will always produce some joule heating and the helium will have to remove the resulting heat in addition to the disturbance energy. Similarly, on the ill-cooled side, there will always be some heat taken away by the helium even with the low heat transfer coefficient of the vapor blanketed strands. But these limits were calculated first to get an idea of the bounds of the stability margin.

5.5.1 Ill-cooled Region: Cable Enthalpy

The cable material in a CICC conductor consists of many different elements besides the superconductor including stabilizing copper and hybrid strands possibly. The cable enthalpy available, per unit volume of the cable, with adiabatic heating to the current sharing temperature, can be given by

$$\Delta H(J/m^3) = \sum_{i=1}^{n} \int_{T_{op}}^{T_{cs}} f_i \, \rho_i \, c_{p_i} \, dT_i \tag{5.12}$$

where f_i is the fraction of the ith material by volume in the cable, ρ_i is its density, c_{p_i} is its specific heat at constant pressure, and T_i is its temperature. With all cable material in the solid state, an isobaric process was considered.

The conduit was ignored in the calculation of cable enthalpies under the assumption that the heat diffusion time to the conduit is much greater than the pulse duration. The cable enthalpy is usually 2-3 orders of magnitude lower than the helium enthalpy.

5.5.2 Well-cooled Region: Helium Enthalpy

Helium enthalpy as given by Eq. 3.1 is usually applied to supercritical helium, which does not go through a phase change during its traversal to the current sharing temperature. The situation in both experiment A and experiment B involved a phase change at 4.22 K and 1 atmospheric pressure. This is because the samples were just sitting inside a liquid helium bath at 1 atm in an open-ended conduit. Since no information about the localized pressure or temperature inside the conduit was available in the experiments, a simple model of enthalpy change with only modest assumptions was constructed.

The experimental situation can be visualized as shown in Fig. 5-16. The cable is considered to be immersed in liquid helium at saturated liquid conditions. Any heat absorbed will first be used in the phase change of helium, and if the energy deposition is large enough, the helium will superheat. Only then will the temperature rise above the bath temperature of 4.2 K. If superheating continues till the current sharing temperature T_{cs}, the stability margin will be completely used and joule heating will pursue. Since, the process is isobaric at 1 atm, the amount of helium available per unit length of the cable changes due to the huge change in helium density as it undergoes a phase change, which continues as it superheats.

This observation allows the helium enthalpy available per unit volume of the cable to be calculated as the sum of differential increases in enthalpy along the P = 1 atm line

$$\Delta H_{total}(J/cc) = \sum_i \frac{\Delta H_i\,(J/g)}{v_i\,(cc/g)} \tag{5.13}$$

where ΔH_i is the enthalpy change per unit mass during the ith interval and v_i is the specific volume of helium at the beginning of the interval. Because the major change in helium enthalpy per unit mass occurs at the phase change at 4.22 K, this region was divided into 1000 intervals [2]. The enthalpy change in helium from saturated liquid to saturated vapor was calculated to be 799.2 mJ/cc. The helium enthalpy and specific volume values were used in the range 4.224-13 K [85] were

[2] An increase to 10000 intervals changed the total volumetric enthalpy change by less than 0.2 %.

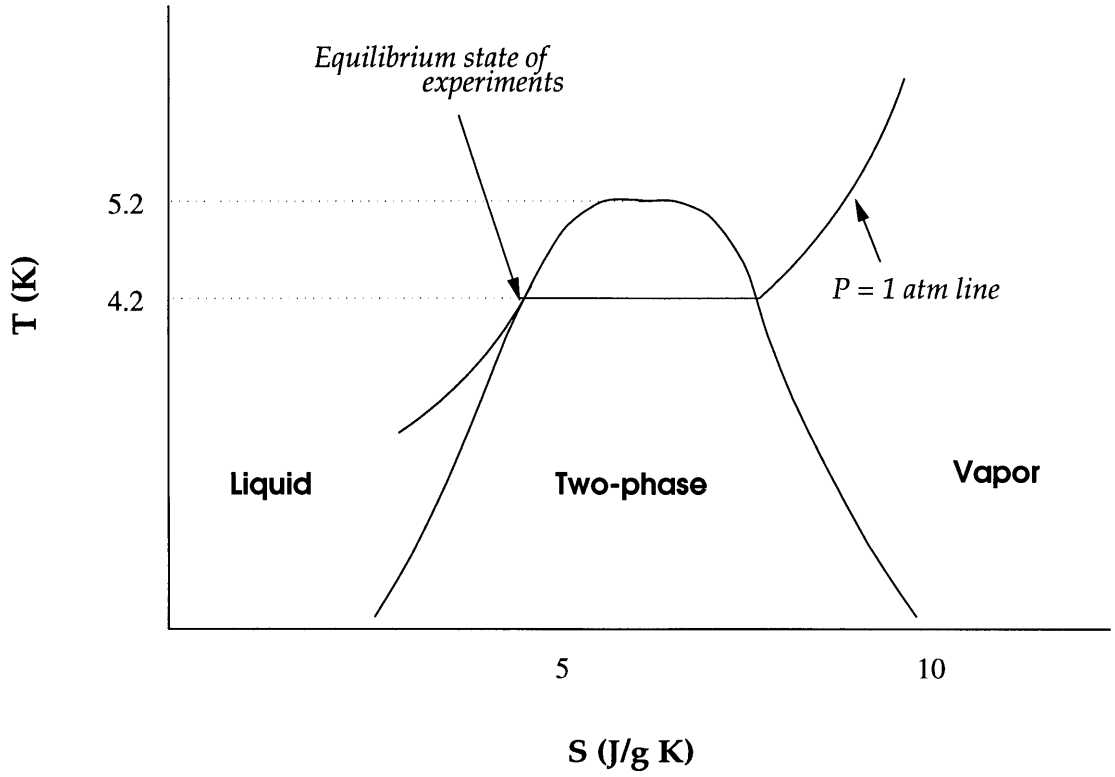

Figure 5-16: T-S diagram for helium showing the P = 1 atm line.

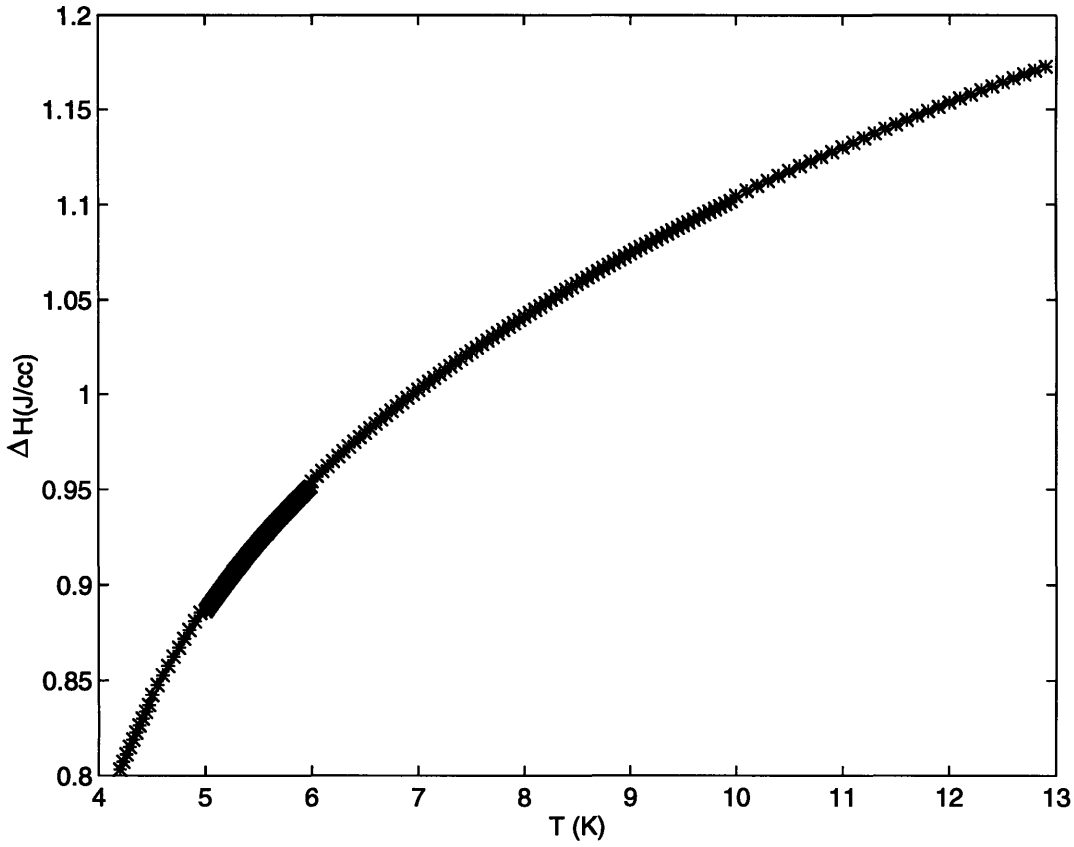

Figure 5-17: Available He enthalpy for helium initially in saturated liquid state.

linearly extrapolated. Based on these calculations, the total enthalpy change per unit volume from 4.2 K to a current sharing temperature in this range is plotted in Fig. 5-17. A seventh order polynomial curvefit to the calculated values is shown as well. The curve-fitted values were used in calculations.

5.5.3 Calculation of Current Sharing Temperature

To be able to determine the cable and helium enthalpies, it was essential to determine the current sharing temperature for the conditions at hand. In Chapter 2, a linear relationship between critical current density and temperature was proposed. Since critical current is is a strong function of magnetic field, temperature, and uniaxial strain ϵ, the linear relationship assumes the constancy of other variables. For

the US-DPC wire, Summers et al. [70] obtained a formula for these dependencies given by

$$J_c(B,T,\epsilon) = C(\epsilon)[B_{c2}(T,\epsilon)]^{-1/2}(1-t^2)^2 b^{-1/2}(1-b)^2 \quad (A/mm^2) \tag{5.14}$$

where

$C(\epsilon) = C_0(1-a|\epsilon|^u)^{1/2} \quad (AT^{1/2})$

$B_{c2}(T,\epsilon) = B_{c20}(\epsilon)(1-t^2)[1-0.31t^2(1-1.77lnt)] \quad (T)$

$B_{c20}(\epsilon) = B_{c20m}(1-a|\epsilon|^u \quad (T)$

$t = T/T_{c0}(\epsilon)$

$b = B/B_{c2}(T,\epsilon)$

$T_{c0}(\epsilon) = T_{c0m}(1-a|\epsilon|^u)^{1/w} \quad (K)$

$a = 900\ for\ \epsilon < 0,\ 1200\ for\ \epsilon > 0$

$u = 1.7$

$w = 3$

B_{c20m} = the maximum (strain-free) upper critical field (T)

T_{c0m} = the maximum zero-field critical temperature (K)

C_0 = the coefficient independent of field, temperature, and strain ($AT^{1/2}$)

ϵ = the uniaxial strain.

Takayasu et al. [73] successfully used this relationship to predict the critical currents of the US-DPC coil. Their parameters of the best fit were:

B_{c20m} = 27.5 T

T_{c0m} = 16 K

C_0 = 8800 $AT^{1/2}mm^{-2}$

while ϵ was varied. The same formula was used with the same parameters to curve fit the available data for the hybrid sample and the US-DPC test sample. In the above parameters, only ϵ is a function of cable fabrication, while the other ones

FIELD (T)	I_c per strand (A)†		
	Hybrid # 1	US-DPC Sample	TPX Sample
1	-	-	648
2	-	-	474
2.5	-	807.5	-
3	-	697.2	366
4	-	539.1	288
5	-	429.2	237.5
6	-	348.1	195
7	215	284.6	162
8	180	224.9	135
9	154	186.4	113.5
10	127	154.4	92.5
11	100	125.9	76
12	80	101.3	61.5

† based on measurements for the whole cable.

Table 5.4: Critical current measurements on the three sample CICCs.

are determined by the material properties of the superconductor. Since, the same superconducting material is used in all superconducting strands of the cables used, the given values were considered appropriate. Takayasu et al. used Incoloy 908 in their experiment as the conduit material. The conduit material used in the sample cables for experiment A was Incoloy 905, and for the TPX sample it was Incoloy 903, which are both closely related to Incoloy 908. Therefore, the value of ϵ was not expected to be very different. This provided some ease in curve-fitting the limited data available on the field and critical current relationships of the sample cables [33, 71]. The data is shown in Fig. 5-18. The critical current values used from the data are listed in Table 5.4.

The available critical current data for a single strand from 27 strand cable measurements is shown in Fig. 5-18. Based on this figure, the values used to establish the relationship between current and temperature are given in Table 5.4.

The resulting curve fits for the two samples are shown in Fig. 5-19. The hybrid sample data did not fit perfectly but the error margins were considered within limits. The intrinsic strain value were $\epsilon = -.0059$ for the hybrid sample and

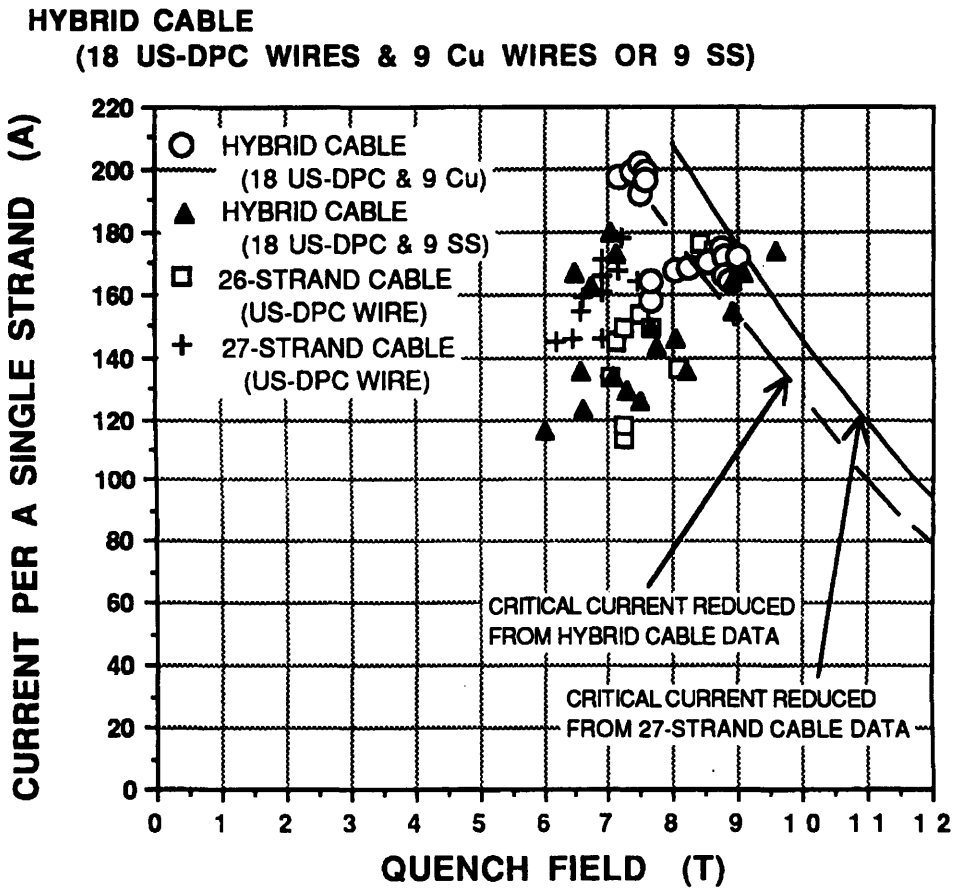

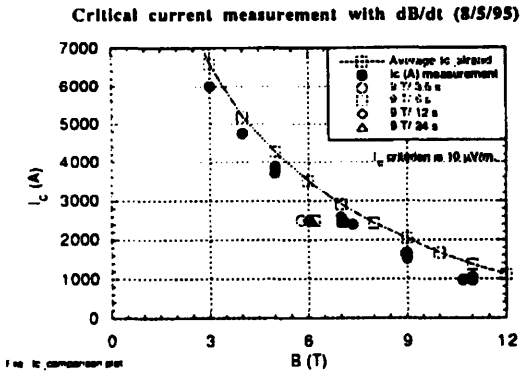

Figure 5-18: Data from critical current measurements done on the three cables: Samples used in experiment A (top) and sample used in experiment B (bottom). (Courtesy of M. Takayasu and S. Jeong.)

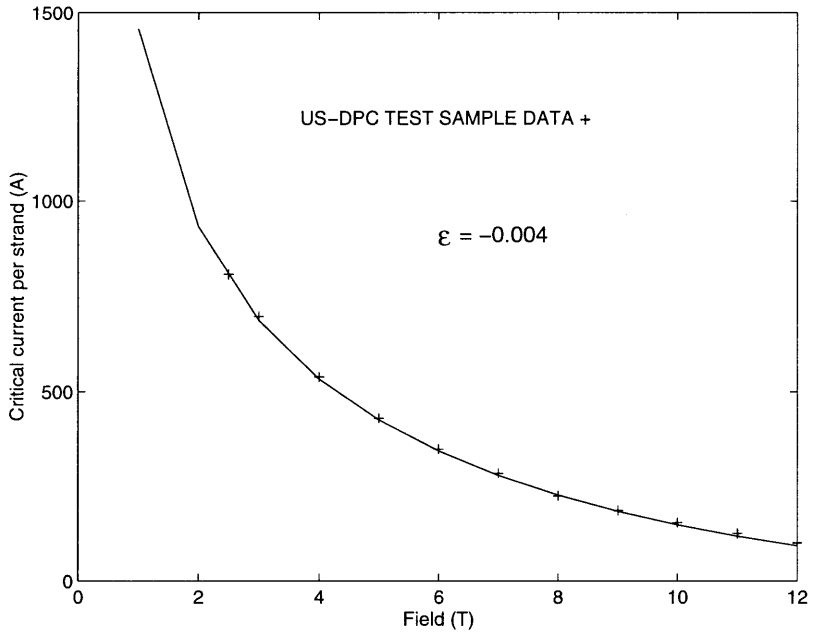

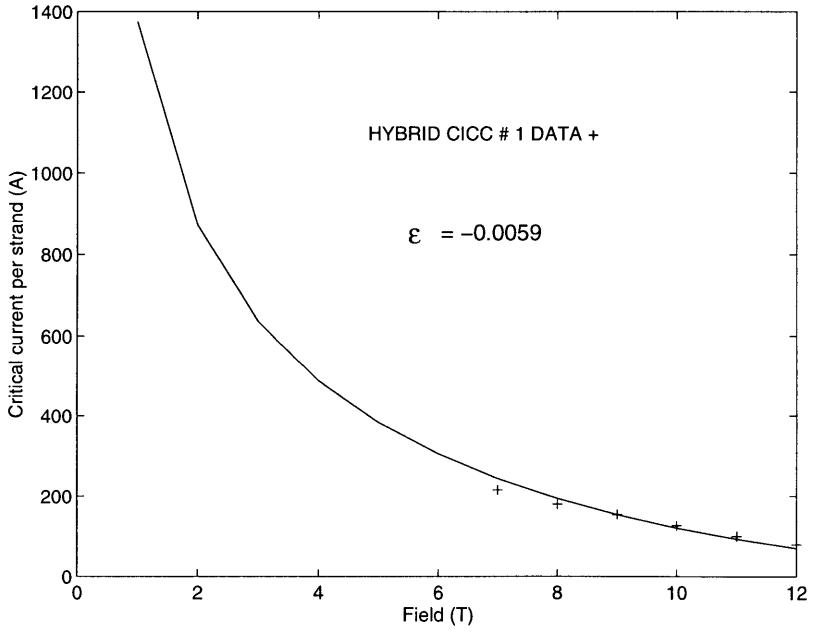

Figure 5-19: The curvefits to the critical current measurement data for: US-DPC data (top); Hybrid cable data (bottom).

$\epsilon = -.004$ for the US-DPC sample cable. Eq. 5.14 gives the current density per unit area of superconductor, hence the correct multiplication factors were used based on Table 4.1 to get the current per strand. The resulting values of intrinsic strain were used to get critical current density as a function of temperature.

5.5.4 Comparison with Results from Experiment A

First, the critical temperatures are evaluated at B = 7 T for the hybrid cable and at B = 9 T for the US-DPC test sample. Since critical current densities are known at these fields for the respective samples, a linear dependence between current and temperature is established as originally proposed. The critical temperature is the temperature at which the critical current goes to zero. With the knowledge of the appropriate intrinsic strain values, Eq. 5.14 was used to determine this piece of information.

Fig. 5-20 shows the results. Both curves are mostly linear but curve a little towards the intersection with critical temperature. The critical temperatures recorded were:

- T_c (B = 7 T) = 11.7 K
- T_c (B = 9 T) = 10.6 K

Instead of using a linear fit, the values for current sharing temperature were calculated directly from the graph by expanding the relevant regions successively using Matlab.

The design specification of the US-DPC wire is as follows:

Stabilizing Copper Volume	46 vol.%
Non-Copper Volume	54 vol.%
Filament	22.9 vol.%
Copper	48.8 vol.%
Tin	15.8 vol.%
Vanadium	12.6 vol.%

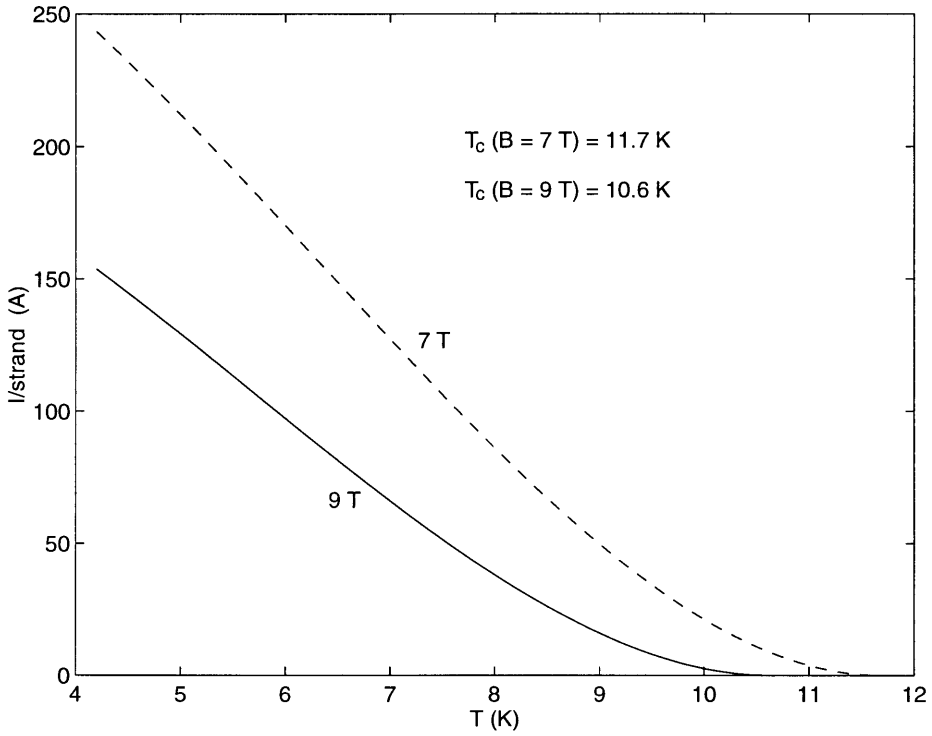

Figure 5-20: Current in a US-DPC superconducting strand as a function of temperature.

Temperature (K)	Copper Enthalpy (J/kg)
4	0.13
6	0.44
8	1.12
10	2.4

Table 5.5: Enthalpy of copper at low temperatures.

This implies that, in terms of volume, copper and superconductor makes almost 87 % of the cable. Because, they do not occupy much volume overall, the heat capacity of tin and vanadium was not calculated but was approximated by that of copper instead. Therefore, by volume, the superconducting filaments make about 10 % of the total superconducting strand. Helium volumetric enthalpy is shown in Fig. 5-17 while the copper enthalpy is available from the literature review by Corruccini and Gniewek [19] [3]. The values used for copper enthalpy are listed in Table 5.5. A linear interpolation was used between the given values. The enthalpy calculation for stainless steel used the specific heat correlation given by Brechna [12, p. 421]

$$c_{pSS}(J/kg.K) = 0.464\,T + 3.8 \times 10^{-4} T^3 \quad (T < 10K). \tag{5.15}$$

This was used for the stainless steel in the hybrid cable. For the US-DPC sample cable the total current was divided by 27 to get the current per strand for use in T_{cs} calculation, while for the hybrid sample the number was 18. The results for I_t in the ill-cooled region for both samples are given in Table 5.6.

The volume percentages of the materials in the cable part of the CICCs are 33.73 % stainless steel, 66.2 % copper and 6.98 % Nb_3Sn for the hybrid cable and 10.5 % Nb_3Sn and 89.47 % Cu for the US-DPC sample cable. The copper percentages include the vanadium and tin contributions.

The densities of the three materials used were:

$$\rho_{Nb_3Sn} = 8910 \text{ kg/m}^3$$

[3] Courtesy of J. Shultz

Hybrid Sample # 1 (B = 7 T) $f_{Cu} = 0.662$; $f_{Nb_3Sn} = 0.07$; $f_{SS} = 0.337$			
I_t (kA)	I_{strand} (A)	T_{cs} (K)	ΔH_{cable} (mJ/cc)
2	111.11	7.384	27.87
2.5	138.88	6.728	20.94
3.0	166.66	6.082	13.91
US-DPC Sample (B = 9 T) $f_{Cu} = 0.895$; $f_{Nb_3Sn} = 0.105$			
2.5	92.59	6.152	3.81
3.0	111.11	5.570	1.69
3.5	129.63	4.988	0.81
4.0	148.15	4.386	0.15

Table 5.6: Cable enthalpies for varying transport currents in the ill-cooled region.

ρ_{SS} = 7900 kg/m^3

ρ_{Cu} = 8950 kg/m^3

An important thing to note is that the calculated critical current value for the US-DPC sample cable by projection of the critical current value for a single strand was I_c (B = 9 T) = 4.15 kA, but the transport current I_t was greater than this value by roughly 13% in shots # 2781-2783.

Cable enthalpies go down quickly with a decrease in current sharing temperature and the differences with the experimentally observed stability margin increases with decreasing T_{cs}. The cable enthalpies only define a lower limit, and due to finite helium boiling and possible conduit participation in heat transfer the actual ill-cooled stability margin is higher than the available cable enthalpy, the results are different by an order of magnitude at low current sharing temperatures. At high current sharing temperatures, higher than 6 K, the cable enthalpies are three times smaller than the experimentally calculated stability margin. The wire enthalpy values for the hybrid cable are in better agreement with the experimental values because of the inclusion of the enthalpy of the stainless steel wires. Without this inclusion, the numbers are very low again for total wire enthalpy because the high heat capacity of stainless steel is not available. The availability of stainless steel

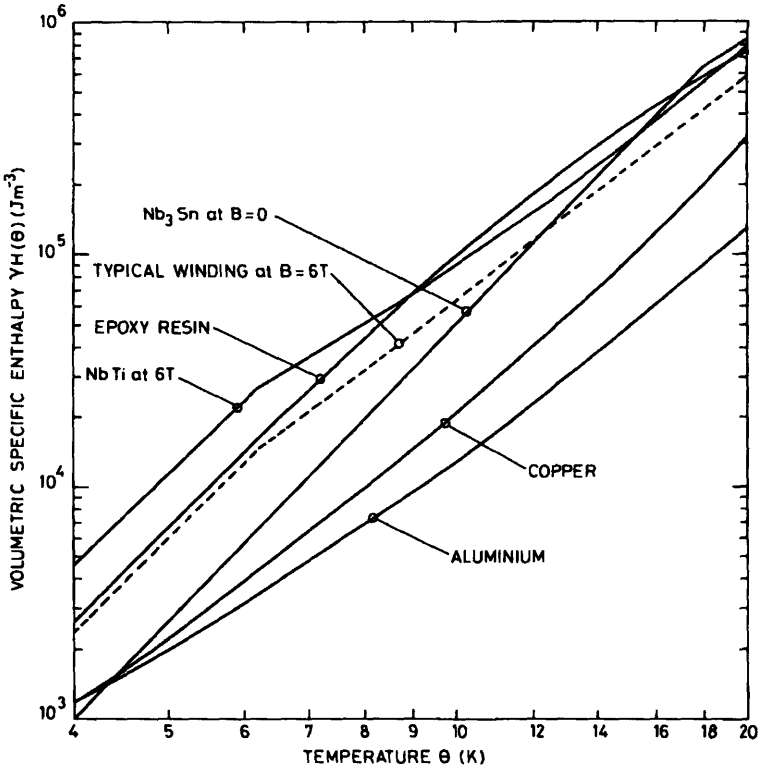

Figure 5-21: Volumetric heat enthalpy of Nb_3Sn.

strands is made more questionable by noticing that in the two cables the calculated energy margins in the ill-cooled regions are comparable if only the superconducting strands are used for the volume calculations. (See Fig. 5-10 and Fig. 5-9).

The stability margins for the well-cooled region were calculated for the US-DPC test sample in the possibly well-cooled region at the transport currents of 0.5 kA and 1.0 kA and the results are:

- Available helium enthalpy ($I_t = 0.5\,kA$; $T_{cs} = 8.86\,K$) = 1074.5 mJ/cc
- Available helium enthalpy ($I_t = 1.0\,kA$; $T_{cs} = 8.04\,K$) = 1044.0 mJ/cc

These values are in good agreement with the trend shown by values computed by the direct method.

The resistivity of copper ρ_{Cu} at 9 T with an RRR value of 403 can be calculated

by

$$\rho(B) = \frac{\rho(B = 0,\ T = 300\,K)}{RRR} + \beta_M B(\Omega.m) \tag{5.16}$$

with $\beta_M = 4.8 \times 10^{-11}$ (Ω. m). The calculated resistivity using $\rho(B = 0,\ T = 300\,K) = 1.7 \times 10^{-8}$ Ω.m is $\rho = 4.742 \times 10^{-10}$ Ω.m. Assuming an I_{lim} of about 1.5 kA for the US-DPC sample, the value of the effective heat transfer coefficient was (using Eq. 3.2)

$$h_e\,(US - DPC\ Test\ Sample) = 361.9\,W/m^2K \tag{5.17}$$

It is fairly low. The effective heat transfer coefficients achieved with supercritical helium can indeed be much higher (See Table 3.2). However, if the upper limiting current value of 2.5 kA is used, the effective heat transfer coefficient becomes 1025.3 W/m^2K.

There was no data available for the critical temperature measurements of the TPX hybrid sample. Without information about current sharing temperatures, the comparisons made with data from experiment A could not be made for experiment B.

The resistive losses are compared with the self-field losses in Chapter 6.

Chapter 6

Self-field Losses

6.1 Introduction

The issue of self-field losses was introduced in Section 1.1.3. It was implied in their introduction that these losses are usually negligible compared to other AC losses due to time-varying fields. Self-field losses are produced by the time-varying field associated with a time-varying transport current current. In essence, the hysteresis losses and coupling losses incurred by the time-varying field of due to the transport current in the conductor are defined as self-field losses. The energy dissipation calculated in the experiments was delivered to the sample from external sources, that is, the DC current power supply and the pulsed current power supply. The losses due to self-field effects, if any, were not computed. The real stability margins should be higher by the amount of self-field losses induced by the pulse. It was assumed that these losses were negligible and therefore the stability margins evaluated without including them in the calculations were close to their true value. The validity of this assumption is tested in this chapter and thereby, the issue of self-field losses is resolved.

6.1.1 Self-field Instability

As previously discussed in Section 2.1.2, coupling losses are highly reduced for multifilamentary composites by twisting, but it is completely ineffective for the self-field case. The conductor tries to shield itself from the field produced by virtue of the transport current by having it flow as near to the surface of the conductor as possible. The field produced by the conductor is in concentric shells around the conductor.

The current shielding the conductor flows in an outer sheath of the conductor at the critical current density J_c and the penetration depth of the sheath is just as much as is required by the transport current. The rest of the conductor is field-free and is therefore shielded from the self-field of the conductor. Another way to look at the situation is in terms of circuit theory. The filaments on the outside have a lower inductance and therefore current preferentially flows in them.

The reason why twisting is not effective in this case is that the self-field flux linkage of the inner and outer filaments is independent of twisting and due to the long length of wires, the time constant of field decay through the matrix resistance is on the order of decades for wires a few kilometers long, as calculated by using Eq. 2.21. Hence, the decay is almost non-existent and the self-field effects in composite superconductors and normal wires are almost identical.

Fig. 6-1 shows the current and field profile of a multifilamentary composite.

Assuming the current flows in the superconducting filaments in outer sheath at the critical current density J_c, the actual density becomes λJ_c for this region with λ as the filling factor or the ratio of superconducting filaments in the composite volume. As the figure suggests, the current-free region extends to the radius $r = c$ and the radius of the composite wire is a. Using Ampere's law for a loop at radius r in the composite with $c < r < a$ the field becomes

$$B(r) = \frac{a}{r}B_0 - \frac{\mu_0 \lambda J_c}{2r}(a^2 - r^2) \tag{6.1}$$

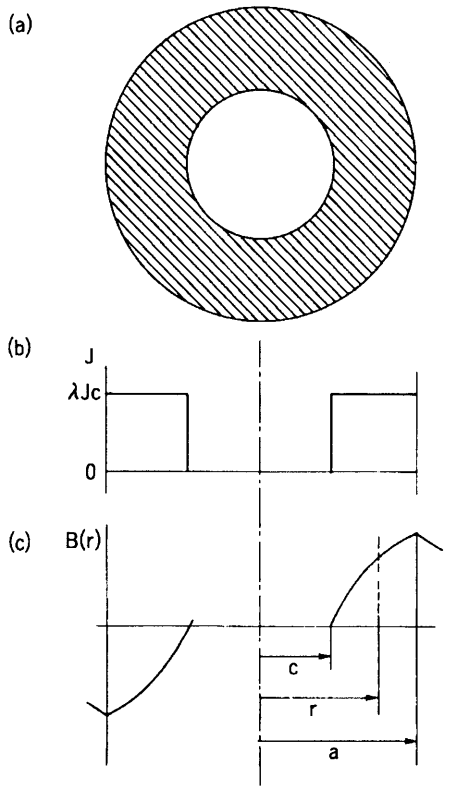

Figure 6-1: Self-field effect in a composite wire: (a) and (b) distribution of the transport current; (c) variation of the self-field.

where

$$B_0 = \frac{\mu_0 I_t}{2\pi a} \tag{6.2}$$

is the magnetic field at the surface which will change with a time-varying I_t. To get an idea of the stability of self-field, I_t can be assumed constant, so that B_0 is constant as well.

Once again, first the flux change seen by circular ring at radius r is calculated due to a change ΔJ_c in critical current density as a result of a slight temperature increase due to heat deposition ΔQ_s.

$$\delta\phi(r) = \int_c^r \Delta B(r)\, dr = \frac{\mu_0 \lambda \Delta J_c}{2} \int_c^r (\frac{a^2}{r} - r) dr = \frac{\mu_0 \lambda \Delta J_c}{2} (a^2 ln\frac{r}{c} - \frac{r^2}{2} + \frac{c^2}{2}) \tag{6.3}$$

The radius of field penetration is given by $c = \lambda J_c \pi (a^2 - c^2)$. This change in flux dissipates energy in the composite wire given per unit volume of cable by [79]

$$\Delta Q = \frac{1}{\pi a^2} \int_c^a \delta\phi(r)\, \lambda J_c 2\pi r dr = \mu_0 \lambda^2 J_c \Delta J_c a^2 (-\frac{1}{2} ln\epsilon - \frac{3}{8} + \frac{\epsilon^2}{2} - \frac{\epsilon^4}{8}) \tag{6.4}$$

where $\epsilon = c/a$. Substituting for ΔJ_c using Eq. 2.34 and establishing heat balance implies

$$\Delta Q_s + \frac{\mu_0 \lambda^2 {J_c}^2 a^2}{(T_c - T_{op})} \Delta T (-\frac{1}{2} ln\epsilon - \frac{3}{8} + \frac{\epsilon^2}{2} - \frac{\epsilon^4}{8}) = \gamma C \Delta T \tag{6.5}$$

where γ is the density and C is the specific heat. The dissipation reduces the effective specific heat $\Delta Q/\Delta T$ which will go to zero resulting in flux jumps if

$$\beta_s = f_1(i) = \frac{\mu_0 \lambda^2 {J_c}^2 a^2}{\gamma C (T_c - T_{op})} = \frac{1}{(-\frac{1}{2} ln\epsilon - \frac{3}{8} + \frac{\epsilon^2}{2} - \frac{\epsilon^4}{8})} \tag{6.6}$$

The self-field stability parameter β_s is plotted in Fig. 6-2 as a function of $i = I_t/I_c = (1-\epsilon^2)$. Unlike the stability parameter for screening currents to external fields with $\beta = 3$ as calculated in Section 2.2.1, β_s varies over a wide range. This is a result of assuming that the heat generation is shared by the matrix material. If that were not the case, as in the case of a high resistance, low thermal conductivity matrix

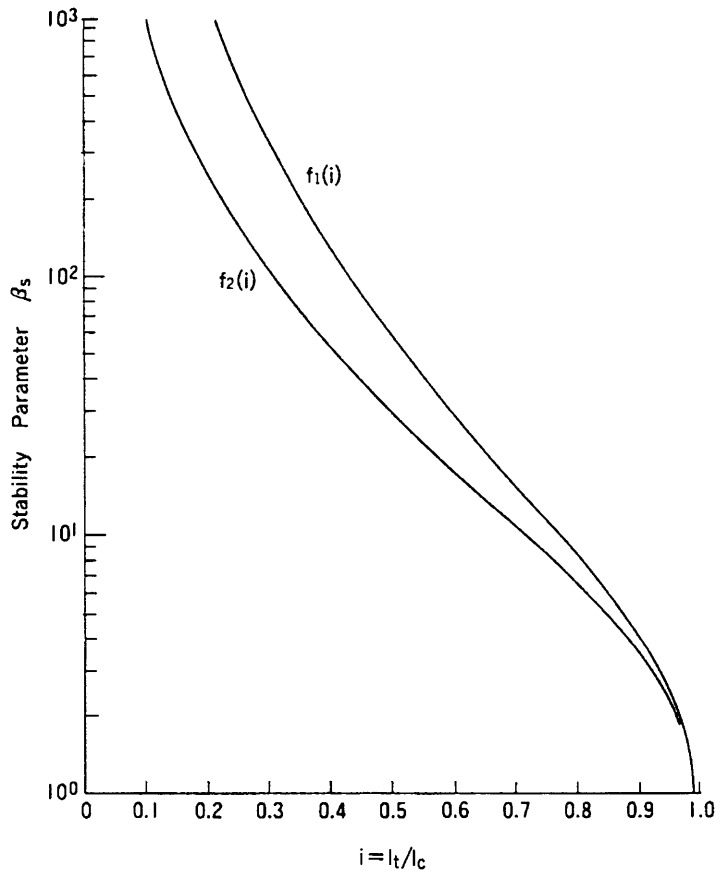

Figure 6-2: Self-field stability parameters as a function of i = I_t/I_c.

materials, the adiabatic condition is applied. This makes heat generation larger by a factor of $a^2/(a^2 - c^2)$ and the stability parameter becomes

$$\beta_s = f_2(i) = \frac{\mu_0 \lambda^2 J_c^2 a^2}{\gamma C(T_c - T_{op})} = i \,.\, f_1(i) \tag{6.7}$$

In contrast with the stability parameter of simple screening currents, β_s goes to zero at operating currents near the critical current or for $i \to 1$. This is due to the imposed condition of the transport current I_t remaining constant [57]. Simple screening currents do not stay constant during a disturbance but decay with an increase in temperature, thereby allowing for the restoration of the superconducting state at a higher temperature.

6.2 Self-field Losses in Multifilamentary Composite

The criterion for stability against self-field induced flux jumps at constant transport current was derived as the stability parameter β_s in Section 6.1.1. The fields due to a time-varying transport current induce AC losses, which occur even if the background external field is constant in time. The self-field for a cylindrical wire takes the form of concentric circles as shown in Fig. 6-3 (a). The field magnitude is directly proportional to the transport current in the wire and increases or decreases with a rise or fall in transport current. This implies that these concentric lines of force move in and out of the cylinder with a time-varying transport current, and thus dissipate energy.

The transport current flows in an outer sheath at the surface of the wire, to screen the inside of the wire from the field produced, and occupies an area just enough to carry the transport current at the critical current density. As the transport current is increased, the required area for this sheath is increased, and the inner edge of the sheath moves deeper into the cylinder, thus allowing the field to penetrate more of the cylinder. For a single strand, whether solid or of composite superconductor, whether twisted or not, the distribution of transport current and self-field is almost identical for reasonable time scales , and there is no transverse field change. The losses are therefore dependent on the level of penetration of field and the number of cycles but not the frequency. They are hysteretic.

In Fig. 6-3, the field profiles for the case of reversing transport current oscillations and unidirectional oscillations is shown. The field amplitude for full penetration can be only defined for reversed oscillations and is just twice the field at the surface when the current-carrying sheath envelops the whole conductor cross-section

$$B_{ps} = \mu_0 \lambda J_c a \tag{6.8}$$

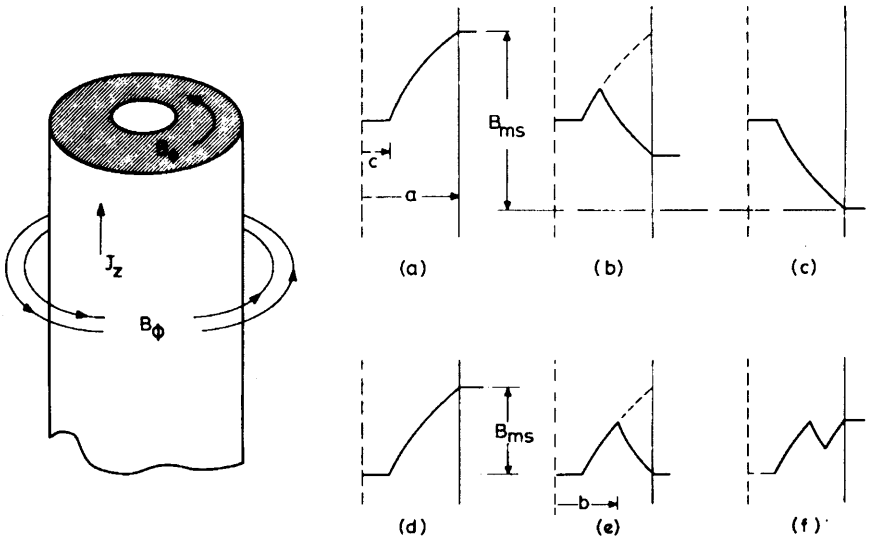

Figure 6-3: Self-field in a filamentary composite with transport current: (a), (b), and (c) show profiles for **B** within the wire for bidirectional oscillations when the field is reversed; (d), (e), and (f) show the effect for a unidirectional oscillations.

If the maximum field change in a cycle is B_{ms} then the loss factor becomes

$$\beta = \frac{B_{ms}}{B_{ps}} = \frac{I_t}{I_c} = i \tag{6.9}$$

and the loss per unit volume per cycle is given by

$$Q = \frac{4}{\pi a^2}\int_c^a 2\pi r\lambda J_c \Delta\phi(r)dr = \frac{4\mu_0\lambda^2 {J_c}^2}{a^2}\int_c^a \frac{r^3}{2} - \frac{c^2 r}{2} - c^2 r ln\frac{r}{c}dr, \tag{6.10}$$

which becomes [79, p. 196]

$$Q = \frac{{B_{ms}}^2}{2\mu_0}[\frac{2}{\beta} - 1 + \frac{2(1-\beta)}{\beta^2}ln(1-\beta)] = \frac{{B_{ms}}^2}{2\mu_0}\Gamma(\beta). \tag{6.11}$$

If the transport current excursion is unidirectional then a full penetration field cannot be defined since the field does not penetrate to the center. The loss factor is

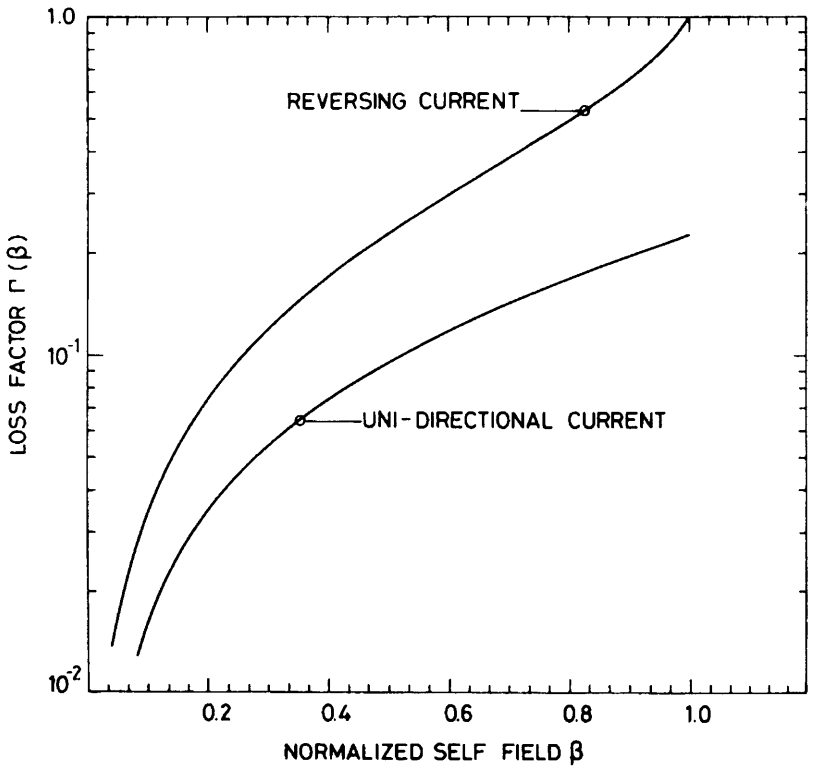

Figure 6-4: Self-field loss factor in a filamentary composite carrying a transport current which undergoes either reversed or unidirectional oscillations.

defined again as the ratio $\beta = I_t / I_c$ and becomes [79, p. 196]

$$Q = \frac{{B_{ms}}^2}{2\mu_0}[\frac{4}{\beta} - 1 + \frac{4(2-\beta)}{\beta^2} ln(\frac{2-\beta}{2})] = \frac{{B_{ms}}^2}{2\mu_0}\Gamma(\beta). \tag{6.12}$$

Eq. 6.11 and Eq. 6.12 are plotted in Fig. 6-4. In the case of unidirectional oscillations, the losses are much reduced compared to the bidirectional case because of the lower total field change. As seen in Fig. 6-4 (e) the currents below $r = b$ are oblivious to the field change during each cycle.

In pulsed magnets made out of solid wires, the self-field losses are negligible compared to other AC losses because the self-field is so much smaller than the background field. But with filamentary composites, when the other losses have been reduced by subdivision i.e. making superconducting filaments of a very small

diameter, the self-filed losses can be large. Eqs. 6.11 and 6.12 along with Eq. 6.8 show that the self-field losses are proportional to the square of the strand diameter which is why strand diameters for filamentary composites tend to be less than a millimeter.

6.3 Extension of Self-field Loss Model to CICCs

In CICCs, a large number of strands have to be cabled together for achieving the high operating currents desired. The way these strands are cabled together takes self-field losses as an important determining factor. If these cables were twisted in a simple manner, that is all the strands were just twisted together with a pre-determined twist pitch with the strands on the outside always staying on the outside, and the strands on the inside always staying on the inside, the whole cable would act as a single strand with the diameter of the cable, thus making the self-field losses unacceptably large. Therefore, the method used to twist the cable inside a CICC must ensure that the strands are fully transposed.

A twisting of the cable similar to the twisting in the multifilamentary composite is required to keep the coupling losses low. As with the coupling losses in a single filamentary composite, the transverse resistivity determines the exact amount of loss. In the case of a multi-strand cable, a treatment similar to the multifilamentary composite can be applied by treating the strands in a similar fashion to the filaments in the composite. The cable transverse resistivity can be a complex function of the cabling methodology and is clearly a function of how tightly packed are the wires inside the conduit. It is usually found experimentally.

In general, calculating self-field losses in a CICC is a complex matter and depends on the multi-stage twist pitches, the transverse conductivity, and the degree of transposition achieved while cabling. All three sample CICCs used in the experiments were prepared in three-stages as a $3\times 3 \times 3$ cable based on triplets. The average twist pitches at the three stages were [1]:

[1]based on hybrid sample 1

- the triplet stage: 51 mm (2.01")
- the 3 × 3 stage: 102 mm (4.02")
- the 3 × 3 × 3 stage: 136 mm (5.35")

The twist direction was clockwise (or right-handed).

6.4 Calculations

The calculations based on experiment A are presented. Since, the motivation of these calculations was to determine how self-field losses compared with the measured resistive losses, it was considered adequate to compare the results for experiment A only.

6.4.1 Self-field Losses in US-DPC Test CICC

The self-field loss calculations primarily stresses on calculating the two major self-filed AC loss mechanisms at work in this particular situation. The hysteresis loss situation was changed due to the presence of background magnetic field. The hysteresis loss calculation in Eq. 6.11 and 6.11 assume a zero background magnetic field. At a DC field, the loss for small deviations in field around the operating point has to produce lesser hysteresis loss, because as seen in Fig. 1-5, the area enclosed in the hysteresis curve is smaller. This calculation therefore serves as a bound. The coupling losses occur on two levels, the strand level due to coupling between the superconducting filaments, and on the cable level, due to the coupling between the strands. The coupling on the strand level and on the cable level, both will be due to the same field change, due to the transverse field created by the single turn CICC shaped as a solenoid. The maximum field change is used to determine an upper limit. The coupling losses on the cable level are calculated in a similar fashion.

As these losses are compared eventually to resistive losses it is advisable to carry out the comparison for points around the stability margin boundary for the highest

levels of operating current. Far away from the stability margin, the resistive losses may be nearly zero, and a comparison would surely be unnecessary. The individual in the highest ranges are computed for each type of loss and the maximum of each type of loss is compared as a ratio to the resistive losses for the corresponding calculations. The only restriction was to use shots in which the sample did not quench, because in the event of a quench the resistive losses increase appreciably.

Hysteresis Losses

Consider the stable case of shot # 2780 [2] with an operating current to critical current ratio of

$$\beta = \frac{I_t}{I_c} = \frac{3.765kA}{5.033kA} = 0.748 \tag{6.13}$$

which gives, from Fig. 6-4, an associated loss factor value of

$$\Gamma(\beta = 0.748) \sim 0.15 \tag{6.14}$$

The maximum field value for the field which is time varying is given by the pulsed field produced at the peak of the pulse. Using the peak pulse value in $B_m = \mu_0 I_p / 2\pi a$ with $a = 0.39\,mm$ and $I_p = 580/27\,A$ gives a maximum field of

$$B_m = 0.011\,T \tag{6.15}$$

which is indeed much smaller than the DC field. The hysteresis loss per strand is given by Eq. 6.12. The total loss for the cable becomes

$$\Delta E_{hys} = 0.975\,mJ/cc. \tag{6.16}$$

and

$$\frac{\Delta E_{hys}}{\Delta E_{res}} = 1.37\% \tag{6.17}$$

[2] This shot was chosen because of its high transport current to get a higher loss factor

For the hysteresis losses due to a high pulsed current instead, consider shot # 2794 with $I_t = 1.47\,kA$ and $I_p = 2.608\,kA$. A similar calculation gives

$$\Delta E_{hys} = 0.0586\,mJ/cc. \tag{6.18}$$

and

$$\frac{\Delta E_{hys}}{\Delta E_{res}} = 1.4 \times 10^{-6}\% \tag{6.19}$$

These calculations have not included the effects of the transport current. Even with a maximum possible transport current equal to I_c, these losses will only increase by a factor of two. These results imply that the hysteresis losses on the strand level are not an issue.

6.4.2 Coupling Losses

The two forms of coupling losses, that is coupling within the filaments of a strand and the coupling between strands, were calculated separately. However, to the first order, the strands and the cable as a whole, see the same transverse field, created by the single-turn current loop effect of the sample cabling. This transverse field is time-varying due to the pulsed current. The transverse field was approximated by a current loop and the maximum value of the field physically on the cable was used for the whole cable. The ratio of cable radius to loop radius $a\,/\,r = 0.04$ implies that the current loop approximation is valid.

Assuming the loop is in x-y plane, with its center at the origin, the solution to the two possible transverse fields are the radial field B_r and the field normal to the loop B_z given by [79, p. 38]

$$B_r = \frac{\mu_0 I}{2\pi}\frac{z}{r}\frac{1}{[(a+r)^2+z^2]^{\frac{1}{2}}}[-K(k) + \frac{a^2+r^2+z^2}{(a-r)^2+z^2}E(k)] \tag{6.20}$$

and

$$B_z = \frac{\mu_0 I}{2\pi}\frac{1}{[(a+r)^2+z^2]^{\frac{1}{2}}}[K(k) + \frac{a^2-r^2-z^2}{(a-r)^2+z^2}E(k)] \tag{6.21}$$

where

$$k = [\frac{4ar}{(a+r)^2+z^2}]^{\frac{1}{2}} \tag{6.22}$$

and K(k) and E(k) are the complete elliptic integrals of the first and second kind given by

$$K(k) = \int_0^{\pi/2} \frac{d\theta}{(1-k^2 sin^2\theta)^{\frac{1}{2}}} \tag{6.23}$$

and

$$E(k) = \int_0^{\pi/2} (1-k^2 sin^2\theta)^{\frac{1}{2}} d\theta. \tag{6.24}$$

Here, a is the radius of the loop, r is the distance in the x-y plane from the origin to the projection of the point on it where the field is evaluated. Also, $2\theta = \pi - \phi$ where ϕ is the angle of the projection in the x-y plane from the starting point of reference. In the plane of the loop, $z = 0$ and B_r reduces to zero. B_z is given by

$$B_z = \frac{\mu_0 I}{2\pi} \frac{1}{[(a+r)^2]^{\frac{1}{2}}} [K(k) + \frac{a^2-r^2}{(a-r)} E(k)] \tag{6.25}$$

The field on the loop will be maximum at the inside edge of the loop, at a small radius r_0 away from the assumed center of the filamentary loop. Hence, B_z is evaluated at $a = 0.047\,m$ and $r = 0.045$. This yields $k = 0.99952741$. Using integration tables, the values of K(k) and E(k) are approximately 4.85 and 1.0015. Using these values, B_z can be given as a function of the current through the loop at (r,z) = (0.043, 0):

$$B_z = 1.10558 \times 10^{-4} I \ \ (in\ A) \ \ \ (T) \tag{6.26}$$

Differentiating this gives us the time variation of the transverse field.

$$\dot{B}_z = 1.10558 \times 10^{-4} \dot{I} \ \ (in\ A/s) \ \ \ (T) \tag{6.27}$$

Coupling losses of the filament

Eq. 6.27 was used to compute the coupling losses. The losses were calculated for the case with the highest pulsed current and therefore, the highest value for field

change. An average value of $\dot{I}$ was taken for the whole pulse width of 2 ms given by

$$\dot{I} = \frac{2I_p}{t_p} \tag{6.28}$$

where t_p was 2 ms. Although, its direction reverses, the power dissipated is proportional to the square of $\dot{B}$.

Using Eqs. 2.17, 6.27 and 2.20, and using the values for the US-DPC sample cable with $\lambda = 0.46$, $L = 1.27\ cm$, and $\rho = 4.742 \times 10^{-10}\ \Omega.m$ the losses are calculated as

$$\Delta E_{cpl} = \bar{P} t_p. \tag{6.29}$$

Consider again shot # 2794. The filamentary coupling loss filaments evaluates to

$$\Delta E_{cpl} = 716.28\, mJ/cc \tag{6.30}$$

which is 123 % of the resistive losses calculated. The coupling losses are overestimated by the assumption of maximum field everywhere on the sample. The field in reality reduces inside the cable, reaches a zero value somewhere near the center of the cable and decreases further to a negative value at the outer edge lower than the maximum value. If the average value is one-half of the maximum field, the losses become one-fourth. These are still about 30 % of the resistive losses. In the case of the pulse width being 5 times as long for the same change in current, the losses are reduced to about 6 % of the resistive losses. Coupling losses on the strand level are a problem which needs to be looked at more carefully to fully determine if they can be neglected.

Coupling losses of the strands

In this case, the effective transverse resistivity was provided by Makoto Takayasu as $\rho_{eff} \sim 0.00016\ \Omega\, m$. Using a twist pitch for the third stage of 136 mm the losses are:

$$\Delta E_{cpl} = 0.243\, mJ/cc \tag{6.31}$$

which are negligible.

The transverse resistivity decreases at high fields and at higher transport currents but not by more than an order of magnitude, so these losses can be neglected.

This concludes the comparison. The self-field losses due to coupling at the filament level have to be investigated further before they can be considered negligible.

Chapter 7

Conclusions

Conclusions based on the experimental results shown in chapter 5 are presented here. The merits and demerits of the stability experiment using pulsed current disturbances are weighed against one another to ascertain its feasibility. The results of the experiments are summarized to support the ideas presented. Finally, recommendations are made for future work. The ways in which this experiment can be made more useful and an appealing alternative to other experimental methods for determination of stability of CICCs are discussed.

7.1 Feasibility of the Pulsed Current Stability Experiment

The determination of stability of CICCs is important for the success of the ITER magnets program because information about the stable or unstable behavior of these cables is essential to ensure safe and reliable operation of the magnets, which are comprised of these cables. The high current carrying capacity, structural integrity, low helium inventory and relatively low AC losses of CICCs makes them the leading choice for large-scale fusion applications. These cables are subjected to mechanical and electromagnetic disturbances during normal operation and it is important that they be stable to such disturbances.

Stability of test cables is analyzed by introducing a sudden energy input to the cable and then verifying whether this input results in quenching the conductor or not. Experiments for the calculation of the stability margin of CICCs have traditionally employed either a pulsed external field or a heater wire embedded in the cable to simulate the disturbances expected during regular operation. The pulsed current method for the same simulation was investigated as an alternative.

7.1.1 Pulsed Current Stability Experiment: Pros and Cons

From a review of the literature, it becomes clear that the dB/dt method for initiating a disturbance in the cable is widely used and the heater wire option is fairly common as well. The pulsed current method was evaluated as an alternative to these two methods and was found promising because of its many unique advantages. The parameters considered important for the success of a method for analyzing the stability of a cable are its ability to predict the available stability margin accurately and to simulate the disturbances likely to be encountered during the regular operation of ITER magnets. The complexity of the calculations required for the analysis and the intricacy of the setup and procedural details of the experiment itself enter the suitability perspective as secondary factors.

Uniform Distribution of Energy

Since stability limits are evaluated in terms of the allowable energy dissipation per unit volume of the cable, it is desirable that the energy introduced by the disturbance have some uniformity in its distribution. The pulsed field and the pulsed current method both have this advantage against the method of localized heating by a wire. The embedded heater deposits heat locally and depends on heat diffusion for disturbance energy propagation in the cable. Although longer heater wires may achieve some uniformity of heat deposition in the longitudinal direction, they are still non-uniform in the transverse direction. The embedded heater wire also takes away valuable space inside the conduit needed for helium flow. Another

problem with heaters is that the energy they produce may not deposit in the cable but directly boil off helium instead due to the non-uniform distribution. This will overestimate the true value of the stability margin. The pulsed field and pulsed current methods produce uniform energy deposition because they bring changes in variables which affect the whole volume of the cable, the background magnetic field in the case of the pulsed field method and the transport current in the case of the pulsed current method.

Circumvention of AC Loss Calculations

The calculation of AC losses is a formidable problem faced when using the pulsed field method. AC losses primarily consist of hysteresis and coupling losses on the filament level in a strand and on a strand level in a multi-strand cable. Calculation of AC losses needs an entire experiment just for calibrating these losses, calculated by calorimetric methods usually, against different values of pulsed field. In the bench mark AC loss tests done for ITER over the past few years, the discrepancy in results has been about 50 % [72] or more. Analytical calculations of AC losses suggest that they are strongly dependent on cable parameters such as twist pitch, matrix transverse resistivity, contact resistance between strands etc. and on field parameters such as orientation and time-variation. All these factors combine to make the calculation of AC losses an experimentally challenging problem. The pulsed current method avoids the calculation of most forms of AC losses due to the fact that the sample and the source of pulsed current are not magnetically coupled. The self-field loss due to the changing self-field in the cable due to its time-varying transport current needs to be calculated though.

Simplicity of Dissipated Energy Calculation

The calculation of resistive energy dissipated inside the cable due to pulsed current is a very simple calculation. The current and voltage measured in the experiment are multiplied and integrated for the duration of the current pulse. The reactive

power integrates to zero. As long as the voltage taps on the sample are intact and the current measurement system is dependable, this method will be robust. It does not need a separate experiment for calibration. This is a major advantage of the pulsed current method. The results of the direct and spectral methods support the authenticity of such a calculation. The direct method of integrating the product of the voltage and current signal gives a satisfactorily accurate and consistent value of the resistive energy dissipated during the duration of the pulsed current disturbance. This calculation is the forte of the pulsed current stability experiment.

Summary of Experimental Results

Two types of pulsed current stability experiments were performed. Stability experiment A used the single pulse current pulser which produced pulses of 2 ms pulse width with peak current value proportional to the charged voltage on the capacitor bank. There were two cable sample CICCs used in experiment A. Besides the 9 stainless steel wires in the hybrid cable # 1, all wires in the two 27-strand cables were US-DPC wire. The stability margins for the two cables were calculated. A more complete stability margin was concluded for the US-DPC test sample including the value of the upper limiting current of about 2.5 kA, and the slope in the transition region. Both cables showed an ill-cooled region stability of about 75 - 100 mJ/cc when the volume of only the superconducting strands was taken into account. Based on the shape of the curve, a well-cooled region stability margin of about 1000 mJ/cc and a lower limiting current of about 1.5 kA was predicted. This resulted in an effective heat transfer coefficient value of 369.1 W/m^2K which was considered low. Using the upper limiting current of 2.5 kA, the heat transfer coefficient becomes 1025.3 W/m^2K which is neither too high nor too low. The low heat transfer coefficient was attributed to the inefficient cooling of liquid helium at 4.2 K with zero flow velocity as opposed the usual ITER magnet conditions of supercritical helium at 1.8 K. The energy margin values in the well-cooled region calculated by the direct method for the US-DPC sample were in good agreement with the values predicted by a bench mark model developed for the prevalent

experimental conditions. The ill-cooled region stability margin predicted based on just cable enthalpy was very low as compared to the calculations, perhaps due to some helium enthalpy available and the use of the enthalpy of the incoloy conduit. However, the stability margin observed in the two sample cables of experiment A, based on the volume of only the superconducting strands, was comparable. This implies that the stainless steel strands do not play a role in stabilizing the CICC, as expected.

Stability experiment B used the double pulse current pulser which output two 10 ms current pulses of the same magnitude but with variable time delay between them. The experiment used the hybrid TPX sample with 9 copper and 18 TPX-IGC wires. Based on the limited amount of data for experiments of type B, only part of the ill-cooled region of the stability curve could be identified, which showed stability margins of about 100 mJ/cc, very similar to the ones identified in experiment A.

The self-field losses for the US-DPC test sample cable were calculated for comparison with the associated resistive losses. All self-field losses were negligible except for the coupling losses on the filamentary level within each strand. These losses were calculated with certain assumptions which clearly overestimated the losses, perhaps by about an order of magnitude. More thorough analysis needs to be done to prove or disprove their negligibility compared to resistive losses.

7.2 Future Prospects and Options

The pulsed current stability experiments were considered successful. It was concluded that the pulsed current method represents a viable alternative to the other methods for determining stability margins of CICCs. The results of the experiment were consistent and in good agreement with the analytical model developed.

The stability margins of the test cables could not be identified in all the regions of conductor operation. More data is needed at the appropriate transport current values to identify the missing sections. The problem of self-field losses could not

be resolved completely but the crude comparison made was promising. A more accurate calculation is needed for the self-field losses in the cable. Also, further experiments should be performed with the more appropriate cooling conditions provided by supercritical helium forced-flow at 1.8 K.

The double pulse double pulser showed a lot of promise in its ability to manipulate the pattern in which energy can be dumped into the cable. The pulse width can be made variable with discrete choices by reconfiguring either the capacitor banks or by providing choices of different inductances for the pulse shaping coil. The delay between the pulse widths can be used to get some interesting results. An experiment is proposed which should investigate the dependence of energy dissipation in the cable for the same pulses in terms of magnitude, as a function of the time delay between the pulses. With the possibility of variable pulse widths, the dependence of stability of the cable to similar energy dissipation at different rates can be studied. The pulsed current method using the double pulse current pulser or other useful pulser configurations can be used to investigate the stability of different CICCs to a variety of constructed disturbances in a simple and reliable way.

Appendix A

Experimental Data

The real data as it was received by the data acquisition system is plotted for a few typical cases of experiment A. A complete set of all experimental data is available from the Superconducting Magnet Development Group at Plasma Fusion Center.

A-1 Shot # 1528: Shows the extent of spikes on the signals. It also displays the lack of oscillations without background magnetic field.

A-2 Shot # 1531: Similar to shot # 1528. Instead of the voltage tap CC′ it shows a trial at balancing the inductive signal at AA′ by adding the reversed signal at DD′ to it.

A-3 Shot # 1708: Shows oscillations with background magnetic field. Even with mild oscillatory behavior the voltage signals are quite distorted.

A-4 Shot # 2619: Shows the damping of the oscillations after the pulse and also shows a value of t_{delay} of about 35 ms i.e. the time it takes the resistive voltage to set in after the end of the pulse.

A-5 Shot # 846: Another shot showing oscillations.

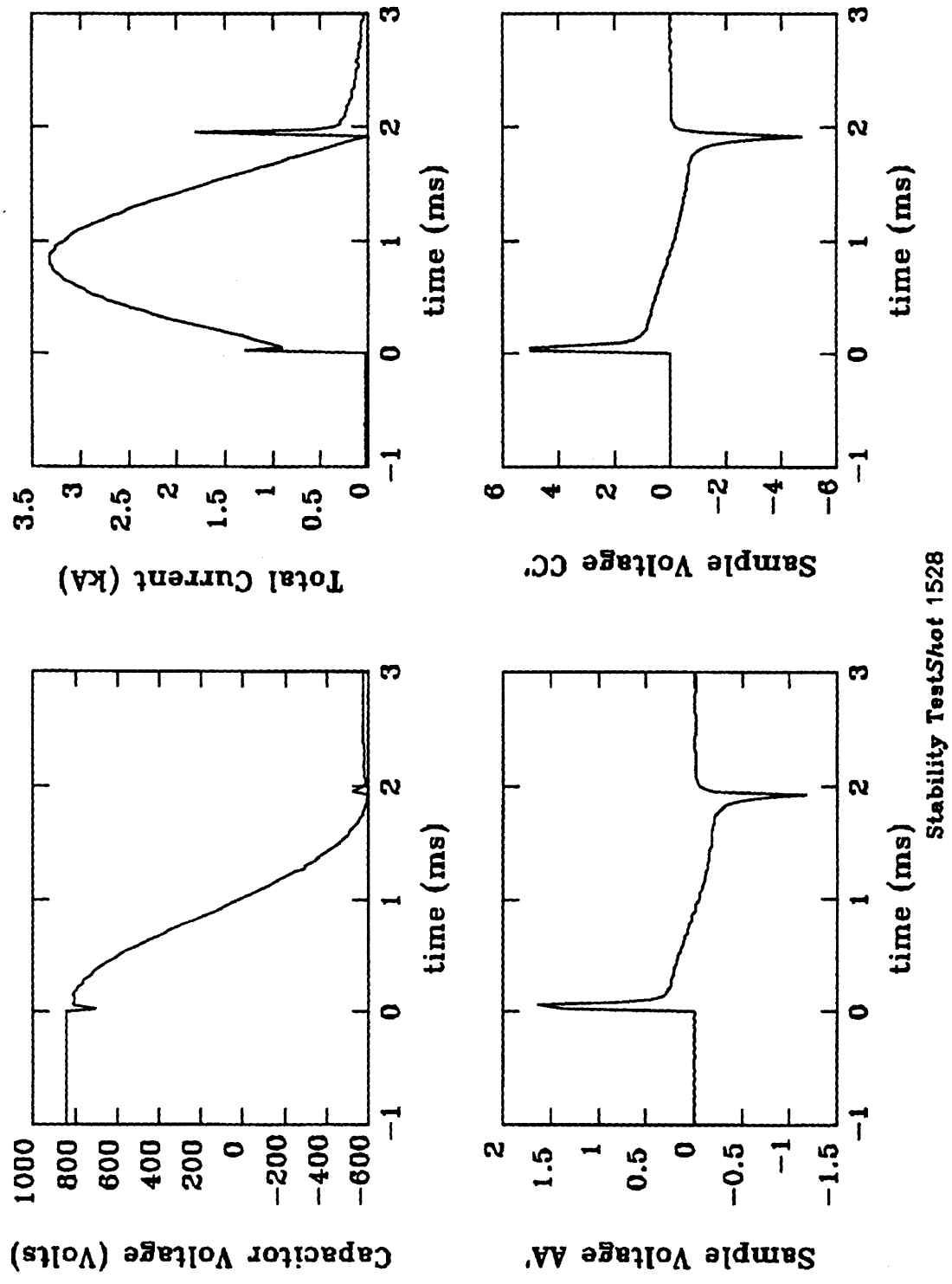

Figure A-1: Shot # 1528

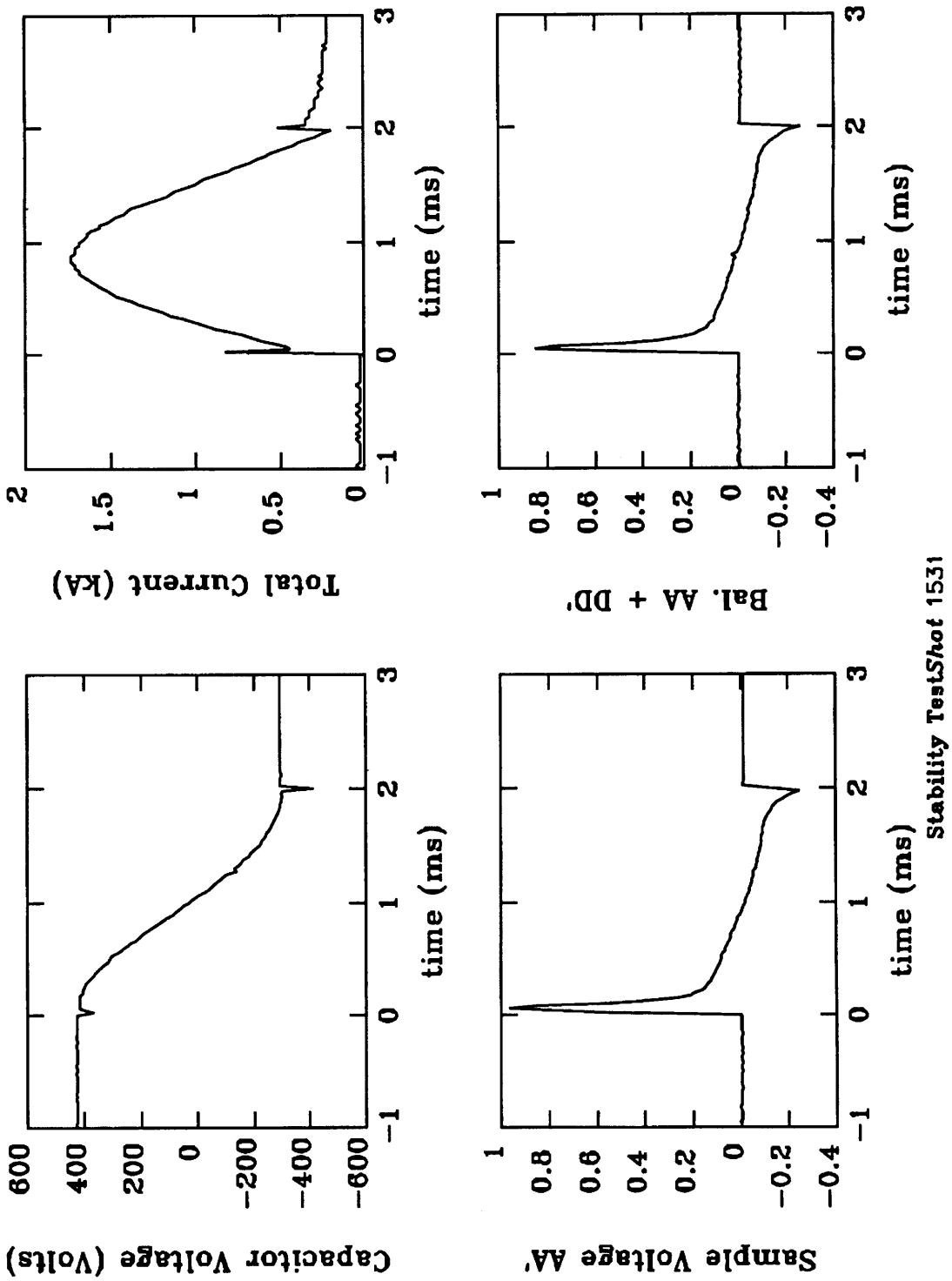

Figure A-2: Shot # 1531

Figure A-3: Shot # 1708

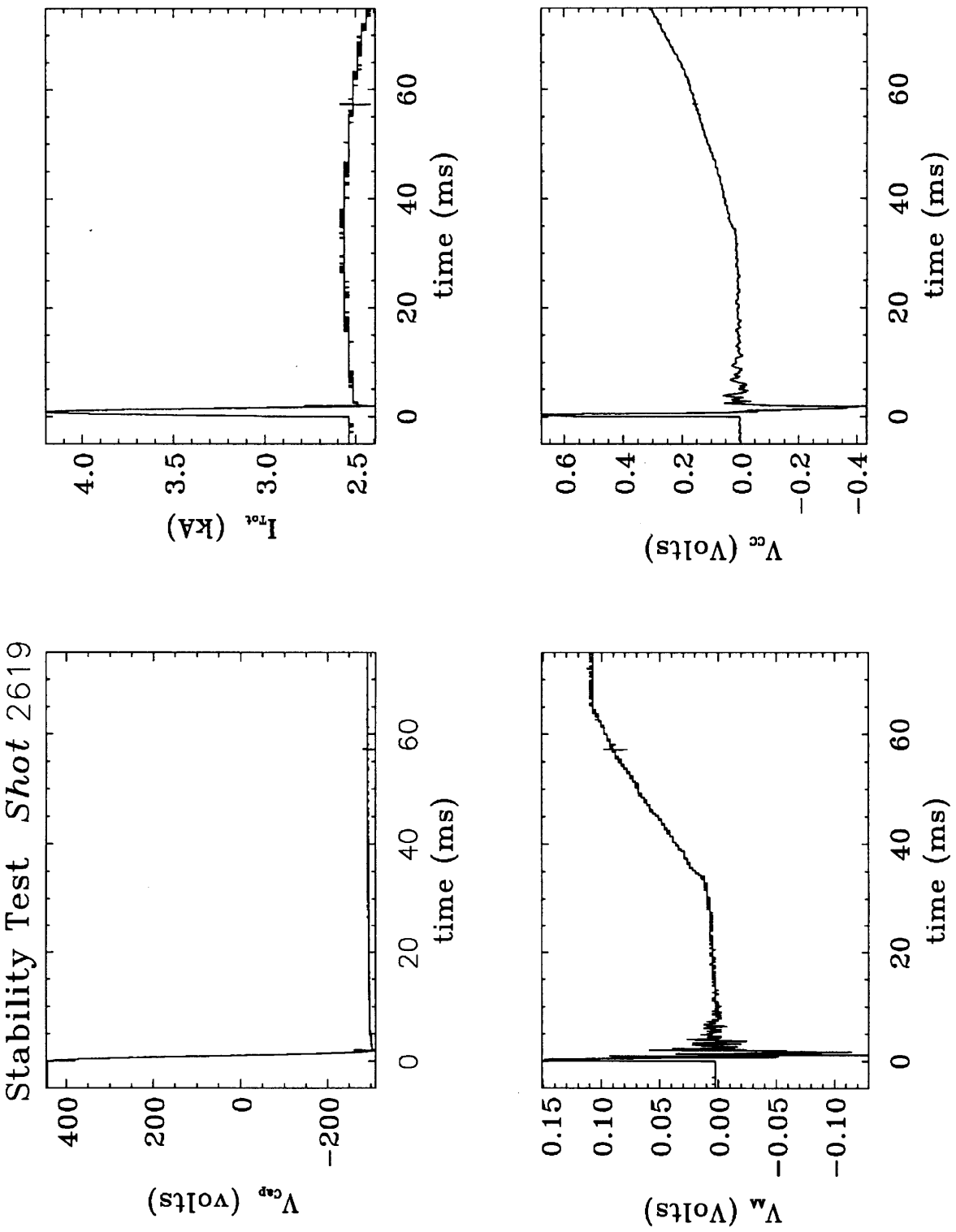

Figure A-4: Shot # 2619

Figure A-5: Shot # 846

Appendix B

Frequency Responses

B-1 20-point 300 hz Cutoff Frequency Low-Pass Filter

B-2 200-point 300 hz Cutoff Frequency Low-Pass Filter

B-3 200-point 1.5 khz Cutoff Frequency Low-Pass Filter

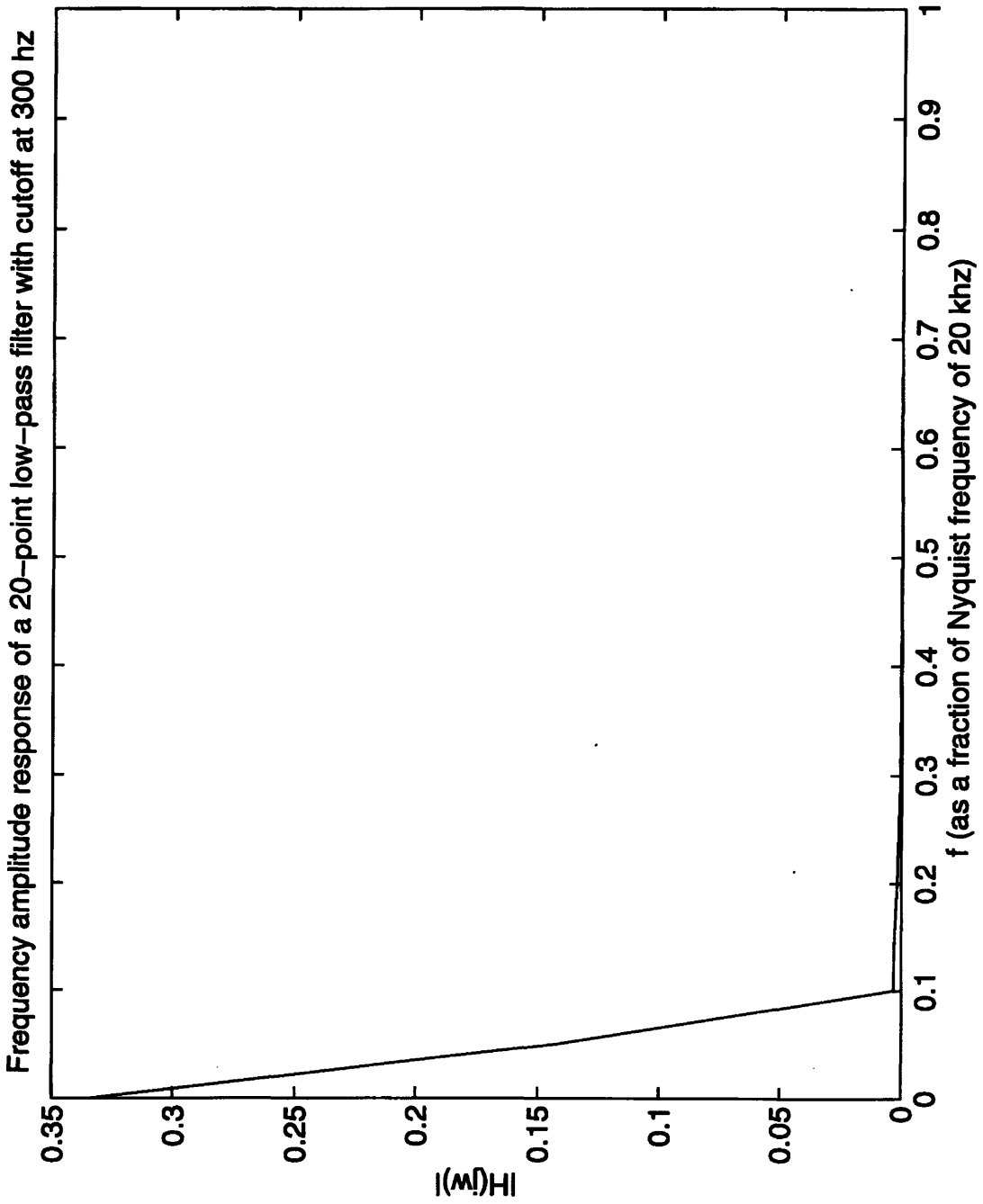

Figure B-1: Frequency amplitude response of 20-point 300 hz cutoff frequency low-pass filter.

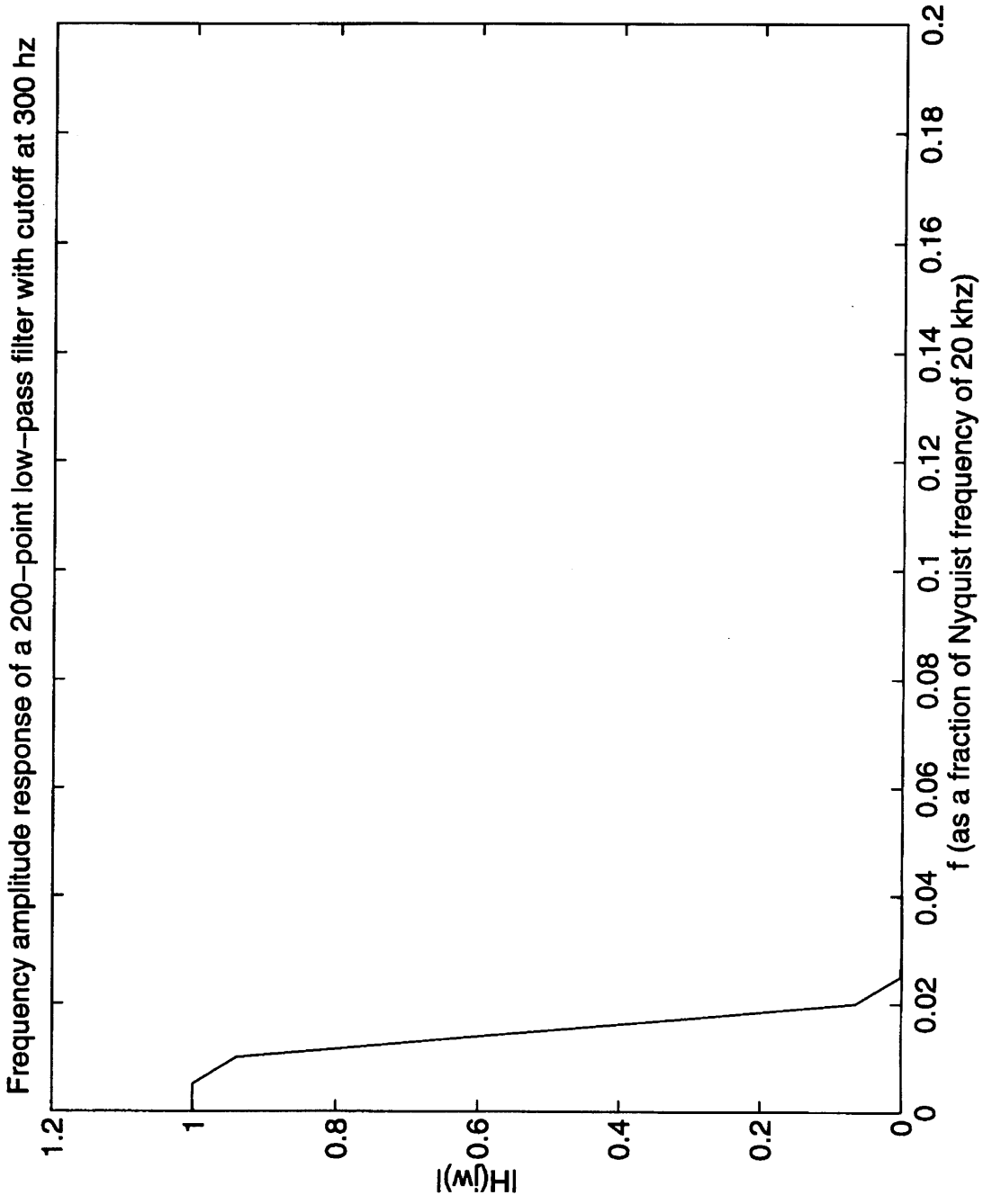

Figure B-2: Frequency amplitude response of 200-point 300 hz cutoff frequency low-pass filter.

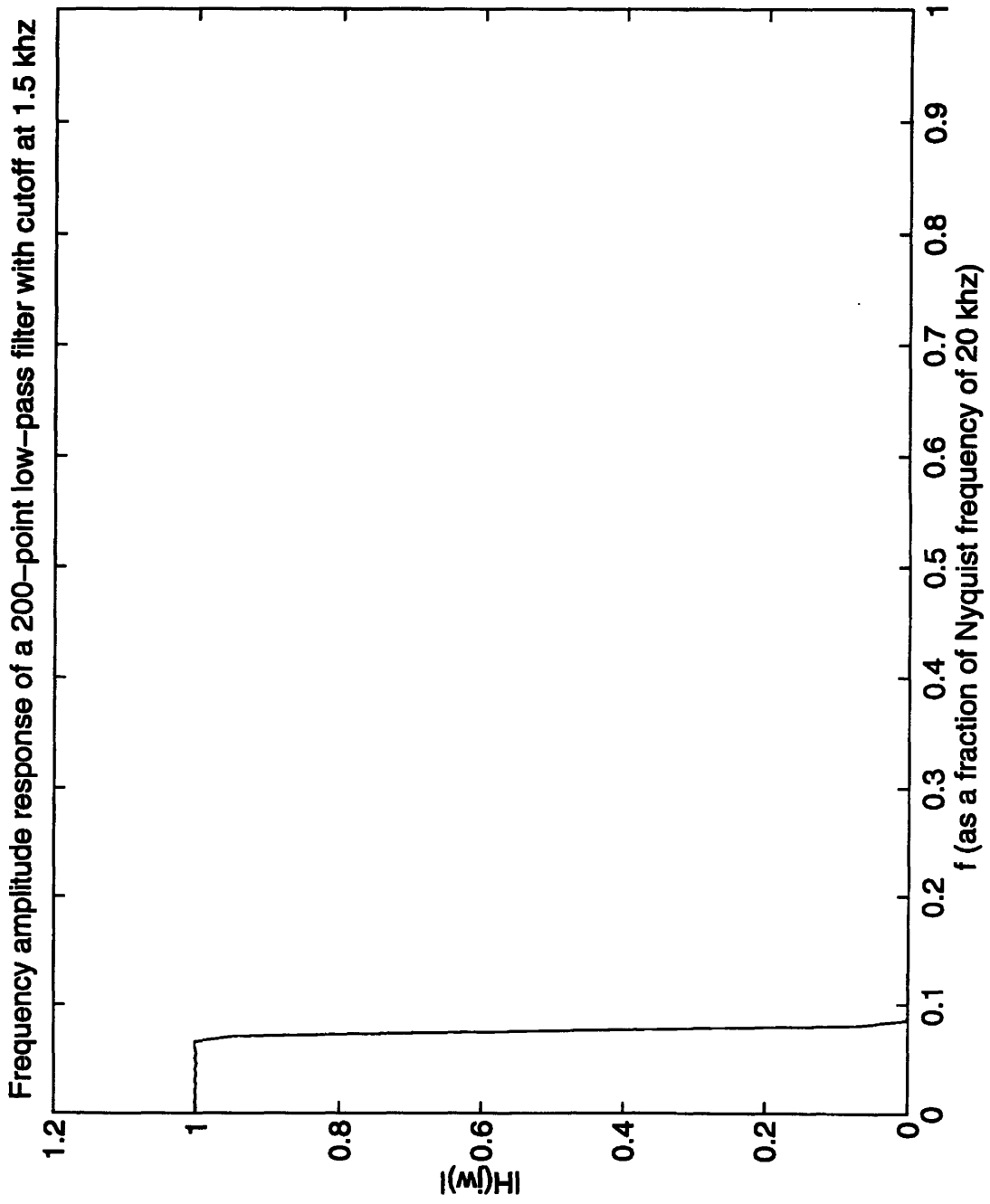

Figure B-3: Frequency amplitude response of 200-point 1.5 khz cutoff frequency low-pass filter.

Appendix C

IDL Code

The IDL code used to retrieve, plot, and analyze data is given here.

C.1 Main plotting program

```
;+++++++++++++++++++++++++++++++++++++++++++++++++++++++++++++++++++++++;
; Procedures for plotting raw data from Stability (ST) RUN              ;
;                              Mustafa K. Ahmed                         ;
;                                 May. 1993                             ;
;+++++++++++++++++++++++++++++++++++++++++++++++++++++++++++++++++++++++;
;
cb = strarr(17) ; Initialize array of channel name strings:
cb(1) = 'sh_8212_01'    ; cb stands for 'channel base'.
cb(2) = 'sh_8212_02'    ; Note that for the sake of clarity,
cb(3) = 'sh_8212_03'    ; cb(0) is not utilized
cb(4) = 'sh_8212_04'
;cb(5) = 'sh_8212_05'
;cb(6) = 'sh_8212_06'
;cb(7) = 'sh_8212_07'
;cb(8) = 'sh_8212_08'
;cb(9) = 'sh_8212_09'
```

```
;cb(10) = 'sh_8212_10'
;cb(11) = 'sh_8212_11'
;cb(12) = 'sh_8212_12'
;cb(13) = 'sh_8212_13'
;cb(14) = 'sh_8212_14'
;cb(15) = 'sh_8212_15'
;cb(16) = 'sh_8212_16'
;
PRINT, '  '
PRINT, '  '
;
ans=' '
print,'Make sure you have the correct calibration factors!'
print,' '
print,'If not, edit calibrationst.dat and rerun program'
print,' '
read,'If calibration file is OK then hit return to continue...',$
ans
openr,1,'calibrationst' ; File of calibration factors
readf,1,numchnls
cb = cb(1:numchnls)
cf = fltarr(2,numchnls,/nozero) ; Create an array of calibration $
factors
readf,1,cf
close,1
;
cfac = cf(1,*)
;
print,' '
print,'                    Terminal type:'
```

```
print,' '
print,'                    1. X windows'
print,' '
print,'                    2. VT 240'
print,' '
read,'Enter number (1 or 2):', term_type
if (term_type eq 1) then ttype='X'
if (term_type eq 2) then ttype='regis'
old_inc=set_inc(1)
shot_list=shots(1-11-11)
n_shots=n_elements(shot_list)
for i=0,n_shots-1 do begin
        old_shot=set_shot(shot_list(i))
        TIME = DATA("SH_8212_TM") ; reads the time base varaible, $
in seconds
        dt=TIME(1)-TIME(0) ; measure of precision
        length = n_elements(time)
        variable = fltarr(length,numchnls)
;
        for j = 0,numchnls-1 do begin
            variable(*,j) = ((data(cb(j))/409.6) - 5.0) * cfac(j)
        endfor
;
;
;Name the variables:
;
        cv  = variable(*,0)     ; Capacitor Voltage (from Pulser)
        aa  = variable(*,1)     ; Sample Voltage AA'
        cc  = variable(*,2)     ; Sample Voltage CC'
        it  = variable(*,3)     ; Total Current (Transport + Pulsed)
```

```
;
        start=-0.41
        fin=0.41
        these=where((time ge start) and (time le fin))
        time1=time(these)
        outfile = 'STA_'+strtrim(fix(shot_list(i)),2)+'.plt/none'
        set_plot,'tek'
        device,filename=outfile,tty=0,/tek4014
        !p.multi=[0,2,2,0,0]
        !p.title='!17Stability Test!18Shot !3' + $
  strtrim(fix(shot_list(i)),2)
        !y.ticks = 0   ; Label Y-axis tick marks,
        !x.ticks = 0  ; and those on the X-axis
        !x.title = '!17time (ms)'
        !y.title = '!17V!S!ICap!N!R (volts)'
        plot,time1*1000,cv(these)
        !y.title = '!17I!S!ITot!N!R (kA)'
        !p.title=' '
        plot,time1*1000,it(these)
        !y.title = '!17V!S!IAA!N!R (Volts)'
        plot,time1*1000,aa(these)
        !y.title = '!17V!S!ICC!N!R (Volts)'
        plot,time1*1000,cc(these)
        device,/close_file
        start=-0.0005
        fin=0.0025
        those=where((time ge start) and (time le fin))
        times=time(those)
; Do the plotting:
;
```

```
        outfile = 'STB_'+strtrim(fix(shot_list(i)),2)+'.plt/none'
        set_plot,'tek'
        device,filename=outfile,tty=0,/tek4014
        !p.multi=[0,2,2,0,0]
        !p.title='!17Stability Test!18Shot !3' + $
strtrim(fix(shot_list(i)),2)
        !y.ticks = 0   ; Label Y-axis tick marks,
        !x.ticks = 0  ; and those on the X-axis
        !x.title = '!17time (ms)'
        !y.title = '!17V!S!ICap!N!R (volts)'
        plot,times*1000,cv(those)
        !y.title = '!17I!S!ITot!N!R (kA)'
        !p.title=' '
        plot,times*1000,it(those)
        !y.title = '!17V!S!IAA!N!R (Volts)'
        plot,times*1000,aa(those)
        !y.title = '!17V!S!ICC!N!R (Volts)'
        plot,times*1000,cc(those)
        device,/close_file
        print,'Done with shot number',shot_list(i)
endfor
stop
end
```

C.2 Main program for energy calculation

Includes the implementation for removing spikes.

```
;+++++++++++++++++++++++++++++++++++++++++++++++++++++++++++++++++++++;
; Procedures for spectrum analysis of stability data                   ;
;                              Mustafa K. Ahmed                        ;
;                                 Aug. 1995                            ;
;+++++++++++++++++++++++++++++++++++++++++++++++++++++++++++++++++++++;
;
cb = strarr(17) ; Initialize array of channel name strings:
cb(1) = 'sh_8212_01'    ; cb stands for 'channel base'.
cb(2) = 'sh_8212_02'    ; Note that for the sake of clarity,
cb(3) = 'sh_8212_03'    ; cb(0) is not utilized
cb(4) = 'sh_8212_04'
ans='a'
done='n'
endp=0.01
openr,1,'calibrationst' ; File of calibration factors
readf,1,numchnls
cb = cb(1:numchnls)
cf = fltarr(2,numchnls,/nozero)
;Create an array of calibration factors
readf,1,cf
close,1
close,11
openw,11,'new1.dat'
printf,11,format='("SHOT #",1X,"It (kA)",1X,"Cap. V. (V)",1X, $
"Spectral in AA(J)",1X,"Direct in AA (J)",1X,"Spectral in CC (J)"$
,1X, "Direct in CC(J)",1X,"Ip_max (kA)")'
cfac = cf(1,*)
old_inc=set_inc(1)
shot_list=shots(1-11-11)
n_shots=n_elements(shot_list)
```

```
cap_volt=fltarr(n_shots)
trans_i=fltarr(n_shots)
peak_pulse_i=fltarr(n_shots)
aaenertl=fltarr(n_shots)
aaenersn=fltarr(n_shots)
ccenertl=fltarr(n_shots)
ccenersn=fltarr(n_shots)
for i=0, n_shots-1 do begin
current_shot=shot_list(i)
shot_num_list=where(shot_list eq current_shot)
shot_no=fix(shot_num_list(0))
old_shot=set_shot(current_shot)
TIME = DATA("SH_8212_TM")
; reads the time base variable, in seconds
dt=TIME(1)-TIME(0) ; measure of precision
length = n_elements(time)
variable = fltarr(length,numchnls)
for j = 0,numchnls-1 do begin
        variable(*,j) = ((data(cb(j))/409.6) - 5.0) * cfac(j)
endfor
   cv  = variable(*,0)  ; Capacitor Voltage (from Pulser)
   aa  = variable(*,1)     ; Sample Voltage AA'
   cc  = variable(*,2)     ; Sample Voltage CC'
   it  = variable(*,3)     ; Total Current (Transport + Pulsed)
aa=aa*0.1
if (shot_list(i) le 846) then aa=aa*0.1
it=it*10
check=intarr(length)
start=0.000
fin=0.002
```

```
tlong=where((time ge 0.0) and (time le 0.002))
coeff=digital_filter(0,15./200.,50,200)
aafilt=convol(aa,coeff)
ccfilt=convol(cc,coeff)
itrans=total(it(0:1000))/1001
cvolt=total(cv(0:1000))/1001
cap_volt(shot_no)=cvolt
peakip=where(time eq 0.001)
peak_pulse_i(shot_no)=it(peakip)-itrans
points=where((time ge start) and (time le fin))
timep=time(points)
n_points=n_elements(points)
cvarr=fltarr(n_points)
itarr=fltarr(n_points)
cvarr=cv(points)
trans_i(shot_no)=itrans
check1=where((time ge (start-0.0002)) and $
(time le (start+0.0006)))
check2=where((time ge (fin-0.0006)) and $
(time le (fin+0.0002)))
ip1=it(check1)-itrans
ip2=it(check2)-itrans
aa1=aa(check1)
aa2=aa(check2)
cc1=cc(check1)
cc2=cc(check2)
n_ck1=n_elements(check1)
n_ck2=n_elements(check2)
ck1=fltarr(n_ck1-1)
ck2=fltarr(n_ck2-1)
```

```
for k=1,n_ck1-1 do ck1(k-1)=ip1(k)-ip1(k-1)
for k=1,n_ck2-1 do ck2(k-1)=ip2(k)-ip2(k-1)
ck_1=fltarr(n_ck1-2)
ck_2=fltarr(n_ck2-2)
for k=1,n_ck1-2 do ck_1(k-1)=ck1(k)*ck1(k-1)
for k=1,n_ck2-2 do ck_2(k-1)=ck2(k)*ck2(k-1)
res1=where(ck_1 lt 0.0)
res2=where(ck_2 lt 0.0)
gtz1=n_elements(res1)
gtz2=n_elements(res2)
last1=res1(gtz1-1)
last2=res2(gtz2-1)
first1=res1(0)
first2=res2(0)
diff1=last1-first1
diff2=last2-first2
if (first1 lt 0) then goto,first
        xod=[first1,first1+diff1+2,first1+2*(diff1+2)$
,first1+3*(diff1+2)]
        yod=ip1(xod)
;       yaa=aa1(xod)
;       ycc=cc1(xod)
        tvec=intarr(3*(diff1+2)+1)
        for l=first1,first1+3*(diff1+2) do tvec(l-first1)=l
        ipnew=spline(xod,yod,tvec,1.0)
;       aanew=spline(xod,yaa,tvec,1.0)
;       ccnew=spline(xod,ycc,tvec,1.0)
        ip1(first1:last1+2)=ipnew(0:diff1+2)
;       aa1(first1:last1+2)=aanew(0:diff1+2)
;       cc1(first1:last1+2)=ccnew(0:diff1+2)
```

```
        first:
        if (first2 lt 0) then goto,second
        xod=[last2+2-3*(diff2+2),last2+2-2*(diff2+2), $
last2-diff2-2,last2+2]
        yod=ip2(xod)
;       yaa=aa2(xod)
;       ycc=cc2(xod)
        tvec=intarr(3*(diff2+2)+1)
        for l=last2+2-3*(diff2+2),last2+2 do  $
tvec(l-(last2+2-3*(diff2+2)))=l
        ipnew=spline(xod,yod,tvec,1.0)
;       aanew=spline(xod,yaa,tvec,1.0)
;       ccnew=spline(xod,ycc,tvec,1.0)
        ip2(first2:last2+2)=ipnew(2*(diff2+2):3*(diff2+2))
;        aa2(first2:last2+2)=aanew(2*(diff2+2):3*(diff2+2))
;        cc2(first2:last2+2)=ccnew(2*(diff2+2):3*(diff2+2))
        second:
        it(check1)=ip1+itrans
        it(check2)=ip2+itrans
;        aa(check1)=aa1
;        aa(check2)=aa2
;        cc(check1)=cc1
;        cc(check2)=cc2
temp=where((time ge start) and (time le fin))
cvdat=cv(temp)
itdat=it(temp)
aadat=aa(temp)
ccdat=cc(temp)
n=n_elements(temp)
poweraa=fltarr(n)
```

```
powercc=fltarr(n)
n0=n_elements(tlong)
pfiltaa=fltarr(n0)
pfiltcc=fltarr(n0)
pfiltaa=aafilt(tlong)*it(tlong)*1000
pfiltcc=ccfilt(tlong)*it(tlong)*1000
poweraa=aadat*itdat*1000
powercc=ccdat*itdat*1000
aaenertl(shot_no)=int_simpson(pfiltaa,0.0,dt,1.0)
aaenersn(shot_no)=int_simpson(poweraa,0.0,dt,1.0)
ccenertl(shot_no)=int_simpson(pfiltcc,0.0,dt,1.0)
ccenersn(shot_no)=int_simpson(powercc,0.0,dt,1.0)
printf,11,format='(/1X,I4,2X,F5.3,5X,F6.1,6X,E10.3,7X, $
E10.3,7X,E10.3,7X,E10.3,7X,F5.3)',shot_list(i),trans_i(i)$
,cap_volt(i),aaenertl(i),aaenersn(i),ccenertl(i), $
ccenersn(i),peak_pulse_i(i)
endfor
device,/close_file
close,11
stop
end
```

C.3 Code for Digital Filter

```
FUNCTION DIGITAL_FILTER,FLOW,FHIGH,A,NTERMS
;+
; NAME:
;       DIGITAL_FILTER
;
```

```
; PURPOSE:
;       Compute the coefficients of a non-recursive, digital
;       filter.  Highpass, lowpass, bandpass and bandstop
;       filters may be constructed with this function.
;
; CATEGORY:
;       Signal processing.
;
; CALLING SEQUENCE:
;       Coeff = DIGITAL_FILTER(Flow, Fhigh, A, Nterms)
;To get coefficients.
;
;       Followed by:
;
;       Yout  = CONVOL(Yin, Coeff)      ;To apply the filter.
;
; INPUTS:
;       Flow:   The lower frequency of the filter as a
;               fraction of the Nyquist frequency.
;
;       Fhigh:  The upper frequency of the filter as a
;               fraction of the Nyquist frequency.
;
;       A:      The size of Gibbs phenomenon wiggles in -db.
;               50 is a good choice.
;
;       Nterms: The number of terms in the filter formula.
;               The order of filter.
;
; * * * * * * * * * * * * * * * * * * * * * * * * * * * * * * *
```

```
; The following conditions are necessary for various types of
; filters:
;
;               No Filtering:   Flow = 0, Fhigh = 1.
;               Low Pass:       Flow = 0, 0 < Fhigh < 1.
;               High Pass:      0 < Flow < 1, Fhigh =1.
;               Band Pass:      0 < Flow < Fhigh < 1.
;               Band Stop:      0 < Fhigh < Flow < 1.
; * * * * * * * * * * * * * * * * * * * * * * * * * * * * * * * *
;
; OPTIONAL INPUT PARAMETERS:
;  None.
;
; OUTPUTS:
;  Returns a vector of coefficients with (2*nterms + 1) elements.
;
; SIDE EFFECTS:
;  None.
;
; RESTRICTIONS:
;  None.
;
; PROCEDURE:
;  This function returns the coefficients of a non-recursive,
;  digital filter for evenly spaced data points.  Frequencies are
;  expressed in terms of the Nyquist frequency, 1/2T, where T
;  is the time between data samples.
;
ON_ERROR,2              ;Return to caller if an error occurs
PI = 3.14159265
```

```
IF (FHIGH LT FLOW) THEN STOP = 1. ELSE STOP = 0.
;
;       computes Kaiser weights W(N,K) for digital filters.
; W = COEF = returned array of Kaiser weights
; N = value of N in W(N,K), i.e. number of terms
; A = Size of gibbs phenomenon wiggles in -DB.
;
IF (A LE 21.) THEN ALPHA = 0. $
        ELSE IF (A GE 50.) THEN ALPHA = 0.1102 *(A-8.7)  $
        ELSE ALPHA = 0.5842*(A-21.)^0.4 + 0.07886*(A-21.)
;
ARG = (FINDGEN(NTERMS)+1.)/NTERMS
COEF = BESELI(ALPHA*SQRT(1.-ARG^2),0)/BESELI(ALPHA,0)
T = (FINDGEN(NTERMS)+1)*PI
COEF = COEF * (SIN(T*FHIGH)-SIN(T*FLOW))/T
COEF = [REVERSE(COEF),FHIGH-FLOW+STOP,COEF] ;REPLICATE IT
RETURN,COEF
END
```

C.4 Frequency Spectrum Plotting Routines

C.4.1 Simple Routine

This is good for a first glance.

```
function power_spectrum,array

fourier=fft(array,-1)
N=n_elements(array)
```

```
if even(N) then begin
  result=fltarr(N/2 + 1)
  result(0)=fourier(0)*conj(fourier(0))
  result(N/2)=fourier(N/2)*conj(fourier(N/2))
  for i=1,((N/2)-1) do result(i)=2*fourier(i) $
*fourier(N-i)
  endif else begin
  result=fltarr((N-1)/2 + 1)
  result(0)=fourier(0)*conj(fourier(0))
  for i=1,(((N-1)/2)-1) do result(i)= $
2*fourier(i)*fourier(N-i)
  endelse
result=result/(N^2)
return,result
end
```

C.4.2 More Involved Routine

This is for the correct picture.

```
function spectrum,data,K,overlap,window_name
datac=complex(data)
;
;
E=n_elements(data)
; find out how many points per segment.
if (overlap) then mtemp=(2*E)/(2*K+1) else $
mtemp=(2*E)/(4*K)
if (mtemp eq fix(mtemp)) then M=fix(mtemp) $
```

```
else M=fix(mtemp)+1
; find out how much zero padding needed
if (overlap) then X=(2*K+1)*M-2*E else X=4*K*M-2*E
datari=fltarr(2*E+X)
; load data into array
for i=0L,E-1 do begin
      datari(2*i)=real(datac(i))
      datari(2*i+1)=imaginary(datac(i))
      endfor
; do zero padding
for i=2*E-1,2*E+X-1 datari(i)=0.0
W1=fltarr(4*M)
W2=fltarr(M)
W3=complexarr(2*M)
MM=M+M
M4=MM+MM
DEN=0.
Window=fltarr(MM)
case window_name of
'SQUARE': for i=0L,MM-1 do Window(i)=1
'PARZEN': Window=PARZEN(MM)
'HANNING': Window=HANNING(MM)
'WELCH': Window=WELCH(MM)
else: begin
      print,'Unknown window: Using default window $
instead!'
      Window=WELCH(MM)
      end
endcase
sumw=total(Window^2)
```

```
p=fltarr(M+1)
X=0
X=X+M
if (overlap) then W2=datari(X-M:X-1)
X=X+M
for kk=1,K do begin
    for joff=-1,0,1 do begin
        if (overlap) then begin
           for j=0,M-1 do W1(joff+j+j+1)=W2(j)
           W2=datari(X-M:X-1)
           X=X+M
           joffn=joff+MM
           for j=0L,M-1 do W1(joffn+j+j+1)=W2(j)
           endif else begin
           for j=long(joff)+1,M4-1,2 do W1(j)= $
datari(M4*(kk-1)+j)
           endelse
        endfor
    for j=0L,MM-1 do begin
        j2=j+j
        W=Window(j)
        W1(j2)=W1(j2)*W
        W1(j2+1)=W1(j2+1)*W
        endfor
    for j=0L,MM-1 do W3(j)=complex(W1(j+j),W1(j+j+1))
    W3=fft(W3,-1)
    for j=0L,M do begin
        if ((j eq 0) or (j eq M)) then begin
           p(j)=p(j)+W3(j)^2
           endif else begin
```

```
            p(j)=p(j)+((W3(j)^2)+(W3(MM-j)^2))
            endelse
         endfor
     DEN=DEN+sumw
     endfor
;
DEN=MM*DEN    ;correct normalization
p=p/DEN
return,p
end
```

C.4.3 Windows

Hanning Window

```
function Hanning, N1, N2
;Hanning window function, 1 or 2 d.
on_error,2
;Return to caller if an error occurs
a = 2 * !pi / (N1 -1)
;scale factor
If n_params(0) eq 1 then begin          ;1d?
        return,.5*(1.-cos(findgen(N1)*a))
   endif else begin              ;2d case
        b = 2 * !pi / (n2-1)     ;dim 2 scale fact
        row = .5*(1.-cos(findgen(n1)*a)) ;One row
        col = .5*(1.-cos(findgen(n2)*b)) ;One column
        RETURN,row # col
   endelse
```

```
end
```

Welch Window

```
function Welch, N1, N2
;Welch window function, 1 or 2 d.
on_error,2
;Return to caller if an error occurs
a1 = (N1-1)/2
a2 = (N1+1)/2
If n_params(0) eq 1 then begin   ;1d?
        return,1.-((findgen(N1)-a1)/a2)^2
   endif else begin              ;2d case
        b1=(N2-1)/2
        b2=(N2+1)/2
        row=1.-((findgen(N1)-a1)/a2)^2    ;One row
        column=1.-((findgen(N2)-b1)/b2)^2 ;One column
        RETURN,row # col
   endelse
end
```

Parzen Window

```
function Parzen, N1, N2
;Parzen window function, 1 or 2 d.
on_error,2
;Return to caller if an error occurs
a1 = (N1-1)/2
a2 = (N1+1)/2
```

```
If n_params(0) eq 1 then begin   ;1d?
        return,1.-abs((findgen(N1)-a1)/a2)
   endif else begin              ;2d case
        b1=(N2-1)/2
        b2=(N2+1)/2
        row=1.-abs((findgen(N1)-a1)/a2)   ;One row
        column=1.-abs((findgen(N2)-b1)/b2);One column
        RETURN,row # col
   endelse
end
```

C.5 Integration Routines

C.5.1 Trapezoidal

```
function int_trapezdl,array,interval
no=n_elements(array)
result=0.0
for i=1,no-1 do result=result+ $
(0.5*interval*(array(i)+array(i-1)))
return,result
end
```

C.5.2 Simpson

```
function int_simpson,data,a,interval,tension
n=n_elements(data)
var=data
x=fltarr(n)
```

```
y=fltarr(n-1)
z=fltarr(n-1)
x=findgen(n)
x=x*interval
x=x+a
y=findgen(n-1)
y=y*interval
y=y+a
y=y+(0.5*interval)
z=spline(x,var,y,tension)
result=0.0
for i=0,n-2 do result=result+ $
(interval*(var(i)+var(i+1)+4*z(i))/6)
return,result
end
```

References

[1] T. Ando et al. Investigation of stability in cable-in-conduit conductors with heat pulse durations of 0.1 to 1 ms. In *Proc ICEC 11*, pages 756–760, Guilford, UK, 1986. Butterworths.

[2] T. Ando et al. Measurements of the stability margin of a Nb_3Sn cable-in-conduit conductor. *IEEE Transactions on Magnetics*, 25(2):2386–2389, 1989.

[3] M. Ashkin. Flux distribution and and hysteresis loss in a round superconducting wire for the complete range of flux penetration. *Journal of Applied Physics*, 50(11):7060, 1979.

[4] C.P. Bean. Magnetization of hard superconductors. *Phys Rev Letters*, 8:250, 1962.

[5] C.P. Bean. The magnetization of high field superconductors. *Revs Mod Phys*, 36:31, 1964.

[6] C.P. Bean and M.V. Doyle. Superconductors as permanent magnets. *Journal of Applied Physics*, 33:3334, 1962.

[7] K. Bennett. Private Communication.

[8] L. Bottura. Stability, protection and AC loss of cable-in-conduit conductors: a designer's approach. *Fus Eng Des*, 20:351–362, 1993.

[9] L. Bottura. Limiting current and stability of cable-in-conduit conductors. *Cryogenics*, 34(10):787–794, 1994.

[10] L. Bottura and J.V. Minervini. Modelling of dual stability in a cable-in-conduit conductor. *IEEE Transactions on Magnetics*, 27(2):1900–1903, 1991.

[11] L. Bottura, N. Mitchell, and J.V. Minervini. Design criteria for stability in cable-in-conduit conductors. *Cryogenics*, 31:510–515, 1991.

[12] H. Brechna. *Superconducting Magnet Systems*. Springer-Verlag, 1973.

[13] W.J. Carr. *AC Loss and Macroscopic Theory of Superconductors*. Gordon and Breach Science Publishers, 1983.

[14] J.W. Carr Jr. Findout. *Journal of Applied Physics*, 46(9):4043, 1975.

[15] J.W. Carr Jr. Findout. *IEEE Transactions on Magnetics*, MAG-13(1):192, 1977.

[16] J.W. Carr Jr. Findout. *IEEE Transactions on Magnetics*, MAG-15(1):240, 1979.

[17] P.F. Chester. Superconducting magnets. *Reports on Progress in Physics*, XXX(II):561–614, 1967.

[18] D. Ciazynski and B. Turck. Stability criteria and critical energy in superconducting cable-in-conduit conductors. *Cryogenics*, 33:1066–1071, 1993.

[19] R.J. Corruccini and J.J. Gniewek. Specific heats and enthalpies of technical solids at low temperatures: a compilation from the literature.

[20] B.S. Deaver. H. Kamerlingh Onnes symposium on the origins of applied superconductivity. *IEEE Transactions on Magnetics*, MAG-23(2):354, 1987.

[21] L. Dresner. Stability optimized, force-cooled, multifilamentary superconductors. *IEEE Transactions on Magnetics*, MAG-13(1):670–672, 1977.

[22] L. Dresner. Stability of internally cooled superconductors: a review. *Cryogenics*, 20:558–563, 1980.

[23] L. Dresner. Parametric study of the stability margins of cable-in-conduit superconductors: theory. *IEEE Transactions on Magnetics*, MAG-17(1):753–756, 1981.

[24] L. Dresner. Superconductor stability, 1983: a review. *Cryogenics*, 24:283–292, 1984.

[25] L. Dresner. Superconductor stability '90: a review. *Cryogenics*, 31:489–498, 1991.

[26] C.Y. Gung. *Energy Dissipation of Composite Multifilamentary Superconductors for High-Current Ramp-field Magnet Applications*. PhD thesis, MIT, Jan 1993.

[27] P.N. Haubenreich et al. Superconducting magnets for fusion. *Nuclear Fusion*, 22:1209, 1982.

[28] D.A. Herrup et al. Time variations of fields in superconducting magnets and their effects on accelerators. *IEEE Transactions on Magnetics*, MAG-25:1643, 1989.

[29] I. Hlásnik. Findout. In *Proc 6th Intl Conf on Magnet Technology*, pages 575–596, Brastilava, 1978. ALFA, Brastilava, Czechoslavakia.

[30] M.O. Hoenig, Y. Iwasa, and D.B. Montgomery. . In *Proc MT-5: Fifth Intl Conf Magnet Tech*, pages 519–524, Rome, Italy, 1975. Laboratori Nazionali del CNEN, Frascati, Italy.

[31] Y. Iwasa. . *Cryogenics*, 19:705, 1979.

[32] Y. Iwasa, M.O. Hoenig, and D.B. Montgomery. Cryostability of a small superconducting coil wound with cabled hollow conductor. *IEEE Transactions on Magnetics*, MAG-13(1):678–681, 1977.

[33] S. Jeong. Data from pulsed field measurements, July, 95.

[34] S. Jeong et al. Ramp-rate limitation experiments in support of the tpx magnets. Unpublished.

[35] A.R. Kantrowitz and Z.J.J. Stekly. A new principle for the construction of stabilized superconducting coils. *Applied Physics Letters*, 6:56–57, 1965.

[36] Y.B. Kim, C.F. Hempstead, and A.R. Strand. Magnetization and critical supercurrents. *Phys Rev*, 129:528, 1963.

[37] E.Y. Klimenko et al. Superconducting magnet for high speed ground transportation. *Cryogenics*, 30:41, 1990.

[38] C. Laverick and G. Lobell. Large high field superconducting magnet systems. *Rev Sci Instrum*, 36(6):825–830, 1965.

[39] A.E. Long. Transverse heat transfer in cicc with central cooling channel. Master's thesis, MIT, 1995.

[40] J.C. Lottin and J.R. Miller. Stability of internally-cooled superconductors in the temperature range 1.8 to 4.2 K. *IEEE Transactions on Magnetics*, MAG-19(3):439–442, 1983.

[41] J.W. Lue. Review of stability experiments on cable-in-conduit conductors. *Cryogenics*, 34:779–786, 1994.

[42] J.W. Lue and J.R. Miller. Heated length dependence of the stability of an internally-cooled superconductor. In *IEEE Proc 9th Symp Eng Prob Fusion Res*, pages 652–655, 1981.

[43] J.W. Lue and J.R. Miller. Parametric study of the stability margins of cable-in-conduit superconductors: experiment. *IEEE Transactions on Magnetics*, MAG-17(1):757–760, 1981.

[44] J.W. Lue and J.R. Miller. Performance of an internally-cooled superconducting solenoid. *Advances in Cryogenic Engineering*, 27:227–234, 1982.

[45] J.W. Lue, J.R. Miller, and L. Dresner. Vapor locking as a limitation to the stability of composite conductors cooled by boiling helium. *Advances in Cryogenic Engineering*, 23:226–234, 1978.

[46] J.W. Lue, J.R. Miller, and L. Dresner. Stability of cable-in-conduit superconductors. *Journal of Applied Physics*, 51(1):772–783, 1980.

[47] B.J. Maddock, G.B. James, and W.T. Norris. composites: heat transfer and steady state stabilization. *Cryogenics*, 9:261–273, 1969.

[48] J.R. Miller and L.T. Summers. The developments of superconductors for applications in high-field, high-current-density magnets for fusion research. *IEEE Transactions on Magnetics*, MAG-23(2):1552, 1987.

[49] Joseph V. Minervini. Private communication.

[50] J.V. Minervini, M.M. Steeves, and M.O. Hoenig. Experimental determination of stability margin in a 27 strand bronze matrix, Nb_3Sn cable-in-conduit conductor. *IEEE Transactions on Magnetics*, MAG-21(2):339–342, 1985.

[51] G.H. Morgan. Theoretical behavior of twisted multicore superconducting wire in a time-varying uniform magnetic field. *Journal of Applied Physics*, 41(9):3673, 1970.

[52] M. Nishi et al. . *J Phys*, 45(C1):131, 1984.

[53] T. Ogasawura et al. Transient field losses in multifilamentary composite conductors carrying dc transport currents. *Cryogenics*, 20:216, 1980.

[54] T. Ogasawura et al. Alternating field losses in superconducting wires carrying dc transport currents: part 2: multifilamentary composite conductors. *Cryogenics*, 21:97, 1981.

[55] A.V. Oppenheim and R.W Shafer. *Discrete-time Signal Processing*. Prentice-Hall, 1989.

[56] T.P. Orlando and K.A. Delin. *Foundations of Applied Superconductivity*. Addison-Wesley, 1991.

[57] K. Osamura, editor. *Composite Superconductors*. Marcel Dekker, Inc., 1994.

[58] T.A. Painter et al. Test results from the Nb_3Sn US-demonstration poloidal coil. *Advances in Cryogenic Engineering*, 37(A):345–354, 1992.

[59] P.E. Phelan et al. Transient stability of a Nb-Ti cable-in-conduit superconductor: experimental results. *Cryogenics*, 29:109–118, 1989.

[60] G. Ries. AC-losses in multifilamentary superconductors at technical frequencies. *IEEE Transactions on Magnetics*, MAG-13(1):524, 1977.

[61] A.C. Rose-Innes and E.H. Rhoderick. *Introduction to Superconductivity*. Pergamon Press, 1978.

[62] D. Saint-James, G. Sarma, and E.J. Thomas. *Type-II Superconductivity*. Pergamon Press, 1969.

[63] T. Sasaki et al. Stability performance of the DPC-TJ Nb_3Sn cable-in-conduit large superconducting coil. *IEEE Transactions on Applied Superconductivity*, 3(1):523–526, 1993.

[64] C. Schmidt. Stability of superconductors cooled by supercritical helium in rapidly changing magnetic fields. *IEEE Transactions on Magnetics*, 28(1):846–849, 1992.

[65] E.A. Scholle and J. Schwartz. MPZ stability under time-dependent, spatially varying heat loads. *IEEE Transactions on Applied Superconductivity*, 3(1):421–424, 1993.

[66] S.R. Shanfield. *Transient cooling in internally cooled, cabled superconductors*. PhD thesis, MIT, 1981.

[67] Z.J.J. Stekly, R. Thome, and B. Strauss. . *Journal of Applied Physics*, 40:2238, 1969.

[68] Z.J.J. Stekly and J.L. Zar. Stable superconducting coils. *IEEE Transactions on Nuclear Science*, NS-12:367–372, 1965.

[69] W.G. Steward. . *Intl J Heat Mass Transfer*, 21:863, 1978.

[70] L.T. Summers et al. A model for the prediction of Nb_3Sn critical current as a function of field, temperature, strain, and radiation damage. *IEEE Transactions on Magnetics*, 27:2041, 1991.

[71] M. Takayasu. Data from ramp-rate limitation test # 14.

[72] M. Takayasu. Personal Communication.

[73] M. Talayasu et al. Critical currents of Nb_3Sn wires of the US-DPC coil. *Advances in Cryogenic Engineering*, 38:619–626, 1992.

[74] O. Tsukamoto and S. Kobayashi. . *Journal of Applied Physics*, 46:1359, 1975.

[75] B. Turck. Coupling losses in various outer normal layers surrounding the filament bundle of a superconducting composite. *Journal of Applied Physics*, 50(8):5397, 1979.

[76] V. Vysotsky, 1995. Group Memo.

[77] V. Vysotsky and V.N. Tsikhon. The stability margins of superconducting cables with two insulated strands. *Cryogenics*, 32(ICEC Supplement):419–422, 1992.

[78] M.N. Wilson. . *IEEE Transactions on Magnetics*, MAG-13:440, 1977.

[79] M.N. Wilson. *Superconducting Magnets*. Oxford Science Publications, 1983.

[80] M.N. Wilson et al. . *J Phys D Appl Phys*, 3:1518, 1970.

[81] Y. Yoshida, T. Isono, Y. Takahashi, and T. Ando. The stability margin and propagation velocity of the Nb_3Sn demo poloidal coil (DPC-EX). *Advances in Cryogenic Engineering*, 37-A:315–322, 1992.

[82] V.B. Zenkevitch, A.S. Romanyuk, and V.V. Zheltov. Losses in composite superconductors at high levels of magnetic field excitation: part 1. *Cryogenics*, 20:703, 1980.

[83] V.B. Zenkevitch, A.S. Romanyuk, and V.V. Zheltov. Losses in composite superconductors at high levels of magnetic field excitation: part 2. *Cryogenics*, 21:13, 1981.

[84] V.B. Zenkevitch, V.V. Zheltov, and A.S. Romanyuk. . *Cryogenics*, 18:93, 1978.

[85] NBS Tech Note # 631, 1972.